A NOVEL HYDRAULIC ENERGY-STORAGE-AND-RETURN PROSTHETIC ANKLE:

DESIGN, MODELLING AND SIMULATION

Anna PACE

A thesis submitted in partial fulfilment of the requirements for the degree of Doctor of Philosophy

School of Science, Engineering & Environment

University of Salford, Salford, UK

2020

To You.

To my family.

To my friends all over the world.

Table of Contents

List of Figures

List of Tables

Acknowledgements

Niamh and Vanessa, who have tolerated, supported and helped me throughout my PhD. Thank you for all this, for what we have shared in these years and for the friendship!

No words are enough to express my deep gratitude towards my beloved family. They have always supported me with their unconditional love, in all my choices, included that of doing a PhD in the UK and going to the US. They have been always ready to cheer me on in good and difficult times. None of the experiences I did in my life would have been possible without them! My mum and dad, my brother and sister in law, and my little nephew Ciccio, thank you! And thank you to all the Pace family, uncles, aunties and cousins for their support!

I miei più sinceri ringraziamenti vanno alla mia famiglia, che mi ha sempre supportata in tutte le mie scelte, comprese le più pazze! Ha sempre rispettato le mie decisioni, tifando per me nei momenti più belli e pieni di soddisfazioni e in quelli più difficili. È sempre stata al mio fianco, sopportando con pazienza il mio essere talvolta pesante e pignola (o, come direbbe mio papà, integralista). Ringrazio quindi mia mamma e mio papà, Paolo, Daniela e il mio piccolo Ciccio, anche se un grazie non sarà mai abbastanza! Ringrazio inoltre dal profondo del mio cuore tutta la famiglia Pace, zii e cugini, per il supporto ricevuto in tutti questi anni.

This PhD would not have started without the intellectual push of a dear friend of mine, Sara Moccia. Since we met at the university, I've always thought very highly of her! She has kept supporting me throughout the PhD, listening to my complains, helping me wisely, and motivating me. I couldn't make it without her guidance.

I want to thank you now all my friends across the world, who supported me, physically and spiritually, because whoever finds a friend, finds a treasure.

Thank you to all my friends in the UK! What an experience in Manchester! A heartfelt thank you to Anna, Kostas and Alex: they have been my Mancunian family, being close to me either in good and in hard times, and always ready to help me. Nicola, Manchester would have not been the same without you! We have shared so much during our PhD journey, and how many conversations in front of a beer (we know pretty much all the Mancunian pubs) or of a nice meal (we tried maybe all the different kinds of cuisine in Manchester). Mariola, you will always

be in my heart! My Hobbit, my friend, who has always warmed my heart and many times helped me to come back down to earth (above all in difficult times). You are a treasure to me and a thank you is not enough. Ti voglio molto bene! A special thank you also to Alessandra, who has always tolerated, supported and helped me (and cheered me up with delicious lasagna)! A huge and heartfelt thank you to all the people in Coniston: Coniston means home for me and I cannot describe how much I have got and learnt from you all! So lucky for having met you in Manchester! Thank you for tolerating me and for your ongoing support! Moreover, thank you to all the friends I had the opportunity to meet in Coniston! Finally, thank you to Anna Maddalena, Arantxa, Enya, Liz, MaJo and Nadia.

A specific thank you to the community of friends met in Chicago, above all Abena, Cristiana, Isme, John-Henry, Rosario, Valentino and all the people of the Elms. Isme, thank you for everything we shared when I was there and for tolerating this crazy Italian girl (I'm waiting for you here in Europe)! Cristiana and Valentino, thank you for listening to me at all times, for the nice chat about everything in life, and for the mutual support. The US experience definitely would not have been the same without you.

And here you are, all my friends in Italy: thank you!! You have always cheered me on, motivated me and gladdened my heart! Thank you for tolerating me because I know that "sometimes" I'm quite annoying, and this PhD has given me challenging times! You all mean a lot to me, a treasure in my heart, Heaven on earth, always with me wherever I will be! Vi voglio un mondo di bene! Without you, I doubt I could make it to complete this PhD and to survive to the UK times! Thank you especially to: Angela (Cugi), Anna Rita, AnnaChiara, Costanza, Fede, Franci, Gabri, Giovi, Giuli, Ila, Jessica, Lucia, Maria Grazia, Minù, Pennino, Pisola, Sara Moccia, Sere, Yhid, Valentina. I hope to celebrate soon with each one of you the end of this PhD journey! Thank you!

As already mentioned, these acknowledgments of course are not enough, because each person I've met in my life has enriched me, and helped me to grow and become what I am. Thus, thanks to Him for putting you all on the path of my life! Last but not least, I want to show my deep gratitude to all "those friends" who have always supported and helped me from up above: don Álvaro, Isidoro, Guadalupe and Toni.

Nomenclature

a	arbitrary constant defining the starting position of the follower in the vertical (y-axis) direction (m)
A	ram bore area (oil side) (m^2)
A	projected pressure area of the O-ring (in^2)
A_{orif}	cross-sectional area of the orifice (m^2)
A_{pipe}	cross-sectional area of the pipes (m^2)
A_w	effective area of the accumulator (m^2)
c	follower overhang (m)
c	parallel spring intercept (Nm)
C	centre of the roller of the follower
C_d	discharge coefficient (dimensionless)
d	piston rod diameter (m)
d_{brg}	stud diameter (m)
$d_{follower}$	follower diameter (m)
d_{O-ring}	O-ring cross sectional diameter (in)
d_{O-ring_OUT}	O-ring outside diameter (in)
$d_{piston\ head}$	piston head diameter (m)
d_{roller}	roller diameter (m)
$d_{valve\_external}$	diameter of the ports of the valve (m)
D	hydraulic ram bore size (m)
D_m	O-ring mean diameter (in)
D_{pipe}	pipe inside diameter (m)
$D_{valve\_internal}$	internal diameter of the valve (m)

e	offset given by the distance between the centre line of the follower and the centre line of the camshaft (m)
E	O-ring Young modulus (Pa)
$E_{gas_{acc}}$	energy stored in the accumulator gas (J)
$E_{oil_{acc}}$	strain energy in the accumulator oil due to oil compressibility (J)
$E_{oil_{cyl}}$	strain energy in the cylinder oil due to oil compressibility (J)
E_{ps}	energy stored in the parallel spring (J)
E_{rs}	energy stored in the return spring (J)
E_{stored}	energy stored in a generic component of the system (J)
f	Darcy friction factor of the pipe (dimensionless)
f_C	linear friction (lb/in)
f_H	friction density (lb/in^2)
F_C	friction component due to O-ring cross-sectional squeeze (lb)
$F_{fr_{cyl}}$	friction force at the piston O-ring (N)
$F_{fr_{guide}}$	total friction at the follower guide (N)
F_{fr1}, F_{fr2}	upper and lower frictional forces at the follower guide (N)
F_h	hydraulic ram force (N)
F_H	friction component due to differential pressure across the O-ring (lb)
F_n	normal force acting on cam profile (N)
$F_{n_{desired}}$	minimum desired value for the normal force between cam and roller (N)
$F_{n_{NO\ spring}}$	normal force between cam and roller when the two return springs are not included in the system (N)
F_s	return-spring force (N)
$F_{s_{required}}$	required return-spring force (N)
F_t	tangential force acting on cam profile (N)
GR	gearbox ratio (dimensionless)

h_{N_2}	convection heat transfer coefficient for nitrogen ($\frac{W}{m^2 \cdot K}$)
H	midpoint between the two lines of action of the two normal forces at the follower guide (N_1, N_2), which lies on the axis of symmetry of the follower
H_S	O-ring shore hardness (°)
I_{rol}	moment of inertia of the roller (kg·m^2)
k	polytropic index (dimensionless)
k	return spring slope (N/m)
k_g	coefficient for the gearbox efficiency (dimensionless)
K	loss coefficient for discrete components (dimensionless)
K_{orif}	discharge coefficient for an orifice ((m^7/kg)$^{1/2}$)
$(ke)_{fol}$	kinetic energy of the follower (J)
$(ke)_{rol}$	kinetic energy of the roller (J)
l	distance between the two lines of action of the two normal forces at the follower guide (N_1, N_2) (m)
$l_{follower}$	follower length (m)
L_{pipe}	pipe length (m)
L_0	O-ring rubbing length (in)
m	roller mass (kg)
m	parallel spring slope (Nm/rad)
m_{N_2}	mass of nitrogen in the accumulator (g)
m_{rol}	mass of the rotating outer part of the roller (kg)
M	follower mass (kg)
M_{brg}	bearing friction moment (Nm)
M_{N_2}	molecular weight of nitrogen (g/mol)
M_{rolres}	rolling resistance moment between cam and roller (Nm)

n_{N_2}	number of moles of nitrogen (mol)
N_1, N_2	upper and lower normal forces at the follower guide (N)
$(pe)_{fol}$	potential energy of the follower (J)
$(pe)_{rol}$	potential energy of the roller (J)
P	point of tangency between cam and roller
P	operating pressure (Pa)
P_a	actual power at the ankle (W)
P_{acc}	accumulator pressure (Pa)
P_{atm}	atmospheric pressure (Pa)
P_{cyl}	cylinder absolute pressure (Pa)
$P_{cyl_{gauge}}$	cylinder gauge pressure (Pa)
$P_{fr_{cyl}}$	power lost due to the friction at the cylinder (W)
$P_{fr_{fol}}$	power lost due to the friction at the follower guide (W)
$P_{fr_{gb}}$	power lost due to the friction in the gearbox (W)
$P_{fr_{rol}}$	power lost due to the friction at the roller bearing (W)
$P_{fr_{rolres}}$	power lost due to the friction at the rolling resistance element (W)
P_{in}	power in input (ankle side) to a generic component of the system (W)
$P_{in_{acc}}$	power in input to the accumulator (W)
$P_{in_{cam}}$	power in input (ankle side) to each cam (W)
$P_{in_{cyl}}$	power in input (ankle side) to each cylinder (W)
$P_{in_{fol}}$	power in input (ankle side) to each follower (W)
$P_{in_{gb}}$	power in input (ankle side) to the gearbox (W)
$P_{in_{ps}}$	power in input (ankle side) to the parallel spring (W)
$P_{in_{rol}}$	power in input (ankle side) to each roller (W)
$P_{in_{rolres}}$	power in input (ankle side) to the rolling resistance element (W)

$P_{in_{tank}}$	power in input to the tank (W)
P_{loss}	power lost in a generic component of the system (W)
$P_{losses_{cyl}}$	power lost in each cylinder (W)
$P_{loss_{HEAT}}$	power lost in the accumulator because of heat transfer (W)
$P_{loss_{tank}}$	power lost in the tank (W)
P_{max}	maximum rated pressure in the accumulator (Pa)
P_{min}	minimum rated pressure in the accumulator (Pa)
P_{out}	power in output (accumulator side) from a generic component (W)
$P_{out_{cam}}$	power in output (accumulator side) from each cam (W)
$P_{out_{cyl}}$	power in output (accumulator side) from each cylinder (W)
$P_{out_{fol}}$	power in output (accumulator side) from each follower (W)
$P_{out_{gb}}$	power in output (accumulator side) from the gearbox (W)
$P_{out_{ps}}$	power in output (accumulator side) from the parallel spring (W)
$P_{out_{rol}}$	power in output (accumulator side) from each roller (W)
$P_{out_{rolres}}$	power in output (accumulator side) from each rolling resistance element (W)
$P_{pre-charge}$	accumulator pre-charge pressure (Pa)
P_{res}	pressure in the reservoir to which the cylinder is connected (either the accumulator or the tank) (Pa)
P_{start}	accumulator initial pressure (Pa)
ΔP_{res}	pressure drop between the cylinder and the reservoir to which it is connected (Pa)
$\Delta P_{to\ acc}$	pressure drop between each cylinder and the accumulator (Pa)
$\Delta P_{to\ tank}$	pressure drop between each cylinder and the tank (Pa)
Q	volumetric flow rate (m³/s)
r	roller radius (m)

R	gas constant (J/mol·K)
R_b	cam base circle radius (m)
R_c	instantaneous rolling radius of the cam surface (m)
R_H, R_V	horizontal and vertical reactions between the roller and the follower stem (N)
R_{rel}	relative rolling radius between cam and roller surface (m)
Re	Reynolds number (dimensionless)
s, u	components of the vector defining the contact point P between cam and roller on cam profile (m)
S_W	actual squeeze of the O-ring cross section (percentage)
T	gas temperature in the accumulator (K)
T_a	actual ankle torque (Nm)
T_{a_r}	required ankle torque (Nm)
T_c	actual torque at the camshaft (Nm)
$T_{c_{PO}}$	push-off cam torque (Nm)
T_{c_r}	required torque at the camshaft (Nm)
$T_{c_{STANCE}}$	stance cam torque (Nm)
$T_{capacity}$	gearbox size (Nm)
T_{env}	environment temperature (K)
T_f	gearbox friction torque (Nm)
$T_{in_{gb}}$	gearbox input (ankle side) torque (Nm)
$T_{pre-charge}$	temperature in the accumulator at pre-charge (K)
T_{ps}	parallel spring torque (Nm)
T_{start}	temperature in the accumulator at the beginning of the gait cycle (K)
T_w	wall temperature (K)
ΔT_{poly}	change in temperature in the accumulator due to polytropic process (K)

$\Delta T_{transfer}$	change in temperature in the accumulator due to heat transfer (K)
ΔT_{total}	total change in temperature in the accumulator for each piston displacement (K)
V	flow velocity across the pipe diameter (m/s)
V_A	accumulator volume (m³)
V_{acc}	oil volume in the accumulator (m³)
$V_{acc_{pre-charge}}$	oil volume in the accumulator at pre-charge (m³)
$V_{acc_{start}}$	oil volume in the accumulator at the beginning of the gait cycle (m³)
V_{cyl}	oil volume in the cylinder (m³)
V_{gas}	gas volume in the accumulator (m³)
$V_{gas_{pre-charge}}$	gas volume in the accumulator at pre-charge (m³)
$V_{gas_{start}}$	gas volume in the accumulator at the beginning of the gait cycle (m³)
V_{max}	maximum accumulator volume (m³)
V_{min}	minimum accumulator volume (m³)
$\Delta V_{oil\ flow}$	change in oil volume in the accumulator over each simulation time step (m³)
ΔV_{β}	total change in oil volume due to its compressibility (m³)
$\Delta V_{\beta_{acc}}$	change in accumulator oil volume due to the oil compressibility (m³)
$\Delta V_{\beta_{cyl}}$	change in cylinder oil volume due to the oil compressibility (m³)
x_{pre}	pre-compression of the return spring (m)
(x_P, y_P)	coordinates of the contact point P between cam and roller (m)
y	piston linear displacement (m)
$\dot{y}$	piston linear velocity (m/s)
$\ddot{y}$	piston linear acceleration (m/s²)
y_0	return spring intercept (N)
Δy	piston incremental displacement (m)

W	hydraulic ram work/cam work (J)
α	cam pressure angle (rad)
α_c	cam angular acceleration (rad/s^2)
β	oil bulk modulus (Pa)
β	roller angle of rotation (rad)
$\dot{\beta}$	roller angular velocity (rad/s)
$\ddot{\beta}$	roller angular acceleration (rad/s^2)
ε	O-ring squeeze ratio (dimensionless)
η_g	gearbox efficiency (percentage)
θ_a	ankle angle of rotation (rad)
θ_c	cam angle of rotation (rad)
μ	fluid viscosity (Pa·s)
μ_{brg}	friction coefficient of the roller bearing (dimensionless)
μ_f	friction coefficient between the O-ring and the cylinder wall (dimensionless)
μ_{rolres}	coefficient of rolling friction (dimensionless)
μ_{sl}	coefficient of sliding friction of the follower bearing (dimensionless)
v_f	fluid kinematic viscosity (m^2/s)
ρ	fluid density (kg/m^3)
ρ_{N_2}	density of nitrogen (kg/m^3)
τ	thermal time constant (s)
ω_a	ankle angular velocity (rad/s)
ω_c	cam angular velocity (rad/s)
ω_{rel}	relative angular velocity between cam and roller (rad/s)

Abstract

In an intact ankle, tendons crossing the joint store energy during the stance phase of walking prior to push-off and release it during push-off, providing forward propulsion. Most prosthetic feet currently on the market – both conventional and energy storage and return (ESR) feet – fail to replicate this energy-recycling behaviour. Specifically, they cannot plantarflex beyond their neutral ankle angle (i.e. a 90° angle between the foot and shank) while generating the plantarflexion moment required for normal push-off. This results in a metabolic cost of walking for lower-limb amputees higher than for anatomically intact subjects, combined with a reduced walking speed.

Various research prototypes have been developed that mimic the energy storage and return seen in anatomically intact subjects. Many are unpowered clutch-and-spring devices that cannot provide biomimetic control of prosthetic ankle torque. Adding a battery and electric motor(s) may provide both the necessary push-off power and biomimetic ankle torque, but add to the size, weight and cost of the prosthesis. Miniature hydraulics is commonly used in commercial prostheses, not for energy storage purposes, but rather for damping and terrain adaptation. There are a few examples of research prototypes that use a hydraulic accumulator to store and return energy, but these turn out to be highly inefficient because they use proportional valves to control joint torque. Nevertheless, hydraulic actuation is ideally suited for miniaturisation and energy transfer between joints via pipes.

Therefore, the primary aim of this PhD was to design a novel prosthetic ankle based on simple miniature hydraulics, including an accumulator for energy storage and return, to imitate the behaviour of an intact ankle. The design comprises a prosthetic ankle joint driving two cams, which in turn drive two miniature hydraulic rams. The "stance cam-ram system" captures the eccentric (negative) work done from foot flat until maximum dorsiflexion, by pumping oil into the accumulator, while the "push-off system" does concentric (positive) work to power push-off through fluid flowing from the accumulator to the ram. By using cams with specific profiles, the new hydraulic ankle mimics intact ankle torque. Energy transfer between the knee and the ankle joints via pipes is also envisioned.

A comprehensive mathematical model of the system was defined, including all significant sources of energy loss, and used to create a MATLAB simulation model to simulate the operation of the new device over the whole gait cycle. A MATLAB design program was also implemented, which uses the simulation model to specify key components of the new design to minimise energy losses while keeping the device size acceptably small.

The model's performance was assessed to provide justification for physical prototyping in future work. Simulation results show that the new device almost perfectly replicates the torque of an intact ankle during the working phases of the two cam-ram systems. Specifically, 78% of the total eccentric work done by the prosthetic ankle over the gait cycle is returned as concentric work, 14% is stored and carried forward for future gait cycles, and 8.21% is lost. A design sensitivity study revealed that it may be possible to reduce the energy lost to 5.83% of the total eccentric work. Finally, it has been shown that the main components of the system – cams, rams, and accumulator - could be physically realistic, matching the size and mass of the missing anatomy.

1. Chapter 1: Introduction

Arnaldo Pomodoro (1990), Sphere

"Call to mind from whence ye sprang:
Ye were not form'd to live the life of brutes,
But virtue to pursue and knowledge high"

(Dante Alighieri (c. 1321), Divine Comedy, Inferno, Canto XXVI, vv. 118-120)

1.1   Background

Lower-limb amputees using prosthetic feet currently on the market generally show a metabolic cost of walking higher than anatomically intact subjects, combined with a reduced walking speed. Higher energy expenditures and lower speeds are associated with higher amputation levels (Waters & Mulroy, 1999).

A major reason for these deficits lies in one particular weakness of most prosthetic feet, both conventional and energy storage and return (ESR), currently on the market: they fail to replicate the energy recycling behaviour of an anatomically intact ankle, where the Achilles tendon stretches during stance prior to push-off and recoils during push-off, helping with forward propulsion and reducing the metabolic cost of walking (Ishikawa *et al.*, 2005; Sawicki & Ferris, 2008). On the contrary, commercially available passive prosthetic feet, including ESR feet with flexible keels, store and return energy in an uncontrolled and untimely manner (Segal *et al.*, 2012). This is because they are characterised by a neutral ankle angle, which is the relative position of the prosthetic foot and shank during standing and, when the foot moves away from neutral, it produces a restoring moment that acts to return it to neutral. Therefore, when the foot is plantarflexed, it will produce a dorsiflexion moment, rather than the plantarflexion moment required for normal push-off. In other words, the conventional and ESR feet currently on the market cannot actively plantarflex beyond their neutral angle, leading to an increase in the metabolic cost of walking compared with anatomically intact subjects (Caputo & Collins, 2014; Collins & Kuo, 2010; Huang *et al.*, 2015).

Different researchers have tried to address the limitations of unpowered (passive) prosthetic feet, both conventional and ESR, and thereby mimic the controlled storage and return of mechanical energy seen in anatomically intact subjects. Moreover, it is believed that prosthetic feet that mimic the slope of the ankle joint's torque-versus-angle curve, which is referred to as "quasi-stiffness", improve amputees' gait (Hansen *et al.*, 2004; Versluys *et al.*, 2009). However, what is often not mentioned is that this curve is not the same in the different phases of gait, implying that a single spring characteristic may not be suitable.

One approach to restoring normal push-off is to power the prosthesis using a battery and electric motor(s). This has the potential to provide both the necessary push-off power and

biomimetic ankle torque. A well-known attempt to improve push-off at the end of stance is that of Hugh Herr and colleagues (Herr & Grabowski, 2012). The resulting commercial device (the Empower, ex-BiOM) relies on electrical power from a battery to produce active push-off. Although there is some elastic energy storage and return, this is similar in nature to that seen in commercial ESR prostheses, with uncontrolled energy return. This critique is supported by the fact that the reduction in metabolic cost for the amputee when using the BiOM, in comparison to using a passive ESR foot, is slightly less than the metabolic equivalent of the energy input from the electric motor, implying that there is no improvement in energy storage and return over commercial ESR prostheses (Herr & Grabowski, 2012). The disadvantages of powered designs are that batteries are poorly suited to the large numbers of charge-discharge cycles that occur in walking, they require charging at regular intervals, and, together with the electric motor(s), they increase the size, weight and cost of the prosthesis. Indeed, in a recently published review of robotic exoskeletons, the electrical power supply problem was highlighted as being "…one (if not the largest) issue…" (Young & Ferris, 2017). For these reasons, the focus in this thesis is to improve passive energy storage and return (ESR) so that it provides all or most of the push-off power, so that much smaller batteries are needed primarily for control, not propulsion.

Whether incorporated in powered or unpowered prostheses, advanced ESR concepts for energy storage and return can be broadly classified as either: a) clutch-and-spring devices; or b) hydraulic devices. Clutch-and-spring devices have two major disadvantages. Firstly, the control is discrete rather than continuous, locking and releasing the spring, thus preventing smooth biomimetic control. Secondly, such an approach makes energy transfer between the knee and the ankle joints difficult, leading to complex, and often heavy, solutions involving the use of mechanical transmissions to inter-connect the joints.

A hydraulic approach based on using an accumulator to store and return energy has several potential advantages. Because they typically operate at pressures of up to $200\ bar$, hydraulic systems have very high power densities and are therefore well suited to miniaturisation, an important requirement in prosthetics. For example, during normal walking, maximum ankle torque is around $100\ Nm$, which would correspond to an actuator that displaces just $5\ cc/radian$ at $200\ bar$. Short term energy storage is another important requirement for

which hydraulic accumulators are well suited. For the relatively small amounts of energy stored and returned over one gait cycle, a $0.05 \ l \ (= 50 cc)$ pressurised gas accumulator would be adequate, operating between 190 and $200 \ bar$. Finally, hydraulic actuation is ideally suited for transferring energy between joints because the transfer mechanism involves only pipes and fluid, rather than gears and linkages. This is of particular importance for higher level amputees who could benefit if the excess of eccentric work at the knee could be stored and used in a controlled manner at other joints.

Whilst the application of miniature hydraulics is common in prosthetics (e.g. for knee/ankle damping), this very rarely involves using a hydraulic accumulator as an energy store. Further, hydraulic transfer of energy between prosthetic joints has not been demonstrated. With the exception of the work that led to this PhD (Gardiner *et al.*, 2017), the few examples that have included an accumulator as an energy store use proportional valves (i.e. variable flow resistances) to control pressures and hence joint torques. This is an inherently dissipative approach that leads to high energy losses. For example, Richter *et al.* (2016) concludes "...the system is highly inefficient in an energetic sense...". The approach adopted by Gardiner *et al.* (2017), and also in this thesis, avoids this problem by continuously controlling the torque through changes in fluid displacement per radian rather than pressure.

Based on the arguments above, previous work at the University of Salford focussed on the development of a lower-limb prosthesis using miniature hydraulics. A concept design was developed based on a hydraulic accumulator and a variable displacement actuator (VDA) driven by the ankle joint (Gardiner *et al.*, 2017). This provides continuous biomimetic control of the ankle torque throughout the gait cycle, mimicking the intact ankle, while storing all of the negative work done from heel strike until maximum dorsiflexion, which is then returned in a controlled and timely manner to power push-off. Furthermore, the accumulator could be used as a common energy store allowing the transfer of energy between the knee and the ankle joints via pipes. The simulation results were promising and suggested that, despite the significant energy losses involved, a hydraulic VDA-based prosthetic ankle could improve amputee gait by restoring normal push-off. However, for this approach to be a success, a new miniature, low-losses, lightweight VDA would be required that is half the displacement of the smallest commercially available device that could be found. A VDA is a highly specialised and

complex component and it would not be appropriate to develop a new VDA just for the prosthetics application.

Therefore, in this PhD a new and simpler concept design has been investigated.

1.2   Aim and Objectives

The overarching aim of this work was to design a novel prosthetic ankle based on simple miniature hydraulic components, including an accumulator for energy storage and return, to imitate the behaviour of an intact ankle. To achieve this, two objectives were defined:

1. Develop a concept design, using simple hydraulic components, that:
    a) Mimics intact ankle torque while storing the negative work done from heel strike to maximum dorsiflexion in the accumulator and returning it during push-off in a controlled way in terms of timing and amount of energy flow.
    b) Allows energy transfer between the knee and the ankle joints via pipes – for example, to store the eccentric work done at the knee and return it at the ankle to assist with forward propulsion during push-off.
2. To demonstrate through simulations that the expected performance of the new design justifies physical prototyping in the future.

1.3   Overview of Thesis

The remainder of this thesis is separated into seven chapters (2-8). Chapter 2 is a literature review that provides a basis for this PhD work, including investigating current issues in lower-limb amputees gait, weaknesses of commercially available passive prosthetic feet, and previous research attempts to mimic the energy recycling behaviour of an intact ankle.

Chapter 3 builds on the literature review to define the primary aim and objectives of the PhD. This is followed by an explanation of the engineering design process including: the definition of design requirements and constraints; and the reasoning leading to the conceptual design.

The novel prosthetic ankle design is described in detail including the rationale behind the selection of each component.

Chapter 4 describes in detail the mathematical model of the new hydraulic ankle, including the equations governing the operation of each component and all significant sources of energy loss, in order to obtain a realistic estimate of the energy efficiency of the new device.

Chapter 5 explains the simulation model implemented in MATLAB, based on the mathematical model described in Chapter 4, which simulates the operation of the new device over the whole gait cycle, as it stores and returns energy at the ankle joint. A design program is also described, implemented in MATLAB, which uses the simulation model to specify key components of the new design.

Chapter 6 explains the process followed for the preliminary design of the main components of the system. The design program described in Chapter 5 was used to specify the size of the key components based on two design objectives, namely to minimise the energy losses while keeping the device size acceptably small.

Chapter 7 first considers the different sources of energy loss in the final design established in Chapter 6, to identify the most significant sources. Secondly, the results of a sensitivity study are presented, in which the values of the design parameters were varied over sensible ranges to establish where energy losses may be particularly sensitive to changes in the design parameters and, hence, strict constraints need to be imposed.

Chapter 8 summarises the PhD work, drawing conclusions with respect to the initially stated aim and objectives, highlighting the novel contributions to the field, discussing limitations, and making proposals for future work.

2.Chapter 2: Literature review
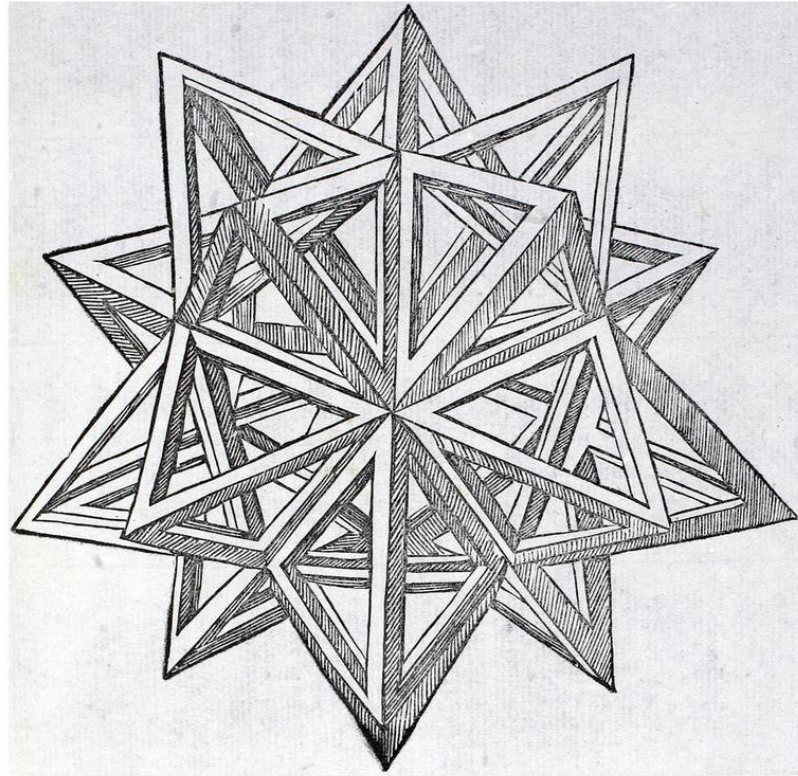
Leonardo Da Vinci, Icosaedron elevatum vacuum

"When you put together the Water Science, remember to put beneath each proposition
its benefits, to what this science is not useless."

(Leonardo Da Vinci)

Lower limb amputees using a prosthetic foot generally show a higher metabolic cost of walking compared with anatomically intact subjects. The higher the level of amputation, the higher is the energy expenditure, measured as the oxygen cost per metre (Genin *et al.*, 2008; Waters & Mulroy, 1999). In addition, this high energy consumption is combined with a decrease of walking speed, with lower speed associated with higher amputation level, as Waters and Mulroy (1999) showed in their study: walking speed for trans-femoral amputees was reported to be approximately 40% of anatomically intact controls. Conversely, Jarvis *et al.* (2017) found that walking speed of young military, unilateral transtibial and transfemoral amputees, after completing their rehabilitation program, is comparable with anatomically intact subjects, but this study cohort was not representative of the general amputee population. Both Jarvis and Perry found that energy expenditure is even greater in bilateral amputees (Jarvis *et al.*, 2017; Perry *et al.*, 2004). A major reason for these deficits lies in one weakness of the vast majority of the prosthetic feet currently on the market: they fail to replicate the energy recycling behaviour of an intact ankle, where the Achilles tendon plays a key role in reducing the metabolic cost of walking (Ishikawa *et al.*, 2005; Sawicki & Ferris, 2008), stretching during stance prior to push-off and recoiling during push-off. Specifically, during walking, the Achilles tendon contributes almost 84% of the total ankle peak power at push-off, while the gastrocnemius muscle provides the remaining 16%.

2.1   Current prosthetic feet

The vast majority of prosthetic feet currently on the market are passive, and can be classified into one of two categories: conventional and energy storage and return (ESR) prosthetic feet. The former represents the first prostheses designed for lower limb amputees, the most common of which is the Solid Ankle Cushion Heel (SACH) foot. The SACH foot comprises a wooden keel embedded in a polymeric material and a polyurethane wedge at the heel, providing shock absorption and (pseudo) plantarflexion at heel strike. During walking, the energy absorbed during stance is mainly dissipated in the viscous material these conventional feet are made of, which likely contributes to a highly reduced peak power during push-off with respect to an intact ankle (see Figure 2.1(A)), and a consequent increase in the metabolic cost of walking (Segal *et al.*, 2012).
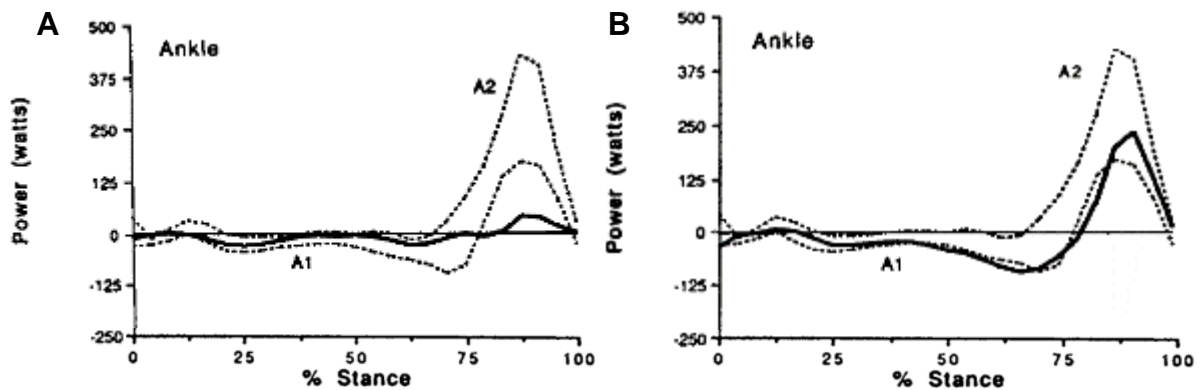
Figure 2.1 Power at the ankle joint in an anatomically intact subject (dotted lines, mean ± 1 SD) and in a transtibial amputee (solid lines) wearing (A) a SACH foot and (B) a Flex-foot. Graphs are plotted as a percentage of the stance phase. Image adapted from Gitter *et al.* (1991).

ESR feet were developed with a view to addressing the observed high metabolic cost of amputee gait with conventional feet. The widely assumed design principle is that by using flexible keels, energy could be stored early in the gait cycle and returned later in the cycle. The Seattle Foot – one of the early ESR feet – was characterised by a keel made of Delrin, while the Flex-foot - the first "advanced" ESR foot – included carbon fibre laminates. The "advanced" prosthetic feet made of carbon fibre, currently widely used by lower limb amputees, are characterised by an increased push-off power with respect to conventional feet (Figure 2.1). Nevertheless, several studies have shown that they are not able to decrease significantly the metabolic cost of walking and gait asymmetries (Gardiner *et al.*, 2016; Hsu *et al.*, 2006; van der Linde *et al.*, 2004; Versluys *et al.*, 2009) and that they return energy in an uncontrolled and untimely manner (Segal *et al.*, 2012):

- The eccentric work stored during load acceptance (i.e. from heel strike up to foot flat, which is maximum plantarflexion (A0 in Figure 2.2)) is completely returned during early mid-stance as the prosthetic ankle returns to its neutral angle (i.e. the angle defined by the relative position of the prosthetic foot and shank during the standing position as Figure 2.3 shows). In this way, this returned energy produces unwanted propulsion early in mid-stance and it is not available for push-off.

- Then, the eccentric work stored from the neutral ankle angle up to maximum dorsiflexion is usually lower than the one stored in an intact ankle (negative area A1 in Figure 2.2), and it is returned during push-off and also too late in stance (i.e. too close to toe-off (Versluys *et al.*, 2009)), but it cannot produce the plantarflexion moment required for a normal push-off, because the ankle cannot actively plantarflex beyond its neutral angle. Thus, the

positive energy (A2 in Figure 2.2) will be lower in a prosthetic ankle than in an intact ankle (Segal *et al.*, 2012; Takahashi *et al.*, 2015), and it will be returned exactly at toe-off, therefore with a delay with respect to an intact ankle (Takahashi *et al.*, 2015) (see peak P1 Figure 2.4 (C) and Figure 2.5).

A
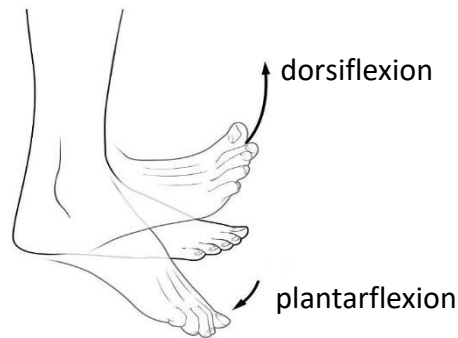
B
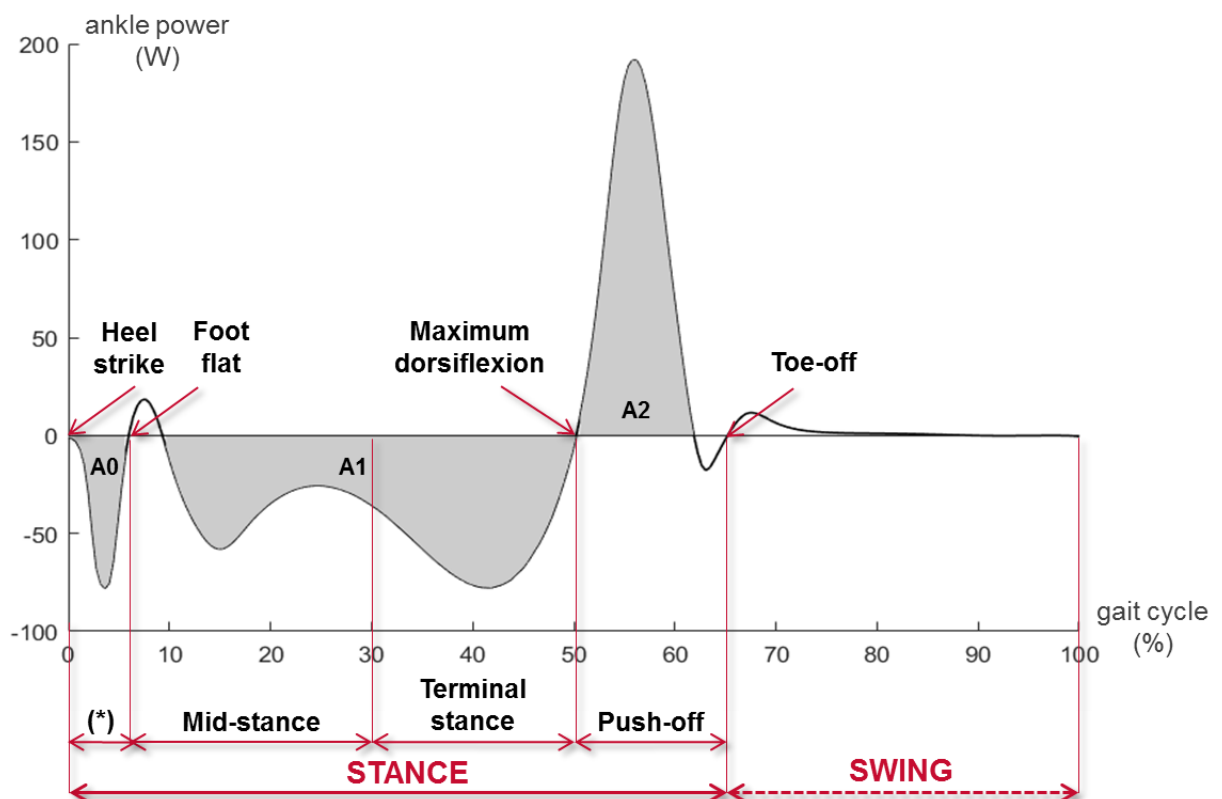
Figure 2.2 (A) Dorsiflexion and plantarflexion at the ankle joint (image sourced from http://sprintfasterdubai.blogspot.com/2015/10/dorsiflexionunderrated.html). (B) Averaged ankle power over the full gait cycle in seven anatomically intact subjects walking at self-selected speed (input data from Bari (2013)). The grey areas delimited by the power curve constitute the ankle energy (work done). The negative areas – A0 and A1 – represent the negative work, that is energy absorption, while the positive area – A2 – represents the positive work, that is energy generation. Muscles (gastrocnemius muscle in particular) and tendons (Achilles tendon specifically) crossing the ankle joint work together to produce a large portion of the mechanical work required for walking. The contribution given by muscles to the total power output is rather small, while tendons store and return a significant amount of mechanical energy (Sawicki & Ferris, 2008). The symbol (*) represents the "load acceptance" phase of the gait cycle.

Figure 2.3 Example of the neutral angle for a prosthetic foot, defined as the angle between the prosthetic foot and the prosthetic shank during standing position. Figure adapted from Medical EXPO (2018).
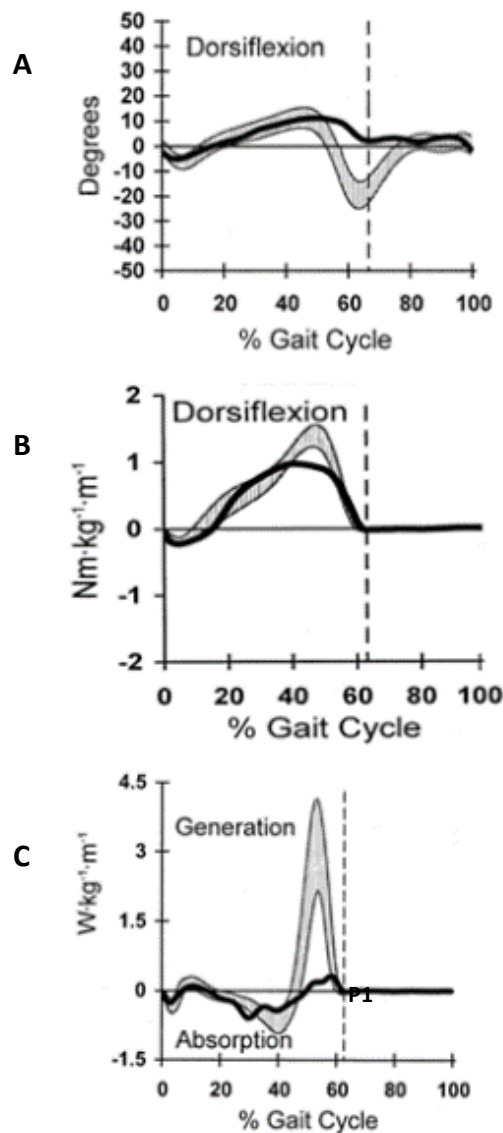
Figure 2.4 (A) Angle curve, (B) moment curve, and (C) power curve of the ankle joint during walking: the black line represents amputee's data (a transfemoral amputee wearing a Seattle Lite foot with Endolite standard Multiflex ankle), while the grey area normative data (±1SD). Graphs are plotted as a percentage of the gait cycle, where 0% is heel strike and 100% is the subsequent heel strike. There is a significant reduction in plantarflexion during push-off (see (A)) and the corresponding energy generation is almost absent (see P1 in plot (C)). Figure adapted from Perry *et al.* (2004).

This finding is not surprising, given that ESR feet act as a spring: as they move away from their neutral angle, during plantarflexion and dorsiflexion, they store strain energy and return all of this energy as they move back to neutral. This also means that, at toe-off, all the stored energy is released as the ankle returns to the neutral angle. Finally, the foot will not produce the plantarflexion, and the associated moment and power burst late in stance as shown in Figure 2.4 and Figure 2.5 (Gardiner *et al.*, 2016).
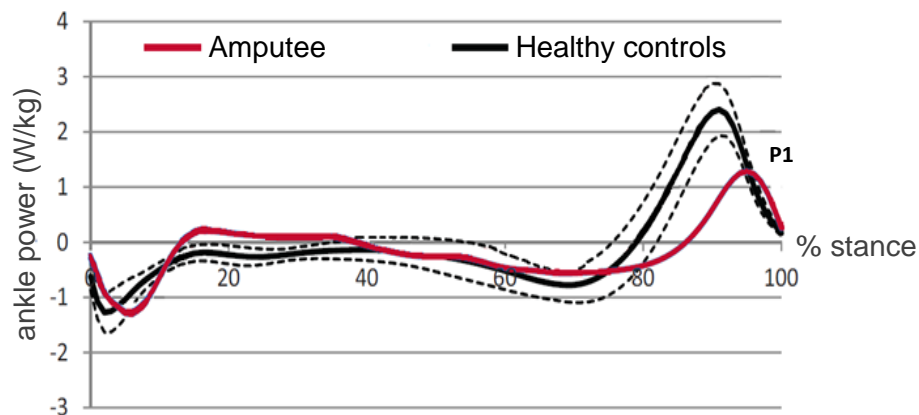
Figure 2.5 Power curve of the ankle joint of the prosthetic-limb of a unilateral transtibial amputee wearing a passive prosthetic foot (i.e. Elation (Össur, Foothill Ranch, CA, USA)) during walking. The black line represents gait data for 11 healthy controls (±1 SD), while the red line represents amputee's data, plotted as a percentage of the stance phase of the gait cycle, where 0% is heel strike and 100% is the toe-off. There is a significant reduction in magnitude and a delay in the energy released during push-off in the amputee (see peak P1). Figure adapted from Takahashi *et al.* (2015).

In conclusion, commercial ESR prosthetic feet fail to provide the necessary net positive work during push-off in a timely manner, leading to an increase of the metabolic cost of walking with respect to anatomically intact subjects (Caputo & Collins, 2014; Collins & Kuo, 2010; Huang *et al.*, 2015).

2.2   Previous research attempts

A number of novel designs have addressed the limitations with commercially available conventional and ESR prosthetic feet, typically by attempting to mimic the controlled storage and release of mechanical energy seen in anatomically intact participants. One of the early researchers to focus on the biomechanics of the ankle-foot mechanism was Hansen *et al.* (2004), who stressed the importance of the torque-angle profile for the ankle joint in the design of new prostheses. This relationship (see Figure 2.6), at any given point, may be

characterised by the slope of the curve, sometimes termed the "quasi-stiffness" of the ankle joint, where the prefix "quasi" refers to torque measurements not conducted at equilibrium. According to Hansen *et al.* (2004) and Versluys *et al.* (2009), prosthetic feet able to mimic the "quasi-stiffness" of the ankle joint are supposed to improve amputees gait.

A number of prosthetic designs aimed at restoring the energy storage and return behaviour seen in anatomically intact participants have been developed in the last two decades, the majority of which have used power sources. The so-called active devices include a power source and an actuator, which may be pneumatic, electrical or hydraulic, to provide an active push-off or to only adjust the ankle angle to different terrains and slopes (i.e. providing stabilization). Active prosthetic feet are also often referred to as "bionic" feet and most of those currently on the market only assist with stabilization (Cherelle *et al.*, 2014).
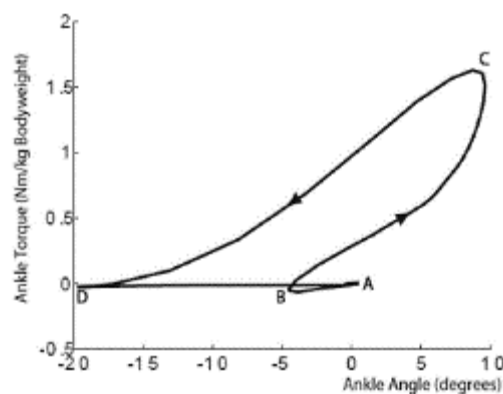
Figure 2.6 Torque-versus-angle curve for an anatomically intact ankle joint: (A) represents the heel strike, (B) foot flat, (C) maximum dorsiflexion, (D) toe-off. Image source: Versluys *et al.* (2009).

The remainder of this chapter reviews the prosthetic designs developed to address the aforementioned limitations of conventional and ESR prosthetic feet. The research for this literature review was conducted during the first six months of this PhD project, from October 2016 until March 2017. Devices including a pneumatic actuator were excluded: their drawbacks - mainly the large size and weight of the components required for autonomy, and the poor mechanical efficiencies - make them particularly unsuitable technologies for lower-limb prostheses (Bari, 2013; Cherelle *et al.*, 2014). Should the reader be interested, a complete review can be found both in Versluys *et al.* (2009) and in Cherelle *et al.* (2014). The review considered, instead, the designs as being either unpowered or powered devices, and classified according to their working mechanisms: either clutch-and-spring or hydraulic. The research

attempts evaluated were analysed mainly in terms of their ability to: mimic the torque and power profiles of an anatomically intact ankle joint, restoring appropriate peak power during push-off; and decrease the metabolic cost of walking. In addition, the small number of transfemoral prostheses that attempt to mimic the energy recycling behaviour of an anatomically intact lower-limb, in which biarticular muscles (e.g. the gastrocnemius muscle (Matthys *et al.*, 2012)) transfer energy between the joints, were included in the study.

The first two subsections focus on prostheses which are based on clutch-and-spring mechanisms; section 2.2.1 focuses on the unpowered designs and section 2.2.2 on their powered counterparts. The third and fourth subsections (2.2.3 and 2.2.4) review the limited applications of hydraulics in lower-limb prostheses, while subsection 2.2.5 briefly reviews orthoses and exoskeletons based on hydraulics. The remainder of the chapter includes a discussion section (2.3) and, finally, an overview of the previous work at the University of Salford (section 2.4).

2.2.1   Unpowered clutch-and-spring prostheses

Collins and Kuo (2010) developed a microprocessor-controlled artificial foot (Figure 2.7), referred to as the Controlled Energy Storing and Returning foot (CESR foot), which aimed to restore ankle push-off to normal. During load acceptance, a spring is compressed storing the associated negative work; a clutch holds it deformed until push-off, when a second clutch, triggered by the forefoot loading, releases the spring to aid push-off. A microcontroller and two micro-motors release the energy-storing spring and reset the mechanism during swing for the next heel strike. As this design uses a microprocessor and associated battery only to control the clutching and reset the spring – and not to provide an active peak power during push-off, it can be categorised as "semi-active".
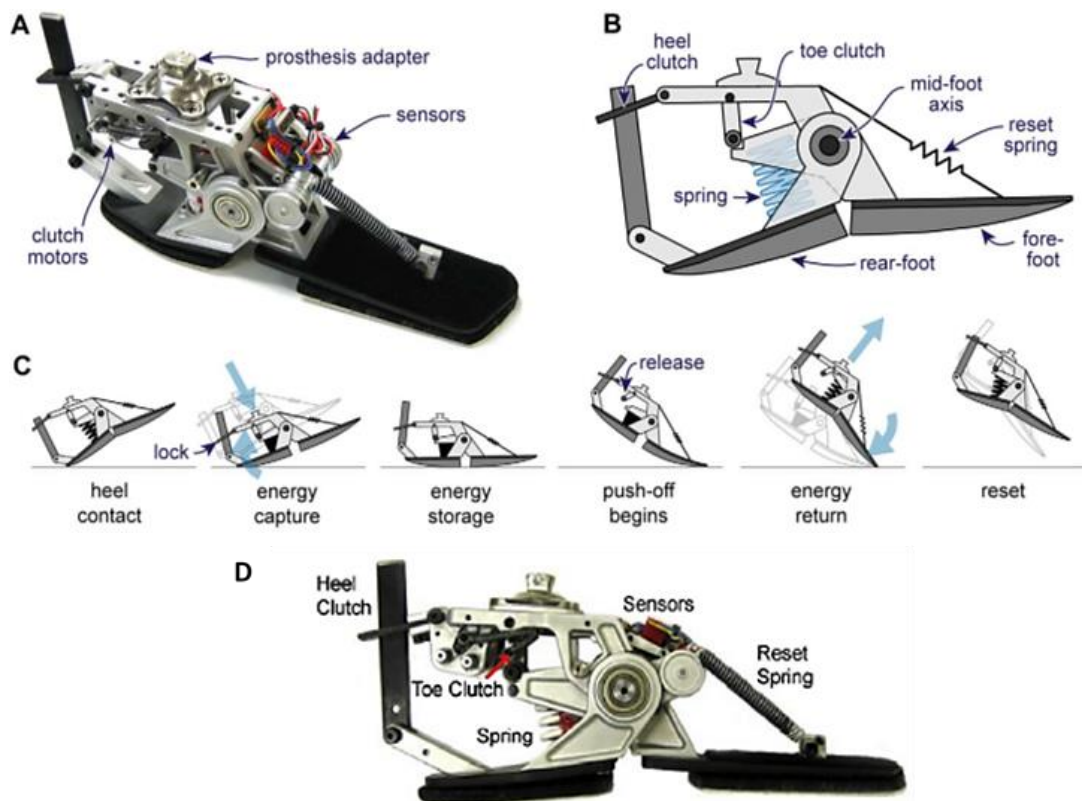
Figure 2.7 The Collins and Kuo (2010) Controlled Energy Storing and Returning foot (CESR foot). (A) Prototype device. (B) Schematic design. (C) Behaviour of the new device: at heel strike, the spring is compressed by the rear-foot, and locked by a clutch to store energy until when the fore-foot is loaded. A force sensor detects this event and release a second clutch, allowing the spring to release energy during push-off. The device is reset during swing. Images source: Collins and Kuo (2010). (D) Lateral view of the prototype. Figure adapted from Segal *et al.* (2012).

When tested on seven transtibial amputees and compared to the performance of one of the early ESR feet (a Seattle Lightfoot2), it stored more energy early in stance (0-20% of the stance), and showed increased peak of the push-off power (58%) (see Figure 2.8) and work (61%).
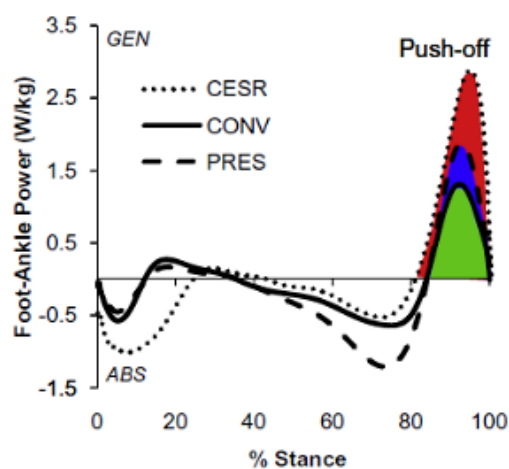
Figure 2.8 Average power at the ankle joint during stance for the amputees wearing the new CESR foot (dotted line), an early ESR foot – which they referred to as "conventional" foot - (solid line), and his personal prosthetic foot (dashed line). The coloured areas represents the energy released during push-off. Image sourced from Segal *et al.* (2012).

Nevertheless, the net metabolic cost of walking throughout stance with respect to the other foot showed no statistically significant changes, although the metabolic cost of walking with the CESR foot was 8.3% larger than with a conventional foot (Segal *et al.*, 2012). The authors suggested that the weight (1.4kg) and size of the first prototype, not individualised for the tested subject, and the potential additional muscular work needed to stabilise the knee specially during load acceptance, may have explained the observed high metabolic cost of walking. The study demonstrated that a design offering controlled and timely store and release of energy improves the push-off power, but concluded that an additional optimization of the design was necessary to decrease the metabolic cost of walking of the amputee (Segal *et al.*, 2012). The device was patented.

One advantage of their approach is that it is a semi-active design, so the electrical power requirements are very low. The design's main limitation is that it captures just the small amount of eccentric work (i.e. negative work) done during load acceptance, from heel strike to foot flat (i.e. A0 in Figure 2.2), failing to capture the negative work done at the ankle during mid and terminal stance (A1 in Figure 2.2), which corresponds to the majority of the energy stored during the gait cycle. Although no data are reported about the ankle torque, it is reasonable to assume that the use of a clutch-and-spring mechanism is unlikely to allow for the ankle torque to be controlled in a "smooth" manner.

In contrast to the CESR foot, the device developed by Williams *et al.* (2009) can store the negative work done during mid and terminal stance (i.e. from foot-flat to maximum dorsiflexion, i.e. A1 in Figure 2.2). It consists of two "neutralising springs" and a locking mechanism (also referred to as "clutch mechanism") engaging and disengaging a "Triceps Surae" (Achilles) spring (Figure 2.9). Since the two neutralising springs are configured so that the point of null ankle torque is when the ankle is neutral or slightly dorsiflexed, during the load acceptance phase one of them is compressed while the other is stretched. The Achilles spring is at its neutral length, while the clutch is free to move, varying its length or rotating in case a rotational component is chosen instead of a linear one (see Figure 2.9). At foot flat, the weight-activated clutch locks, determining the neutral length for the Achilles spring at the maximum plantarflexion angle. All the negative work done from foot-flat to maximum dorsiflexion is stored in the stretched Achilles spring, and then returned during push-off when

the ankle plantarflexes and the spring returns to its neutral length, which corresponds to the angle of maximum plantarflexion. When the foot is not loaded anymore, the clutch is unlocked, and the two neutralising springs allow the foot to recover the point of null ankle torque for ground clearance. By setting the neutral length for the Achilles spring at the angle of maximum plantarflexion, the mechanism can automatically adapt to different slopes, since the angle of foot-flat depends on the slope on which the amputee is walking (Williams *et al.*, 2009). This ability to provide slope adaptation for each step without any active control (i.e. without any microprocessor, motor, battery, etc.) is a major strength of the design.
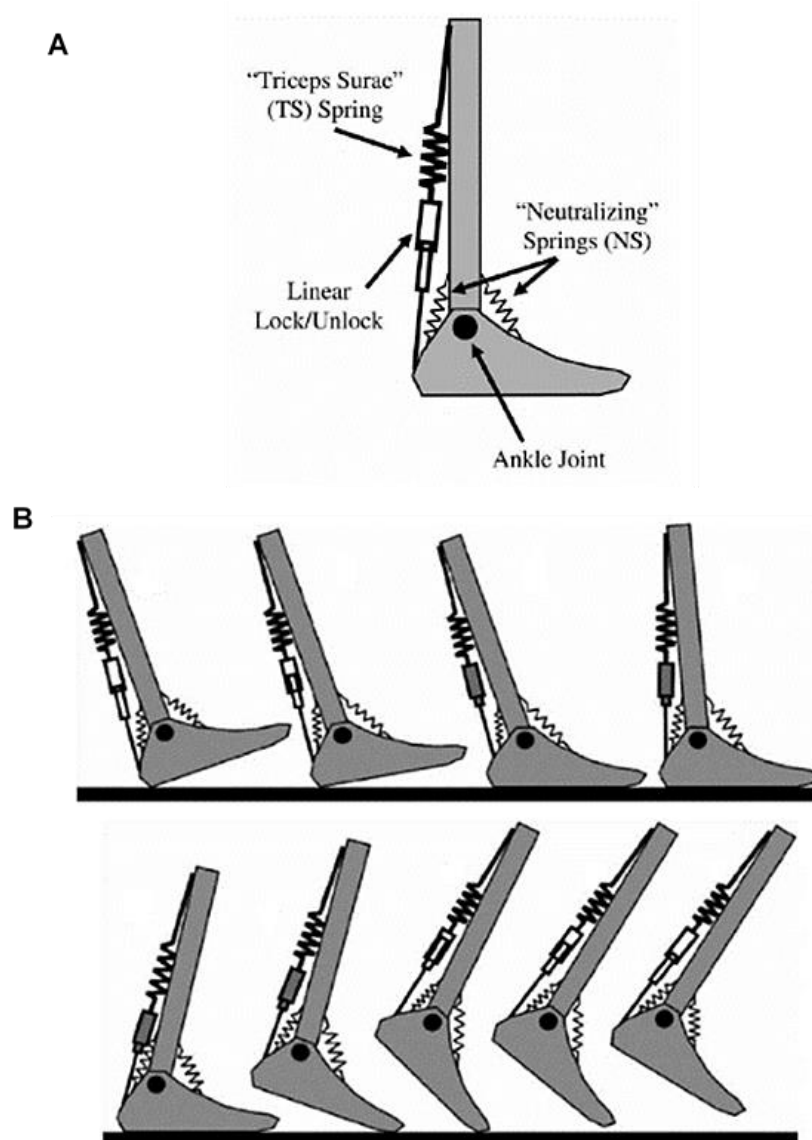
Figure 2.9 The Williams et al. foot. (A) Design concept: the NS springs allow the foot to return to neutral during swing, while the TS spring stores and releases energy between foot-flat and toe-off. A locking mechanism is used to engage the TS spring at foot flat and to disengage it at toe off. (B) The energy recycling sequence. The locking mechanism is represented in grey when locked and in white when unlocked. The figure is sourced from Williams *et al.* (2009).

A prototype of the Williams *et al.* design, based on a cam mechanism engaging a high stiffness rubber bumper at foot flat, was manufactured (see Figure 2.10 and Figure 2.11), and patented. It was tested on three unilateral transtibial amputees, demonstrating that a slope-dependent shift of the ankle torque-angle curve is seen during stance. No results for ankle power or the metabolic cost of walking were reported. The authors reported that further design work was needed to address wear issues, reduce the weight, size and noise associated with the mechanisms.
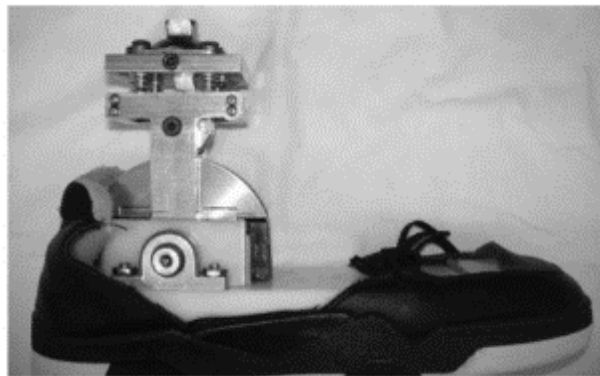
Figure 2.10 Lateral view of the prototype by Williams et al. (2009).
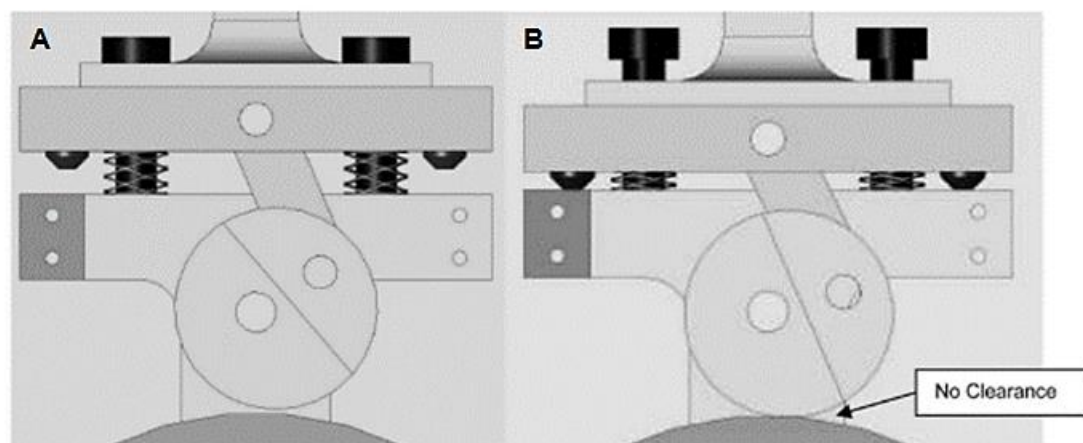
Figure 2.11 Lateral view from CAD of the working principle of the cam mechanism: at foot-flat (B), the user's weight leads the cam to engage the base (i.e. the arc with a grey shaded area at the bottom of the figure) and, thus, a stiff rubber bumper (not showed in the figure). In this way, the ankle-foot mechanism varies its impedance: from low (A) to high (B). The figure is sourced from Williams *et al.* (2009).

Nickel *et al.* (2014) reported a revised version of Williams' design, made of a foot plate and a cam clutch mechanism to engage and disengage the foot plate (see Figure 2.12). At foot flat, as the user loads the prosthesis, the clutch is locked, with the angle of maximum plantarflexion corresponding to the equilibrium angle of the foot plate with respect to the shank, allowing energy storage in the foot plate that flexes under the user's weight during mid and terminal

stance. When the prosthesis is unloaded, the foot plate recovers its equilibrium angle. In this way, energy is returned until the foot is back in its plantarflexion position. During swing, the clutch is disengaged and the foot plate returns to its dorsiflexed position for ground clearance through a neutralising bumper. Testing on a unilateral transtibial amputee revealed that the device (1.49kg) provides slope adaptation and the user reported less fatigue, although metabolic cost data were not reported and it was not possible to understand the performance of the device in terms of ankle torque and power. Further work was still needed to improve the design in terms of weight, a better foot plate and a more robust clutch (Nickel *et al.*, 2014).
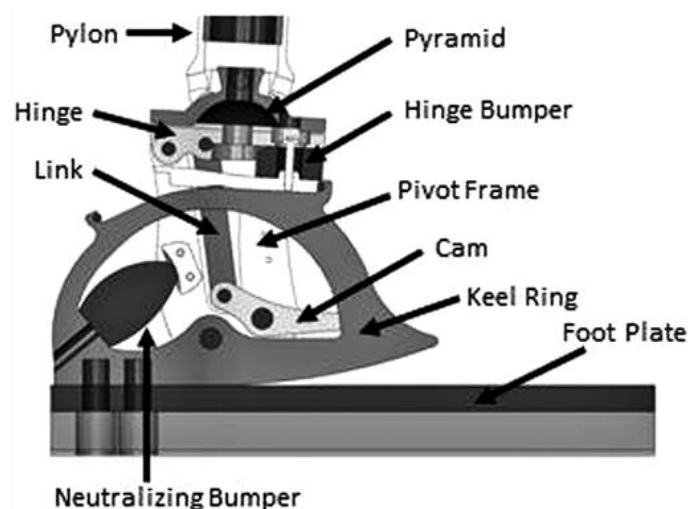
Figure 2.12 Lateral view from CAD of the prototype by Nickel *et al.* (2014).

Both the designs reported by Williams *et al.* (2009) and Nickel *et al.* (2014) address a major limitation of the Collins and Kuo's design by storing all the eccentric work done during mid and terminal stance. The designs also, by setting the neutral length of the Achilles spring at maximum plantarflexion, provides slope adaptation within the same gait cycle. However, in common with Collins and Kuo's design, the use of springs, clutches and bumpers, suggest the ankle torque was not controlled in a smooth manner.

Mitchell *et al.* (2013) modified an ESR foot (Talux foot by Össur) (Figure 2.13) to exploit the advantages of a timely energy storage and return on gait efficiency. A cable connects the shank to the toes of the prosthetic foot: it is kept in tension during mid and terminal stance dorsiflexion by a spring acting via a clutch, so that elastic energy is stored by keeping the carbon fibre laminates of the foot under compression; it is, then, extended through an electric brake to allow plantarflexion and the foot to recover its equilibrium position after each step.

A microprocessor controls the rate and timing of the cable extension and, thus, of the energy release during push-off, at fixed intervals after heel strike, which is dissipated by the next step when the foot recovers its equilibrium configuration. However, if the brake is used just to delay plantarflexion allowing, then, an un-braked plantarflexion, the energy dissipated will be very low.
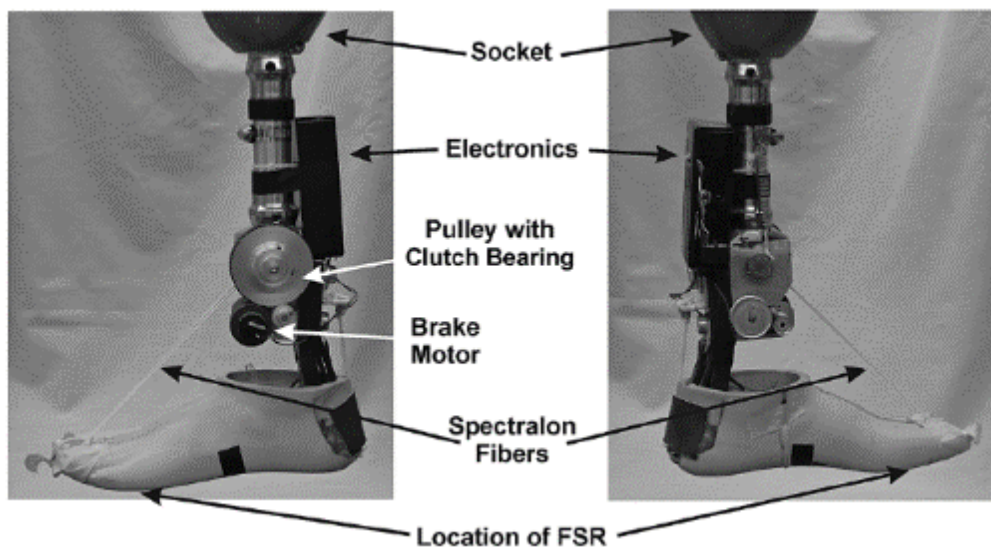
Figure 2.13 Prosthetic ankle design described in Mitchell *et al.* (2013). The Spectralon Fibers and the clutch are used to lock the foot once it reaches maximum dorsiflexion during stance. The electric brake is then used to delay or slow push-off plantarflexion.

The new device was tested on two transtibial amputees: delays allow for an ankle angle range close to normal, while moments and power do not improve. Therefore, it seems that any improvement over the standard ESR foot is minimal, as the energy stored during stance is similar to with a standard foot. Anyway, the two subjects reported that the device with a specific push-off timing was more comfortable than an ESR foot, but no data were provided on whether the walking efficiency improved.

Koopman and his team at the University of Twente developed an unpowered fully-passive clutch-and-spring transfemoral prosthesis (Unal, Carloni, *et al.*, 2010) consisting of two linear springs responsible for the energy storage and release during gait at the knee and at the ankle joint, and for the transfer of energy from the knee to the ankle joint in order to assist ankle push-off (see Figure 2.14 and Figure 2.15). The primary aim of this integrated device was to mimic the energy flow at these two joints. The spring placed between the upper leg and the foot (C_2 in Figure 2.14 (A)) connects the knee and the ankle joints: it stores energy partially at

the ankle during stance, and mainly at the knee during swing, thanks to a temporary change in the attachment point of its bottom extremity from the heel to the forefoot (i.e. from P_1 to P_2 in Figure 2.14 (B)), keeping its length constant to save the energy stored. The other spring (C_3 in Figure 2.14 (A)) connects the heel to the lower leg through a lever arm at the ankle joint. It stores energy during mid and terminal stance at the ankle joint.
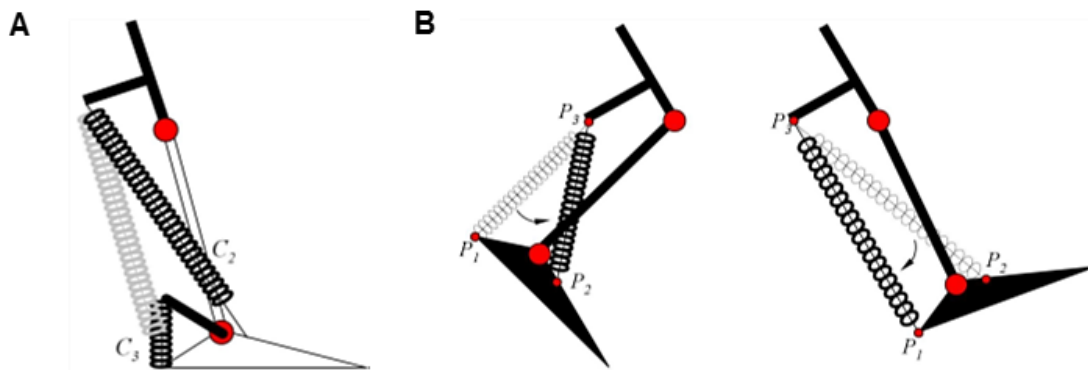
Figure 2.14 Design by Unal, Behrens*, et al.* (2010). (A) The two linear springs and (B) the change in the attachment point of the bottom extremity of the C_2 linear spring, after push-off and at the end of the swing phase.

Figure 2.15 Lateral view of the prototype by Unal, Behrens*, et al.* (2010).

At the end of terminal stance, the two springs are loaded and ready to release energy at the ankle during push-off. Simulations showed that the device can store up to 64% of the total amount of energy that is possible to store during gait in an anatomically intact subject both at the ankle and at the knee joint, to be used to assist with push-off at the ankle joint. The rest of the push-off energy is provided by the amputee to the detriment of his metabolic energy (Unal, Carloni*, et al.*, 2010). A prototype was built and tested in a test-bed used on a treadmill walking simulator: according to the authors, the prototype showed a walking pattern similar

to the one of an anatomically intact subject (Unal, Behrens*, et al.*, 2010), even though it is not possible to know if both kinematics and kinetics were mimicked.

This design was further improved by Behrens *et al.* (2011), to better mimic the energy flow between the knee and ankle joints and, thus, to decrease the metabolic cost of walking. A third component was added: a proper linkage system connecting the knee and ankle joints, made of a pulley and two gears realising a kinematic chain between the two joints (see Figure 2.16 (A)). This allows the ankle torque during push-off to be transmitted to the knee joint, and the energy at the knee to be transferred to the ankle during push-off. Simulation-based testing of this new device named "WalkMECH" (2.49kg, Figure 2.16 (B)) followed to justify prototyping: the device can release up to 76% of the energy required for forward propulsion during push-off, against the only 50% released by the concept design with just two springs (Unal *et al.*, 2012).
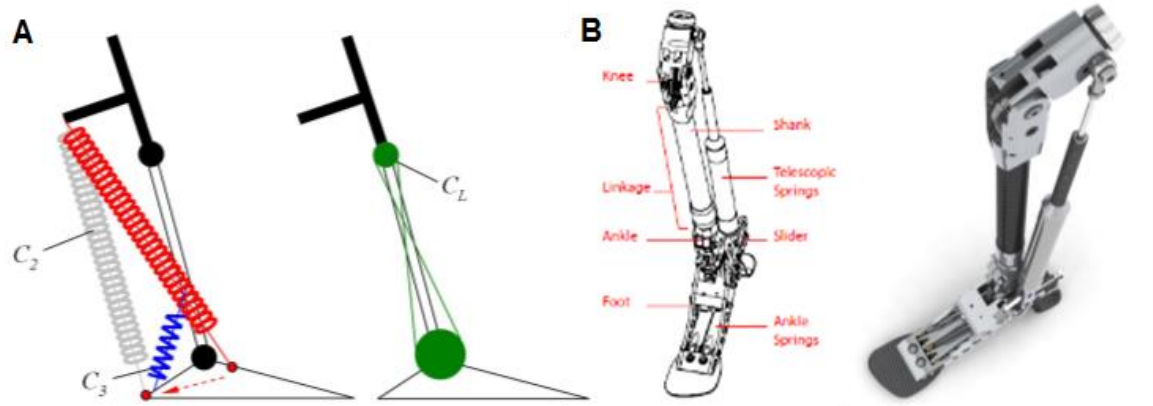
Figure 2.16 (A) Revised design by Behrens *et al.* (2011), with the two gears and a pulley connecting the knee and ankle joint. (B) CAD and prototype of the WalkMECH by Unal *et al.* (2013).

The design was further optimised (Figure 2.16 (B)) through simulation and testing with a unilateral amputee (Unal *et al.*, 2013). Figure 2.17 shows as the device can release a large amount of energy at the ankle joint during push-off, even though the lack of a match with the anatomically intact ankle power suggests that further improvements are needed. The knee power profile (Figure 2.17) was also reported to be a poor match to that of an anatomically intact subject.
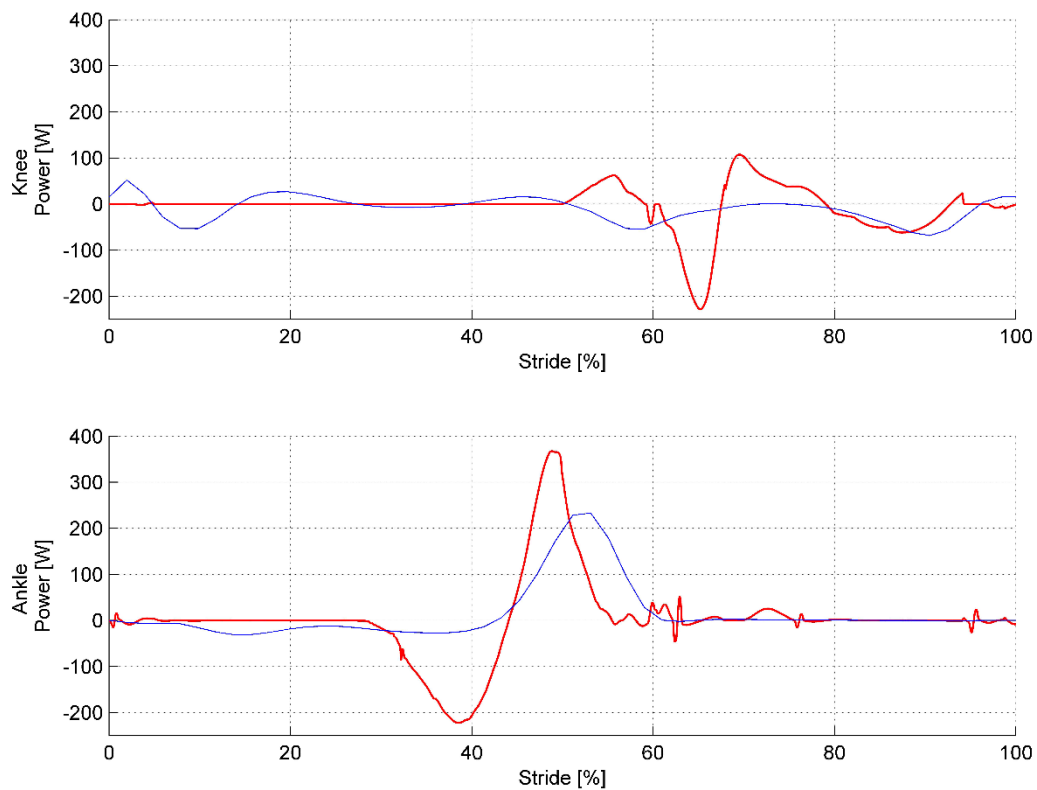
Figure 2.17 Knee power (top) and ankle power (bottom): comparison between an atomically intact subject (blue line) and an amputee wearing the WalkMECH (red line). The figure is adapted from Unal *et al.* (2013).

The joint torques from experimental test are not reported, while the ones from the simulation model show a poor match with the ones of an intact ankle and knee. The main reason for the former, according to the authors, is that the ankle spring becomes active for ankle angles larger than 0° (Unal *et al.*, 2013). In common with the designs discussed above, the use of springs limits the ability to vary the ankle and knee torques in a natural way, following any desired profile over the gait cycle.

The University of Twente design was optimised by Unal *et al.* (2014) for adaptation to different walking speed, and referred to as the "WalkMECH*adapt*". It included the two linear springs together with a torsional spring at the knee joint to store energy during push-off and transfer it during swing to the linear spring connecting the upper leg and the foot (Unal, Carloni*, et al.*, 2010). They realised the adaptation of the device to different walking speeds and, thus, to different amounts of energy stored and released, through a change in the configuration of one of the linear springs. Specifically, by varying the attachment point and hence equilibrium position of the spring connecting the upper leg to the foot when the foot is not loaded, it was possible to vary its energy storage capacity, allowing speed adaptation. They tested the

WalkMECH*adapt* on an experimental set-up with an anatomically intact subject mainly to evaluate the control of the device. Results showed that the device successfully adapts to different speeds. Nevertheless, no testing was conducted with amputees, and no data were reported about the kinetics of the ankle joint.

A similar attempt was made at the Vrije Universiteit Brussel (VUB) with the "Harvest Energy from the Knee and Transfer it to the Ankle (HEKTA)" (Matthys *et al.*, 2012). The prototype, fully-passive transfemoral prosthesis, harvests the energy that would be otherwise dissipated at the knee during swing, and transfers it to the ankle through springs and mechanical linkages to provide active push off. By contrast to the University of Twente designs, it allows knee flexion during the stance phase. A prototype of the system, made of two springs and a cable, was built (see Figure 2.18) but not tested.

Figure 2.18 Prototype of the HEKTA. Image source: Matthys *et al.* (2012).

The possibility of changing the equilibrium position of the foot spring was not included in this prototype. Even if no data are reported, this last feature and, in general, the use of springs and clutches at the knee do not allow the control of the knee and ankle torque profiles to suite different speeds and slopes. Despite the advantages of energy transfer between the knee and ankle, both the WalkMECH and the HEKTA use purely passive mechanical linkages and springs to realise this transfer, making the system complex and heavy (Cherelle *et al.*, 2014).

A last example of unpowered clutch-and-spring mechanism is the "CamWalk" by Rice and Schimmels (2014), the conceptual design of which is shown in Figure 2.19. It is characterized by four springs and a slider mechanism. Spring k_1 acts as the primary shock absorber. Spring

k_3 is responsible for the ankle stiffness mainly from heel strike until foot flat, while spring k_4 for the ankle stiffness from foot flat until maximum dorsiflexion. Spring k_2 provides partially shock-absorption and mainly the connection between the foot and the shank. At maximum dorsiflexion, the cam disengages the spring k_1, so that the slider moves forward under the user's weight. The link of the slider (in grey in Figure 2.19 and in red in Figure 2.20) becomes parallel to the slot where the slider is, locking in this way the spring k_2 and compressing it. The energy stored in the spring will be released when the foot A rotates with respect to the body B during push-off. During swing the position of the link and slider is reset.
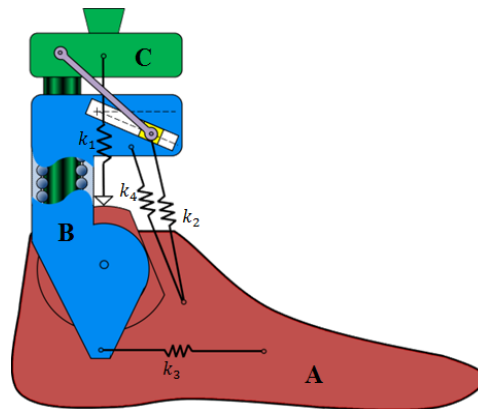
Figure 2.19 Conceptual design of the CamWalk by Rice and Schimmels (2014).
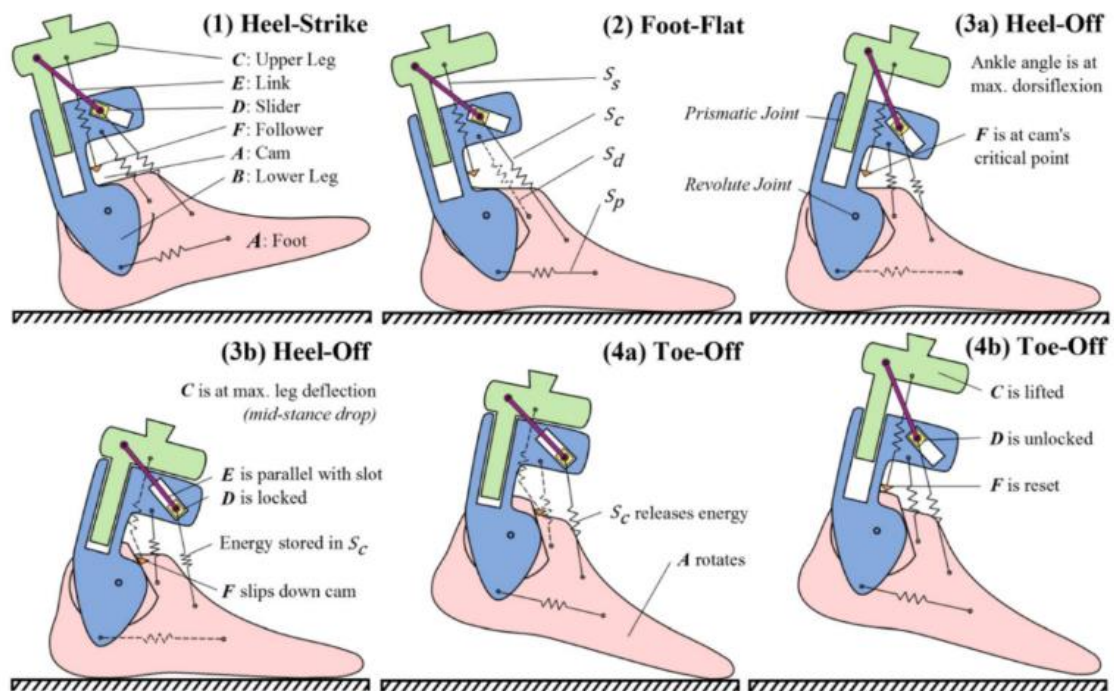
Figure 2.20 CamWalk during the gait cycle, from heel strike until toe-off. Springs drawn in dashed lines are not working in that specific instant of the gait. Image source: Rice and Schimmels (2015).

Different springs with different stiffness can be selected for each user, in order to match the individual torque-angle profile. After simulation, a prototype of 2.2kg and 17cm from ground to the pyramid adapter was built and tested with four transtibial amputees (Rice & Schimmels, 2015). An important issue was reported: at heel off, the cam disengages the spring k_1, suddenly increasing knee flexion – which was reported by the participants to be uncomfortable. Despite the work at the ankle being approximately 48% of the work done at the contralateral anatomically intact ankle per step, the authors reported that the sudden increase in knee flexion means the users were not able to benefit from the energy return during push-off (Rice & Schimmels, 2015). No data were reported for the experimental ankle torque with the new device, but simulation showed a poor match between the simulated ankle torque and the one for an anatomically intact subject (Rice & Schimmels, 2014).

In summary, the research attempts described in this section are all either entirely passive or semi-active (i.e. CESR foot by Collins and Kuo (2010) and Mitchell's design), requiring small amounts of power for the microprocessor: this means they are generally lighter and smaller than their active counterparts, which include batteries and motors. Nevertheless, even if data about the joints torque are missing in some studies, the use of clutch-and-spring mechanisms is unlikely to allow for the ankle torque and the knee torque to be controlled in a "smooth" manner. Springs, for instance, are characterised by a fixed mechanical stiffness, which has to be selected for specific tasks and users. For this reason, it is improbable that a device made of springs and locking mechanisms could mimic the quasi-stiffness behaviour of an intact ankle throughout the gait cycle (Figure 2.6). Moreover, as a further result of their design, and with the exception of the CESR foot and the WalkMECH, these prostheses are generally not able to replicate the anatomically intact power profile at the ankle joint. Likewise, speed and slope adaptation are provided only by the WalkMECH*adapt* by Unal *et al.* (2014), and by the Williams and Nickel's designs, in which the possibility for setting the neutral length of the Achilles spring at maximum plantarflexion provides slope adaptation within the same gait cycle. Worthy of remark is the concept of fully-passive transfemoral prostheses (i.e. WalkMECH and WalkMECH*adapt* at the University of Twente, and HEKTA at the Vrije Universiteit Brussel), since they allow for energy transfer between the knee and the ankle joints: braking energy stored at the knee at the end of the swing phase, which is normally

dissipated, can assist with ankle push-off. However, the purely mechanical linkages which these devices are made of make them really complex and somewhat heavy.

As a result of the limitations of these unpowered devices, several research groups have started to develop in the last two decades prostheses combining clutches and springs together with a power source (i.e. active prostheses), to better mimic the joint torque of anatomically intact subjects, including the quasi-stiffness of the ankle joint (Hansen *et al.*, 2004) (Figure 2.6), and the power profile, in addition to adjusting the joint angle to different speeds and slopes.

2.2.2   Powered clutch-and-spring prostheses

In 1995 Pratt and Williamson developed a compliant actuator to be used for a humanoid robot. It was a series elastic actuator (SEA), made of a compliant element (i.e. the spring) placed in between the motor and the mechanical transmission block and the load. This configuration showed many advantages with respect to stiff actuators: the compliant element acts as shock absorber; it increases the force accuracy as the output force depends now on the spring displacement, which can be controlled more easily than force; it provides for some energy storage and release assisting walking (G. A. Pratt & Williamson, 1995). Given these advantages, the SEA has found broad use in prosthetic applications, specifically in powered lower-limb prostheses.

By introducing a spring in series between the motor output and load, as the spring stores and returns energy and the work in output is the sum of the work generated by each component, the work required from the electric motor is lowered. Therefore, as the motor, the spring and the load are in series, while the required motor torque does not change, the motor speed may be lowered and, thus, the peak power that the motor should deliver. Consequently, since the peak power influences the motor size and weight, a smaller motor can be used (Everarts *et al.*, 2012), matching the need for small components in prosthetic applications. Other, context-specific, advantages of SEAs are: the possibility to store energy in the spring during mid and terminal stance to be released during push-off, helping with forward propulsion (Grimmer *et al.*, 2014; J. Pratt *et al.*, 2002);the elastic component provides for shock tolerance, preserving the motor (G. A. Pratt & Williamson, 1995; J. Pratt *et al.*, 2002); low impedance; and, by being

a force controllable actuator through the control of the spring compression, a maximum value of the output force can be set so as not to harm the subject (Au *et al.*, 2006). Last but not least, including an elastic component may help with stability on different terrains (Grimmer *et al.*, 2014). This and other similar configurations with variations – such as the motor in parallel with a spring or a series elastic actuator in parallel with a second spring - have been widely exploited in the design of prostheses, exoskeletons and robots. The use of a second spring in parallel with the SEA, for instance, can further increase the performance of the device: it decreases the peak torque and, thus the peak power that the motor should provide with a consequent increase of its efficiency (Holgate 2014). The powered prostheses, based on SEAs, are presented below.

One well-known attempt of powered clutch-and-spring prosthesis driven by a SEA is the "Spring Ankle with Regenerative Kinetics" (SPARKy) project. The SPARKy 1 by Hitt *et al.* (2007) (see Figure 2.21) is based on a "Robotic Tendon (RT)" actuator (Hollander *et al.*, 2006). This actuator, referred to as "Jack Spring™", is made of a motor in series with a helical spring, whose stiffness is tuned by adjusting the number of active spring coils through a position controller driven by a low-energy motor (Hollander *et al.*, 2005), to decrease the required peak power and the energy in output from the motor during push-off. During mid and terminal stance, as the shank rotates over the foot, the spring stretches storing energy, and additional energy is stored in it as the motor further stretches the spring. During push-off, all the energy stored in the spring is released.

It was tested and it showed to be able to provide ankle angle, torque and power profiles which were closer to those of an anatomically intact ankle than those seen with an ESR foot, while no data are reported about the metabolic cost of walking (Hitt, Sugar, *et al.*, 2010). It was able to store and release 16J per step (Bellman *et al.*, 2008), whereas an anatomically intact subject (80kg) needs 36J per step (Hitt *et al.*, 2007). Hitt *et al.* (2007), in the design objectives, envisioned the use of a battery allowing up to 8 hours of walking, but no further information are provided about the autonomy of the battery used in the prototype. A second prototype – the SPARKy 2 (see Figure 2.21) – was smaller, lighter (2kg vs 2.7kg) and with a more powerful motor, and was used for jogging when tested (Bellman *et al.*, 2008). The main feature of a third prototype – the SPARKy 3 (see Figure 2.21)– was the 2 degrees of freedom biomimetic

ankle offering controlled motion in both the sagittal and coronal planes. Despite the two joints and two motors, the design simulation showed it was smaller than the previous version, even if slightly heavier (2.1kg), and was reportedly potentially suitable for running and jumping. However, the design reportedly required control optimisation before a physical prototype was built (Bellman *et al.*, 2008).

Figure 2.21 From left to right: SPARKy 1, 2, and 3. Image source: Bellman *et al.* (2008).

The same research group developed also a mechanism characterised by one motor in parallel with one spring, connected to the ankle joint through a movable body (Holgate & Sugar, 2014), and referred to as the "Active Compliant Parallel Mechanism (ACPM)" (see Figure 2.22 for a comparison between the RT and the ACPM actuators). It offered all the previously mentioned advantages of a compliant element in parallel with a motor, in terms of torque and energy. The Odyssey ankle-foot prosthesis (see Figure 2.23), commercialised by SpringActive Inc. (an American company, whose some of the researchers included both in this and in the SPARKy project are part-owners of), includes the ACPM mechanism (Holgate & Sugar, 2014).
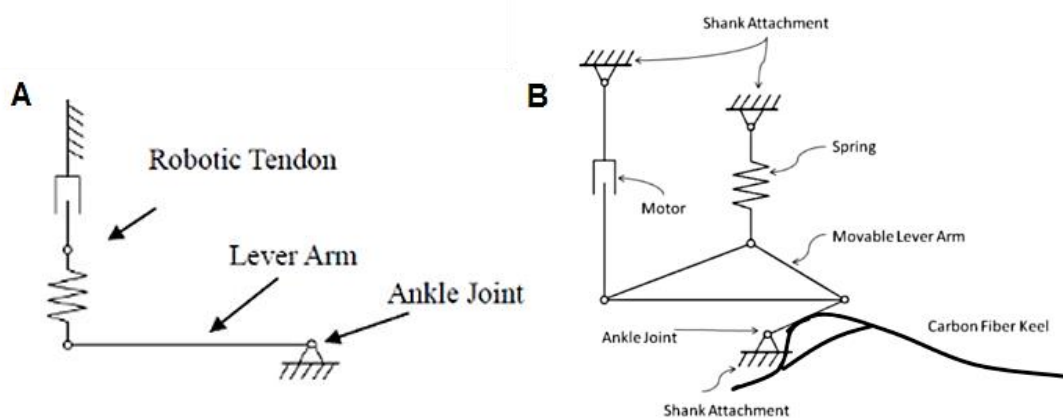
Figure 2.22 (A) Robotic Tendon actuator, which constitutes the working principle at the base of the SPARKy design: the linear motion of the motor and spring complex is converted in the rotary motion of the ankle joint through the fixed lever arm. (B) The new ACPM, with the spring in parallel with the motor and connected to the ankle joint through a movable arm. Figures adapted from Holgate and Sugar (2014).

Figure 2.23 (A) Odyssey ankle-foot. Source: www.springactive.com. (B) Details of the ACPM contained in the Odyssey ankle-foot. Figure adapted from Holgate and Sugar (2014).

Additional studies led to the development and testing of another ankle for walking and running, a first version in 2011 with two motors (Hitt, Merlo, *et al.*, 2010), and a second one in 2012 (Grimmer *et al.*, 2016) - named "Walk-Run" (see Figure 2.24). This last prototype (1.9kg without the battery and electronics) included one motor in series with a spring that stores energy during load acceptance and releases it during push-off. The motor generates trajectories given by reference torques and angles from anatomically intact subjects (reference motor trajectories used by the control system). The roller-screw and belt drive allow ankle plantarflexion and dorsiflexion. It was tested in an able-bodied subject wearing an ankle-foot orthosis and the device mounted in parallel to it. It showed a good match with the biomechanics of an intact ankle during walking in terms of angle, torque and peak power,

while, during running, differences in the angle and torque profiles were seen (Grimmer *et al.*, 2016). At the time of this review, it still needed to be tested with amputees to investigate its performance. The Walk-Run was also commercialised by SpringActive Inc. and a ruggedized version (Grimmer *et al.*, 2016) was commercialised under the name of "Ruggedized Odyssey" (see Figure 2.25).
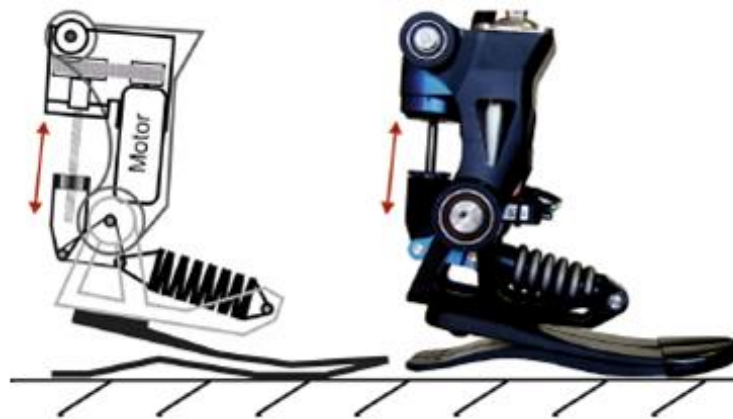
Figure 2.24 Walk-Run ankle-foot prosthesis. Image source: Grimmer *et al.* (2016).

Figure 2.25 Ruggedized Odyssey ankle-foot prosthesis. Image source: Ward *et al.* (2015).

As an active device, it was rather heavy and large in size due to the power supply. Further, producing a peak power at the ankle during push-off that mimics anatomically intact gait, does not necessarily mean a reduction of the metabolic cost of walking and gait asymmetries. Hence, experimental data on amputees are necessary to draw further conclusions.

A number of other designs, similar or with added compliant elements, have been reported, which are discussed below, grouped by the research team which led the work.

Université Catholique de Louvain

A prosthesis based on a SEA was reported in 2011 (Cherelle *et al.*, 2014; Everarts *et al.*, 2011). Despite their advantages, SEAs have a main limitation: the spring stiffness is fixed, so that it may be optimised just for a specific user/activity. Therefore, there may be advantages to being able to vary the stiffness of the compliant element to adapt to different slopes and speeds, in order to minimise the energy that the motor should provide. This concept has led to the development of Variable Stiffness Actuators (VSAs), which allow the actuator stiffness to be changed within the same gait cycle, and requiring no additional energy (Everarts *et al.*, 2012). The group developed a VSA made of a continuous variable transmission (CVT): it allows the stiffness of the actuator, and thus the amount of energy that can be stored in it, to be changed for different slopes, speeds and tasks, within the same gait cycle, without losing any of the stored potential energy in the elastic element (Everarts *et al.*, 2012). They also introduced an infinitely variable transmission (IVT) able to vary the transmission ratio at rest, as well as during gait (Everarts *et al.*, 2015), but further work was needed to reduce the device's size before the design could be tested with amputees.

Marquette University

In this design the ankle rotation is driven by a SEA with a torsional spring through a four-bar mechanism (see Figure 2.26 (A)). Testing on an amputee on level walking revealed that the torque and power profiles are still far from those of an anatomically intact ankle, although improvements in both compared to a passive prosthetic foot. A limitation of the design was the inability to move back to a neutral angle during swing for ground clearance (Sun *et al.*, 2014). No further improvements were made to this design.

Peking University

The "Powered transtibial prosthesis with ANkle and TOE joints" (PANTOE) by Zhu *et al.* (2014) uses a SEA at the ankle joint and a second one at the toe-joint. A prototype of 1.47kg without the battery was built (see Figure 2.26 (B)), tested with an amputee, and found to improve some aspects of his gait with respect to a passive prosthesis: the vertical component of the GRF and the joint angles of the prosthetic and sound limb were symmetrical. However, just knee, ankle and toes angle and vertical GRF are reported and during level-ground walking.
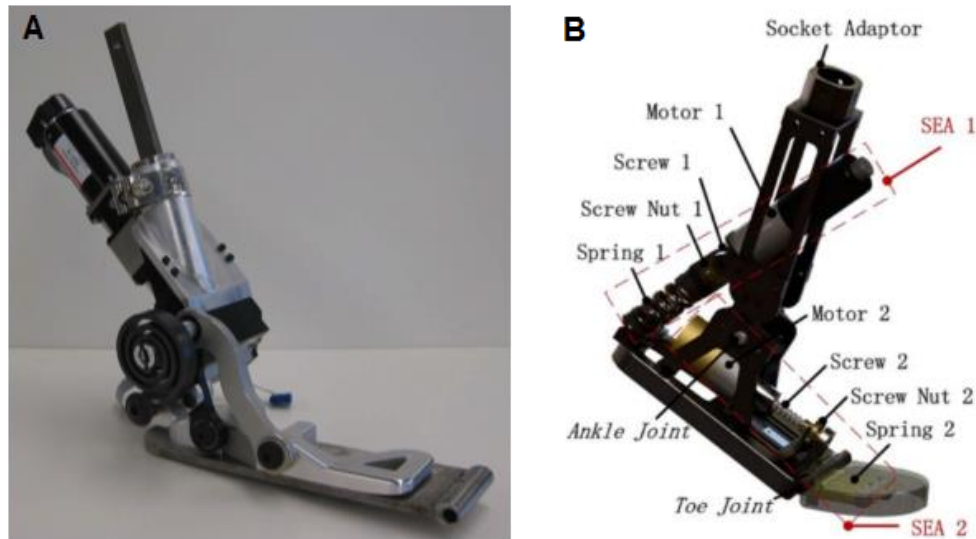
Figure 2.26 (A) Ankle-foot prosthesis developed at Marquette University. Image source: Bergelin and Voglewede (2012). (B) CAD of the PANTOE by Zhu *et al.* (2014), with two SEAs: one for the ankle joint and another one for the toe joint.

Vanderbilt University

A self-contained powered transfemoral prosthesis of 4.2kg was developed based on two ball screws driven by two motors for the two joints: the knee and the ankle (Sup *et al.*, 2009a). At the ankle, a compression spring in parallel with the ball screw mechanism helps in providing the proper power output during push-off, reducing the required output torque the motor delivers (Sup *et al.*, 2009a, 2009b). Although sometimes described in review papers as a system containing a SEA (Cherelle *et al.*, 2014), the drive contains a spring in parallel with the motor. Testing on a unilateral transfemoral amputee showed that the device provides peak torque and power at the ankle during push-off similar to those of an anatomically intact subject, but both parameters are not well matched over the rest of the gait cycle. The device, although reported to be noisy, provides up to 1.8h of level ground walking at self-selected speed with a single charge, corresponding to nearly 4500 strides and 9km according to the author.

Shultz *et al.* (2013) developed the "Vanderbilt Transtibial Prosthesis" (2.3kg, battery included) driven by a motor in parallel with a spring (see Figure 2.27).
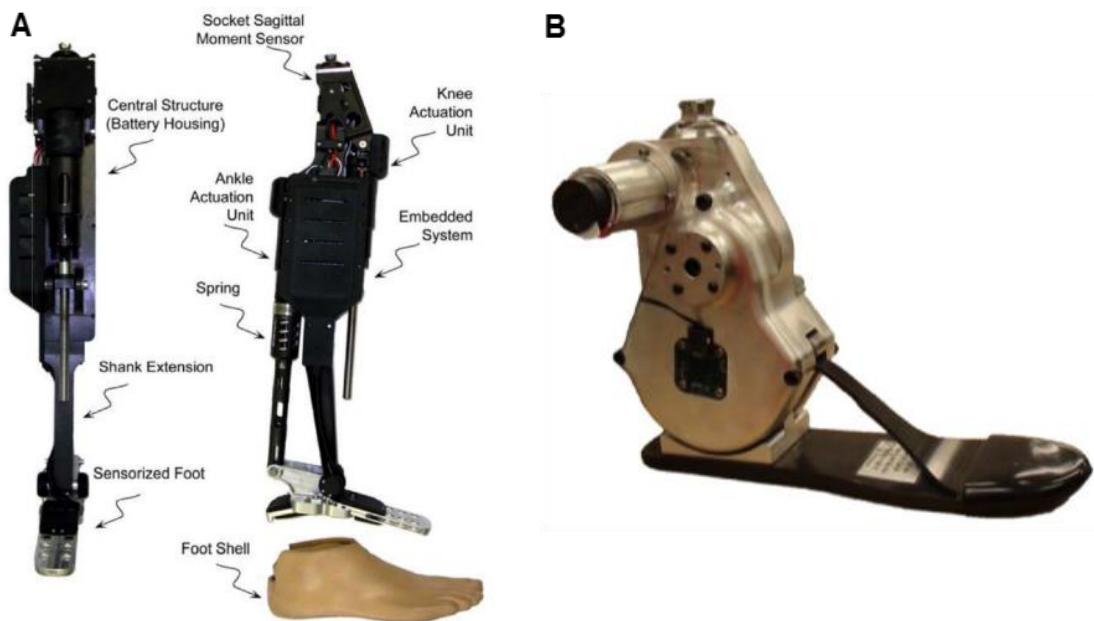
Figure 2.27 (A) Self-contained powered transfemoral prosthesis by Sup *et al.* (2009a). (B) Vanderbilt Transtibial Prosthesis by Shultz *et al.* (2013).

Testing of the new device on an anatomically intact subject wearing an adapter connected to the prosthesis showed a good match with an anatomically intact ankle in terms of joint angle throughout the gait cycle, and estimates of peak power during push-off. However, the estimates of the ankle torque and power profiles during the rest of the gait cycle differ from those of an anatomically intact subject. This prosthesis was then integrated in the powered transfemoral prosthesis (approximately 5kg) reported by Lawson *et al.* (2014) (see Figure 2.28), in which both the knee and ankle units include a motor. At the ankle, a parallel spring consisting of a carbon-fibre leaf spring is also included, assisting the motor in terms of torque and power output. It was tested on three amputees showing a match with the ankle joint kinematics of an anatomically intact subject during walking. However, both the ankle and knee torque and power profiles were lower than in the anatomically intact subject. Again, further work was needed to address these issues. No data were reported in terms of the metabolic cost of walking.
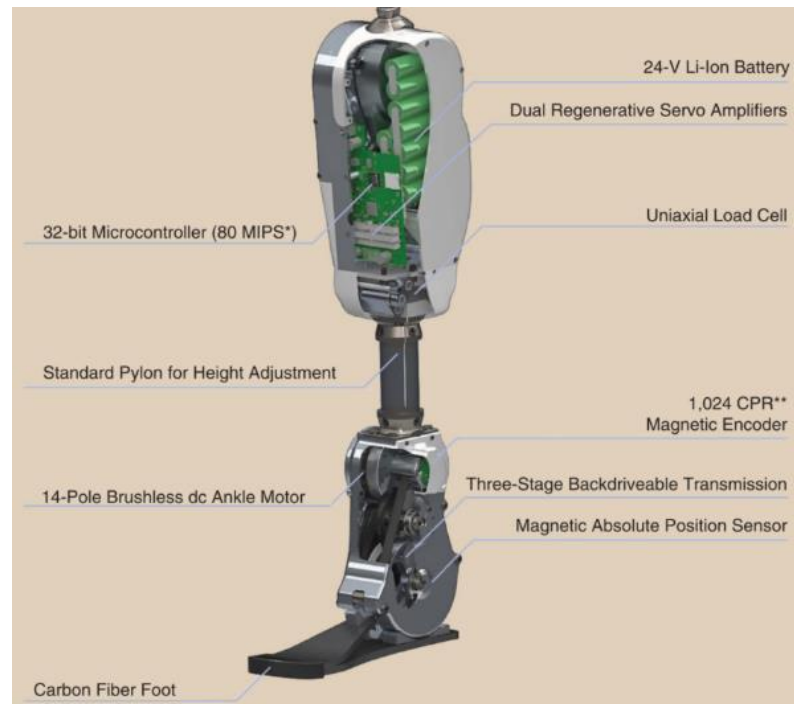
Figure 2.28 CAD of the powered transfemoral prosthesis developed at Vanderbilt University by Lawson *et al.* (2014).

The Chinese University of Hong Kong

Another attempt of powered ankle-foot prosthesis based on a parallel elastic actuator (PEA) was made by Gao *et al.* (2015), to reduce the required output torque from the motor, therefore the required power. Simulation results showed that the output torque differs from the one of an intact ankle, but the peak power during push-off seems to be close to the one for an intact ankle – thanks to the powered push-off typical of all these active prostheses. A prototype was supposed to be built in the future to investigate energy consumption.

MIT ankle foot

The "bionic ankle-foot prosthesis" (BiOM) by Herr and Grabowski (2012) represents one of the most well-known design of active prosthetic foot. The core design comprises a SEA with a second spring in parallel to the motor with a total mass of 2kg. The SEA consists of a motor, a ball-screw transmission and a compliant element - a carbon fibre leaf spring (Figure 2.29) (Herr & Grabowski, 2012). It allows for control of joint stiffness, and provides the required peak torque and power in output during push-off (Au *et al.*, 2007). The transmission converts the motor's rotary motion into linear motion, which causes the rotation of the ankle joint through the series spring (Au *et al.*, 2007). The in-series leaf spring stores and returns some of the

energy generated by the motor, while a parallel spring provides a rotational ankle joint stiffness, compressing only for ankle angles less than 90° and storing energy.
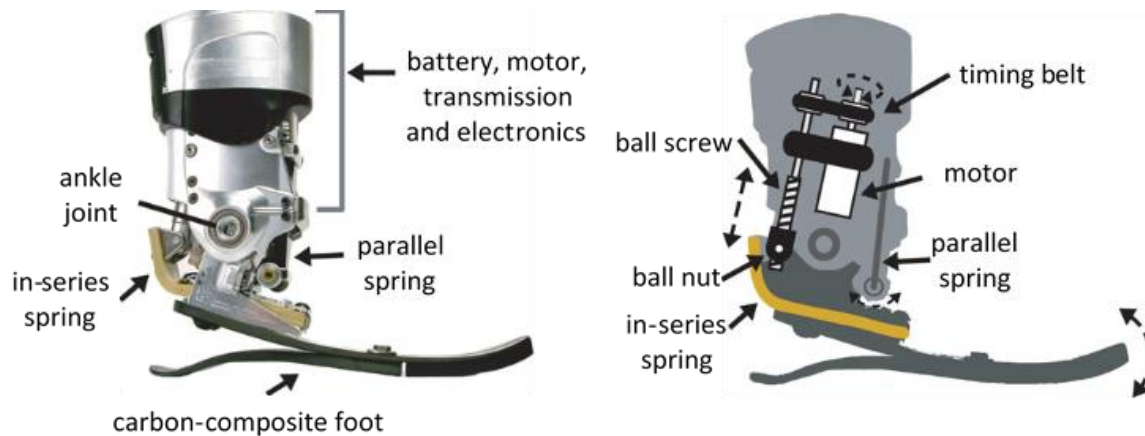
Figure 2.29 The BiOM foot including a linear actuator with series and parallel springs, adapted from Herr and Grabowski (2012).

By moving the linear actuator when the ankle torque is low to change the neutral ankle angle (i.e. zero torque) for the series spring, this design could achieve slope and speed adaptation similar to that reported by Williams *et al.* (2009). The ankle-foot prosthesis generates positive work during push-off using a battery and taking advantage of the fact that the actuator and the series spring can extend simultaneously. The system was tested with eight unilateral transtibial amputees and eight matched control subjects during level ground walking. It demonstrated that the ankle power during stance in the prosthetic leg is similar to the one of a non-amputee, with peak power matching non-amputees data during push-off (Grabowski *et al.*, 2011), and being 54% larger than the figure obtained with an ESR foot according to Mancinelli *et al.* (2011). The Mancinelli's study, conducted on five unilateral transtibial amputees, showed that ankle angle, torque and power are closer to those of an anatomically intact ankle than those seen with an ESR foot, even though the peak of the ankle moment at maximum dorsiflexion was not significantly different between the BiOM and an ESR foot on level walking, and reported a decrease in oxygen consumption of about 8.4%, although this difference was not statistically significant. A last study on seven unilateral transtibial amputees and seven matched control subjects showed that the preferred walking speed with the BiOM was the same as non-amputees, and the metabolic cost of walking was within the range seen in anatomically intact participants, again 8% smaller than the one of amputees using passive-elastic prosthesis (Herr & Grabowski, 2012).

In the BiOM, the compliant element of the SEA is a carbon fibre leaf spring, and the whole mechanism is fixed to a carbon composite foot (see Figure 2.29), a typical ESR feet. This composite component allows some elastic energy storage and return, similar in nature to that seen in commercial ESR prostheses, with similar problems of uncontrolled and untimely energy return from the springs, although the actuator does allow ankle torque to be controlled. This critique is supported by the fact that the reduction in metabolic cost for the amputee when using the BiOM, in comparison with using a passive ESR foot, is slightly less than the metabolic equivalent of the energy input from the electric motor (both measured in $\frac{J}{Nm}$) (Herr & Grabowski, 2012). This suggest that the advantages over commercial ESR prostheses come largely from the addition of an external power source, as the device does not take advantages of all the eccentric (negative) work made in an intact ankle during mid and terminal stance (Figure 2.2), and it only relies on the power provided by the battery to assist with forward propulsion during push-off. This analysis is supported by the study by Russell Esposito *et al.* (2015) on six unilateral transtibial amputees and six matched control subjects: despite the benefits over ESR feet in terms of metabolic rate on level ground, the BiOM performs as an ESR foot during slope walking. Ferris *et al.* (2012), in a study on eleven unilateral transtibial amputee and eleven matched control subjects, showed that the use of the BiOM does not allow a normative gait kinematics and kinetics: joint asymmetries (knee and hip) between the prosthetic and the contralateral anatomically intact leg still exist. Therefore, specific trainings may be useful to allow amputees to fully exploit the functionality of this active device.

The BiOM (Figure 2.30 (A)) was firstly commercialised by iWalk (founded in 2007 by Hugh Herr) - which changed its name to BionX a few years later - and now it is distributed by Ottobock with the name of "Empower" (Figure 2.30 (B)).

Figure 2.30 (A) The BiOM foot in an earlier version (figure sourced from Mancinelli *et al.* (2011)). (B) Version currently commercialised by Ottobock with the name of "Empower" (image sourced from shop.ottobock.us).

Nanjing Institute of Technology

Another attempt of ankle prosthesis based on a SEA and a parallel spring is the one by Yali *et al.* (2013). Simulations showed that it can reproduce human walking, but a prototype was not built and tested. Moreover, the only paper found is entirely in Chinese, except for the abstract.

Vrije University Brussels (VUB)

Geeroms et al. (2013) and Flynn et al. (2014) presented the CYBERLEG α-Prosthesis for transfemoral amputees (Figure 2.31), the main components of which are an active ankle, a passive knee and an energy transfer system.

Figure 2.31 The CYBERLEGs Alpha-Prosthesis. Image source: Geeroms et al. (2013)

In this design, of mass 5kg without batteries, a variable stiffness actuator for the ankle (named MACCEPA) generates torque through a series spring, whose pre-tension can be adjusted to modify the output torque and, thus, it provides slope and speed adaptation. This mechanism also lowers the peak power required by the motor during push-off. A passive knee utilising two springs and locking mechanisms (a ratchet mechanism) to store braking energy from the knee (i.e. the negative work the knee performs at the end of swing which is normally dissipated) to be used at the ankle for powering push-off. The energy is transferred in the late stance phase from the knee to the ankle via a cable, further reducing the torque that the actuator at the ankle joint must produce. As a result, the ankle torque at maximum

dorsiflexion seems to be similar to that of an anatomically intact subject, but it differs during the rest of the gait. The use of springs and clutches at the knee does not allow for the knee torque profile to be adjusted to suit different speeds and slopes.

Improvements to this design led to the CYBERLEG β-Prosthesis, whose primary difference with respect to the previous version lay in the active knee joint, which provides power for several activities (e.g. stairs climbing). The main actuator, made of a SEA, is supposed to provide only a minimum torque during level ground walking allowing the device to work mainly as a passive device, and positive energy only when needed: either when a change in the prosthesis behaviour is required during level ground walking or when activities that require more energy are performed. Testing of the new integrated prosthesis on two unilateral amputees showed that subjects could walk with the new device on level ground, but further improvements of the control for stairs climbing and investigations about the metabolic energy of the user and the energy consumption by the motors were still to be done (Flynn *et al.*, 2015). No data were reported about the ankle torque and power.

The same research group at the VUB developed another powered clutch-and-spring prosthesis: the Ankle Mimicking Prosthetic Foot (AMP-Foot). They started with a first semi-active (power source only for the microcontroller) prosthetic foot tested on a transfemoral amputee, made of a planetary gearbox with a locking mechanism (ratchets) to vary the rest position of a spring that stores energy during mid and terminal stance and releases it during push-off (Brackx *et al.*, 2013). Then, additional improvements to the design led to two versions of the AMP-Foot, culminating in the AMP-Foot 3 (Cherelle *et al.*, 2016). It is based on a "Explosive Elastic Actuator (EEA)" made of a SEA actuator in series with a second spring and a locking mechanism. It can store energy and release it at a specific time of the gait cycle, i.e. during push-off for forward propulsion. Despite the required output torque being the same as the SEA, the power and the speed required for the motor are further decreased thanks to the added spring and locking system. A crank-slider mechanism transmits forces and torques from the actuator to the ankle joint (see Figure 2.32).
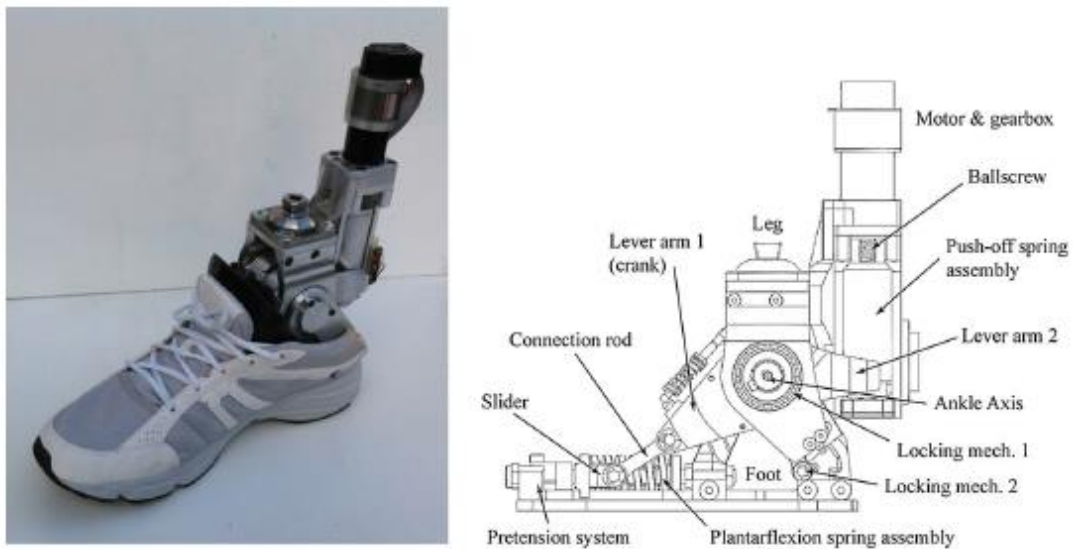
Figure 2.32 The AMP-Foot 3. Image source: Cherelle *et al.* (2016).

A "plantarflexion spring" is mounted on the foot plate, and another spring, referred to as the "push-off spring", is placed right after the motor-ball screw system. The plantarflexion spring stores energy during mid and terminal stance through the motion of the slider of the crank-slider mechanism, while the push-off spring is compressed by the actuator independently from the rest of the ankle joint. During push-off, then, the energy stored both in the push-off spring and in the plantarflexion spring is released for propulsion, providing the required power and torque at the ankle joint. One clutch ("Locking mech. 1" in Figure 2.32) allows the design to maximise the energy stored in the plantarflexion spring during mid and terminal stance, as well as control the amount of energy stored in the plantarflexion spring by varying its equilibrium position at foot-flat. A second clutch ("Locking mech. 2" in Figure 2.32) disconnects the ankle joint from the electric actuator when this is loading the push-off spring. Thanks to the first clutch, it was possible to reduce the motor power to just 50W, which compares favourably to other active devices (Cherelle *et al.*, 2016). When tested on a 75kg unilateral transfemoral amputee, the ankle power profile matches the one of an anatomically intact subject, with approximately 13J stored in the plantarflexion spring – the authors say "during early stance", which should correspond to mid and terminal stance - and 26J released during push-off. However, the ankle torque poorly matches that of an anatomically intact subject, even though it reaches a peak at maximum dorsiflexion. The same authors affirmed that some optimisation is needed to decrease the weight of the prototype (3kg), and also to improve its control system and better exploit the second clutch to provide automatic speed and slope adaptation (Cherelle *et al.*, 2016).

In summary, in contrast to the unpowered clutch and spring devices, most of the powered clutch-and-spring devices are able to provide torque and peak power at maximum dorsiflexion close to those of an anatomically intact subject, in large part as a result of the external power source. Common feature of all the active devices of this section is the ability of generating a biomimetic ankle angle during level ground walking. The SPARKy, the Walk-Run and the BiOM, generate a torque profile which is closer to that of an anatomically intact ankle than typical ESR feet can do throughout the gait cycle, and the same devices together with the AMP-Foot 3 are also able to match the power profile. Therefore, by being able to mimic the non-linear torque-angle relationship of an intact ankle as well as its power flow, these designs are better than the other active clutch-and-spring prostheses. Only the BiOM and the AMP-Foot 3, when tested, seem to provide slope and speed adaptation by varying the equilibrium position of the compliant element included in the actuator. The CYBERLEG α- and β-Prostheses should adjust too, but the latter was tested just on level walking, and no data are reported about speed and slope adjustment for all the other tested devices.

Nevertheless, as the example in Figure 2.33 shows, the torque and power at the ankle joint, and at the knee joint for transfemoral prostheses, during the rest of the gait cycle is less well matched in most of these powered clutch-and-spring devices.
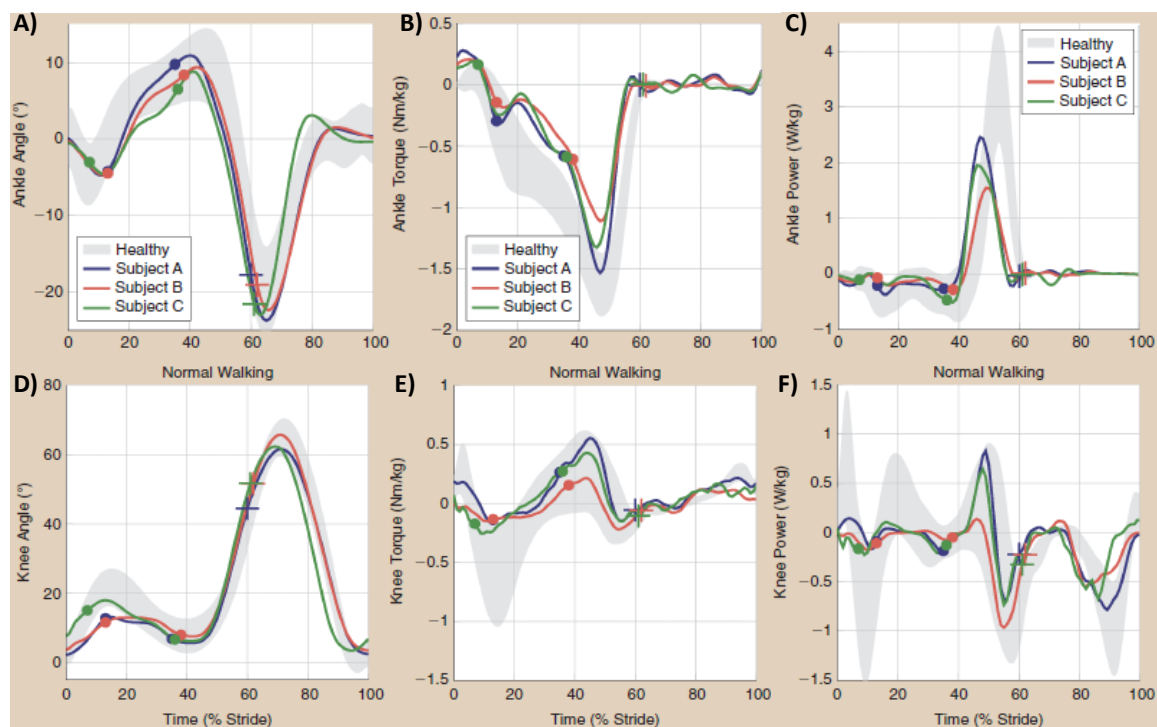
Figure 2.33 Ankle (A) angle, (B) torque (positive torque is a dorsiflexive torque) and (C) power; and knee (D) angle, (E) torque (positive torque is a flexion torque) and (F) power for three amputees using the powered transfemoral prosthesis by Lawson *et al.* (2014).

As mentioned in the previous section, this inability to closely track the torque and power or mimic the quasi-stiffness of the ankle joint (Figure 2.6) profiles is likely due to the use of compliant elements and locking mechanisms. Therefore, active clutch-and-spring devices, with a few exceptions, do not outperform both their unpowered counterpart and ESR feet.

A device with powered push-off, at the appropriate timing and the appropriate magnitude should contribute to a decrease of the metabolic cost of walking with respect to a passive conventional or ESR foot. Nevertheless, the use of springs, clutches and a power supply makes these active devices rather heavy and large in size, likely contributing to an increase in the metabolic cost and gait asymmetries (J. D. Smith & Martin, 2013), which may nullify the advantages of a powered push-off. In transfemoral prostheses this issue is amplified as mechanical linkages are used to transfer energy between the knee and the ankle joints. Likewise, the introduction of variable stiffness actuators as in the CYBERLEG α- and β-Prostheses or explosive elastic actuators as in AMP-Foot 3 at the ankle joint adds further weight, volume and complexity to the system (Cherelle *et al.*, 2014). Further evidence is necessary, then, to judge the real effectiveness of these new active devices. At the time of this review, there are few experimental studies investigating amputee's metabolic cost of walking with active devices, all related to the well-known BiOM, with experimental data collected on small samples of amputees, and only four of them conducted with a matched control group. For this specific foot, for instance, while some studies demonstrated its superiority in terms of metabolic cost over ESR feet during level walking, data collected by Russell Esposito *et al.* (2015) showed no metabolic advantage over ESR feet on slope walking. Likewise, gait asymmetries between the prosthetic and the contralateral anatomically intact leg still exist in unilateral transtibial amputees wearing the BioM, leading to compensatory mechanism at the proximal joints of the prosthetic leg (Ferris *et al.*, 2012). This finding led to assumptions that a specific training regime may help amputees with a moderate-to-active lifestyle to fully exploit the functionality of active devices (Ferris *et al.*, 2012).

These active clutch-and-spring devices were mainly designed to mimic the ankle quasi-stiffness, and to exploit the electric actuation to provide a net positive ankle power during push-off to assist with forward propulsion. However, it appears that little effort was made to harness the energy that may be stored and released during the gait cycle. The BiOM foot

serves as an example: by relying only on the power provided by the battery during push-off, the device, in common with commercial ESR feet, seems not to take advantage of the eccentric (negative) work done during mid and terminal stance (Figure 2.2). Furthermore, replicating the ankle peak torque and power during push-off, for a 75kg subject, means that a torque of approximately 122Nm should be provided at the ankle joint, corresponding to a peak power between 250W and 350W (Winter, 1991). Although the use of SEAs allows the system to lower considerably the peak power (and also the peak torque in cases where compliant elements in parallel are also used) and, thus, the motor size and weight, the use of electric motors and batteries to supply power in prosthetic applications remains fundamentally difficult. The main issues are related to the use of batteries:

- The duration of a single charge of the battery limits amputee's autonomy. For instance, with a single charge, the battery (0.22kg) of the BiOM foot allows for approximately 4000 - 5000 steps according to Herr and Grabowski (2012), while the self-contained transfemoral prosthesis by Sup *et al.* (2009a) at Vanderbilt University provides up to 1.8 hours of level ground walking at self-selected speed (corresponding to about 4500 strides according to the authors). In both cases, these values exceed the approximate 3065 steps per day walked by a lower-limb amputee (Stepien *et al.*, 2007), but they do not take into account the level of activity of the amputee and the frequent braking and accelerating required in everyday life, which require more energy than steady-state walking at self-selected speed. This may lead to a battery discharging sooner than expected, with an associated dramatic reduction in the device performance during its use.

- The frequent charge and discharge cycles will damage the battery over time (Han *et al.*, 2019).

- The electronic and mechanical components may require frequent maintenance in highly specialised facilities.

- Active devices currently on the market are very expensive, so only a small percentage of lower-limb amputees can afford them. The BiOM, for example, is about $80,000 according to Caputo *et al.* (2015).

In conclusion, the active devices described in this section, despite the apparent advantage of a powered push-off, still have limitations which need to be overcome to make them really biomimetic, suitable in size, weight and complexity for a lower-limb prosthesis, and affordable

by a large number of amputee (of any activity level too). Springs and clutches seem not to be the most efficient way to mimic the joint torque and harvest mechanical energy during gait to be released with an appropriate timing, so alternative technologies should be explored, such as hydraulics, which can exploit the energy recycling behaviour characterising a human joint together with providing a continuous control of the joint torque.

2.2.3 Hydraulics for damping and/or transmission

The previous sections have reviewed designs based on mechanical linkages (i.e. clutches and springs), both with and without external power sources. This section and the following one focus on lower-limb prostheses based on hydraulics. Hydraulics technology has been used in prosthetics broadly for two main purposes: damping or actuation (i.e. electrically powered).

In this section, those prostheses in which hydraulics is used for damping and/or stabilising the foot, for synchronisation between the knee and the ankle joints, and for actuation are briefly reviewed.

Designs using hydraulics for damping and/or terrain adaptation
Many hydraulic ankles have been commercialised in the last decades, containing hydraulic cylinders that provide for only shock absorption at heel strike, acting as dampers dissipating energy, or also terrain adaptation. The latter may include a microprocessor that varies the hydraulic resistance level (such as the Elan foot by Blatchford and the Raize foot by Fillauer) to automatically optimise foot stability when walking on slopes and uneven terrain, and also during standing. The same working principle has been used in a number of knee prostheses, like the C-Leg (Dedić & Dindo, 2011).

Designs using hydraulics for damping and synchronisation between the knee and the ankle joints
A few examples of knee-ankle prosthetic legs based on hydraulics exist. Some of them were developed in the second half of the 20th century and are still available today. In summary, these designs provide coordinated motion of the ankle and the knee joints to ensure ankle dorsiflexion for ground clearance (e.g. the HydraCadence (Wilson, 1968)), but without

providing any additional energy at the ankle joint for push-off (Flynn *et al.*, 2014). The HydraCadence also provides for swing control in term of a hydraulic resistance at the knee joint through a hydraulic cylinder, likewise the Mauch SNS, which also provided for stance control (Wilson, 1968).

Electrically-powered devices using hydraulic actuation

Flowers and Mann (1977) developed a simulator of knee prostheses based on an electrohydraulic servo system, in which knee flexion and extension is allowed by a hydraulic cylinder driven by a power supply. By actively providing power at the knee joint, it is possible to perform activities such as walking on slope and stair climbing. Different studies investigated the use of an electrically powered hydraulic system for the actuation also of the ankle joint: for instance, the ankle-foot prosthesis by Woo *et al.* (2014), or the transfemoral prosthesis SmartLeg by Dedić and Dindo (2011), which incorporates one hydraulic actuator at the knee and a second one at the ankle, both electrically powered. The use of an actuator at the ankle joint allows, as for powered clutch-and-spring prostheses, to assist with forward propulsion during push-off through a peak torque and power similar to those ones of an anatomically intact subject, but with often no advantage in the rest of the gait cycle.

2.2.4   Hydraulics for energy storage and release

This section reviews the small number of designs in which hydraulics is used neither as a passive damper nor as an actuator with a power supply, but as a means of energy storage and release.

A hydraulic prosthetic knee developed at the Cleveland State University by van den Bogert et al. (2012) and patented by Smith et al. (2014) uses a hydraulic accumulator for energy storage and return. The knee is composed of a rotary hydraulic actuator, which is a fixed displacement actuator; a spring-loaded hydraulic accumulator responsible for energy storage; and a low-pressure accumulator that absorbs changes in volume without pressure change (Figure 2.34).
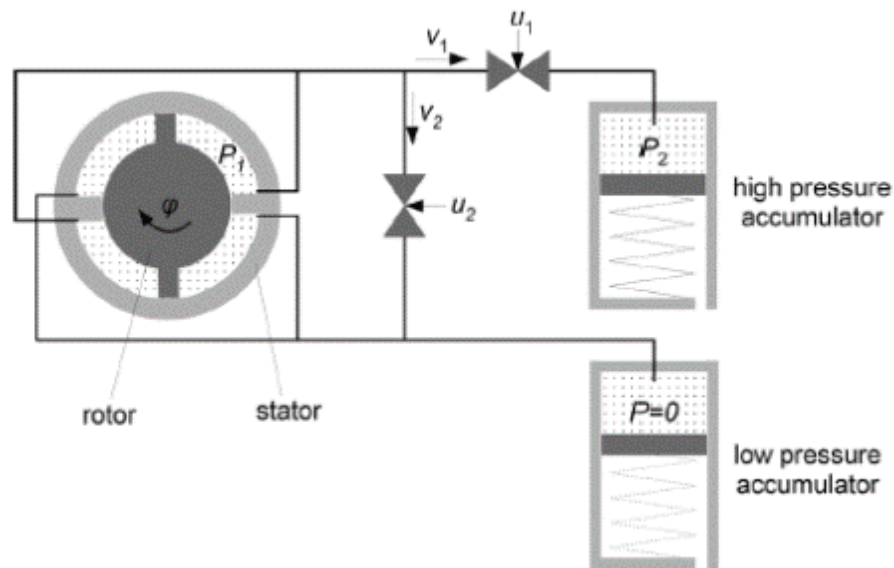
Figure 2.34 Hydraulic circuit diagram by van den Bogert et al. (2012) for a prosthetic knee joint with a rotary actuator, two valves and two accumulators. The rotor is attached to the socket, while the stator and the rest of the hydraulic circuit are attached to the shank. *P* is the pressure, *v* the flow rates, *u* indicates the valve control and φ the knee flexion angle.

Two valves control the actuator: valve 1 allows flow to the high-pressure accumulator where energy is stored, while valve 2 bypasses the accumulator. During stance, valve 2 is closed while valve 1 is open to allow flow into the accumulator for energy storage, and out of the accumulator for energy return) During swing, valve 2 is open and valve 1 is closed to allow the leg to swing. This last configuration corresponds to a normal knee prosthesis providing controlled damping, like the C-Leg, as the high-pressure accumulator is not used. The joint torque can only be controlled by throttling the flow through the valves to adjust the pressure drop across them. This means introducing significant energy dissipation, and hence inefficiencies, into the system. The authors also noted that it may be necessary to partially close valve 1 during stance to allow some energy dissipation. Further, the authors assumed no leakages in the actuator, as well as small loss coefficients for the valves, so further work is needed to evaluate the system performance with commercially available valves. Simulation conducted using a computational model to derive the optimal control of the valves for different activities, such as walking, running and sitting-standing, showed that the device can replicate knee angles and torques (see Figure 2.35), which positions it favourably compared to most of the unpowered and powered clutch-and-spring transfemoral prostheses (see Figure 2.17 and Figure 2.33). Energy stored into the accumulator can be used for those activities requiring net positive work over many gait cycles. A sensor-based controller should

be added to manage the valves opening and closing in view of a possible commercialisation (van den Bogert *et al.*, 2012).
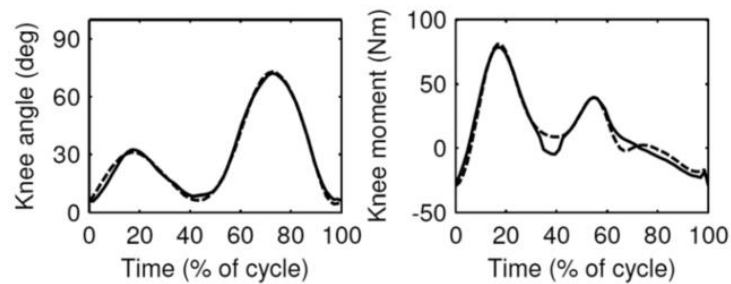
Figure 2.35 Outputs of the simulation of the hydraulic prosthetic knee by van den Bogert et al. (2012): knee angle (left) and torque (right) during walking with an optimal valves control. Dotted lines represent the desired profile from an anatomically intact subject, while the solid lines represent the simulated output of the knee prosthesis.

The same research group developed another knee prosthesis able to harvest energy, replacing the rotary actuator with a linear one (i.e. a hydraulic cylinder) (Wilmot *et al.*, 2013). Figure 2.36 shows as the rest of the hydraulic circuit is basically the same as the previous design: a high-pressure accumulator (HPA), a low-pressure bladder accumulator (LPA) to keep the pressure constant and two valves. Also in this case, the authors only ran simulations of the new device, which showed a good tracking of the thigh and the knee angle (the former is better). Optimisation is still necessary before commercialisation.
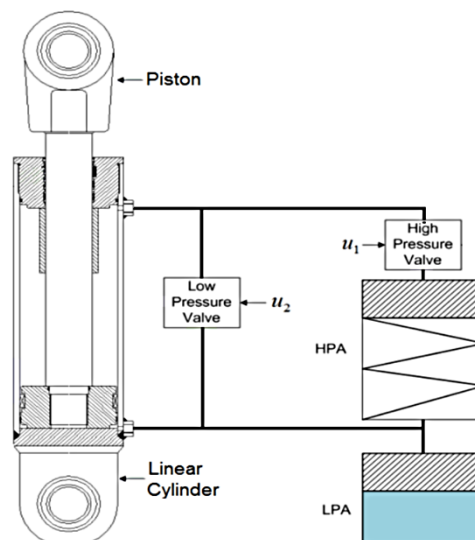
Figure 2.36 Hydraulic circuit of the prosthetic knee by Wilmot *et al.* (2013), with the hydraulic cylinder, and the high and low-pressure accumulators (*u* indicates the valve control).

A last study was conducted by Richter *et al.* (2016) based on the design developed by van den Bogert *et al.* (2012), replacing the rotary actuator with a linear one integrated in a crank-slider mechanism, often used in knee prostheses (see Figure 2.37).
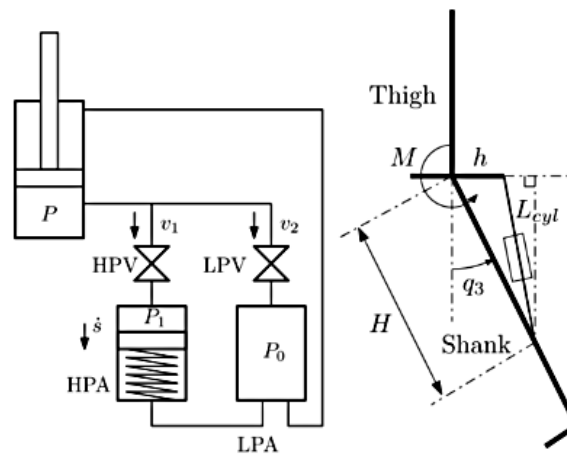
Figure 2.37 Hydraulic knee prosthesis by Richter *et al.* (2016).

The working principles of the system are the same as the van der Bogert's model. The design was tested using a robotic hip emulator that reproduces gait on a treadmill. Results showed that, despite the system being able to mimic knee kinematics, it is highly inefficient from the energetic point of view: the power at the accumulator is much smaller than the power transferred from the knee joint, and most of the input power is dissipated across the valves. Nevertheless, the authors speculated that the use of this device with the accumulator that stores and releases energy during walking could reduce the metabolic cost of walking of transfemoral amputees (Richter *et al.*, 2016).

In summary, all the devices designed at Cleveland State University are semi-active: power is required only to activate the valves and the controller. Therefore, the required capacity of the battery would be much smaller than those required for active prostheses. The key feature, the use of a hydraulic accumulator allows for the storage of energy that can be used when needed, either within the same gait cycle or during following cycles. These devices can generate a smooth profile for knee biomechanical parameters such as angle, torque and power, whereas all the other clutch-and-spring based designs cannot (see Figure 2.33 and Figure 2.35 for a comparison). Nevertheless, a common feature of the three Cleveland State designs discussed here, is that knee torque can only be controlled by using valves to throttle

the flow to adjust the pressure drop across them, hence dissipating energy and making the system inherently inefficient. This observation suggests that a similar biomimetic design could be used for the ankle joint to match the non-linear torque of an intact ankle, purely relying on the storage of eccentric work during gait in terms of pressurised fluid.

Koganezawa *et al.* (1987) reported an unpowered transfemoral prosthesis (WLP-7R) with a hydraulic circuit integrated in the shank (2.4kg). The cylinder at the knee joint is connected to the one at the ankle joint, so that the two joints are counterbalanced (see Figure 2.38). When the ankle dorsiflexes during stance, port B is closed thanks to an upward motion of the ankle piston. This leads also to an upward motion of the knee piston during stance, preventing knee buckling during weight bearing. During this phase, energy is stored in the spring accumulator via the flow through port A. When the knee starts to bend at the end of the stance, both the knee and ankle piston move downward, opening port B. In this way, flow is allowed from the accumulator to the cylinder, releasing energy to assist with knee extension during swing (Figure 2.38). The prosthesis allowed knee-ankle coordination, a smooth transition from stance to swing phase and stairs walking, but it did not reach the market (Elliott, 2014).
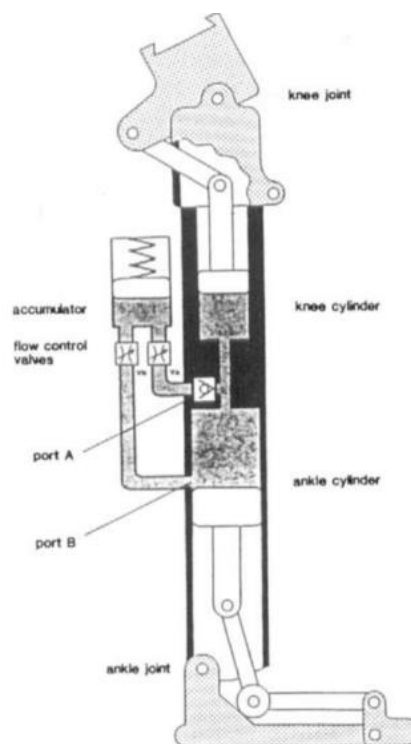
Figure 2.38 Transfemoral prosthesis (WLP-7R) by Koganezawa *et al.* (1987).

This design was resumed a few decades later by Sophyn and Koganezawa (2015): their prosthesis (1.9kg), despite still based on hydraulics to prevent knee buckling under user's weight during stance and to generate knee extension, did not allow for energy storage and return to and from an accumulator (see Figure 2.39).
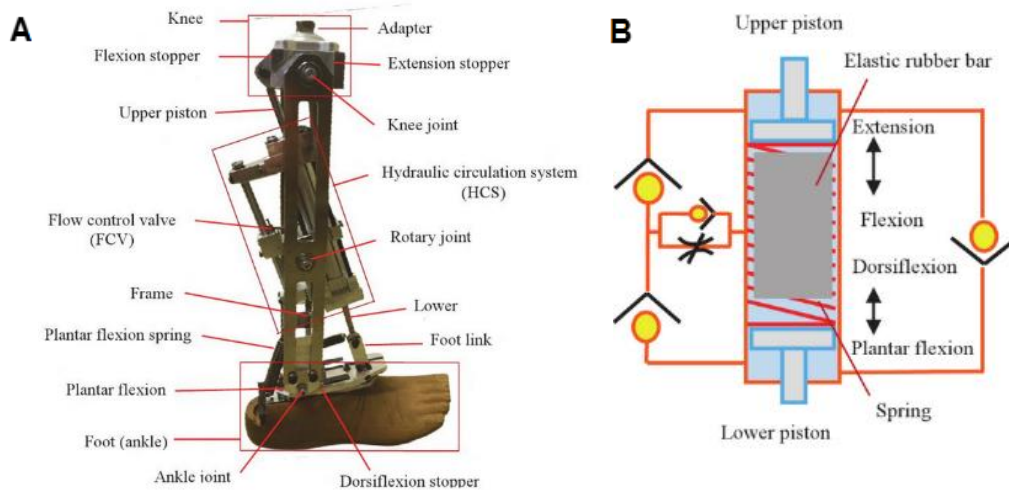
Figure 2.39 (A) Hydraulic transfemoral prosthesis developed by Sophyn and Koganezawa (2015) and (B) its hydraulic circuit.

2.2.5   Orthoses and exoskeletons which use hydraulics to store and return energy

Given the scarcity of prostheses based on hydraulics for energy storage purposes, the review was enlarged to include orthoses and exoskeletons. In most of these devices hydraulics is still used as an actuator. For instance, Durfee's team at the University of Minnesota developed an active ankle-foot orthosis (AFO) driven by electrically-powered hydraulic actuators to assist with ankle dorsiflexion and plantarflexion. Hydraulics was preferred to pneumatics, given the higher force/torque and power density it provides (Neubauer *et al.*, 2014). For the same reasons, it was preferred to electric actuation in some exoskeletons (Ansari *et al.*, 2015; Kim *et al.*, 2015; Otten *et al.*, 2015; Young & Ferris, 2017), together with the possibility of placing the power supply (i.e. motor and hydraulic pump) distally and transfer pressurised fluid to the actuators placed at the different joints via hoses and valves, avoiding the need for one motor and actuator per joint – as in the case of electric actuation - and, thus, reducing the device size and weight (Huo *et al.*, 2016; Otten *et al.*, 2015). Consequently, hydraulic actuators tend to be used for military and manufacturing purposes, or whenever quick movements are required, while electric actuators are preferred for rehabilitation purposes (Huo *et al.*, 2016; Kim *et al.*,

2015). Nevertheless, drawbacks of hydraulic actuators with respect to their electric counterparts are: lower accuracy due to a poorer force control (Kim *et al.*, 2015); an inherent inefficiency due to the pressure drops across valves; and possible safety issue due to the hydraulic pump (Veale & Xie, 2016). An accumulator is often included in those exoskeletons based on hydraulic actuation not as an energy store but as a damper to absorb volume variation and to decrease pulsation effects caused by valve switching (Kogler *et al.*, 2010), keeping the pressure constant in the circuit (Cao *et al.*, 2010).

Only one attempt of using hydraulics for energy storage purpose was found: Kangude *et al.* (2009), working with Durfee's team at the University of Minnesota, explored the combination of functional electrical stimulation (FES) with an orthosis which uses a hydraulic circuit to harvest and release energy in a controlled manner during gait. Specifically, through FES, the quadriceps are stimulated to generate knee extension, storing excess energy which can be transferred to the hip joint to assist with forward progression: one cylinder at the knee stores energy in the hoses, which work as an accumulator, and transfers it through hoses to the other cylinder placed at the hip joint, which acts as an actuator, to assist hip extension and, thus, forward propulsion (Figure 2.40).
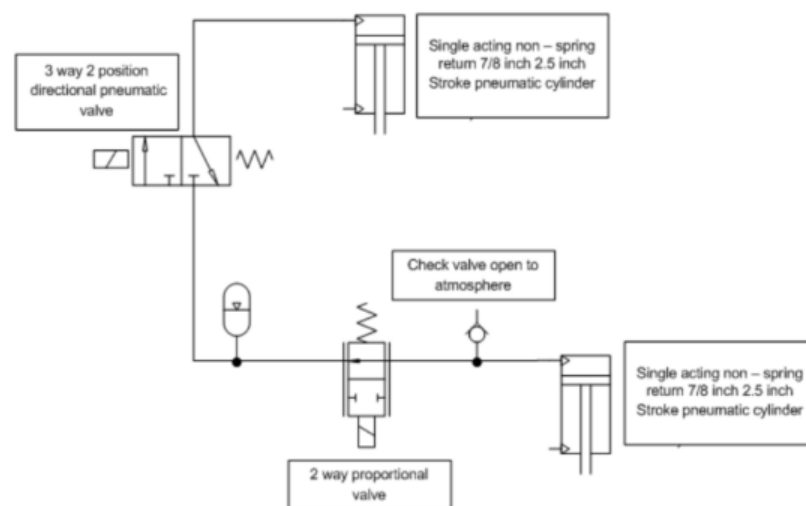
Figure 2.40 Pneumatic circuit by Kangude *et al.* (2009). The same layout is used also when hydraulic cylinders are considered.

Simulations showed that, of the approximately $14\,J$ from quadriceps work, $5.4\,J$ (i.e. about 39%) were stored in the accumulator (i.e. hoses), of which $5\,J$ (i.e. about 92.60%) were lost at the proportional valves because of high friction losses, and just $0.4\,J$ (i.e. the remaining 7.40%) were available for hip extension. Thus, they decided to build a prototype using

pneumatic cylinders. Just a small battery was needed for the microprocessor to control valves opening and sensors, so that it may still be considered as an unpowered device.

Finally, Chin *et al.* (2012) investigated the harvesting of mechanical energy from human motion in terms of fluid power, without the need for a power source. A bellow integrated in the shoe sole allows fluid flow, under the user's weight, to a pneumatic or hydraulic cylinder external to the shoe, harvesting pneumatic or hydraulic power. In their study, the authors did not use the stored energy, but they speculated that this mechanism could be used to power orthoses.

2.3   Discussion

Although unpowered clutch-and-spring devices represent a cost-effective solution, the use of clutches and springs offers only discrete control, through spring locked and spring released, rather than continuous, preventing the adjustment of the ankle torque in a controlled and "smooth" manner (Richter *et al.*, 2016). As a consequence of the fixed mechanical properties of these compliant components, most of these devices are not able to replicate the ankle torque, storing all the negative work done during the stance phase of walking (Figure 2.2): some of them just store the small amount of negative work at load acceptance- (e.g. the Collins and Kuo's device), while others are able to store the eccentric work done during mid and terminal stance. With the exception of Williams and Nickel's designs (Nickel *et al.*, 2014; Williams *et al.*, 2009), and the WalkMECH*adapt* (Unal *et al.*, 2014), most of these designs cannot adapt the ankle torque profile to suit different speeds and slopes.

The issues of the complexity and, in some cases, weight of clutch-and-spring based designs is particularly stark in the integrated transfemoral prostheses (e.g. the WalkMECH and the HEKTA), which allow energy transfer from the knee joint to the ankle joint using mechanical linkages, springs and cables. Despite the additional weight and complexity, transfemoral amputees would benefit from this transfer: for instance, the eccentric work done at the knee at the end of the swing phase, usually dissipated through damping systems in commercially available prosthetic knees, and approximately amounting to 13J in an 80kg person according to Geeroms *et al.* (2013), may be stored and released later on during push-off at the ankle

joint to assist with forward propulsion, when about 18J are needed in an 80kg person (Geeroms *et al.*, 2013). Nonetheless, the stored energy is completely returned during push-off, and the whole system is reset during swing in preparation for the next gait cycle, meaning any excess energy captured during a given gait cycle cannot be exploited in subsequent gait cycles. Hence, given the drawbacks of these integrated designs, alternative technologies should be investigated to realise an efficient energy transfer.

The second group of devices uses a battery and electric motor in combination with clutch-and-spring mechanisms. The electric actuator generally controls ankle angle throughout the gait cycle, and various designs have demonstrated peak torque and power during push-off close to those of an anatomically intact joint. Nevertheless, matching the quasi-stiffness of the ankle joint (Figure 2.6) throughout the gait cycle is still a distant goal for most of these devices: only the SPARKy, the Walk-Run and the BiOM foot show a biomimetic ankle torque, and these same devices together with the AMP-Foot 3 also match the power profile. Those devices able to vary the equilibrium position of the compliant element included in the actuator (such as the BiOM foot, the ankle component of the CYBERLEG α- and β-Prostheses, and the AMP-Foot 3) allow for slope and speed adaptation, which is clearly an advantage over passive devices. All the other devices cannot vary their mechanical properties to adapt to different tasks.

However, the power supply further increases the weight and size of the device, leading likely to an increase of the metabolic cost and gait asymmetries (J. D. Smith & Martin, 2013). This issue is amplified in transfemoral prostheses where mechanical linkages are used for the energy transfer between the knee and the ankle joints (e.g. the CYBERLEG α- and β-Prostheses), and when variable stiffness actuators or explosive elastic actuators are used, making the device also too complex for a prosthesis (Cherelle *et al.*, 2014). Therefore, although an appropriate magnitude and timing of the energy return during push-off should contribute to a decrease of the metabolic cost of walking with respect to a passive conventional or ESR foot, added weight and volume may nullify this advantage. In addition, the number of studies investigating the real effectiveness of these new active devices on the metabolic cost of amputee's walking is still small and with small samples.

Moreover, batteries introduce issues related to the duration of a single charge, which limits amputee's autonomy, and limited battery life, in part due to frequent charge/discharge. Finally, the commercial devices are extremely expensive and need access to highly specialised facilities for repair because of their complexity.

In conclusion, despite designed to mimic the ankle quasi-stiffness, most of these active clutch-and-spring devices struggle in mimicking the non-linear quasi-stiffness of the ankle joint: they mainly provide a net positive peak power at the ankle joint during push-off to assist with forward propulsion, which does not necessarily lead to a reduction of the metabolic cost of walking (Russell Esposito *et al.*, 2015) or gait asymmetries (Ferris *et al.*, 2012). In addition to the device weight and size, training issues may further compound this apparent disconnect (Ferris *et al.*, 2012). Springs included in these designs seems not to be the most effective technology to replicate the ankle torque, harnessing the energy that may be stored during the gait cycle and released later at the right instant for forward propulsion.

The review, then, goes through prostheses based on hydraulics. In addition to those ones in which hydraulics is mainly used for damping and/or transmission (both powered and unpowered), unpowered prostheses in which hydraulics is used for energy storage purposes are investigated. The designs developed at Cleveland State University by Van den Bogert et al. (2012), Wilmot *et al.* (2013) and Richter *et al.* (2016) use a fixed displacement actuator. Therefore, the prosthetic joint torque can only be controlled by throttling the flow through the valves to adjust the pressure drop across them and, hence, dissipating energy. So, unless the valves are fully closed or fully open (no torque control), this is an inherently inefficient approach. The design by Kangude *et al.* (2009) confirmed the inefficiencies introduced by the use of proportional valves. This is a well-known issue of hydraulic actuation also in robotics applications, as Guglielmino *et al.* (2010) stated: "From an energetic point of view proportional control is dissipative and inefficient".

The hydraulics-based prosthesis designs, despite the energy losses due to proportional valves, showed that it is possible to continuously control the torque profile at a joint, storing and releasing energy in terms of pressurised fluid. In addition, by storing energy in a hydraulic accumulator, this energy can be returned also in subsequent gait cycles. These features

contrasts with all the powered and unpowered clutch-and-spring devices discussed above. The hydraulics-based orthoses and exoskeletons, although mainly using fluid for actuation rather than energy storage and return, highlighted some of the potential benefits: the power supply can be placed distally and pressurised fluid transferred to the actuators via hoses and valves. Finally, the design by Kangude *et al.* (2009) showed the potential for a simple, light and flexible solution based on hydraulic technology, demonstrating features of energy storage and release and transfer of energy via pressurised fluids.

In conclusion, harvesting energy from human motion in prosthetic design has the potential to improve amputee mobility by reducing the metabolic cost of walking, and it has received more attention in recent years. However, electrical systems are not well suited to the rapid energy storage and return requirements of gait. Mechanical springs are better, but inflexible and not well suited to producing biomimetic ankle torque or transferring energy between prosthetic joints. This review has highlighted the potential advantages of using miniature hydraulics and, in particular, using an accumulator as an energy store and transferring energy between joints through simple fluid connections (i.e. pipes).

2.4   Previous work at the University of Salford

As a result of the drawbacks of the attempts described above and the advantages associated with the use of hydraulics, work at Salford has focussed on the feasibility of using miniature hydraulics to satisfy the following design requirements for a new advanced lower-limb prosthesis:

- Allow control of ankle torque throughout the gait cycle to provide a natural gait and also slope adaptation.
- Store all of the mainly negative work done from heel strike until the end of the terminal stance phase, corresponding to maximum dorsiflexion.
- Release the stored energy during push-off.
- Allow the transfer of energy between the knee and the ankle joints at any time during the gait cycle.

The first concept design was studied by Bari (2013) during his PhD, based on a hydraulic accumulator, a low-pressure tank, and a variable hydraulic displacement actuator (VDA), which provides ankle torque driving the ankle joint via a gearbox to reduce the VDA size. The VDA stores energy from heel strike to maximum dorsiflexion, working as a pump that pumps oil from the tank to the accumulator, and energy is then returned during push-off through fluid flow from the accumulator to the tank, through the VDA working as a motor. Despite simulations showed improvements on conventional and ESR feet and designs based on clutch-and-spring mechanisms in terms of peak power during push-off and ankle torque throughout the gait cycle, size and weight were incompatible with those of a lower-limb prosthesis. A second design addressed this issue by adding a parallel spring (a hydraulic cylinder) to reduce the torque load on the VDA and, thus, its size and weight (Bari, 2013). In this case, the hydraulic cylinder (Figure 2.41) is the major work provider: the foot rotation around the ankle joint causes piston motion inside the cylinder and, therefore, fluid flow from the cylinder to the accumulator. As no fluid flow between the cylinder and the tank exists, the VDA, which does not drive directly the ankle joint, provides the difference between the required work and the work done by the cylinder, working as a pump during the eccentric phase of stance, and as a motor during push-off. Moreover, the VDA rotation causes the cylinder rotation and, consequently, a linear motion of the sliding plate, varying the lever arm of the spring from the ankle joint and, thus, controlling the ankle torque.
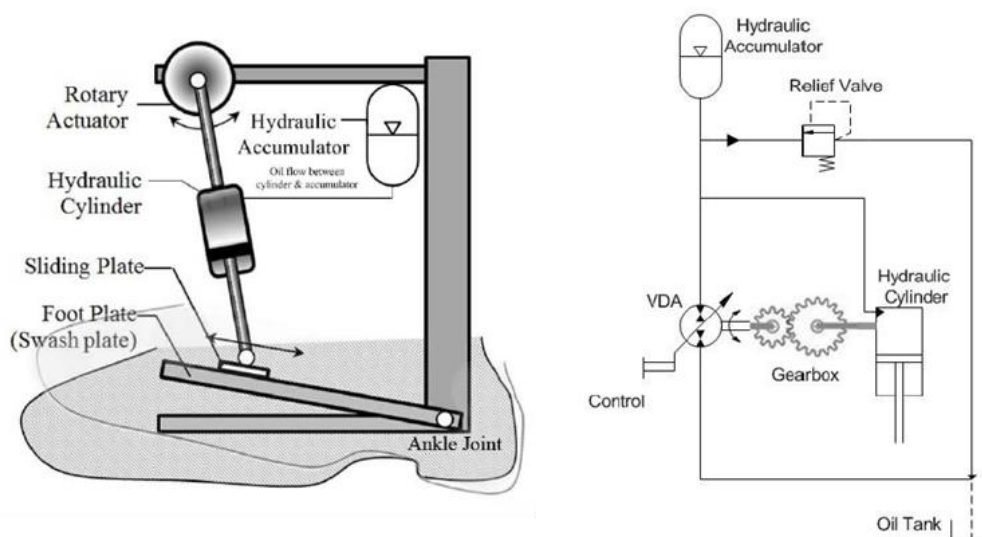
Figure 2.41 (A) Sketch and (B) hydraulic circuit of the second concept design developed by Bari (2013).

This last concept design proved to be feasible for a prosthesis in terms of size and weight, amounted to 2.9kg for the foot and the shank segment, which may be reduced using bespoke

components. Simulations showed a continuous torque control and higher peak power than the first design on level and downhill walking , with smaller losses, while uphill walking is poorly matched, and a feasibility study demonstrated size and weight compatible with a prosthesis. According to Bari, this was the first study showing that a conceptual design of a lower-limb prosthesis, specifically an ankle joint, based on miniature hydraulics with performances equal to those of active devices is feasible: it can mimic the energy recycling behaviour of the ankle joint during gait while controlling its torque. Moreover, in the same study, the potential of hydraulic accumulators for an efficient energy storage and release is proved, given their inherent high-power density, which makes them well suited to miniaturisation, and ability to be charged and discharged over a huge number of life cycles. In addition, they can easily be used also to obtain energy transfer between joints. It is therefore unsurprising that others have explored this approach (see sections 2.2.5). Nevertheless, a prototype of Bari's design was not realised.

However, a third concept design was studied by Gardiner *et al.* (2017) at the University of Salford and it is shown in Figure 2.42: it was based on a hydraulic accumulator, a VDA driven by the ankle joint via a gearbox, with a parallel ankle joint spring to reduce the torque demand on the VDA.
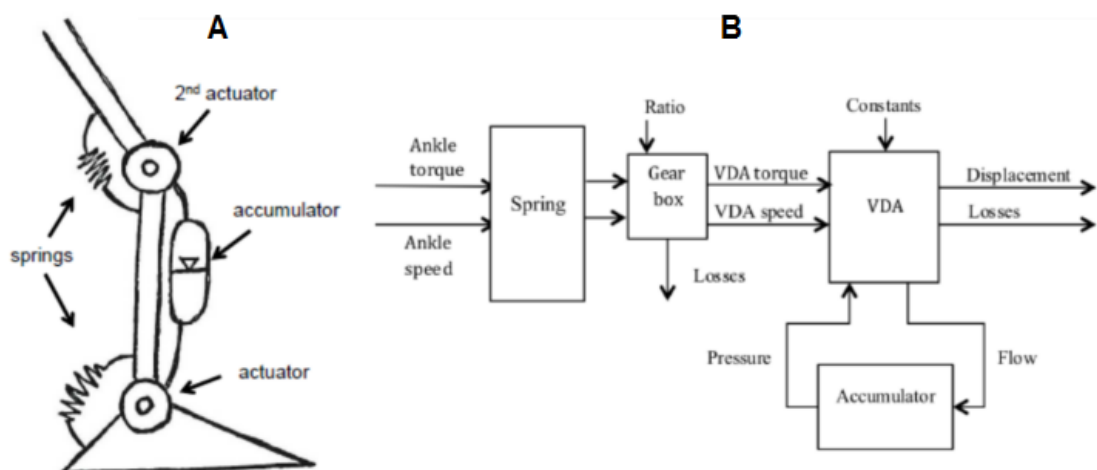
Figure 2.42 (A) A multi-joint version of the Salford's hydraulic VDA based design using a single accumulator and the VDAs at the two joints (knee and ankle). (B) Schematic of the concept design. The figure is sourced from Gardiner and Howard (2016).

Its most important features are:

- The VDA allows continuous control of ankle torque such that it can follow any desired profile over the gait cycle, but without the need for throttling losses across valves as is the

case for the designs discussed above which use fixed displacement actuators. However, the disadvantage is that leakage losses are greater in VDAs than in fixed displacement devices because of seal clearance.

- It is a fully-passive device and, therefore, does not require an external power supply such as a battery.

- Any eccentric (negative) ankle work done in stance prior to push-off is stored in the accumulator and returned whenever concentric (positive) work is required, mainly for push-off.

- The accumulator can store and return energy over many gait cycles, which could be used to assist short periods of uphill walking.

- Energy transfer between the knee and the ankle joints is allowed through the accumulator and pipes. A multi-joint version of the design uses a single accumulator and two VDAs at the knee and ankle joints to produce the required torques at any point in the gait cycle with no synchronisation problem between joints.

- A parallel spring placed between the foot and the shank of the prosthesis, with a stiffening profile, minimises the torque required from the VDA and hence its size.

In this new concept design, high energy losses are avoided through continuous control of the torque by adjusting fluid displacement per radian, rather than by adjusting pressure using throttling valves. This allowed the design to mimic intact ankle torque with an acceptable energy efficiency. Simulations showed that this design provides controlled and timely energy storage and release: in level walking, normal push-off is achieved and, per gait cycle, the energy stored in the accumulator increases by 22% of the requirements for normal push-off, which can be used to assist with short periods of uphill walking. Although the results are promising since energy losses amount to approximately 10% during stance, the feasibility study revealed some problems with the potential prototype. In particular, for this design to be a success, a new miniature, low-losses, lightweight VDA would be required characterised by half the displacement of the smallest commercially available device. As the application area is very small in industrial terms, it was highly unlikely that the fluid power industry would devote the major resources needed to attempt such a dramatic reduction in size. Nevertheless, this study confirmed the potential of hydraulics to recycle energy efficiently at the ankle joint over many gait cycles with a continuous control of the ankle torque, suggesting

further work is warranted. Hydraulic accumulators seem to be the best option to efficiently store and release energy, while the pipes represent the best choice to allow a lightweight and flexible energy transfer between the knee and the ankle joints, avoiding the use of complex mechanical linkages and gears. In this way, braking energy at the knee may be stored to be used at the ankle during push-off for forward propulsion (Bari, 2013; Gardiner *et al.*, 2017).

The review and the previous designs developed at the University of Salford informed the direction of this PhD project, as there is still an opportunity for a truly transformative research to innovate current ESR prostheses using miniature hydraulics.

3.Chapter 3: Conceptual Design

Leonardo Da Vinci, Mechanical hammer with eccentric cam

" Study science first and then practice science born from it."

(Leonardo Da Vinci)

3.1   Introduction

Building on the potential of an accumulator-based system with energy transfer between joints via pipes, a novel concept design is presented in this chapter. Results of the previous work at Salford highlighted that complex hydraulic components beyond the expertise of prosthetic companies, like a VDA smaller than those existing on the market, are to be avoided. Thus, the primary aim of this PhD project was as follows: to design a novel prosthetic ankle using simple miniature hydraulic components, including an accumulator for energy storage and return, to imitate the behaviour of an intact ankle. Specifically, the following objectives were set:

1. To develop a concept design of the ankle mechanism, using simple hydraulic components, to:

   • Mimic intact ankle torque, to store the mainly negative work done from heel strike to maximum dorsiflexion in the accumulator and release it during push-off in a controlled way in terms of timing and amount of energy flow.

   • Allow energy transfer between the knee and the ankle joints via pipes – for example, storing the eccentric work done at the knee at the end of the swing phase to be used at the ankle to assist with forward propulsion during push-off.

2. To demonstrate through simulations that the expected performance of the new design justifies physical prototyping in the future.

To achieve these ambitious objectives, a research programme was planned according to a typical engineering design process. Different models exist for the design process, and one of the most common was developed by Pahl and Beitz (Pahl *et al.*, 2007), with the following main phases: definition of the requirements and constraints on the design; conceptual design to develop alternatives solutions to the same problem; embodiment design – or preliminary design – to engineer the best solution, defining the preliminary shape and materials; finally, detail design to specify all the details of the final design, producing the related technical drawings and documentation. Consistent with this model, the process of moving from requirements to testing of a design with amputees might be considered as follows:

1. Requirements and constraints definition.

2. Conceptual design.

3. Mathematical modelling of the new design.

4. Implementation of the simulation model in MATLAB (R2018b, The MathWorks, Inc., Natick, MA, USA) and testing.

5. Simulation based design.

6. Simulation based performance assessment to justify continuing to the following stages.

7. Design for prototype manufacture.

8. Prototype manufacture by the industrial partners.

9. Mechanical testing according to the ISO standards.

10. Testing with a small cohort of amputees for initial proof of concept.

This PhD was concerned primarily with stages one to six of the list. The remainder of this chapter focuses on requirements and constraints definition, conceptual design, and a description of the main components of the chosen concept design. The mathematical model of the new design is developed in Chapter 4, while Chapter 5 covers the explanation of the simulation model for the whole system, implemented in MATLAB. Chapter 6 focuses on the preliminary design, based on simulations, while a sensitivity study to assess the performance of the new system is described in Chapter 7. Chapter 8 sums up the whole PhD drawing the main conclusions.

3.2 Requirements and constraints

As the first step of the design process, a list of technical requirements and constraints was defined, which can be used to evaluate the design as it evolves. The technical requirements (i.e. demands the new device must necessarily meet) of the novel prosthetic ankle were:

1. To mimic the torque of an intact ankle in order to store energy during the stance phase of walking, prior to push-off.

2. To mimic the torque of an intact ankle during push-off to release the stored energy for forward propulsion.

3. To allow energy transfer between joints, starting with the ankle joint and the knee joint.

The constraints were:

1. To use a hydraulic accumulator for the energy storage and release process, and pipes for the energy transfer.
2. To prioritise simplicity in the selection of other hydraulic components, such that they could be easily manufactured or sourced externally, by prosthetic companies.
3. The prosthesis should match the shoe size and height of the missing anatomy, and weigh no more than the missing anatomy. The typical lower-leg length from the ground to the knee joint is 0.285 times the height of the subject, while the typical mass of the foot and shank segments is 0.061 times the mass of the subject (Winter, 2009). Considering a $70\ kg$ subject, with a height of $175\ cm$ (Winter, 1984), this means a lower-leg length of $49.88\ cm$ with a corresponding mass not more than $4.27\ kg$. The average stump length in transtibial amputees according to Isakov *et al.* (1996) is $15.1 \pm 3.2\ cm$. Hence, an average distance from the ground to the distal connection with the socket is obtained by subtracting the average stump length from the lower-leg length: $(49.88 - 15.1)\ cm = 34.78\ cm$. Furthermore, to be conservative, an upper value for the stump length may be calculated by adding $2\ SDs$ to the mean, which then includes 97.72% of amputees: $(15.1 + 3.2 * 2)\ cm = 21.5\ cm$. This leads to a smaller (more conservative) distance from the ground to the distal connection with the socket: $(49.88 - 21.5)\ cm = 28.38\ cm$. This is the available height for the new prosthesis assembly and corresponds to a mass of approximately $2.43\ kg$ (an estimate based on the proportion of the lower-leg).

3.3   Conceptual design

The conceptual design process started with brainstorming involving the whole team, made up of the PhD student and supervisors, to explore a range of possible design concepts consistent with the design objectives, requirements and constraints, opting always in favour of the simplest solution, and finally selecting the solution to be implemented.

By assuming an accumulator-based system for the novel hydraulic ankle, fluid flow to and from the accumulator must be allowed to respectively store and release hydraulic energy in it. Consequently, a continuous power conversion in a controlled and timely manner during the

gait cycle is necessary: conversion of mechanical power given by the rotation of the ankle joint to fluid power and vice versa. Hence, the first step is the selection of a hydraulic actuator to allow this power conversion and, thus, to provide torque. The remainder of this section covers this topic and the definition of the final layout of the new system.

3.3.1   Power conversion

The most common and simple design of hydraulic actuators to convert mechanical power to fluid power and vice versa is the hydraulic cylinder, which is a linear actuator. Developing miniature hydraulic components is challenging not only in terms of size and weight required, but above all in terms of efficiency, as Xia (2015) explained. Nevertheless, small-scale hydraulic cylinders are used in a number of assistive technologies such as surgical tools, prosthetic fingers, prosthetic hands and exoskeletons, and other non-medical applications, for instance robots (Neubauer, 2017). Therefore, they were chosen to store and return energy from the accumulator.

Considering the design of a basic hydraulic circuit (Cundiff, 2002), it must include:

- A prime mover that provides mechanical power input to the system.
- A way to convert mechanical power to fluid power.
- A way to convert fluid power to mechanical power.
- Valves.
- An accumulator and a tank.
- Pipes.

In this novel prosthetic ankle, the prime mover is the ankle joint: the rotation of the prosthetic shank relative to the prosthetic foot during the gait cycle causes rotation of the ankle shaft, corresponding thus to mechanical power input to the system (in terms of torque and angular velocity). This mechanical power has to be transmitted to the rest of the system, so that the hydraulic cylinder can convert it in fluid power to be stored in the accumulator. The same process needs to happen also in the opposite direction: the hydraulic cylinder must convert the fluid power into mechanical power to be transferred to the ankle joint. Therefore, a mechanical transmission and a system to convert the ankle joint rotation into the linear

motion of the piston inside the cylinder and vice versa was needed. A gearbox was included in the system, in the "transmission line" of the ankle rotation to the rest of the system. Depending on the gears' configuration, it may cause either a reduction or an increase of the force transmitted from the ankle to the cylinder.

Many ways exist, then, to realise the rotary-to-linear conversion. The most popular are:

* slider-crank mechanisms;
* ball screw mechanisms;
* cams.

Slider-crank mechanisms are widely used in many different applications, including endoscopic surgical tools (Yagi *et al.*, 2006). They also find applications in prosthetic devices: a crank-slider mechanism is used, for instance, in the powered clutch-and-spring prosthesis AMP-Foot 3 by Cherelle *et al.* (2016), and in prosthetic knees (e.g. Sup *et al.* (2008), Warner *et al.* (2016)). Ball screw mechanisms find applications in prosthetic devices too: the powered ankle-foot prosthesis BiOM relies on a ball screw driven by an electric motor to generate the angular rotation of the ankle (Au *et al.*, 2007). Lastly, cams are characterised by being able to produce and control any output motion – translational, rotational or oscillating (Zhang *et al.*), and they are widely used in engineering for reciprocating motion applications, for which they are considered the gold standard (MachineDesign, 2007). Moreover, they are well suited for miniaturisation; they tend to be cheaper than the other mechanisms; they show better dynamic properties and can transmit more power as they permit the highest speed and load function (Rothbart, 2004).

The first two requirements of the new ankle mechanism are related to the mimicking of the torque of an intact ankle. A target behaviour for an ankle prosthesis during the stance phase of walking is known to be given by the quasi stiffness of the ankle joint, as previously mentioned (Au *et al.*, 2007; Hansen *et al.*, 2004), which is the non-linear torque-angle relationship depicted in Figure 3.1.
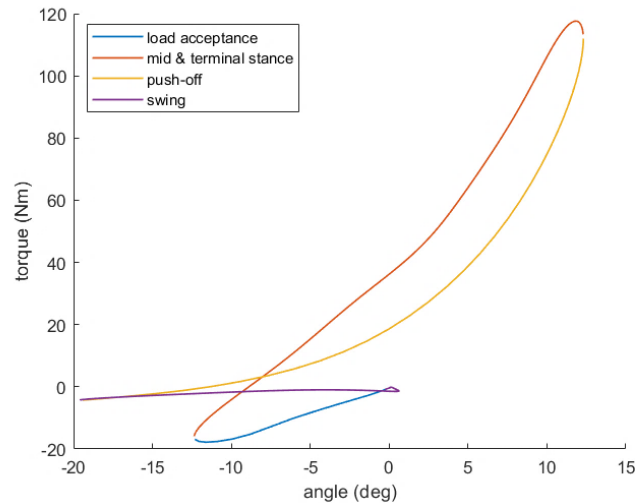
Figure 3.1 Torque-versus-angle curve for an anatomically intact ankle joint during level walking. The slope of this curve during stance is commonly referred to as "quasi stiffness" (Au *et al.*, 2007; Hansen *et al.*, 2004). Load acceptance, stance, push-off and swing are displayed with different colours according to the legend.

During swing the prosthesis should only recover its equilibrium position, which in general corresponds to a null ankle torque when the prosthesis recovers its neutral angle. For this reason, the new ankle mechanism is designed to generate a non-linear torque-angle curve similar to the one of an intact ankle mainly during stance. As a result, cams appeared to be best suited to this: the possibility of manufacturing cams with specific profiles allows to draw the appropriate profile to generate the required torque. In the proposed design, the ankle rotation is transmitted to the cam through the gearbox and the camshaft, to which the cam is fixed, and then, through cam rotation, is converted in the linear motion of the piston inside the cylinder (see Figure 3.2) and vice versa.
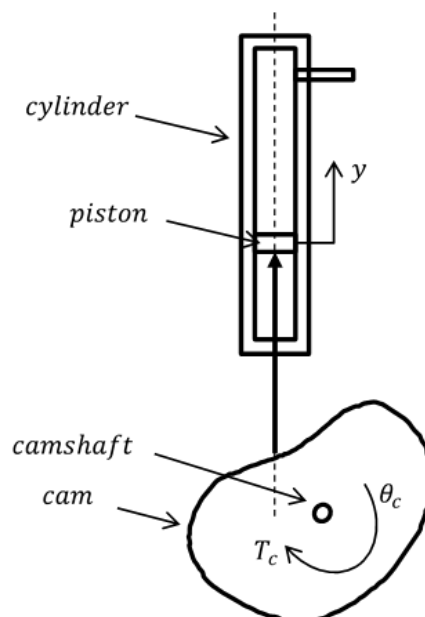
Figure 3.2 Schematic of the approximate layout of a cam and one hydraulic cylinder.

3.3.2 System design

Figure 3.1 shows the torque-angle curve of an intact ankle joint to be characterised by four distinct parts, the transition between each is defined by the events of the gait cycle (see Figure 2.2): load acceptance (in blue); mid and terminal stance (in red); push-off (in yellow); and swing (in purple). Four cam-ram systems, in which the cams drive the hydraulic rams, would be necessary to exactly mimic the four distinct phases of the required ankle torque.

Alternatively, the system could be simplified by accepting less than perfect replication of the four phases. The difference between the eccentric work in stance and the concentric work in push-off is the most significant. Therefore, complexity could be reduced if only this excess of eccentric work is stored and carried forward to assist during short periods of uphill walking. Thus, to simplify the design, just two cam-ram systems may be considered for the two periods during which the largest amount of energy is stored and returned - mid and terminal stance (in red), and push-off (in yellow) (see Figure 3.1). Therefore, two different cams were used: one with a profile that replicates the ankle torque during mid and terminal stance (i.e. ankle dorsiflexion), and a second one with a profile that matches the ankle torque during push-off (i.e. ankle plantarflexion). Then, since the prosthesis should only recover its equilibrium position during swing as previously explained, and because the design should be kept simple, just one spring in parallel to the two cam-ram systems may be included to mimic the ankle torque during load acceptance. A torsional spring could be used to store the small amount of eccentric work done during load acceptance (see also Figure 2.2). However, the use of the same spring to bring the ankle back to its neutral angle during the swing phase may introduce some drawbacks as, for instance, there may be more energy stored in it during plantarflexion at the end of push-off than is needed to return the foot to neutral during swing.

It is worth noting that all of the components discussed to this point, the accumulator, the two hydraulic cylinders, the two cams, the spring and the gearbox, should be easy to manufacture, even at the small-scale.

To make the hydraulic circuit complete, auxiliary components were added: pipes to connect mainly the cylinders and the accumulator; a tank; and valves. These last components are fundamental to either connect or disconnect the two cylinders to or from the accumulator in

a timely manner during gait, providing only on/off control and hence not dissipating energy, by contrast to proportional control valves that provides flow resistance. For this reason, directional control valves (DCVs) were included.

By combining together all these components to fulfil the design requirements/constraints, the layout of the final design implemented for this novel prosthetic ankle was obtained. It includes (see Figure 3.3):

- A torsional spring that provides for standing stability, load acceptance and swing with the two rams switched off. Its equilibrium point coincides with the neutral angle of the prosthesis during standing, so that, by being placed in parallel to the gearbox and the cam-ram systems and driven by the ankle joint, it reduces the torque they need to supply at the ankle joint.

- A gearbox, placed in parallel to the spring, is driven by the ankle shaft and drives the camshaft, possibly increasing the ankle angle and reducing the ankle torque transmitted to the cam. Its starting design includes a two-gears train and, depending on the gear ratio, idler gears may be added.

- A ram and cam combination referred to as "stance cam-ram system", which in its working phase – i.e. mid and terminal stance, from maximum plantarflexion at the end of load acceptance to maximum dorsiflexion - adds to the spring torque to provide the ankle torque required and stores the eccentric ankle work done. Please, note that here the word "stance" refers to mid and terminal stance, so it is not used with its standard definition.

- A ram and cam combination referred to as "push-off cam-ram system", which adds to the spring torque to provide the right ankle torque for plantarflexion during its working phase – i.e. push-off, which is the concentric phase after maximum dorsiflexion.

- A gas-charged accumulator, which stores and releases energy by compressing the gas.

- Directional control valves to connect the hydraulic rams both to the gas-charged accumulator and to the tank (DC valve 1 and DC valve 2).

- A tank (i.e. a low-pressure accumulator) at atmospheric pressure (P_{atm}).

- Pipes to connect the hydraulic rams to the gas-charged accumulator.

Figure 3.3 shows that the rotation of the prosthetic shank relative to the prosthetic foot, in the sagittal plane during the gait cycle, causes rotation of the ankle shaft and, in turn, rotation

of the camshaft through the gearbox. The two cams then convert the rotary motion of the ankle into linear motion of the pistons inside the two hydraulic rams. During mid and terminal stance, the stance ram is connected to the accumulator, via DC valve 1 that allows fluid flow between the stance ram and the accumulator, but not between the ram and the tank; its piston moves up, and, as a result, oil flows into the accumulator, storing energy. At the same time, the push-off ram is connected to the tank so that its ram force is negligible. Then, during push-off, the push-off ram is connected to the accumulator as DC valve 2 allows fluid flow only between the push-off ram and the accumulator, its piston moves down, and, as a result, oil flows out of the accumulator, releasing energy. At the same time, the stance ram is connected to the tank so that its ram force is negligible.
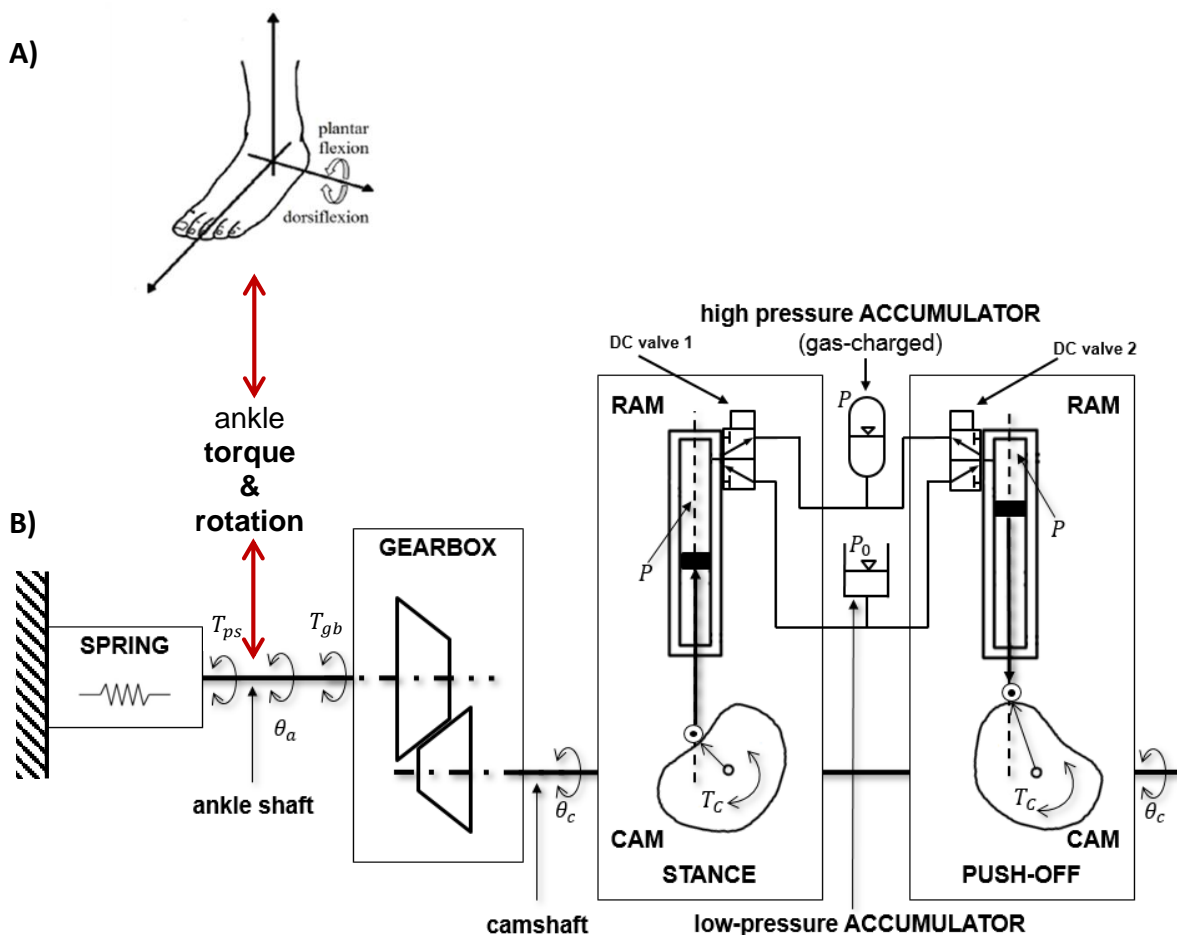
Figure 3.3 (A) Ankle joint rotation in the sagittal plane: plantarflexion and dorsiflexion. (B) Schematic of the new concept design, with the parallel spring (T_{ps}) that reduces the torque demand on the two cam-ram systems, and the gearbox (T_{gb}), which possibly increases cam rotation and reduces the ankle torque transmitted to the cam.

The ground frame represents the shank, to which the spring is fixed on its left side and to which the cylinders and gearbox casing are also fixed. The ankle shaft is fixed to the foot and

drives the cam shaft via the gearbox. In other words, here the foot is seen as rotating relative to the shank. A solid model of the main components of this novel hydraulic ankle was developed during the final stage of this PhD project and is shown in Figure 8.1 and Figure 8.2 of Chapter 8.

The novel prosthesis for the ankle joint is primarily aimed at the transtibial amputee. However, as a modular component to be placed between the foot segment, which may be a simple carbon fibre laminate, and the shank segment of the prosthesis, it would be suitable for people with more proximal levels of amputations. Furthermore, energy transfer is envisioned in a multi-joint version of the design, in which a similar device is placed at the knee joint, a single hydraulic accumulator is used to store energy, and pipes transfer energy between the knee and ankle joints in terms of pressurised fluid. However, the work described in this thesis focuses on the ankle joint design, while the implementation of the energy transfer system is envisioned in future work.

The literature review confirmed the originality of this PhD project, since there are no concept designs matching the one proposed. The remainder of this chapter gives more details about each component of the system and the rationale behind their selection.

Note that, throughout the remainder of the thesis, "low-pressure accumulator" and "tank" will refer to the same components, as will "ram" and "cylinder".

3.4   System components

3.4.1   Cam

Cams are machine elements with a curved profile that, through their oscillation or rotation, transmit a specific motion to another element called the follower. The follower constraint may be realised: through gravity only; with a return spring; it may be "positive-driven" using a follower moving in a groove cut on the face of a closed cam; or through multiple conjugate cams in which every cam has its own roller, but they are mounted on the same reciprocating or oscillating follower. Different shapes exist also for the follower (Zhang *et al.*). The most

common are (see Figure 3.4): a knife-edge follower; a flat-faced follower; a roller follower; and a spherical-faced follower.
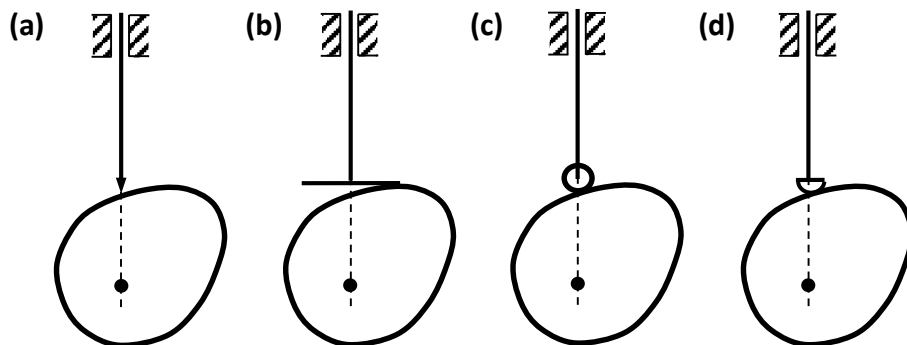
Figure 3.4 Typical followers of a disk cam: (a) a knife-edge follower; (b) a flat-faced follower; (c) a roller follower; (d) and a spherical-faced follower.

Only configurations with a rotating cam and a translating follower are shown in Figure 3.4, as this is the is the input/output motion desired for this specific application. In all the configurations shown above (Figure 3.4), the follower centre line coincides with the camshaft centre line: this is referred to as an "in-line" follower. Otherwise, it is possible to have the same configurations with an "offset" follower, where the offset is the distance between the two aforementioned centre lines (see Figure 3.5 (b)) causing a reduction of the lateral thrust in the follower.
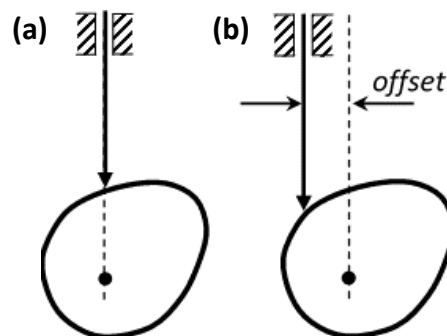
Figure 3.5 (a) "In-line" follower and (b) "offset" follower.

In the design presented here, a disk cam was chosen, given its advantages over a closed cam, in which the follower moves in a groove in the cam face: less manufacturing precision is required; it is cheaper; there is no backlash if the follower is properly constrained to keep the contact between cam and follower. Possible disadvantages of a disk cam come with the introduction of a spring to avoid the follower lifting off: the spring force usually makes the

contact force between cam profile and follower greater than in an equivalent closed cam, potentially reducing the life of the cam and increasing, in turn, other forces on the frame of the device (MechDesigner, 2017).

A roller-follower mainly consists of a pre-assembled stem supporting a needle or ball bearing, and it was chosen for the following advantages: its availability on the market as it is widely used; it rolls on cam profile generating less scuffing wear than a follower that slides (MechDesigner, 2017); and it is most likely to accurately implement the contact constraint with the cam profile (Rothbart, 2004). Finally, a cam-follower configuration with an offset was chosen as it can be associated with a decrease in the forces acting on the cam-follower system, specifically between cam and follower and at the follower guide. Figure 3.6 shows the final cam-follower mechanisms chosen for this application.
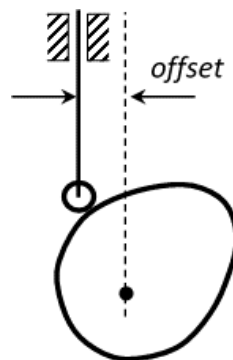
Figure 3.6 Cam-follower configuration chosen for the present application: a disk cam with a roller follower with offset.

3.4.2   Hydraulic ram

Two single-acting hydraulic cylinders were chosen for the design. The linear displacement of the piston inside the cylinder is given by the linear displacement of the follower of the cam system, as a fixed joint connects these two components. Friction is an important issue in hydraulic components, particularly small-scale ones. O-ring seals are necessary at the piston head to avoid leaks, and they generate friction and the modelling of these is covered later in the thesis (see section 4.4). Friction at the follower was also considered, as this must be as low as possible to avoid jamming. A really simple solution is the use of a sleeve with lubricant, but coefficients of sliding friction could range between 0.1 and 0.25, depending on the sliding velocity and the specific applied loads (Staros & Murphy, 1964). A better solution is the use of

a linear ball bearing as a guiding mechanism that supports the translating follower: typical values for the coefficient of friction of lubricated linear ball bearings with non-contact seals range from 0.0015 for heavy loads to 0.005 for light loads; if there are seals, the coefficient of friction will be higher due to the added friction from the seals (SKF, 2011, p. 43). Finally, the use of two self-aligning linear ball bearings offers the advantage of dealing with misalignment of the shaft which may come with the moment of the force applied by the cam to the roller. These allow an angular adjustment of ± 30 minutes of arc (i.e. 0.5°) without affecting the dynamic load rating (SKF, 2011, p. 34). For these reasons, two self-aligning linear ball bearings were chosen. Friction at the follower guide bearings is evaluated in section 4.3.3.

A return spring allows the piston to recover to its starting position, and is fundamental for the stance ram: during its working phase, the piston moves upwards inside the cylinder pumping oil into the accumulator, while, during its non-working phase, it moves downwards sucking oil down from the accumulator into the cylinder. In this last case, the cam rotates in the opposite direction with respect to the working phase. Consequently, to ensure the contact between the cam and the follower, the cam should work in tension, requiring either the use of a magnetic cam or a return spring. In this design, a linear return spring is chosen to help in holding the follower in contact with the cam, counteracting the follower inertia and all the friction terms. This is implemented via a preloaded compression spring, usually a helical coil, embodied within the single-acting cylinder: it may be fixed, for instance, at one end to the rod-side of the piston head and at the other to the rod-side inner cap of the hydraulic cylinder. As a result, the spring is stretched when the stance piston moves upwards (i.e. during mid and terminal stance), and it comes back when the piston moves downwards (i.e. during push-off). If the spring force is too small, it will allow the detachment of the follower from the cam; but an excessive spring force may be reflected throughout the system (e.g. more wear) (see section 5.2.2 for return spring sizing).

3.4.3   Accumulator

Hydraulic accumulators are generally classified by the way they store energy (MachineDesign, 2002): spring-loaded, weight-loaded, and gas-loaded. Weight loaded accumulators were not appropriate for obvious reasons. Gas-loaded (or gas-charged) accumulators are the most

common type and were used in the previous design by Gardiner *et al.* (2017) and they are not subject to friction losses as is the case with spring-loaded accumulators. They store energy through the compression of a gas, usually nitrogen. Gas-charged accumulators are further divided into three different types: diaphragm, bladder and piston accumulators (see Figure 3.7 for a comparison). For this application, small size and weight are critical requirements. A review of the literature on accumulators, including technical data sheets (e.g. HYDAC (2015); REXROTH (2013); Parker Hannifin), confirmed that the best option for this application is a gas-charged diaphragm accumulator because it is lighter and better suited to miniaturisation than the others (see also Gardiner *et al.* (2017)). It is characterised, indeed, by the smallest weight and dimensions (nominal volumes starting from 0.075l (Parker Hannifin)), and also the lowest price; and it is recommended for applications characterised by small fluid volumes and low flow rates (see also Figure 3.7). Moreover, diaphragm accumulators may be mounted in any orientation.

Type	Design	Nominal Volume	MAWP (psi)	Pressure Ratio	Flow Rate	Mounting Position	Weight	Cost
Diaphragm	• small volume and flow • low weight • compact design • good for shock applications *(good response characteristics)*	5 in³ to 1 gal	3000, 5000 (up to 10,000)	8:1 typically (up to 10:1)	up to 60 gpm	any	lowest	lowest
Bladder	• best general purpose • wide range of standard sizes • good for shock applications *(good response characteristics)*	1 qt. to 15 gal	3000, 5000 (up to 10,000)	4:1	up to 480 gpm	prefer vertical	middle	middle
Piston	• best for large stored volumes • best for high flow rates • not recommended for shock applications • best for use with backup nitrogen bottles	1 qt. to 100 gal	3000, 5000 (up to 10,000)	∞:1	up to 2000 gpm	prefer vertical	highest	middle to highest

Figure 3.7 Comparison of standard gas-charged accumulators. Image source: HYDAC (2015, p. 5).

As Figure 3.8 shows, in a diaphragm accumulator there are two compartments: one for the hydraulic fluid and another for the gas, separated by an elastomeric diaphragm. The fluid compartment is connected to the rest of the hydraulic circuit. When pressure increases, fluid enters the accumulator compressing the gas; likewise, when pressure decreases, the compressed gas expands and fluid flows out of accumulator. Diaphragm deformation is not

an issue as, generally, the changes in shape of the diaphragm are very small due to the tiny changes in oil volume, given the small flows that usually characterize this type of accumulator.

Hydraulic systems typically operate at pressures of up to $200\ bar$ (Gardiner *et al.*, 2017). To be conservative, in this work a maximum accumulator pressure of $100\ bar$ was set. To allow excess eccentric work (i.e. eccentric minus concentric work) to be stored during level and downhill walking and then utilised during uphill walking, the accumulator should be as large as is practical given size and weight constraints. A nominal volume of $250\ cc$ was chosen as this was considered to be small enough to be integrated with the pylon of the prosthesis. A steel diaphragm accumulator of this volume would weigh around $1\ kg$ (Parker Hannifin). However, composite construction would reduce this by around 75% (Crompton Technology Group Ltd, 2020). Furthermore, the pylon and accumulator could share structural elements, reducing the increase in mass associated with the accumulator.

For illustrative purpose only, assuming it operates between 80 and $100\ bar$ and assuming adiabatic changes in gas volume, a $250cc$ accumulator stores approximately $220\ J$, according to a rough estimate based on trapezoidal integration. Assuming no losses, over each gait cycle of level walking there is excess eccentric work at the ankle joint of about $2.2\ J$ (based on gait data from Lay *et al.* (2006)) that can be carried forward to be used in uphill walking. This means that around one hundred gait cycles will fill the accumulator, increasing the pressure from 80 to $100\ bar$. Downhill walking ($-15°$ slope) involves more eccentric work at the ankle and there is an excess over each gait cycle of about $14.6\ J$ (based on gait data from Lay *et al.* (2006)). Therefore, around fifteen gait cycles will fill the accumulator. Once the accumulator is full (at its maximum pressure of $100\ bar$), a pressure relief valve would dissipate eccentric work in the form of heat, thus continuing to provide the necessary braking during downhill walking. In uphill walking there is net energy expenditure. On a $+15°$ slope, there is excess concentric ankle work of about $21.6\ J$ (based on gait data from Lay *et al.* (2006)). This means that, with a full accumulator, the novel design could power approximately ten uphill gait cycles, during which the pressure would drop from 100 to $80\ bar$.

The hydropneumatic accumulator is a tank divided into two chambers by a flexible separator. One chamber is for fluid under pressure, the other for nitrogen gas.

It is charged with nitrogen to a pressure p_o.

When a fluid travels through the accumulator, and the pressure p_1 of that fluid is greater than the pre-charge pressure po of the accumulator, then the gas compresses to p_1, the separator changes shape, and the accumulator can take in the corresponding volume of fluid.

Any pressure drop in the hydraulic circuit causes the accumulator to return fluid to the circuit, until pressure reverts to the initial p_o.

Figure 3.8 How a diaphragm accumulator works. Image source: HYDRO LEDUC (2010, p. 1).

3.4.4 Directional control valve (DCV)

Two directional control valves (DCV) were included in the design to provide on/off control with low pressure drop between the two cylinders and the accumulator and the tank. Two 3/2 DCV are used in this specific hydraulic circuit: they present three working ports (or ways) - inlet, outlet, and exhaust (or tank), and two working positions (or flow paths) (see Figure 3.9). The DCV is assumed to be mounted directly onto the ram to avoid further energy losses along additional hydraulic conduits in between the same ram and the accumulator and tank. The tank holds fluid at atmospheric pressure. In this design, it is designed to surround the DCV attached to the ram, assuming no pipes at all between ram and tank, minimising therefore energy losses between these two components. A pressure relief valve is also necessary to limit pressure in the hydraulic circuit.
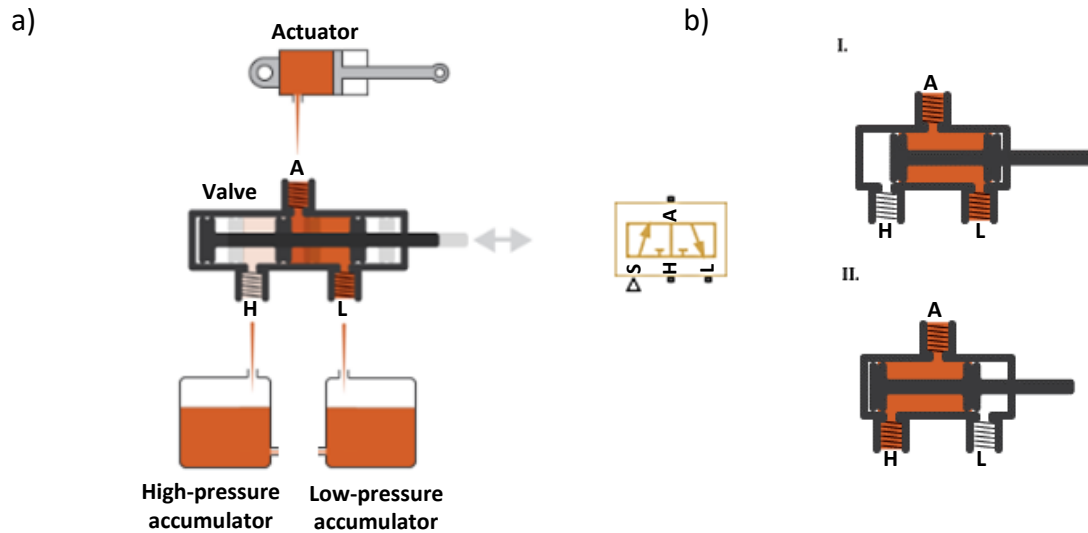
Figure 3.9 (a) On the left, a typical 3/2DCV set-up and its symbol. The three ports connect a high-pressure accumulator (**H**), a low-pressure accumulator (**L**), and a single-acting actuator (**A**). (b) The valve shifts between two working positions through the displacement of a control member - a ball, spool, or diaphragm – denoted by the signal at port **S**. One orifice is typically closed in these positions while the others two are fully open. Position **I**: the **A**-**L** orifice is maximally open and the **H**-**A** orifice is maximally closed. Position **II**: it is the reverse arrangement, with the **H**-**A** orifice being maximally open and the **A**-**L** orifice maximally closed. No physical connection exists between ports **H** and **L** and, therefore, no flow can develop across them. Image adapted from MATLAB R2016b, The MathWorks, Inc., Natick, MA, USA.

3.4.5   Auxiliary components

Two main types of hydraulic conduits exist: those ones with a rigid fixed geometry - e.g. manifolds and metal tubes - and others with a flexible geometry – e.g. elastomer hoses. In case of flexible hoses, the elastic stretch of the conduit represents a source of compliance in small-scale hydraulic actuation systems (Neubauer, 2017). To overcome this issue, rigid pipes can be used in the hydraulic circuit between the ram and the accumulator, even if their weight will be higher. No conduits exist between the ram and the tank in this concept design, as previously explained. Considering the compressibility issues, the bulk modulus of the fluid, a measure of a fluid's resistance to being compressed, is the reciprocal of compressibility (see section 4.6.2). If air is entrained in the fluid, the bulk modulus is significantly reduced and system stability decreases. For this reason, high pressures are used in small-scale hydraulic systems, in which trapped air may significantly impact the dynamic performance (Neubauer, 2017, p. 16). In this design, a reduction in the compressibility losses is achieved reducing the fluid volume between ram, tank and accumulator through a minimisation of the pipe length between these components, as explained above.

3.5   Conclusions

In this chapter, the aim of the PhD project and its objectives were defined: the design of a novel prosthetic ankle based on simple miniature hydraulics and a hydraulic accumulator to replicate the energy recycling behaviour of an intact ankle, while providing continuous control of the ankle torque. In addition, energy transfer between the knee and the ankle joint should be allowed through pipes. A typical engineering design process has been followed, whose first two stages have been described in this chapter: the definition of the requirements and constraints of the design, and the conceptual design process to reach a final concept design for the novel prosthesis.

By assuming an accumulator-based system to store and release energy, the first step has been the selection of a simple miniature hydraulic cylinder for converting the mechanical power given by the ankle joint rotation to fluid power and vice versa. A mechanical transmission is then necessary to convert the ankle rotation into the linear motion of the piston inside the cylinder and vice versa. Cams represent the best solution, as they are the gold standard for reciprocating motion applications: the ankle rotation is transmitted to the camshaft, to which the cam is fixed and then, through its rotation, the cam allows the linear motion of the piston inside the cylinder to store and release the required amount of energy in the accumulator in the different phases of gait. Moreover, if manufactured with a specific profile, through its rotation, the cam generates a specific torque in output. For this application, to allow biomimetic ankle kinematics and kinetics, two different cams need to be used: one with a profile mimicking the ankle torque during mid and terminal stance (ankle dorsiflexion), and a second one with a profile that matches the ankle torque during push-off (ankle plantarflexion). Therefore, two cam-ram systems are considered for the two periods involving the largest energy flow: a "stance cam-ram system" to store energy during mid and terminal stance, and a "push-off cam-ram system" to return energy during push-off. A torsional spring, in parallel to the two cam-ram systems, is also included to mimic the ankle torque during load acceptance: by being its equilibrium point defined during standing, it also bring the ankle back to its neutral angle during the swing phase, when the prosthesis should only recover its equilibrium position. In addition, by being placed in parallel to the cam-ram systems and driven by the ankle joint, it reduces the torque they need to supply at the ankle joint. Lastly, a

gearbox is also included in the "transmission line" of the ankle rotation to the two cam-ram systems, in parallel to the spring.

Therefore, the final novel concept design defined in this chapter includes: a torsional spring; a gearbox; two cam-ram systems; a gas-charged accumulator; a tank; two directional control valves to connect the hydraulic rams both to the accumulator and to the tank; and pipes to connect the rams to the accumulator. All these components should be easy to manufacture, even at the small-scale. The next chapter illustrates in detail the mathematical equations governing the working of each component.

4.Chapter 4: Mathematical modelling
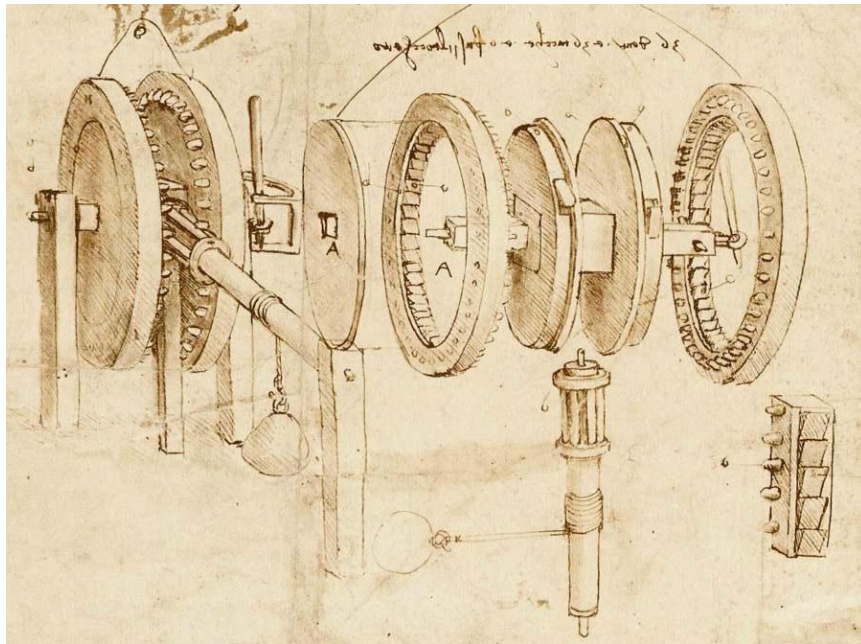
Leonardo Da Vinci (c. 1485), Toothed Gears and Hygrometer, Codex Atlanticus (folio 30v)

"Mechanics is the paradise of mathematics because the fruits can be reaped here. There is no certainty in science if mathematics cannot be applied to it, or if it is not related to it anyway."

(Leonardo Da Vinci)

Using free-body diagrams and applying the laws of kinematics, kinetics and hydraulics, a mathematical model of the new hydraulic ankle design was established. In the following sections the mathematical modelling of each component is described in a sequence beginning with the components that are directly coupled to the ankle (i.e. parallel spring and gearbox), then considering the two cam-roller-followers which are driven by the gearbox, and finally the hydraulic system made up of rams, valves, pipes and accumulator. Care was taken to include all significant sources of energy losses so that simulations based on the mathematical modelling are realistic with regard to energy efficiency and, hence, the stored energy available to power push-off.

4.1   Parallel spring

A torsional spring is placed in parallel with the two cam-ram systems. With the two rams switched off, it provides for standing, load acceptance, and swing. The spring characteristic is fitted to the relationship between ankle torque and ankle angle, usually referred to as the "quasi stiffness" of the ankle (Figure 4.1). Note that a positive ankle angle corresponds to a dorsiflexed ankle. Furthermore, a positive ankle torque is an external dorsiflexion torque (i.e. it acts to dorsiflex the ankle). Therefore, when both ankle angular velocity and ankle torque are positive, then work is being done on the ankle by the external forces and this should be absorbed and stored by the new ESR design. In other words, positive ankle power ($P_a = T_a \omega_a$) corresponds to eccentric work (stored by the system) and negative ankle power corresponds to concentric work (returned by the system). Note that, although this engineering sign convention is adopted for the mathematical modelling, this is the opposite of the traditional biomechanics sign convention used elsewhere.

During mid and terminal stance and push-off (i.e. the working phases of the two cam-ram systems), the required ankle torque is achieved through the two cam-ram systems. Therefore, the role of the spring is to provide good load acceptance and contribute to standing stability and swing. So the following spring characteristic was used and fitted just to load acceptance:

$$T_{ps} = m\theta_a + c \tag{4.1}$$

An "ordinary least square" regression fit to the ankle torque data was used to determine the best fit slope (m) and intercept (c) for the spring characteristic. Specifically, only the ankle torque data during load acceptance was used, and the resulting slope and intercept are $58.40\ Nm/rad$ and $0\ Nm$ respectively. The spring torque acts to return the ankle to its neutral angle. Therefore, a positive T_{ps} acts to plantarflex the ankle, opposing a positive ankle torque.
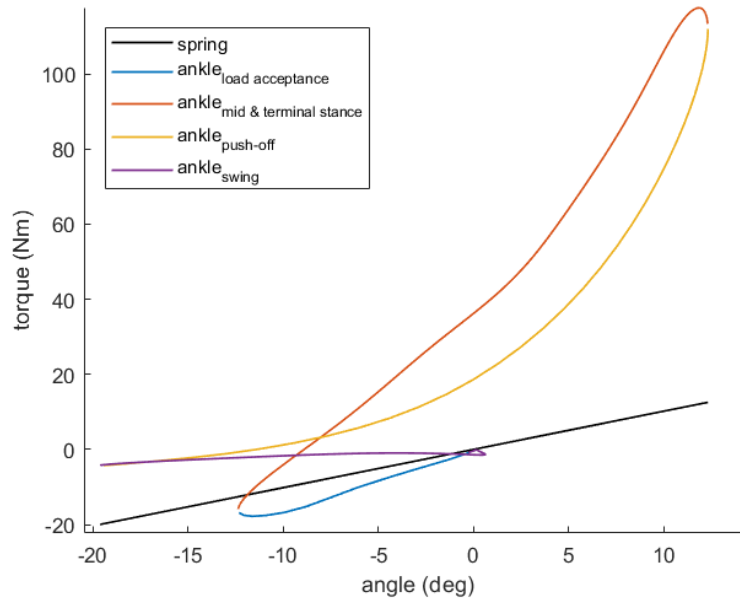
Figure 4.1 Torque-versus-angle curve for an anatomically intact ankle joint for level walking. A positive angle corresponds to a dorsiflexed ankle and a positive ankle torque is an external dorsiflexion torque (i.e. it acts to dorsiflex the ankle). The linear spring function (solid black line) is fitted to the load acceptance phase (blue solid line) of gait only. Input data from Bari (2013).

4.2   Gearbox

The gearbox is placed in parallel to the spring (both being driven by the ankle joint) and, in turn, it drives the two cam-ram systems. Note that this description applies when power flows are positive, meaning that eccentric work is stored by the system. When power flows are negative, which means that concentric work is returned by the system, the ankle joint is being driven by the new ESR ankle. In other words, the system transmits power in both directions: from the ankle to the two cam-ram systems and vice versa.

For a given gearbox ratio (GR), the output angular displacement, velocity and acceleration are given by:

$$\theta_c = \theta_a GR \tag{4.2}$$

$$\omega_c = \omega_a GR \tag{4.3}$$

$$\alpha_c = \alpha_a GR \tag{4.4}$$

with positive camshaft (i.e. gearbox output) angles corresponding to positive ankle (i.e. gearbox input) angles.

Ankle torque overcomes the resistance provided by the parallel spring (T_{ps}) and the two cams via the gearbox ($T_{in_{gb}}$) as follows:

$$T_a = T_{ps} + T_{in_{gb}} \tag{4.5}$$

where positive spring and gearbox input torques act to oppose a positive ankle torque. The gearbox input torque ($T_{in_{gb}}$) overcomes the resistance provided by gearbox friction and the two cam torques as follows:

$$T_{in_{gb}} = T_c \cdot GR + T_f \tag{4.6}$$

where $T_c = T_{c_{PO}} + T_{c_{STANCE}}$ is the total camshaft torque, $T_f = sign(\omega_a)|T_f|$ is the friction torque, and positive camshaft and friction torques act to oppose a positive gearbox input torque. The sign of the input angular velocity ($sign(\omega_a)$) is used to ensure that the friction torque always opposes the direction of rotation. Although the gearbox input is defined as being the connection with the ankle, this does not imply that power always flows from the ankle.

The magnitude of the friction torque is a function of the gearbox ratio (GR) and gearbox size ($T_{capacity}$) and is therefore a constant for a given gearbox. Using gearbox efficiency data from Bari (2013), sourced from manufacturers' catalogues, the following model was found to be a good fit to the data:

$$|T_f| = T_{capacity} \frac{(100 - \eta_g)}{100} \tag{4.7}$$

where $T_{capacity} = \max |T_{in_{gb}}|$ corresponds to the gearbox size, $\eta_g = 100 - (GR - 1)^{k_g}$ is the gearbox efficiency (percentage), and k_g is a coefficient obtained by finding the least squares fit to the data. Gearbox size ($T_{capacity}$) is assumed to be equal to the maximum value of the gearbox input torque. For a given gearbox, $|T_f|$ is evaluated just once, as it then remains constant.

When the cam profiles are given, the equations above are used as they are presented. In particular, the total camshaft torque is an input which is used to calculate $T_{in_{gb}}$ and hence T_a. When the cam profiles are being determined, the required ankle torque (T_{a_r}) is the input and the torque equations are rearranged as follows to give the required camshaft torque (T_{c_r}):

$$T_{in_{gb}} = T_{a_r} - T_{ps} \tag{4.8}$$

$$T_{c_r} = \left(\frac{T_{in_{gb}} - T_f}{GR} \right) \tag{4.9}$$

4.3   Cam-Roller-Follower

4.3.1   Cam profile

In the proposed design, two cams are used to convert rotary motion of the ankle into linear motion of the pistons inside the two hydraulic cylinders. The two cam-ram systems serve different purposes:

- The stance cam-ram pushes oil into the accumulator during stance prior to push-off to store eccentric ankle work.

- The push-off cam-ram receives oil from the accumulator during push-off to return previously stored energy to the ankle, producing concentric ankle work.

A cam is a machine element with a curved profile, which through its rotation gives a specified translational motion to another element called the follower. Given the required displacement of the follower as a function of cam angle, it is possible to calculate the cam profile using different methods described in the cam design literature. Alternative methods were implemented and tested in MATLAB (see Appendix B.2, (1)). Following a comparison of the alternatives, an approach based on mapping between coordinate frames was selected and this is described below. The cam profiles designed herein match the torque of an intact ankle for level walking. Slope adaptation should be investigated in future work.

Referring to Figure 4.2, the coordinates of the contact point P between cam and roller can be mapped between the fixed frame $\{fix\}$ and the cam frame $\{cam\}$, both of which have their origins coincident with the centre of rotation of the cam. The cam frame is attached to the cam, so that it's rotation relative to the fixed frame is θ_c.
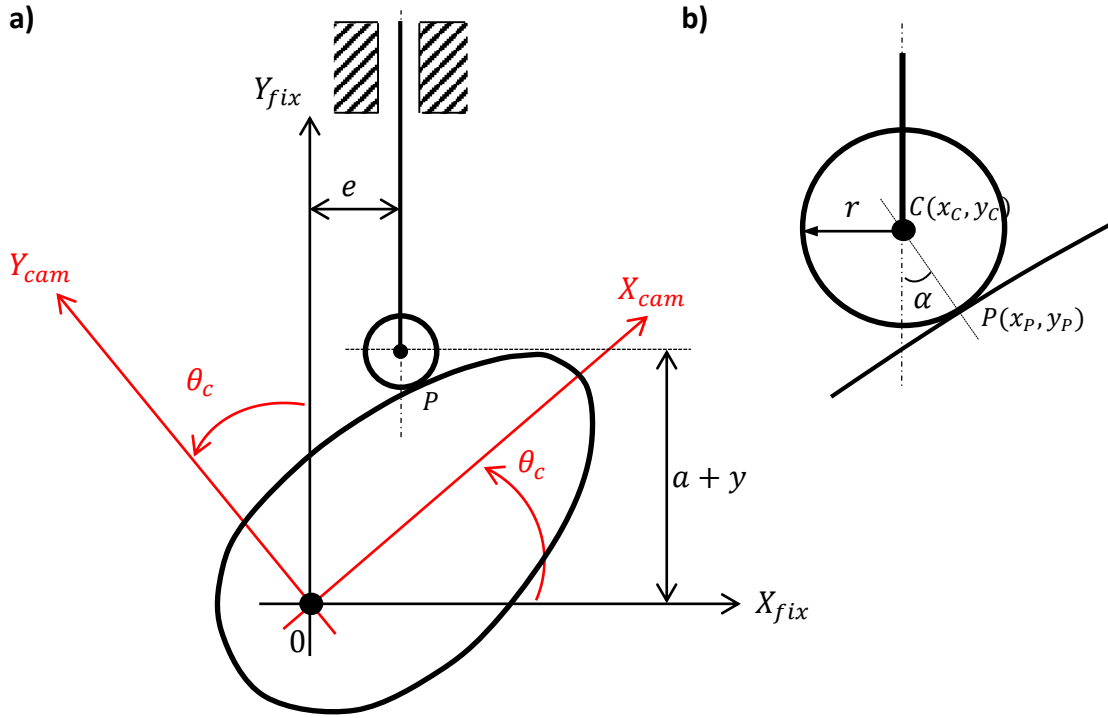
Figure 4.2 (a) Mapping the contact point $P(x_P, y_P)$ between two reference frames: cam frame (X_{cam}/Y_{cam}) and fixed frame (X_{fix}/Y_{fix}). (b) Zoom in on the roller-follower, with the roller radius r, the cam pressure angle α, the contact point $P(x_P, y_P)$, the roller centre $C(x_C, y_C)$.

In the fixed frame, the coordinates of the contact point P depend on the required follower translation y and the pressure angle α, which in turn depends on y and it's derivative (see equation (4.31)). In this context, the pressure angle is the angle between the follower axis, corresponding to the y-axis of the fixed frame, and the normal to the cam surface at the contact point P. In particular, in the fixed frame, the coordinates of P are $(x_P, y_P) = (e + r\sin\alpha, (a + y) - r\cos\alpha)$. Then the coordinates in the cam frame can be obtained using the 2x2 rotation matrix $^{cam}_{fix}R$ (Craig, 2005). This rotation matrix is formed from the two unit vectors describing the axes of the fixed frame written in the cam frame, which are $^{cam}\widehat{X_{fix}} = \begin{bmatrix} \cos(\theta_c) \\ -\sin(\theta_c) \end{bmatrix}$ and $^{cam}\widehat{Y_{fix}} = \begin{bmatrix} \sin(\theta_c) \\ \cos(\theta_c) \end{bmatrix}$. Stacking these two unit vectors together as the columns of the 2x2 rotation matrix leads to:

$$^{cam}_{fix}R = \begin{bmatrix} \cos\theta_c & \sin\theta_c \\ -\sin\theta_c & \cos\theta_c \end{bmatrix} \tag{4.10}$$

Thus, the coordinates of P in the cam frame are obtained as follows:

$$\vec{P}_{cam} = {}^{cam}_{fix}R\,\vec{P}_{fix} \tag{4.11}$$

Then by substituting:

$$\begin{bmatrix} x_P \\ y_P \end{bmatrix}_{cam} = \begin{bmatrix} \cos\theta_c & \sin\theta_c \\ -\sin\theta_c & \cos\theta_c \end{bmatrix} \begin{bmatrix} x_P \\ y_P \end{bmatrix}_{fix} = \begin{bmatrix} \cos\theta_c & \sin\theta_c \\ -\sin\theta_c & \cos\theta_c \end{bmatrix} \begin{bmatrix} e + r\sin\alpha \\ (a+y) - r\cos\alpha \end{bmatrix} \tag{4.12}$$

Given y as a function of θ_c and also calculating pressure angle α from y and it's derivative (see equation (4.31)), a set of contact points can be evaluated in the cam frame, the union of which is the cam profile (see Appendix B.2, (2) and (3), for some geometry checks on cam profile generation).

$$\vec{P}_{cam} = {}^{cam}_{fix}R\,\vec{P}_{fix}$$

4.3.2 Roller kinematics

Referring to Figure 4.3, after careful consideration and for the sake of simplicity, the decision was made to work just in quadrant I (see Appendix B.3 for checks on the roller kinematics). The main reason for this is that a positive (i.e. anticlockwise) rotation θ_c of the cam about the origin O corresponds to ankle dorsiflexion, visualised as an anticlockwise rotation of the foot with respect to the shank. Therefore, a positive offset e is appropriate for the stance cam-ram system as the piston should move up during dorsiflexion, and also for the push-off cam-ram system as the piston should move down during plantarflexion. Hence, with a positive offset e and by ensuring that the length $(a + y)$ is always positive, only the first quadrant needs to be considered. In this context it should be noted that larger values of $(a + y)$ are advantageous as they lead to smaller cam pressure angles (see equation (4.31)) and, hence, lower friction losses.
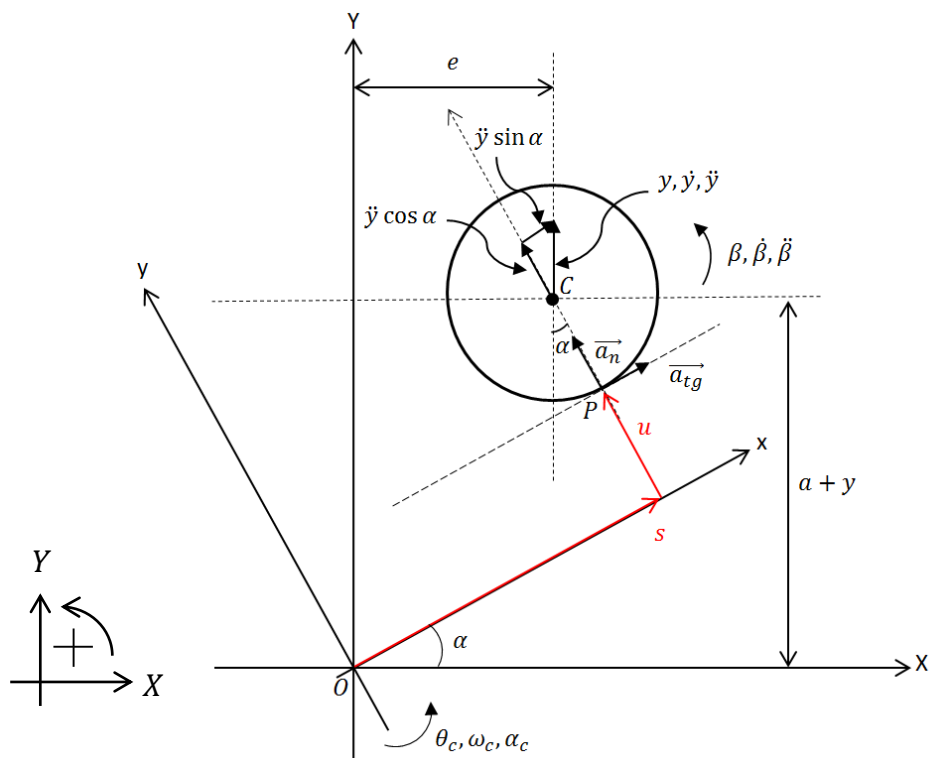
Figure 4.3 Roller-follower on cam surface in quadrant I with the local reference frame (xy) rotated anticlockwise relative to the fixed frame (XY) by an angle equal to the pressure angle α. The components of the vector $\vec{P}$ are in red and the sign convention is on the left.

In cases where a cam rotates continuously, the follower displacement is characterised by rise, dwell and return phases, in which case $a = \sqrt{(R_b + r)^2 - e^2}$, where R_b is the radius of the cam base circle. However, because the ankle does not rotate continuously, in this design there are only rise and a return phases and the cam operates as a non-linear lever. Therefore, a is

simply an arbitrary constant that can be chosen to optimise the design, which defines the starting position of the follower in the vertical (Y-axis) direction.

Figure 4.3 shows in red the two components s and u of the vector $\vec{P}$ defining the contact point P with respect to the stationary cam centre O. In other words:

$$\vec{P}_{local} = \begin{bmatrix} s \\ u \end{bmatrix} \tag{4.13}$$

which is written in a local reference frame (xy), whose x-axis is parallel to the tangent between cam and roller at point P. This local frame is rotated anticlockwise relative to the fixed frame (XY) by an angle equal to the pressure angle α. Furthemore, the vector $\vec{C}$ in both the local frame and the fixed frame is given by:

$$\vec{C}_{local} = \begin{bmatrix} s \\ u + r \end{bmatrix} \quad \text{and} \quad \vec{C}_{fix} = \begin{bmatrix} e \\ a + y \end{bmatrix} \tag{4.14}$$

These are related by the rotation matrix $^{local}_{fix}R$, which is formed from the two unit vectors describing the axes of the fixed frame written in the local frame, which are $^{local}\widehat{X_{fix}} = \begin{bmatrix} \cos(\alpha) \\ -\sin(\alpha) \end{bmatrix}$ and $^{local}\widehat{Y_{fix}} = \begin{bmatrix} \sin(\alpha) \\ \cos(\alpha) \end{bmatrix}$. Thus, the coordinates of C in the fixed frame are obtained as follows:

$$\vec{C}_{local} = {}^{local}_{fix}R\,\vec{C}_{fix} \tag{4.15}$$

Then by substituting:

$$\begin{bmatrix} s \\ u + r \end{bmatrix} = \begin{bmatrix} \cos\alpha & \sin\alpha \\ -\sin\alpha & \cos\alpha \end{bmatrix} \begin{bmatrix} e \\ a + y \end{bmatrix} \tag{4.16}$$

Hence:

$$s = e\cos\alpha + (a + y)\sin\alpha = [e + \tan\alpha(a + y)]\cos\alpha$$
$$u = -e\sin\alpha + (a + y)\cos\alpha - r \tag{4.17}$$

To establish the acceleration relationships, the analysis begins with the following standard equation for the acceleration of a fixed point in a rotating body (Ruina & Pratap, 2019, p. 762):

$$\vec{a} = \overrightarrow{a_{tg}} + \overrightarrow{a_n} = \vec{\alpha} \times \vec{r} + \vec{\omega} \times (\vec{\omega} \times \vec{r}) \tag{4.18}$$

where $\vec{\omega}$ and $\vec{\alpha}$ are angular velocity and acceleration respectively and $\vec{r}$ is the position of the fixed point relative to the centre of rotation. Because the system is 2-dimensional, this simplifies as follows:

$$\vec{a} = \vec{\alpha} \times \vec{r} - \omega^2 \vec{r} \tag{4.19}$$

To evaluate roller angular acceleration, the linear acceleration of its centre C was calculated as follows:

$$\overrightarrow{a_C} = \overrightarrow{a_P} + \overrightarrow{a_{C/P}} \tag{4.20}$$

where $\overrightarrow{a_{C/P}}$ is the acceleration of the roller centre C with respect to the contact point P:

$$\overrightarrow{a_{C/P}} = -\overrightarrow{a_{P/C}} = -(\overrightarrow{\alpha_{rol}} \times \vec{r} - \omega_{rol}{}^2 \vec{r}) = -\left(\begin{bmatrix} 0 \\ 0 \\ \ddot{\beta} \end{bmatrix} \times \begin{bmatrix} 0 \\ -r \\ 0 \end{bmatrix} - \dot{\beta}^2 \begin{bmatrix} 0 \\ -r \\ 0 \end{bmatrix} \right)$$

$$\overrightarrow{a_{C/P}} = - \begin{bmatrix} r\ddot{\beta} \\ r\dot{\beta}^2 \\ 0 \end{bmatrix} \tag{4.21}$$

and $\overrightarrow{a_P}$ the acceleration of the contact point P with respect to the frame origin O:

$$\overrightarrow{a_P} = \overrightarrow{\alpha_c} \times \vec{P} - \omega_c{}^2 \vec{P} = \begin{bmatrix} 0 \\ 0 \\ \alpha_c \end{bmatrix} \times \begin{bmatrix} s \\ u \\ 0 \end{bmatrix} - \omega_c{}^2 \begin{bmatrix} s \\ u \\ 0 \end{bmatrix} = \begin{bmatrix} -u\alpha_c - s\omega_c{}^2 \\ s\alpha_c - u\omega_c{}^2 \\ 0 \end{bmatrix} \tag{4.22}$$

Therefore, equation (4.20) becomes:

$$\begin{bmatrix} \ddot{y}\sin\alpha \\ \ddot{y}\cos\alpha \\ 0 \end{bmatrix} = \begin{bmatrix} -u\alpha_c - s\omega_c{}^2 \\ s\alpha_c - u\omega_c{}^2 \\ 0 \end{bmatrix} + \begin{bmatrix} -r\ddot{\beta} \\ -r\dot{\beta}^2 \\ 0 \end{bmatrix} \tag{4.23}$$

90

From this expression, the angular acceleration of the roller is derived:

$$\ddot{\beta} = \frac{1}{r}[-u\alpha_c - s\omega_c{}^2 - \ddot{y}\sin\alpha] \tag{4.24}$$

To evaluate roller angular velocity, the linear velocity of its centre C was calculated as follows:

$$\overrightarrow{v_C} = \overrightarrow{v_P} + \overrightarrow{v_{C/P}} \tag{4.25}$$

where

$$\overrightarrow{v_{C/P}} = -\overrightarrow{v_{P/C}} = -(\overrightarrow{\omega_{rol}} \times \vec{r}) = -\left(\begin{bmatrix}0\\0\\\dot{\beta}\end{bmatrix} \times \begin{bmatrix}0\\-r\\0\end{bmatrix}\right) = -\begin{bmatrix}r\dot{\beta}\\0\\0\end{bmatrix} \tag{4.26}$$

and

$$\overrightarrow{v_P} = \overrightarrow{\omega_c} \times \vec{P} = \begin{bmatrix}0\\0\\\omega_c\end{bmatrix} \times \begin{bmatrix}s\\u\\0\end{bmatrix} = \begin{bmatrix}-u\omega_c\\s\omega_c\\0\end{bmatrix} \tag{4.27}$$

As a result, equation (4.25) becomes:

$$\begin{bmatrix}\dot{y}\sin\alpha\\\dot{y}\cos\alpha\\0\end{bmatrix} = \begin{bmatrix}-u\omega_c\\s\omega_c\\0\end{bmatrix} - \begin{bmatrix}r\dot{\beta}\\0\\0\end{bmatrix} \tag{4.28}$$

From this expression, the angular velocity of the roller is derived:

$$\dot{\beta} = \frac{1}{r}[-u\omega_c - \dot{y}\sin\alpha] \tag{4.29}$$

Starting from equation (4.28), cam pressure angle α is also evaluated:

$$\dot{y}\cos\alpha = s\omega_c$$
$$\frac{dy}{d\theta_c} = \frac{s}{\cos\alpha} \tag{4.30}$$

Remembering that $s = [e + (a + y)\tan\alpha]\cos\alpha$ (see equation (4.17)), it follows:

$$\alpha = \tan^{-1} \frac{\dfrac{dy}{d\theta_c} - e}{a + y} \qquad (4.31)$$

It is clear that a larger $(a + y)$ leads to a smaller pressure angle. In addition, considering equation (4.30), it follows that the component s will be always positive as $|\alpha| < 90°$ and $\frac{dy}{d\theta_c}$ is always positive, because positive rotation (dorsiflexion) corresponds to positive follower displacement.

4.3.3 Dynamic analysis of the roller-follower system

To evaluate the force transmitted between cam and roller and the energy losses due to the different friction phenomena, a dynamic analysis has been conducted for the two components: the roller and the follower (see Figure 4.4).
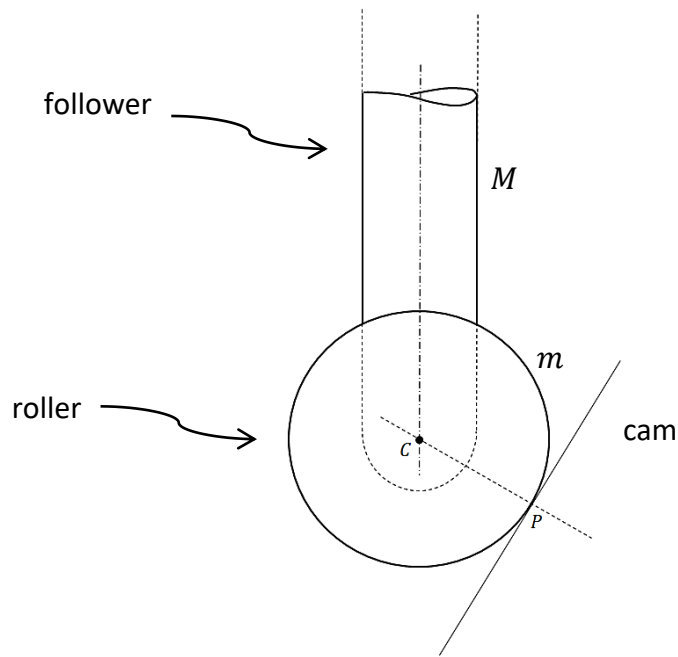
Figure 4.4 The roller-follower system: C is the roller centre and P the contact point between cam and roller.

ROLLER

Figure 4.5 shows the free-body diagram for the roller with all the forces and moments acting on it. Note that all forces and moments are positive as shown in the diagram. When their magnitudes are negative, this corresponds to a reversal of direction. The forces and moments include:

F_t – the tangential cam contact force

F_n – the normal cam contact force

M_{rolres} – the rolling resistance moment

M_{brg} – the bearing friction moment

mg – the roller's weight

R_H – the horizontal follower reaction

R_V – the vertical follower reaction
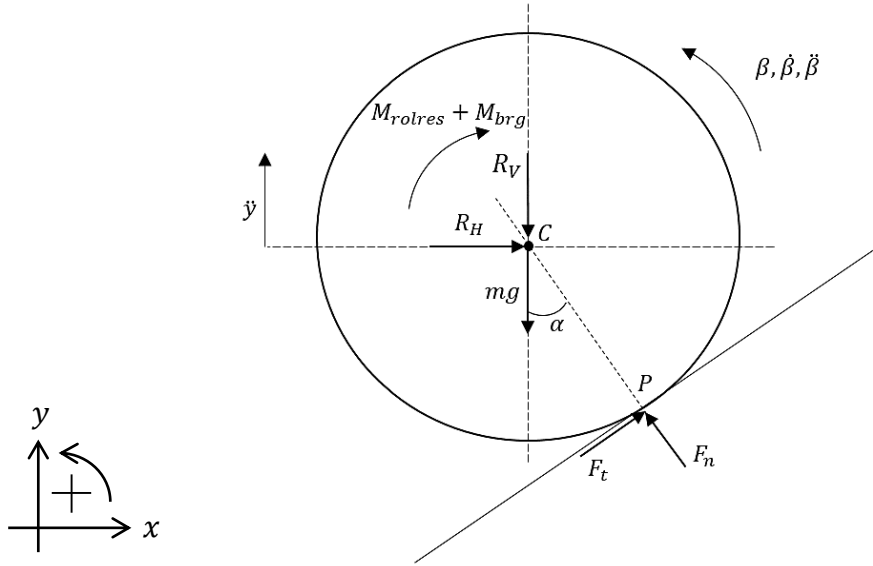
Figure 4.5 Free-body diagram of the roller with all the forces and the moments acting on it (with r roller radius).

Considering the free-body diagram for the roller (Figure 4.5), and applying Newton's 2nd law and Euler's equation, yields:

$$\sum F_x = m\ddot{x} = 0 \qquad F_t \cos \alpha - F_n \sin \alpha + R_H = 0 \tag{4.32}$$

$$\sum F_y = m\ddot{y} \qquad F_t \sin \alpha + F_n \cos \alpha - R_V - mg = m\ddot{y} \tag{4.33}$$

$$\sum M_C = I_{rol}\ddot{\beta} \qquad F_t r - M_{rolres} - M_{brg} = I_{rol}\ddot{\beta} \tag{4.34}$$

where I_{rol} is the moment of inertia of the rotating outer part of the roller-follower, and $\ddot{\beta} = \frac{1}{r}[-u\alpha_c - s\omega_c{}^2 - \ddot{y} \sin \alpha]$ is the angular acceleration of the roller (see section 4.3.2).

Figure 4.6 shows a typical roller, often referred to as a "cam follower", which consists of a thick-walled outer ring, supported by a roller bearing which can accommodate high radial loads, and a solid threaded pin for attachment to other components (i.e. the follower in this case). Bearing friction (M_{brg}) is the result of rolling and sliding friction in the contact areas, between the rolling elements and raceways, cage and other guiding surfaces within the roller. Friction is also generated by lubricant drag and contact seals.
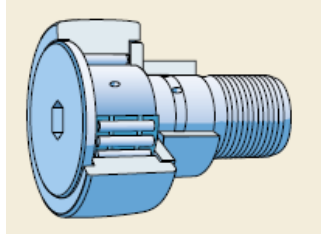
Figure 4.6 Typical cam follower (SKF, 2013, p. 1104).

The frictional moment M_{brg} can be estimated using the following expression (SKF, 2013, p. 98):

$$M_{brg} = sign(\dot{\beta}) \cdot \mu_{brg} \cdot \frac{d_{brg}}{2} \cdot |P| \ (Nm) \tag{4.35}$$

where μ_{brg} is a constant coefficient of friction for the bearing, P is the equivalent dynamic bearing load (N), d_{brg} is the bearing bore diameter (m), and the sign of the roller angular velocity ensures that the frictional moment at the bearing always opposes the direction of rotation of the roller. Here it is assumed that $P = F_n$, the normal cam contact force. In Appendix A.1, it is shown that the error introduced by this approximation is negligible.

The moment M_{rolres} is given by the following expression:

$$M_{rolres} = sign(\omega_{rel}) \cdot \mu_{rolres} \cdot |F_n| \cdot r \ (Nm) \tag{4.36}$$

where μ_{rolres} is the coefficient of rolling friction, and $\omega_{rel} = \dot{\beta} - \omega_c$ is the relative angular velocity between cam and roller. Here, the sign of the relative angular velocity ensures that the rolling resistance always opposes the roller's direction of rotation relative to the cam. In other words, it takes account of the fact that the roller is rolling over a surface that is not stationary because the cam is rotating too.

Because the roller is rolling over a curved surface, a complete expression for the rolling resistance between the two surfaces should include the evaluation of a relative rolling radius (R_{rel}), given the radii of the two surfaces (Ai *et al.*, 2011):

$$M_{rolres} = sign(\omega_{rel}) \cdot \mu_{rolres} \cdot |F_n| \cdot R_{rel} \tag{4.37}$$

95

where:

$$R_{rel} = \frac{rR_c}{r + R_c} \qquad (4.38)$$

and r is the roller radius and R_c is the instantaneous rolling radius of the cam surface (Ai *et al.*, 2011). It is reasonable to assume that $R_c = nr$ where $n > 1$. Substituting leads to $R_{rel} = \frac{nr^2}{(n+1)r} = \frac{n}{(n+1)}r$ and, since $\frac{n}{(n+1)} < 1$, this yields $R_{rel} < r$. Therefore, assuming a conservative approach, it is possible to assume $R_{rel} = r$, so that equation (4.36) can be used and the need to know R_c is avoided.

To ensure conservative simulation results that do not overestimate the energy efficiency of the system, the largest expected values for the friction coefficients have been used as follows:

- $\mu_{brg} = 0.002$ is the worst case coefficient of friction both for needle roller bearings and for cylindrical roller bearings (SKF, 2013, p. 98).

- $\mu_{rolres} = 0.002$ is a high value for rolling resistance coefficient for steel on steel. Based on an internet search, it is typically quoted as being between 0.001 and 0.002 for railroad steel wheels on steel rails (The Engineering Toolbox, 2008), and between 0.0002 and 0.001 also for steel wheel on rail (Engineering-abc.com, n.d.).

FOLLOWER

Figure 4.7 shows the free-body diagram for the follower with all the forces and moments acting on it. Note that all forces and moments are positive as shown in the diagram. When their magnitudes are negative, this corresponds to a reversal of direction. The forces and moments include:

F_{fr1} – upper guide friction force

F_{fr2} – lower guide friction force

F_h – hydraulic ram force

F_s – follower return-spring force

M_{brg} – the bearing friction moment (equal and opposite to that on the roller)

Mg – the follower's weight

N_1 – upper guide normal force

N_2 – lower guide normal force

R_H – the horizontal roller reaction (equal and opposite to that on the roller)

R_V – the vertical roller reaction (equal and opposite to that on the roller)
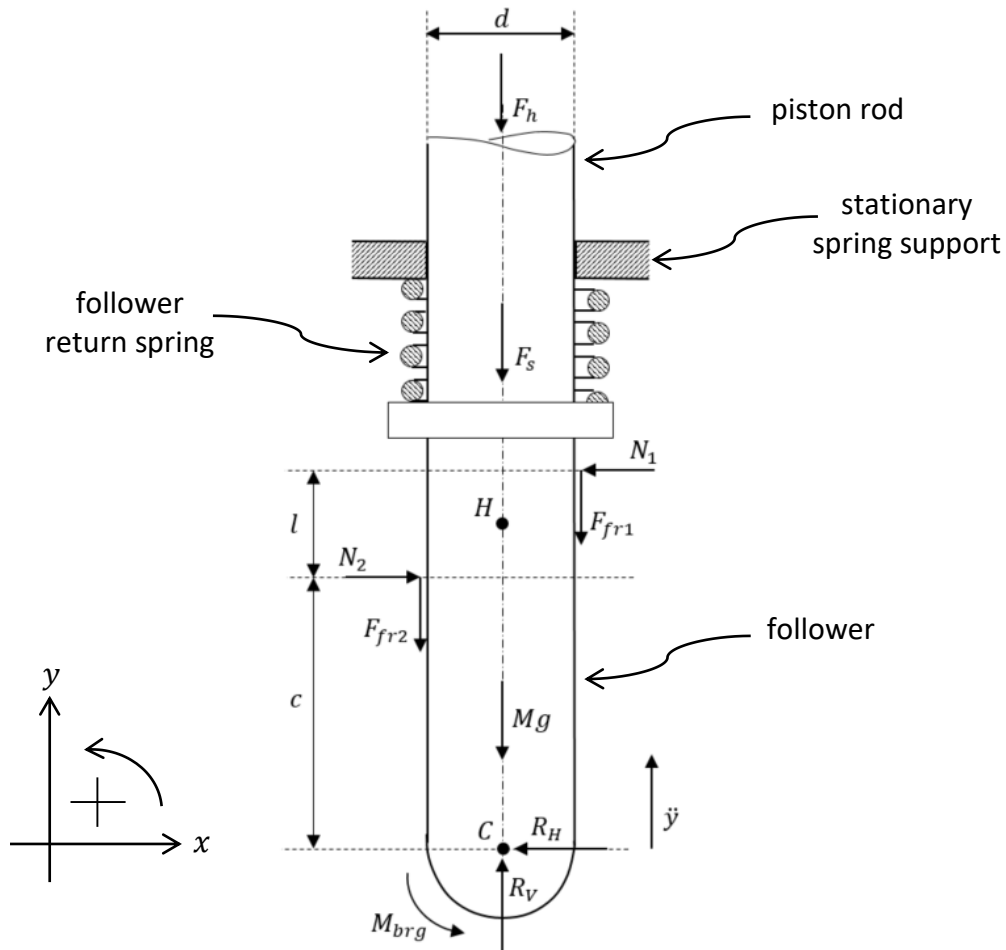
Figure 4.7 Free-body diagram for the follower system with all of the forces and moments acting on it.

In Figure 4.7, l is the distance between the lines of action of the two normal forces (N_1, N_2) acting at the follower guides, which are two self-aligning linear ball bearings, chosen to avoid jamming of the follower; and c represents the follower overhang.

Considering the free-body diagram for the follower (Figure 4.7) and applying Newton's 2nd law and Euler's equation yields:

$$\sum F_x = M\ddot{x} = 0 \qquad N_2 - R_H - N_1 = 0 \tag{4.39}$$

$$\sum F_y = M\ddot{y} \qquad R_V - F_h - Mg - F_{fr1} - F_{fr2} - F_s = M\ddot{y} \qquad (4.40)$$

$$\sum M_H = 0 \qquad M_{brg} - R_H\left(c + \frac{l}{2}\right) + N_1\frac{l}{2} + N_2\frac{l}{2} - M_{fr1} + M_{fr2} = 0 \qquad (4.41)$$

The two sliding friction forces, F_{fr1} and F_{fr2}, acting at the upper and lower guides (i.e. at the two self-aligning linear ball bearings) (Figure 4.7) are defined as follows:

$$F_{fr1} = sign(\dot{y}) \cdot \mu_{sl}|N_1| \qquad (4.42)$$

$$F_{fr2} = sign(\dot{y}) \cdot \mu_{sl}|N_2| \qquad (4.43)$$

The sign of the follower velocity in equations (4.42) and (4.43) ensures that guide friction always opposes the direction of motion. Typical values for the coefficient of friction of lubricated linear ball bearings range from 0.0015 for heavy loads to 0.005 for light loads (SKF, 2011, p. 43), and $\mu_{sl} = 0.003$ is used here.

The two moments M_{fr1} and M_{fr2} are due to the above-mentioned frictional forces, and they are defined as follows:

$$M_{fr1} = sign(N_1) \cdot \frac{d}{2}F_{fr1} \qquad (4.44)$$

$$M_{fr2} = sign(N_2) \cdot \frac{d}{2}F_{fr2} \qquad (4.45)$$

The signs of the two forces N_1 and N_2 in equations (4.44) and (4.45) are used because the direction of the two moments depends on which side of the follower F_{fr1} and F_{fr2} act, which in turn depends on which side of the follower N_1 and N_2 act and, hence, their signs.

A linear return-spring characteristic is assumed and the pre-compression of the spring (x_{pre}) corresponds to a piston displacement of $y = 0$. Therefore, the spring force is given by:

$$F_s = k(y + x_{pre}) = F_0 + ky \qquad (4.46)$$

where the preload $F_0 = kx_{pre}$.

4.3.4 Cam torque evaluation

The normal force (F_n) and tangential force (F_t) acting on the cam profile, as well as the rolling resistance acting on the cam (M_{rolres}), together with the vector $\vec{P}$, determine the cam torque (see Figure 4.8).
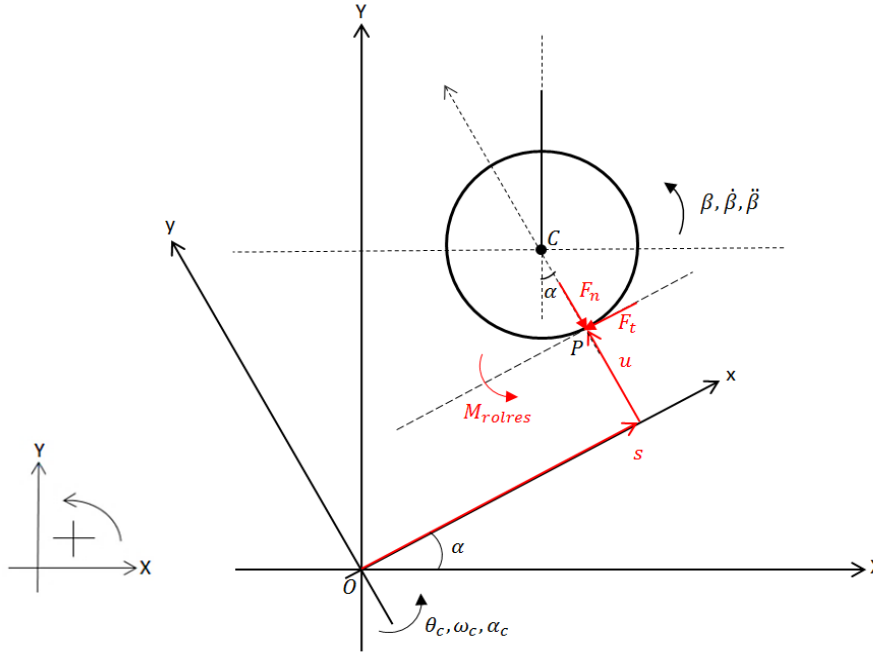
Figure 4.8 Roller on cam surface in quadrant I with fixed (XYZ) and local (xyz) reference frames. The sign convention is on the left. Shown in red are the components of the vector $\vec{P}$. The contact forces F_t and F_n, and the rolling resistance M_{rolres} are shown as they act on the cam surface.

The cam torque generated by the two forces F_n and F_t acting on the cam profile equals:

$$\vec{T_c} = \vec{P} \times \vec{F} + \overrightarrow{M_{rolres}} \tag{4.47}$$

where

$$\vec{P} = \begin{bmatrix} S \\ u \\ 0 \end{bmatrix} \tag{4.48}$$

and

$$\vec{F} = \begin{bmatrix} -F_t \\ -F_n \\ 0 \end{bmatrix} \tag{4.49}$$

The minus signs are a result of the fact that, when F_t and F_n are positive, they are acting in the directions shown in Figure 4.8, which means that the corresponding force vector components should be negative. Therefore, the torque applied to the cam by the roller is:

99

$$T_c = u \cdot F_t - s \cdot F_n + M_{rolres}$$ (4.50)

where the two components of $\vec{P}$ are defined in equation (4.17) and M_{rolres} in equation (4.36).

4.4   Hydraulic ram

For this application, single-acting cylinders were chosen for both the stance and push-off rams. Therefore, hydraulic fluid only occupies the volume on the rod-less side of the piston, while air at atmospheric pressure occupies the rod side, so the hydraulic pressure and/or the follower return springs push the pistons down against the cams. Furthermore, this means that only piston seals are necessary to avoid leaks; but not rod seals. Hence, in Figure 4.9, only the friction force at the piston O-ring ($F_{fr_{cyl}}$) is considered. Remember that the rod and follower are one and the same; so friction in the follower guide bearings has already been accounted for in the follower dynamics (see section 4.3.3). Similarly, the combined mass of the follower, rod and piston have also been accounted for in the follower dynamics. Therefore, the forces shown in the free-body diagram (Figure 4.9) are in equilibrium.
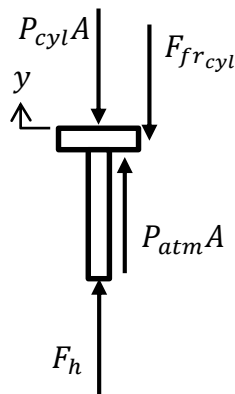
Figure 4.9 Free-body diagram of the piston rod and head.

From equilibrium, the hydraulic ram force (F_h) that acts on the piston rod, which is equal and opposite to that acting on the follower, is given by:

$$F_h = P_{cyl_{gauge}} A + F_{fr_{cyl}} \tag{4.51}$$

where $P_{cyl_{gauge}} = P_{cyl} - P_{atm}$ and $P_{atm} = 101325 \; Pa$. Absolute values are used instead of gauge values to simplify the thermodynamics calculations for the accumulator. Because P_{atm} is not taken into account in the free-bodies for the other components (e.g. follower), it is appropriate to use the full piston area (A) in this term.

To calculate O-ring friction force, two alternative models of small hydraulic cylinder performance have been considered to increase confidence in the results and these are described in the following sub-sections.

4.4.1   Xia and Durfee O-ring model

Xia and Durfee (2011b) developed a simple mathematical model to describe O-ring friction, where the friction force is given by:

$$F_{fr_{cyl}} = \pi \mu_f D d_{O-ring} E \varepsilon \sqrt{2\varepsilon - \varepsilon^2} \qquad (4.52)$$

The O-ring squeeze ratio (ε) is defined as:

$$\varepsilon = 1 - \frac{d_1 - d_2}{2d_{O-ring}} \qquad (4.53)$$

where: d_1 is the cylinder bore diameter (i.e. D); d_2 is the piston groove diameter; and d_{O-ring} is the O-ring cross-sectional diameter. To perform well, a typical range for the O-ring squeeze ratio (ε) is between $7\% - 15\%$ (Campos & Durfee, 2015; Xia & Durfee, 2014), while a value over 15% is not recommended as the friction increases significantly and the O-ring can stretch. In this work, $\varepsilon = 0.14$ has been used. In validation studies of the O-ring model (Xia & Durfee, 2011b), $\mu_f = 0.3{\sim}0.5$ was used, representing well machined and lubricated sealing surfaces.

This model was implemented in a previous study at Salford, the simulation results compared with Xia & Durfee's simulation results, and also with their experimental validation for small cylinders (Gardiner, 2017). Although the experimental validation is very encouraging, a doubt remains because their model does not include a pressure related term due to the difference in oil pressure between the rod-less side and the rod-side of the piston. In other words, the friction depends only upon the squeeze ratio and various constant properties, but does not vary with pressure. For this reason, the model described in the next sub-section was also

implemented even though there are no experimental validations specifically for small cylinders.

4.4.2 Martini O-ring model

This friction model is also referenced in O-ring catalogues such as Parker Hannifin (2007a, pp. 5-7). The model includes two force terms, F_C to account for O-ring cross-sectional squeeze, and F_H to account for the differential pressure across the O-ring (Martini, 1984). Hence, the total O-ring friction force is given by:

$$F_{fr_{cyl}} = F_C + F_H \tag{4.54}$$

The pressure dependent term is given by:

$$F_H = \mathrm{A} f_H \tag{4.55}$$

where: $\mathrm{A} = \pi D_m d_{O-ring}$ is the O-ring projected pressure area; d_{O-ring} is the original O-ring cross-sectional diameter; $D_m = (d_{O-ring\_OUT} - d_{O-ring})$ is the mean diameter; d_{O-ring_OUT} is the outside diameter of the O-ring; and $f_H = 0.545(\Delta P)^{0.61}$ is the friction density.

The cross-sectional squeeze dependent term is given by:

$$F_C = L_0 f_C \tag{4.56}$$

where: $L_0 = \pi(d_{O-ring\_OUT})$ is the O-ring rubbing length; $f_C = (-0.884 + 0.0206H_S - 0.0001H_S{}^2)S_W$ is the linear friction; H_S is the shore hardness of the O-ring ($H_S = 70°$); and S_W the actual squeeze of the O-ring cross-section as a percentage ($S_W = 100 * \varepsilon$, $\varepsilon = 0.14$). Note that all of the values used by Martini (1984) are expressed in the British Imperial System of units.

Xia et al.'s friction model is compared with Martini's friction model in Appendix A.3. Martini's model turned out to be the most conservative (i.e. characterised by the highest friction losses) and it also properly accounts for the differential pressure across the O-ring. Therefore, in this work, Martini's model has been used.

4.5 Flow losses

Flow losses are classified as major losses, which are those due to friction in pipes and hoses, and minor losses, which are associated with discrete components such as inlets/exits, bends, valves and other fittings. For Reynolds numbers below 2300, corresponding to a laminar flow (see Appendix A.4), the pressure drop due to pipe friction is proportional to flow, whereas the pressure drop across discrete components is assumed to be proportional to flow squared.

4.5.1 Pipe losses

Referring to Appendix A.4, based on the assumed hydraulic oil properties, the maximum flow seen in the simulations, and a pipe diameter of $D = 0.005m$, the Reynolds number is Re $\cong$ 24.35. This indicates fully developed laminar flow ($Re < 2300$) and, therefore, the pressure drop due to friction in a smooth cylindrical pipe of uniform diameter D is given by (Cundiff, 2002):

$$\Delta P = f \frac{L_{pipe}}{D_{pipe}} \left(\frac{\rho \bar{V}^2}{2} \right) = f \frac{\rho L_{pipe}}{2 D_{pipe}} \left(\frac{Q}{A_{pipe}} \right)^2 \tag{4.57}$$

where f = Darcy friction factor of the pipe (dimensionless)

L_{pipe} = length of the pipe (m)

D_{pipe} = pipe inside diameter (i. e. hydraulic diameter, m)

ρ = fluid density (kg/m^3)

$\bar{V}$ = mean flow velocity (m/s) across the pipe diameter measured as the volumetric flow rate Q per unit cross-sectional wetted area: $\bar{V} = \frac{Q}{A_{pipe}} = \frac{4Q}{\pi D_{pipe}{}^2}$

The Darcy friction factor f for laminar flow (Re < 2300) in a circular pipe is:

$$f = \frac{64}{\text{Re}} \tag{4.58}$$

Reynolds number for a circular pipe is given by:

$$Re = \frac{4Q}{\pi D_{pipe} v_f}$$

(4.59)

where v_f = fluid kinematic viscosity (m²/s);

Q = volumetric flow rate (m³/s).

This in turn leads to:

$$\Delta P = 128 \left(\frac{\rho v_f L_{pipe}}{\pi D_{pipe}^4} \right) Q$$

(4.60)

4.5.2 Losses associated with discrete components

The pressure drop associated with discrete components such as inlets/exits, bends and other fittings, also referred to as minor losses, is assumed to be proportional to flow squared and is given by (Cundiff, 2002; Durfee *et al.*, 2015):

$$\Delta P = K \left(\frac{\rho \bar{V}^2}{2} \right) = \frac{\rho K}{2 A_{pipe}^2} Q^2$$

(4.61)

where K is a dimensionless loss coefficient experimentally determined for each discrete element, with typical values shown in Figure 4.10. For the same component, different values for the dimensionless loss coefficient K may be found in different sources (textbooks and catalogues), so it can be difficult to select an appropriate value.

a)

Fitting	K
90 ° deg elbow	0.2
45 ° deg elbow	0.15
Tee fitting	0.9
Sharp-edged entrance	0.5
Rounded entrance	0.05
Sharp-edged exit	1.0
Rounded exit	1.0

b)

Fitting	K Factors
Standard tee	1.8
Standard elbow	0.9
45° elbow	0.42
Return bend (U-turn)	2.2

Figure 4.10 Loss coefficients K for some common fittings and geometries. (a) Image source: Durfee *et al.* (2015). (b) Image source: Cundiff (2002).

The pressure drop across valves is also proportional to flow squared. However, valves are treated slightly differently, with the orifice equation being adopted as follows (Cundiff, 2002; Durfee *et al.*, 2015):

$$Q = K_{orif}\sqrt{\Delta P} \tag{4.62}$$

Or by solving for ΔP:

$$\Delta P = \frac{Q^2}{K_{orif}{}^2} \tag{4.63}$$

where $K_{orif} = C_d A_{orif}\sqrt{2/\rho}$, C_d is the discharge (or valve) coefficient, and $A_{orifice}$ is the cross-sectional area of the orifice. The first variable (C_d) changes with valve position, but here a constant value of 0.62 is used (Durfee *et al.*, 2015). For a directional control valve (DCV), which is either fully open or fully closed, A_{orif} does not change while it is open and the orifice area is given by $A_{orif} = \pi D_{valve\_internal} d_{valve\_external}$ ("Lecture 21: FLOW AND FORCE ANALYSIS OF VALVES," 2017). The diameter of the valve ports ($d_{valve\_external}$) is assumed to be equal to the pipe diameter, here assumed to be $0.005m$. Referring to DCV catalogues, the internal diameter of the valve ($D_{valve\_internal}$) is usually slightly larger than the diameter of the valve ports, and here $D_{valve\_internal} = 1.4 d_{valve\_external}$ is used. As a result $A_{orif} = \pi * 0.007m * 0.005m$.

4.5.3   Losses for the combined system

For the system as described in Chapter 3, there are two flow resistances: one which applies when a ram is connected to the accumulator; and another when a ram is connected to the tank. As mentioned previously, the flow losses can be split into major losses, which in this case are proportional to flow and due to laminar pipe flow, and minor losses which are proportional to flow squared and associated with discrete components. Therefore, the general equation for pressure drop can be written as follows:

$$\Delta P = 128 \left(\frac{\rho v_f L_{pipe}}{\pi D_{pipe}{}^4} \right) Q + sign(Q) K_{total} Q^2 \tag{4.64}$$

where $K_{total} = \frac{\rho K}{2A_{pipe}^2} + \frac{1}{K_{orif}^2}$ and $sign(Q)$ ensures that the direction of the pressure drop corresponds to the direction of the flow.

a) Ram connected to accumulator

In this case a pipe length of $L_{pipe} = 0.050m$ and pipe diameter of $D_{pipe} = 0.005m$ are assumed. The discrete components include: one contraction at the exit of the ram ($K_{exit} = 0.5$ for sharp-edged exit (Durfee *et al.*, 2015)); one expansion at the inlet of the accumulator ($K_{entrance} = 1$ for sharp-edged entrance (Durfee *et al.*, 2015)); one 90° elbow ($K_{elbow} = 0.9$ for a standard elbow (Cundiff, 2002)); and the DCV. Therefore, from equations (4.61) and (4.63), the combined flow resistance for the discrete components to be used in equation (4.64) is given by:

$$K_{total} = \frac{2.4\rho}{2A_{pipe}^2} + \frac{1}{K_{orif}^2} \qquad (4.65)$$

When the flow into the accumulator is positive, the pressure in the cylinder will be greater than the pressure in the accumulator. When the flow into the accumulator is negative, the pressure in the cylinder will be lower that the pressure in the accumulator. This yields:

$$P_{cyl} = P_{acc} + \Delta P_{to\ acc} \qquad (4.66)$$

where $\Delta P_{to\ acc}$ is the total pressure drop due to major and minor flow losses between each ram and the accumulator, evaluated using equation (4.64).

b) Ram connected to tank

In this case, to minimise losses, it is assumed that the DCV is mounted directly onto the ram and surrounded by the tank at atmospheric pressure. Therefore, there is no connecting pipe ($L_{pipe} = 0m$) and, thus, there are no major flow losses. The discrete components include: one contraction at the exit of the ram ($K_{exit} = 0.5$); one expansion at the inlet of the tank ($K_{entrance} = 1$); and the DCV. Therefore, from equations (4.61) and (4.63), the combined flow resistance for the discrete components to be used in equation (4.64) is given by:

$$K_{total} = \frac{1.5\rho}{2A_{pipe}^2} + \frac{1}{K_{orif}{}^2} \qquad (4.67)$$

When the flow into the tank is positive, the pressure in the cylinder will be greater than the pressure in the tank. When the flow into the tank is negative, the pressure in the cylinder will be lower that the pressure in the tank. This yields:

$$P_{cyl} = P_{atm} + \Delta P_{to\ tank} \qquad (4.68)$$

where $\Delta P_{to\ tank}$ is the total pressure drop between each ram and the tank due to minor flow losses, evaluated using equation (4.64).

4.6 Accumulator

The model used here for the gas-charged diaphragm accumulator is based on the model developed in Bari (2013), but it has been further developed to include losses due to oil compressibility and heat transfer.

4.6.1 Accumulator parameters

Some of the main parameters defining the accumulator are as follows:

- The **maximum or nominal volume** ($\boldsymbol{V_A}$) is the total volume of the accumulator including both the oil and gas within it. V_A is $250cc$ for the reasons explained in Chapter 3.
- The **maximum rated pressure** ($\boldsymbol{P_{max}}$) is the maximum pressure the accumulator can hold during normal operation. At this pressure, there is the maximum volume of oil V_{max} stored in the accumulator and the minimum volume of gas. P_{max} equal to $100\ bar$ was chosen.
- The **minimum rated pressure** ($\boldsymbol{P_{min}}$) is the minimum pressure the accumulator should hold during normal operation. At this pressure, there is the minimum volume of oil V_{min} stored in the accumulator and the maximum volume of gas. $\frac{P_{max}}{P_{min}} = 2$ is recommended by some suppliers (HYDAC, 2015, p. 80), which gives $P_{min} = 50bar$.
- The **pre-charge pressure** ($\boldsymbol{P_{pre-charge}}$) is the gas pressure in the accumulator at room temperature when it is not connected to the hydraulic circuit (REXROTH, 2013, p. 5), and so this corresponds to there being no fluid in the accumulator ($V_{acc_{pre-charge}} = 0m^3$), which is therefore completely filled by the gas (effective gas volume at pre-charge corresponds to the nominal volume of the diaphragm accumulator, i.e. $V_{gas_{pre-charge}} = V_A = 250cc$ (HYDAC, 2013, 2017)). When the accumulator is connected to the hydraulic circuit, hydraulic fluid will only enter the accumulator when the system pressure exceeds the pre-charge pressure. If the circuit pressure falls below $P_{pre-charge}$, then a vacuum condition will follow as no more oil can leave the accumulator; so this must be avoided. When the accumulator is used for energy storage purposes, it is recommended that $P_{pre-charge} = 0.90 * P_{min} = 45bar.$

4.6.2   Oil flow into the accumulator

The oil flow into and out of the accumulator depends on piston displacement and oil compressibility. No fluid is truly incompressible, even if they are often assumed to be incompressible. Because the energy efficiency of the proposed ESR ankle design is critical, in this case oil compression has been accounted for. In this design, compression losses due to the oil bulk modulus are experienced during valve transition events, which occur at specific moments in the gait cycle, and also at each simulation time step because of the incremental changes in pressure.

The bulk modulus is a measure of a fluid's resistance to being compressed and is the reciprocal of compressibility. It is defined as the pressure increase for a unit change of volumetric strain (i.e. increased compression):

$$\beta = -V\frac{dP}{dV} \tag{4.69}$$

As explained in Appendix A.4, a bulk modulus of $\beta = 1.657e + 09\ Pa$ has been used here. To calculate the change in accumulator oil volume due to the compressibility of the oil, including oil in the connecting pipe, equation (4.69) is rearranged to give the change in volume:

$$\Delta V_{\beta_{acc}} = -V_{acc1}\frac{\Delta P}{\beta} = -V_{acc1}\frac{(P_{acc2} - P_{acc1})}{\beta} \tag{4.70}$$

where P_{acc1} and P_{acc2} are the accumulator pressure before and after a change respectively, and V_{acc1} is the oil volume in the accumulator before the change.

Similarly, the change in oil volume in the cylinder is given by:

$$\Delta V_{\beta_{cyl}} = -V_{cyl1}\frac{\left(P_{cyl2} - P_{cyl1}\right)}{\beta}$$

$$\Delta V_{\beta_{cyl}} = -V_{cyl1}\frac{((P_{res2} + \Delta P_{to\ res2}) - (P_{res1} + \Delta P_{to\ res1}))}{\beta} \tag{4.71}$$

where P_{res1} and $\Delta P_{to\ res1}$ are the pressure in the reservoir to which the cylinder is connected, and the pressure drop to it, before a change; P_{res2} and $\Delta P_{to\ res2}$ are the same variables after the change; and V_{cyl1} is the oil volume in the cylinder before the change. The reservoir is either the accumulator or the tank.

The total volume change due to oil compressibility (expansion is positive) is given by:

$$\Delta V_\beta = \Delta V_{\beta\ acc} + \Delta V_{\beta\ cyl} \tag{4.72}$$

Hence, the change in oil volume in the accumulator over each simulation time step is given by:

$$\Delta V_{oil\ flow} = \Delta yA + \Delta V_\beta \tag{4.73}$$

where ΔyA is the change due to the incremental piston displacement Δy.

4.6.3   Accumulator thermodynamics

The gas in the accumulator is considered to be an ideal gas and subject to polytropic compression and expansion. In other words, the following equations apply:

$$PV = nRT$$
$$PV^k = constant$$
$$\text{also written as } P_1 V_1{}^k = P_2 V_2{}^k \tag{4.74}$$

Also, by substituting the first equation into the second, pressure can be eliminated as follows:

$$\frac{nRT_1}{V_1} V_1{}^k = \frac{nRT_2}{V_2} V_2{}^k \tag{4.75}$$

$$T_1 V_1{}^{k-1} = T_2 V_2{}^{k-1} \tag{4.76}$$

This yields:

$$T_2 = T_1 \left(\frac{V_1}{V_2}\right)^{k-1} \tag{4.77}$$

In the accumulator literature, gas volume changes are considered approximately isothermal ($k = 1$) if they take place over a long period of time, so that the temperature of the gas remains constant. Conversely, gas volume changes are considered approximately adiabatic ($k = 1.4$) when the changes occur quickly, so that there is very little time for heat transfer from the accumulator to the surrounding environment. Generally, isothermal conditions are assumed if the accumulator is used as a volume compensator, leakage compensator, pressure compensator or lubrication compensator. In all other cases, such as energy accumulation, pulsation damping, emergency power source, dynamic pressure compensator, shock absorber, hydraulic spring etc., adiabatic conditions are assumed ("Lecture 28: ACCUMULATORS," 2017). One accumulator manufacturer (Epe Italiana Srl, 2012, p. 51) uses an empirical rule to choose the appropriate value for the polytropic index k:

- If the cycle duration is smaller than one minute, the change is adiabatic ($k = 1.4$).
- If the cycle duration is larger than three minutes, the change is isothermal ($k = 1$).
- If the cycle duration is between one and three minutes, there is some heat transfer during compression and expansion ($1 < k < 1.4$) .

Therefore, over the period of one gait cycle lasting approximately one second, it is reasonable to assume that charge and discharge of the accumulator is approximately adiabatic ($k = 1.4$). So the changes in pressure as a result of changes in gas volume during each gait cycle are calculated assuming $k = 1.4$. However, over many gait cycles, there will be heat loss to the surroundings, resulting in a slow change in both temperature and pressure. This is modelled using the thermal time-constant described by Pourmovahed and Otis (1990), which is used to model the relaxation process of the gas after a rapid compression or expansion. The rate of change of the gas temperature T is given by:

$$\frac{dT}{dt} = \frac{(T_w - T)}{\tau} \tag{4.78}$$

where T_w is the wall temperature, which is equal to the temperature of the surrounding environment (T_{env}). The calculation of the time constant τ is described in Appendix A.5.

The solution of this differential equation leads to:

$$T(t) = [\,T(0) - T_w\,]e^{-\frac{t}{\tau}} + T_w \tag{4.79}$$

where $T(0)$ is the temperature when $t = 0$.

4.6.4   Accumulator initialisation

Initially, before the accumulator is installed in the hydraulic circuit of the new ankle design, the gas is at the pre-charge pressure. In this pre-charge condition, the gas pressure and volume follow the ideal gas law:

$$P_{pre-charge} = \frac{n_{N_2} R T_{pre-charge}}{V_{gas_{pre-charge}}} \tag{4.80}$$

where $T_{pre-charge} = T_{env} = 293K$ (i.e. 20°C, the environment temperature). From this equation, it is possible to calculate the number of moles of nitrogen in the accumulator:

$$n_{N_2} = \frac{P_{pre-charge} V_{gas_{pre-charge}}}{R T_{pre-charge}} = \frac{45bar \cdot 250e - 06\ m^3}{8.314\ ^J/_{mol\cdot K} \cdot 293K} \cong 0.462\ mol \tag{4.81}$$

Given the molecular weight of N_2 ($M_{N_2} = 28.014\frac{g}{mol}$), the corresponding mass of N_2 in the accumulator when $V_A = 250e - 06\ m^3$ is:

$$m_{N_2} = n_{N_2} \cdot M_{N_2} = 0.462mol \cdot 28.014\ ^g/_{mol} = 12.942g \tag{4.82}$$

With the accumulator installed in the hydraulic circuit, the desired initial pressure at the beginning of the gait cycle was set at $P_{start} = 0.90 * P_{max} = 90\ bar$. The initial charging process of the accumulator, before any cyclic working activity over the gait cycle, was assumed to be isothermal (i.e. $T_{start} = T_{env} = 293K$). Therefore, this can be modelled by the polytropic equation $PV^k = C$, with $k = 1$ for an isothermal process. Hence, $V_{gas_{start}}$ is evaluated as follows:

$$P_{pre-charge}V_{gas_{pre-charge}} = P_{start}V_{gas_{start}}$$

(4.83)

$$V_{gas_{start}} = V_{gas_{pre-charge}}\left(\frac{P_{pre-charge}}{P_{start}}\right) = 1.25e - 04\ m^3$$

(4.84)

Then the oil volume is obtained as follows:

$$V_{acc_{start}} = V_A - V_{gas_{start}} =$$
$$= 250e - 06m^3 - 1.25e - 04\ m^3 = 1.25e - 04m^3$$

(4.85)

Moreover, the initial values of gas pressure and volume should also follow the ideal gas law:

$$P_{start} = \frac{n_{N_2}RT_{start}}{V_{gas_{start}}}$$

(4.86)

Therefore, as a check, the number of moles in the accumulator can be calculated and this is still the same as that calculated for the pre-charge condition, as it should be:

$$n_{N_2} = \frac{P_{start}V_{gas_{start}}}{RT_{start}} = \frac{90bar \cdot 1.25e - 04m^3}{8.314\ ^J/_{mol\cdot K}\cdot 293K} \cong 0.462mol$$

(4.87)

4.6.5 Modelling valve transitions - sequence of calculation

a) Connecting cylinder to accumulator

Valve transition events occur at the beginning of each working phase, when the directional control valve connects the relevant cylinder to the accumulator. This involves a small drop in accumulator pressure and a large increase in cylinder pressure, which correspond to small oil volume changes, respectively an expansion and a compression. Based on the theory presented in section 4.6.2, the changes in the two oil volumes are evaluated as follows:

$$\Delta V_{\beta\,acc} = -V_{acc1}\frac{(P_{acc2} - P_{acc1})}{\beta} \tag{4.88}$$

$$\Delta V_{\beta\,cyl} = -V_{cyl1}\frac{((P_{acc2} + \Delta P_{to\,acc}) - (P_{atm} + \Delta P_{to\,tank}))}{\beta} \tag{4.89}$$

where V_{acc1} and V_{cyl1} are the oil volumes in the accumulator and cylinder before connecting to the accumulator; P_{acc1} and P_{acc2} are the accumulator pressures before and after connecting; and $(P_{atm} + \Delta P_{to\,tank})$ and $(P_{acc2} + \Delta P_{to\,acc})$ are the cylinder pressures before and after connecting. The accumulator pressure after connecting (P_{acc2}) depends on these volume changes and, therefore, it is evaluated within an iteration loop (see Appendix C.3.8). The initial estimate used to begin the iterative solution is $P_{acc2} = P_{acc1}$.

Using equations (4.72) and (4.73), the oil flow into the accumulator and hence the change in gas volume are given by:

$$\Delta V_{oil\,flow} = \Delta V_{\beta} = \Delta V_{\beta\,acc} + \Delta V_{\beta\,cyl} \tag{4.90}$$

$$V_{gas2} = V_{gas1} - \Delta V_{oil\,flow} \tag{4.91}$$

Then, based on the theory presented in section 4.6.3 and assuming no heat transfer because the valve transition is assumed to occur instantaneously, the gas temperature and pressure in the accumulator are given by:

$$T_2 = T_1 \left(\frac{V_{gas1}}{V_{gas2}}\right)^{k-1} \tag{4.92}$$

$$P_{acc2} = P_{acc1} \left(\frac{V_{gas1}}{V_{gas2}}\right)^{k} \tag{4.93}$$

This new estimate for P_{acc2} is used in the next iteration to recalculate the changes in oil volumes, which in turn allow another new estimate for P_{acc2}. Iterations stop when the

difference between two consecutive estimates of P_{acc2} is $\leq 1Pa$. Then the new oil volume in the accumulator after connecting is $V_{acc2} = V_A - V_{gas2}$.

b) Connecting cylinder to tank

Valve transition events also occur at the end of each working phase, when the directional control valve connects the cylinder to the tank. This involves a large drop in cylinder pressure and a corresponding small expansion of oil in the cylinder, some of which therefore flows into the tank. Nonetheless, it is not necessary to take this explicitly into account as its effect is seen when the cylinder is next connected to the accumulator, at which point there is a small oil flow from the accumulator into the cylinder because of oil compression as the cylinder is re-pressurised.

4.6.6   Modelling incremental accumulator changes - sequence of calculation

a) Working phases

Each incremental piston displacement at each time step of a working phase causes a change in accumulator oil volume and hence pressure. Based on the theory presented in section 4.6.2 and in a similar manner to the valve transition calculations in the previous section, the oil volume changes and corresponding accumulator gas volume change are calculated as follows:

$$\Delta V_{\beta_{acc}} = -V_{acc1} \frac{(P_{acc2} - P_{acc1})}{\beta} \tag{4.94}$$

$$\Delta V_{\beta_{cyl}} = -V_{cyl1} \frac{((P_{acc2} + \Delta P_{to\ acc2}) - (P_{acc1} + \Delta P_{to\ acc1}))}{\beta} \tag{4.95}$$

$$\Delta V_{oil\ flow} = \Delta y A + \Delta V_{\beta} = \Delta y A + (\Delta V_{\beta_{acc}} + \Delta V_{\beta_{cyl}}) \tag{4.96}$$

$$V_{gas2} = V_{gas1} - \Delta V_{oil\ flow} \tag{4.97}$$

Then, based on the theory presented in section 4.6.3 and, in this case, including heat transfer because the incremental changes occur over a finite time step, the new gas temperature and pressure in the accumulator are given by:

$$\Delta T_{poly} = T_1 \left(\frac{V_{gas1}}{V_{gas2}}\right)^{k-1} - T_1 \qquad (4.98)$$

$$\Delta T_{transfer} = [T_1 - T_{env}]e^{-\frac{\Delta t}{\tau}} + T_{env} - T_1 \qquad (4.99)$$

$$\Delta T_{total} = \Delta T_{poly} + \Delta T_{transfer} \qquad (4.100)$$

$$T_2 = T_1 + \Delta T_{total} \qquad (4.101)$$

$$P_{acc2} = nR\frac{T_2}{V_{gas2}} \qquad (4.102)$$

where ΔT_{poly} is the change in temperature due to polytropic compression and $\Delta T_{transfer}$ is the change in temperature due to heat transfer. Solving for the total change in temperature (ΔT_{total}) in this sequential manner is justified because the incremental changes are small. In other words, this is a numerical approximation.

As for the valve transition events, the new accumulator pressure (P_{acc2}) depends on the volume changes and, therefore, it is evaluated within an iteration loop (see Appendix C.3.9). The initial estimate used to begin the iterative solution is $P_{acc2} = P_{acc1}$.

b) Non-working phases with accumulator isolated

During load acceptance and swing, the accumulator is not connected to either cylinder. Nevertheless, there are still gas temperature and pressure changes as a result of heat transfer. Therefore, the calculation of the accumulator gas volume change is simplified as follows:

$$\Delta V_{\beta_{acc}} = -V_{acc1} \frac{(P_{acc2} - P_{acc1})}{\beta} \tag{4.103}$$

$$V_{gas2} = V_{gas1} - \Delta V_{\beta_{acc}} \tag{4.104}$$

Apart from this, the calculations for the new gas temperature and pressure in the accumulator are the same as those presented above (see equations (4.98) - (4.102)).

5. Chapter 5: Simulation

Leonardo da Vinci, Studies of Turbulent Water, Royal Collection Trust

"No human investigation can be a real science
if it does not go through mathematical demonstrations"

(Leonardo Da Vinci)

Based on the mathematical modelling described in Chapter 4, a simulation model of the whole system was implemented in MATLAB, including all of the components previously described. For a given engineering design, this simulates the new device working throughout the gait cycle, storing and releasing energy at the ankle joint. Secondly, a design program was created that uses the aforementioned simulation model to:

a) Design the profiles of the two cams in such a way as to replicate the torque of an intact ankle;

b) Specify the two follower return springs.

The simulation model and design program are explained in the next two sections and in the corresponding high-level pseudo code (i.e. a simplified representation of the MATLAB code), which can be found in Appendix C. The final section describes a power-audit-based check that the simulation model has been correctly implemented.

5.1   Simulation model

Once the engineering design of the new device has been defined, the main input that drives the system is the ankle angle over the gait cycle, which is the only variable the amputee can control (experimental data collected by Bari (2013) was used). Conversely, the ankle torque depends on the torques applied by the two cam-ram systems, which in turn depend on the cam profiles – which are fixed – and on the changing pressure in the accumulator (see section 4.3.4). Therefore, a simulation model was implemented in MATLAB to simulate a given engineering design (i.e. given all fixed parameters that are needed for mathematical modelling) over one gait cycle, driven by the input of ankle angle versus time obtained from experimental gait data. This calculates the changes in pressure and oil volume in the accumulator, and therefore the energy stored and released, and the total torque at the ankle joint as the output from the device, while considering the physical phenomena that may impair the efficiency of the new device. Table 5.1 illustrates the main stages of the MATLAB script, while Appendix C explains the MATLAB script in detail. In the sequence in which they occur, these calculation stages are as follows.

Stage 1 – Initialisation

The properties of all components – cams, hydraulic rams, return springs, accumulator, pipes, directional control valves, fittings, and also the oil and the gas – are defined at the beginning of the code. Also the gas volume, pressure and temperature in the accumulator are initialised as explained in section 4.6.4 for the first gait cycle or to the final values at the end of the previous gait cycle for the second gait cycle onwards.

Stage 2 – Array-based calculations for whole gait cycle

Given ankle angle versus time as input to the model, the parallel spring torque and the kinematics of the gearbox and two cams are evaluated. As the two cams profiles are given, the ratio of piston incremental displacement to cam incremental angle is known for the two cam-ram systems. Therefore, given the cam rotation angles, the kinematics of the two pistons is evaluated (i.e. incremental displacements, total displacement, linear velocities and accelerations), together with the kinematics of the two rollers (angular velocities and accelerations). This, in turn, allows the calculation of the two return spring forces, fluid flows, major and minor flow losses, and the initial pressures and oil volumes in the two rams.

Stage 3 – Time-stepping loop

A time-stepping loop evaluates the states of the directional control valves (DCVs), including modelling valve transitions, solves the cam-ram dynamics, and models the filling and emptying of the accumulator. This is necessary because the solutions at each time instant of the gait cycle depend on the solutions at the previous time instant. The time-stepping loop includes three stages of calculation as follows.

The first stage evaluates the states of the directional control valves (DCVs), including modelling valve transitions (see section 4.6.5). During the working phases of the stance and push-off cam-rams, these valves allow fluid flow from the stance ram to the accumulator and from the accumulator to the push-off ram respectively. Therefore, through a valve transition, a connection is made between ram and accumulator at the start of each working phase, and the change in gas volume and, hence, pressure and temperature in the accumulator due to oil compressibility is evaluated. This occurs at the first time instant of mid-stance and the first time instant of push-off. Conversely, during their non-working phases, the two valves connect

the rams to the tank. Consequently, for each cam-ram, the first time instant of the non-working phase that immediately follows that cam-ram's working phase is characterised by a small oil expansion in the corresponding cylinder, which need not be explicitly accounted for as explained at the end of section 4.6.5.

The second stage of the time-stepping loop evaluates the friction losses in the two cylinders and, thus, calculates the two net hydraulic ram forces, given by the sum of hydraulic force and friction force, and runs the dynamic analysis to evaluate all forces and moments acting within the two cam-ram systems (see Appendix B.4).

The third stage of the time-stepping loop models the fluid flow into and out of the accumulator for each time step of the working phases of the two cam-ram systems, caused by the incremental displacements of the pistons. The resulting gas volume, pressure and temperature in the accumulator are evaluated for each time instant in the two working phases by accounting for piston displacement, oil compressibility and heat transfer. During load acceptance and swing the accumulator is isolated (i.e. not connected to a ram) and the changes in gas volume, pressure and temperature only depend on heat transfer between the accumulator and the environment (see section 4.6.6).

Stage 4 – Further array-based calculations for whole gait cycle
Finally, the total torque at the camshaft throughout the gait cycle is obtained by adding the two cam torques ($T_c = T_{c_{PO}} + T_{c_{STANCE}}$). Then, the ankle torque is the sum of the parallel spring torque and the gearbox input (ankle side) torque (see equations (4.5) and (4.6)).

**ankle angle versus time
over the gait cycle**

Stage 1 – Initialisation

- Define fixed properties of all components.
- Initialise gas volume, pressure & temperature in the accumulator.

**Stage 2 – Array-based calculations
for whole gait cycle**

- Evaluate parallel spring torque.
- Evaluate kinematics of gearbox and cams.
- Evaluate kinematics of pistons.
- Evaluate kinematics of rollers.
- Evaluate return spring forces, fluid flows, major and minor flow losses; and initial pressures & oil volumes in the rams.

Stage 3 – Time-stepping loop

- Evaluate DCV states.
- Model valve transitions.
- Evaluate cylinder friction forces.
- Evaluate hydraulic ram forces.
- Solve dynamics for 2 cam-ram systems to obtain 2 cam torques.
- Evaluate oil flow to accumulator and changes in gas volume, pressure & temperature.

**Stage 4 – Further array-based
calculations for whole gait cycle**

- Evaluate total camshaft torque by adding 2 cam torques.
- Evaluate ankle torque
(sum of parallel spring torque and gearbox input torque).

Table 5.1 Overview of the simulation model.

5.2 Design program

A design program was implemented in MATLAB that uses the simulation model described above to:

a) Design the profiles of the two cams in such a way as to replicate the torque of an intact ankle;

b) Specify the two follower return springs.

This MATLAB script is characterised by three nested loops. The two outer loops are for design purposes – one to size the return springs (explained in section 5.2.2) and a second one to determine the cam profiles (explained in section 5.2.1). The inner time-stepping loop is almost identical to the one in the simulation model described in the previous section, modelling the states of the directional control valves, the dynamics of the cam-rams and the filling and emptying of the accumulator. Other parts of the code are also adapted from that of the simulation model. Table 5.2 presents the main calculation stages of the MATLAB script, while the high-level pseudo-code can be found in Appendix C.

5.2.1 Iterative calculation of cam profiles

The second of the two outer loops converges iteratively to find two cam profiles that enable the system to produce ankle torque curves during the working phases of the two cam-rams that match the required curves, taken from in-vivo experimental data collected by Bari (2013). Given the required ankle torque, it is possible to use an inverse model of the parallel spring and gearbox to obtain the required camshaft torque, which corresponds to the sum of the two cam torques. In particular, from equations (4.8) and (4.9), the required camshaft torque (T_{c_r}) is:

$$T_{c_r} = \left(\frac{T_{in_{gb}} - T_f}{GR}\right) = \left(\frac{(T_{a_r} - T_{ps}) - T_f}{GR}\right) \tag{5.1}$$

Thereafter, an iterative solution is necessary because the actual camshaft torque depends upon the dynamics of the two cam-ram systems, which includes velocity and acceleration

dependent terms that are determined by the cam profiles. In other words, simulation over the gait cycle requires a priori knowledge of the cam profiles. So, beginning with initial estimates of the two cam profiles, which are used as inputs, the design program runs the simulation model to calculate the corresponding camshaft torque curves in the two working phases. The error between the calculated (i.e. actual) and required torque curves is then used to update the cam profiles. This iteration loop is repeated numerous times until a solution is reached, such that the actual camshaft torque curves in the two working phases, as calculated by the simulation model, match the required ones derived from the required ankle torque curves within a small tolerance.

a) **Estimating an initial cam profile**

The purpose of each cam profile is to define the ratio of piston incremental displacement to cam incremental angle ($\frac{dy}{d\theta_c}$) as a function of cam rotation angle θ_c. In other words, defining a cam profile is synonymous with defining $\frac{dy}{d\theta_c}$ as a function of cam rotation angle θ_c. The method of estimating an initial cam profile is the same for both cam-ram systems, so here it is explained for the stance cam-ram only. For the initial estimate only, all friction terms are neglected including the torque generated by the non-working cam-ram, which is connected to tank. Therefore, it can be assumed that, during its working phase, the stance cam torque $T_{c_{STANCE}} = T_{c_r}$ and the work done by the stance cam is equal to the work done by the piston on the hydraulic fluid. In other words:

$$W = T_{c_{STANCE}}d\theta_c = T_{c_r}d\theta_c = F_h dy \qquad (5.2)$$

Where, by neglecting piston O-ring friction, the hydraulic ram force is the product of gauge cylinder pressure and piston area (see Figure 4.9):

$$F_h = (P - P_{atm})A \qquad (5.3)$$

where $P = P_{cyl} = P_{acc}$ because the pipe, fittings and valve friction between cylinder and accumulator is being neglected. Furthermore, for the initial estimate only, a constant accumulator pressure of $P_{acc} = 0.90 * P_{max}$ was assumed.

Therefore, by rearranging (5.2), the initial estimate for the ratio of piston incremental displacement to cam incremental angle during the cam's working phase is given by:

$$\frac{dy}{d\theta_c} = \frac{T_{cr}}{F_h} = \frac{T_{cr}}{(P - P_{atm})A} \tag{5.4}$$

This is used to calculate $\frac{dy}{d\theta_c}$ as a function of cam rotation angle θ_c over the cam working phase.

Since there is no clutch mechanism to disengage the cam-ram outside of its working phase, the cam profile will be followed over the complete gait cycle, including during its non-working phases when the ram is connected to tank. For cam angles outside the range of cam angles seen during the working phase, the ratio $\frac{dy}{d\theta_c}$ is set to zero, so that there is no change in piston displacement, corresponding to a constant cam radius. For cam angles within the range of cam angles seen during the working phase, the ratio $\frac{dy}{d\theta_c}$ in the non-working phase is determined by interpolation of the working phase results. Consequently, for all time steps within the gait cycle, the incremental changes in piston displacement (Δy) are evaluated, together with the overall piston displacement (y) by cumulatively summing the incremental changes, with the minimum value of y set to zero (see Appendix C for the exact calculation). Figure 5.1 shows piston displacement over time for the two cam-ram systems. Piston displacement y and the ratio $\frac{dy}{d\theta_c}$ are used to calculate the cam profile (see equations (4.12) and (4.31)).
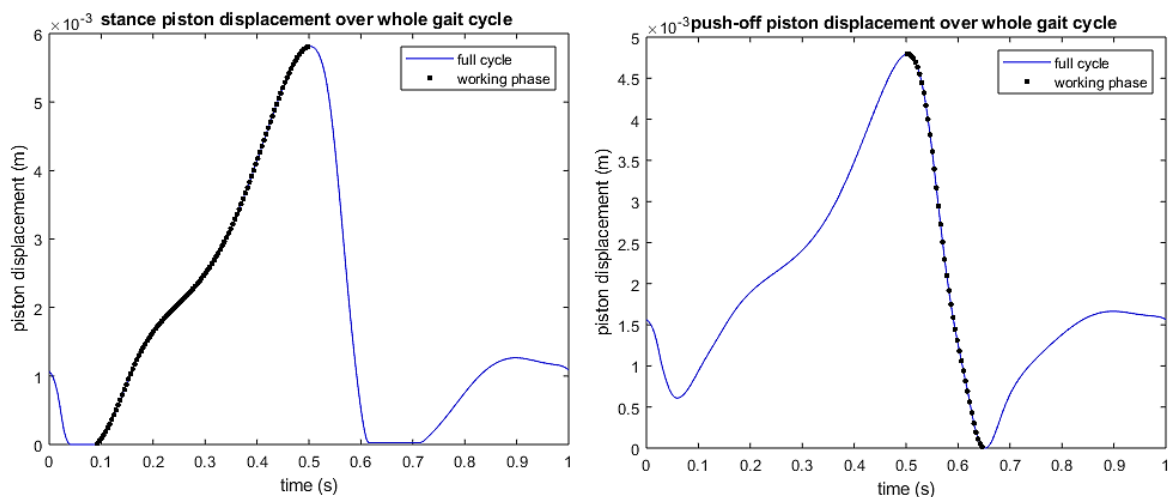
Figure 5.1 Piston displacement during the working phase (black dots) and over the complete gait cycle (blue solid line) for the stance cam-ram (on the left) and the push-off cam-ram (on the right). During the non-working phases, the working phase cam surface is followed within its range of cam angles; outside this range the piston displacement is constant (flat sections of blue line).

b) Iteratively updating the cam profile

For the first iteration, the initial cam profile, specifically the initial ratio $\frac{dy}{d\theta_c}$ as a function of cam rotation angle θ_c, is used to drive the simulation model, taking full account of all friction terms and the torque generated by the non-working cam-ram. This provides an accurate calculation of the actual camshaft torque T_c, which is used to update $\frac{dy}{d\theta_c}$ as a function of cam rotation angle θ_c over the working phase of the cam and, hence, the cam profile. This is done using a modified version of equation (5.4) as follows:

$$\left(\frac{dy}{d\theta_c}\right)_{n+1} = \frac{T_{c_{r_{n+1}}}}{F_{h_{n+1}}} \cong \frac{T_{c_{r_n}} + T_{c_{error}}}{F_{h_n}} = \left(\frac{dy}{d\theta_c}\right)_n + \frac{T_{c_{error}}}{F_{h_n}} \qquad (5.5)$$

Where $T_{c_{error}} = T_{c_{r_n}} - T_{c_n}$ (i.e. required camshaft torque minus the actual torque), F_{h_n} is the actual ram force including piston O-ring friction, and n is the iteration index. In other words, $\frac{dy}{d\theta_c}$ for iteration $n + 1$ is equal to the previous $\frac{dy}{d\theta_c}$ for iteration n plus an adjustment which corresponds to adding the error in camshaft torque ($T_{c_{error}}$) so that, in the absence of further changes to the cam-ram dynamics, the error would be zero in iteration $n + 1$.

For the second and subsequent iterations, the updated cam profile calculated using equation (5.5) is used to drive the simulation model, again taking full account of all friction terms and the torque generated by the non-working cam-ram. This process is repeated until a stable solution is reached. The residuals ($T_{c_{error}}$) for the two working phases were observed to decrease as the number of iterations increased from one to five; after which they increased slightly up to the eighth iteration and then remained constant. Therefore, five iterations were used and the resulting maximum difference between the required torque T_{c_r} and the actual one T_c was just under $0.02Nm$ (see Figure 5.2 (b)).

(a)

(b)
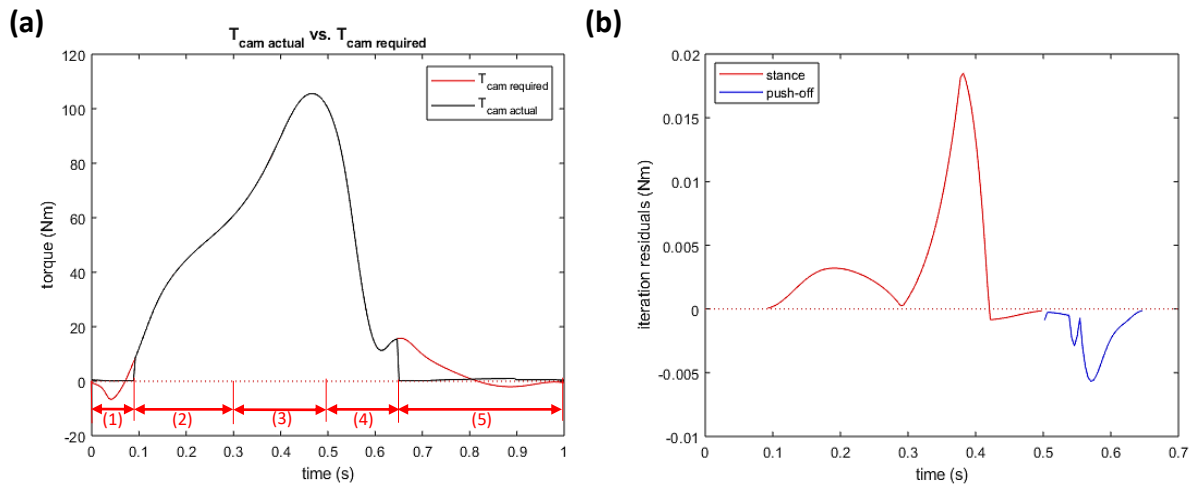
Figure 5.2 (a) On the left, a comparison of the required camshaft torque (red solid line) and the actual torque (black solid line) throughout the gait cycle (load acceptance (1), mid-stance (2), terminal stance (3), push-off (4), and swing phase (6)). (b) On the right, the camshaft torque residuals (required torque minus actual torque) during the working phases of the two cam-ram systems after five iterations.

Figure 5.3 shows the actual versus required ankle powers produced by the new system after the design program has converged on suitable cam profiles. This includes the effect of the parallel spring, which is not perfectly matched to load acceptance and swing.
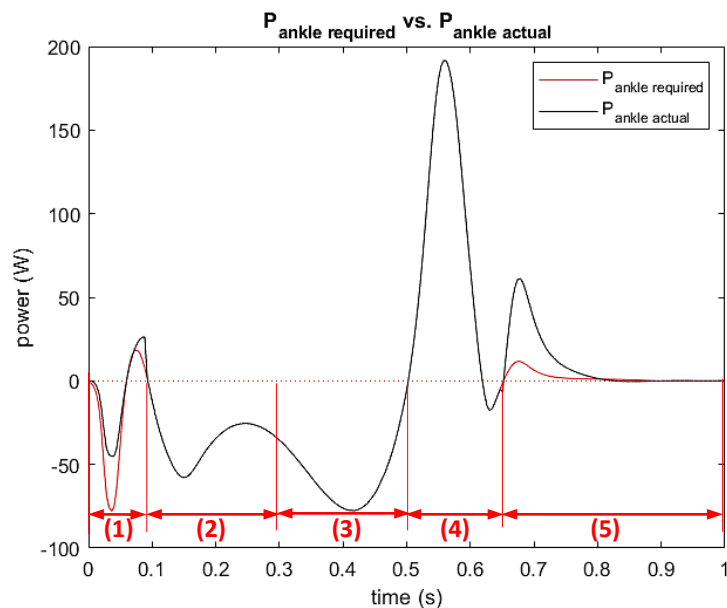
Figure 5.3 Comparison of the required power at the ankle joint (red solid line) and the actual power (black solid line) throughout the gait cycle (load acceptance (1), mid-stance (2), terminal stance (3), push-off (4), and swing phase (6)).

129

ankle angle & torque versus time
over the gait cycle

Initialisation

- Define fixed properties of all components.
- Set initial return spring characteristics (zero slope and intercept).
- Evaluate the parallel spring torque.
- Model the gearbox to evaluate the required camshaft torque.

UPDATED slope & intercept
for the return springs characteristics

Return springs sizing (2 iterations)

- Evaluate kinematics of cams.
- Initialise gas volume, pressure & temperature in the accumulator.
- Initialise ram force, neglecting all friction terms.
- Estimate initial cam profiles (i.e. the ratio of piston incremental displacement to cam incremental angle over the gait cycle).

Iterative calculation of
cam profiles (5 iterations)   **UPDATED cam profiles**

- Evaluate kinematics of pistons.
- Evaluate kinematics of the rollers.
- Evaluate return spring forces, fluid flows, major and minor flow losses; and initial pressures & oil volumes in the rams

Time-stepping loop

- Evaluate DCV states.
- Model valve transitions.
- Evaluate cylinder friction forces.
- Evaluate hydraulic ram forces.
- Solve dynamics for 2 cam-ram systems to obtain 2 cam torques.
- Evaluate oil flow to accumulator and changes in gas volume, pressure & temperature.
- Evaluate total camshaft torque by adding 2 cam torques.
- Update cam profiles (i.e. the ratio of piston incremental displacement to cam incremental angle over the gait cycle).

- Evaluate the characteristics of the two return springs (slope and intercept), to be used in the 2nd iteration.

- Draw cam profiles.
- Undertake power audit.

Table 5.2 Overview of the design program.

5.2.2 Follower return springs sizing

The outer loop described in the previous section and the inner time-stepping loop are both nested within a second outer loop (see Table 5.2.), the purpose of which is to specify the two follower return springs. As explained in section 3.4.2, the linear return spring is part of the follower assembly and it ensures contact between the cam and the roller. In particular, cams must normally operate with only compressive (positive) normal forces between cam and roller (F_n in Figure 4.5). To guarantee this, a minimum positive value was chosen for the normal cam force of $F_{n_{desired}} = 20N$, and the two return springs specified in order to satisfy this constraint.

To specify the follower return springs requires knowledge of the normal cam forces F_n over the gait cycle, but to calculate F_n requires a priori knowledge of the follower return spring parameters. Therefore, an iterative approach is necessary to converge upon suitable spring parameters. In practise an approach involving just two iterations proved sufficiently accurate, particularly given the fact that the minimum positive value chosen for F_n was to some extent arbitrary.

In the first iteration, the return springs were omitted and the simulation model run to evaluate the normal cam forces without return springs ($F_{n_{NO\ spring}}$) over the whole gait cycle. This data was used to calculate the return spring force that would be required, at every time instant, to make F_n equal to the chosen minimum of $F_{n_{desired}} = 20N$. Specifically, the required return spring force is given by:

$$F_{s_{required}} = F_{n_{desired}} - F_{n_{NO\ spring}} \qquad (5.6)$$

$F_{s_{required}}$ is plotted against piston displacement in Figure 5.4. These plots illustrate one-to-many relationships because the pistons reciprocate as the cams rotate. During the working phases of the cam-ram systems, when the hydraulic ram is connected to the accumulator, the normal cam forces are large and, therefore, $F_{s_{required}}$ is negative with a large magnitude (see Figure 5.4, left hand side). This negative data is not relevant as it indicates that the minimum constraint on normal cam force has been met without the need for a return spring. Conversely,

when $F_{s\,required}$ is positive, this indicates that $F_{n_{NO\,spring}}$ is less than $F_{n_{desired}} = 20N$ and a return spring is necessary (see Figure 5.4, right hand side, for the positive data only).
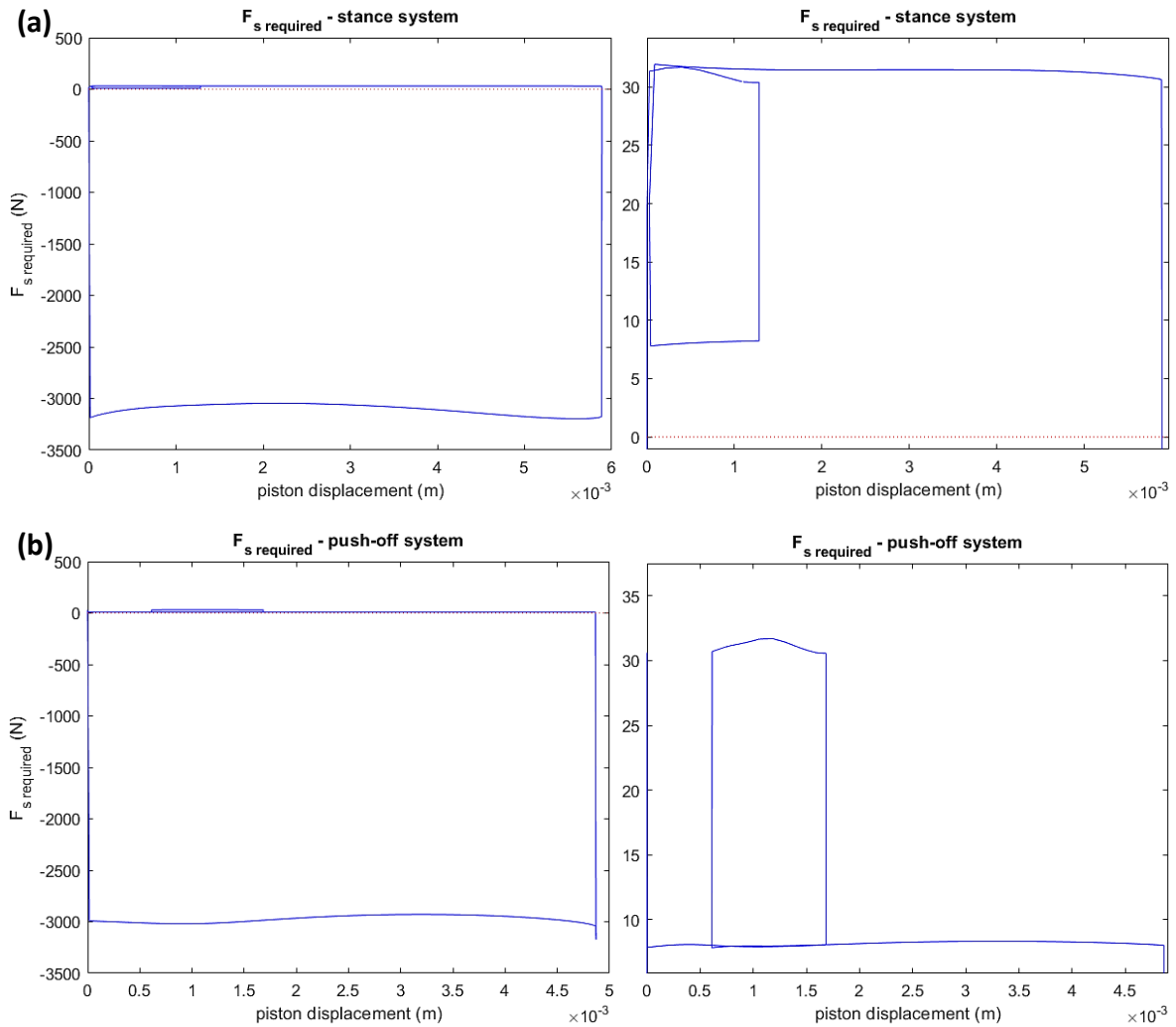
Figure 5.4 On the left, $F_{s_{required}}$ plotted against piston displacement throughout the gait cycle. On the right, only the positive values are plotted. The two plots at the top (a) refer to the stance system; the two plots at the bottom (b) to the push-off system.

Linear follower return springs were then specified such that the spring force always equals or exceeds $F_{s_{required}}$ (Figure 5.4, right hand side), with a slope larger than zero to be consistent with the physical meaning of spring stiffness, and which minimises the area included between itself and the upper $F_{s_{required}}$ curve. In other words, the following mathematical constraints and objective function were imposed:

$$F_s = ky + y_0 \qquad (5.7)$$

$$F_s \geq F_{s_{required}} \text{ at each time instant}$$

$$0 < k < 500{,}000 \; N/m$$

$$minimise \int (F_s - F_{s\,required})dy$$

The stiffness (i.e. slope) was constrained to be less than $500{,}000 \; N/m$ to provide an upper bound for the search algorithm. To provide a lower bound for the intercept y_0, it was constrained to be greater than or equal to $max(F_{s\,required})$ at zero piston displacement, which explicitly guarantees $F_s \geq F_{s\,required}$ at zero piston displacement. To provide an upper bound, the intercept y_0 was constrained to be less than the peak value of the required spring force ($y_0 < max(F_{s\,required})$), which guarantees that a spring characteristic can be found which makes contact with the peak value of the $F_{s\,required}$ curve given $k > 0$, thus minimising $\int (F_s - F_{s\,required})dy$.

A search algorithm was implemented, which applies the bounds defined above and, for each value of the intercept y_0, finds the smallest value of the slope k that satisfies the constraint $F_s \geq F_{s\,required}$ at each time instant. This is the value of k which leads to the spring characteristic just making contact with the $max(F_{s\,required})$ curve. Then, from the resulting set of alternative springs (k, y_0), the one that minimises the objective function ($\int (F_s - F_{s\,required})dy$) is selected.

Using this algorithm, the best two follower return springs were found to be:
   a) Stance cam-ram: $k_{STANCE} = 461.80 \; N/m$ and $y_{0_{STANCE}} = 31.90 \; N$;
   b) Push-off cam-ram: $k_{PO} = 66.50 \; N/m$ and $y_{0_{PO}} = 31.61 \; N$.

Figure 5.5 shows these spring characteristics (red solid line) superimposed on the $F_{s\,required}$ plots (blue solid line).

In the second iteration, these follower return springs were included and the simulation model run to evaluate the normal cam forces over the whole gait cycle. Referring to Figure 5.6, the normal force F_n is always larger than the chosen minimum value $F_{n_{desired}} = 20N$. The minimum value of F_n was less than $22N$ and, given the fact that the chosen value of $20N$ was

to some extent arbitrary, it was not considered necessary to run more iterations to further reduce the objective function.
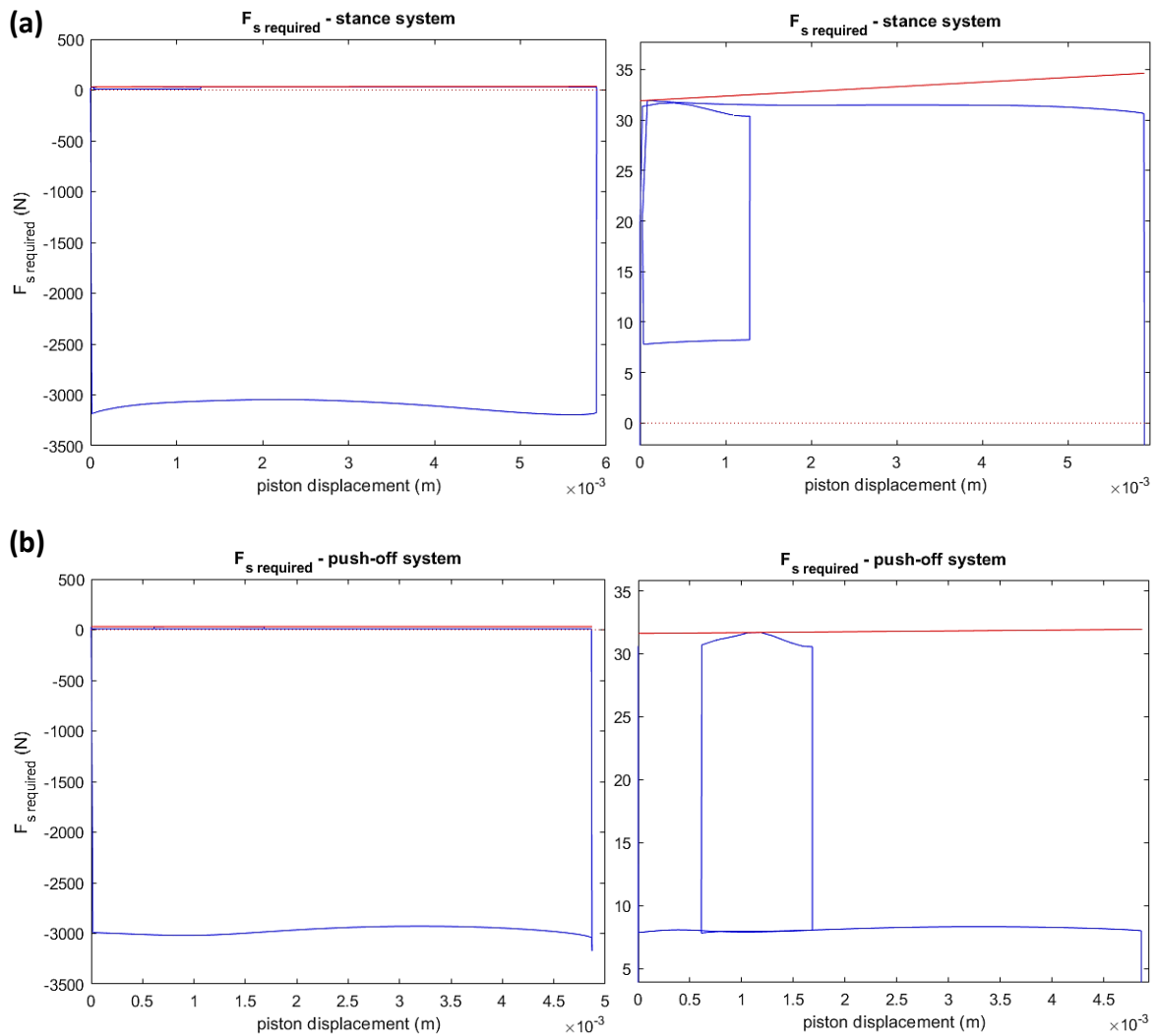
Figure 5.5 On the left, $F_{s_{required}}$ (blue solid line) and the actual spring force F_s (red solid line) plotted against piston displacement throughout the gait cycle. On the right, only the positive values of $F_{s_{required}}$ together with F_s are plotted. The two plots at the top (a) refer to the stance system; the two plots at the bottom (b) to the push-off system.

134

(a)

(b)
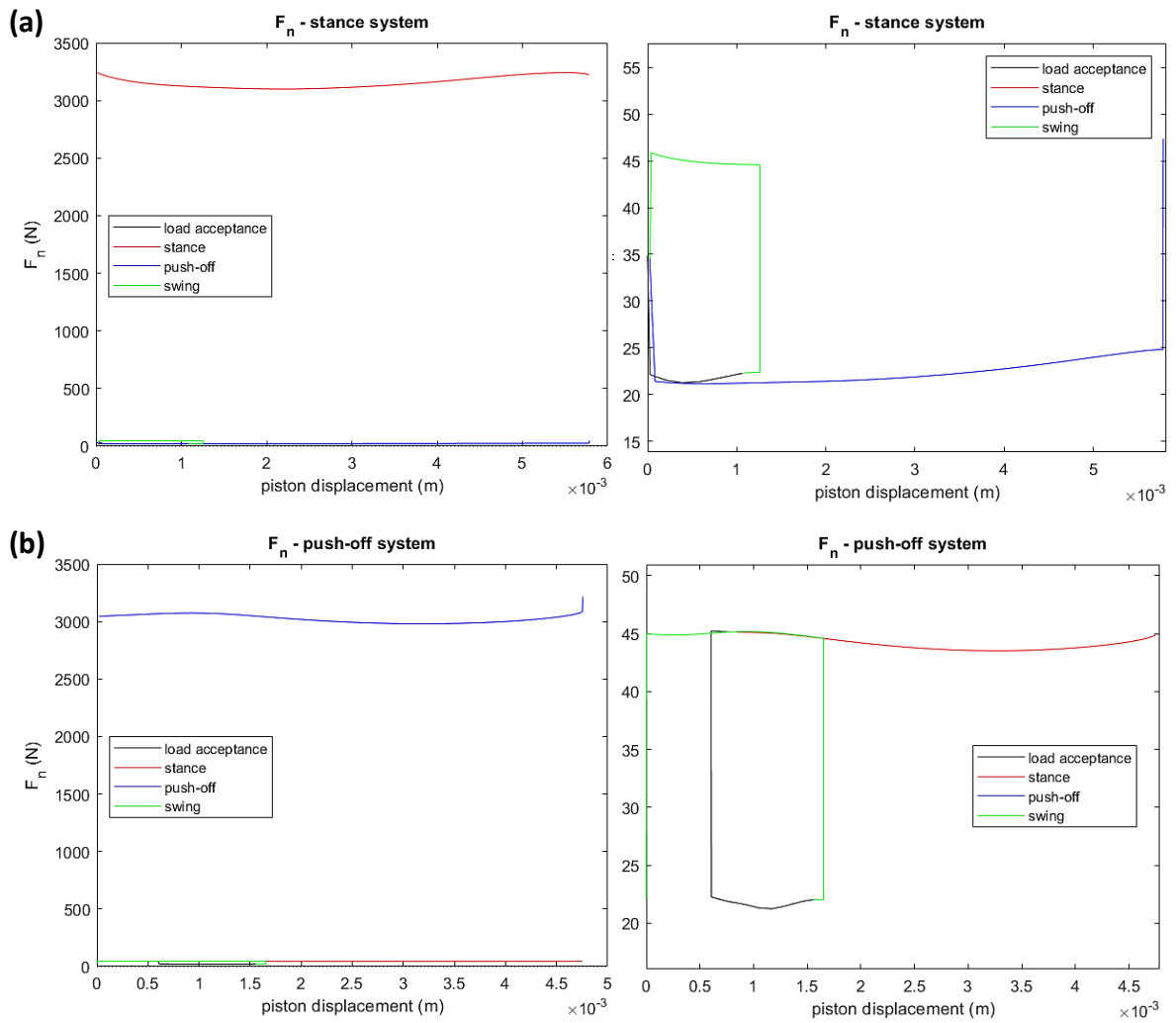
Figure 5.6 On the left, plots of the normal force F_n between cam and roller after the introduction of the return spring. On the right, only the smallest values are plotted to check that they are larger than $20N$. The two plots at the top (a) refer to the stance system; the two plots at the bottom (b) to the push-off system.

5.3   Power audit

A power audit was undertaken as a verification that the whole system has been modelled correctly, obeying the laws of physics, over the whole gait cycle. This was done because the mathematical modelling, upon which the simulation is based, used a Newton-Euler approach and, therefore, using an alternative energy approach provides a somewhat independent check that the underlying physics has been correctly modelled. The power balance was assessed for each component of the system, considering power input, power output, all losses, and the rate of change of energy stored in the component. All power terms are considered positive when power flows into the component so that the sum of all the power terms is equal to the rate of change of the stored energy (see equation (5.8) and Figure 5.7). Therefore, power losses are always negative as they involve energy flowing to the external environment in the form of heat.

$$P_{out} + P_{in} + P_{loss_1} + P_{loss_2} = \frac{\partial E_{stored}}{\partial t} \tag{5.8}$$
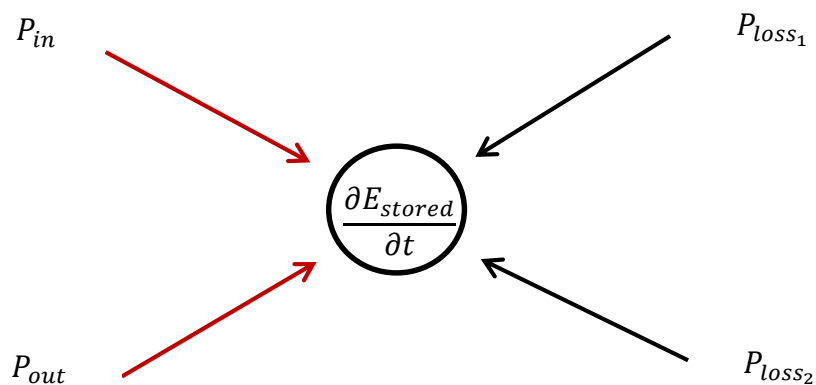
Figure 5.7 Power balance for each component of the system. Subscripts "in" and "out" refer to a power flow on the ankle side of the component and on the accumulator side respectively.

The subscripts "in" and "out" associated with the power terms in equation (5.8) have their normal meanings when power flows from the ankle towards the accumulator. In other words, "in" refers to a power flow on the ankle side of the component and "out" refers to a power flow on the accumulator side of the component, regardless of the actual power flow direction. In this way, the signs look after themselves in every phase of the gait cycle.

The power audit equations for each component were derived by evaluating P_{in} as defined below, and P_{out} is obtained by rearranging equation (5.8) as follows:

$$P_{out} = -P_{in} - P_{loss_1} - P_{loss_2} + \frac{\partial E_{stored}}{\partial t} \qquad (5.9)$$

The power audit equations for each component, as they were implemented in MATLAB, are presented below.

5.3.1 Ankle and Parallel spring

$$P_{in_{ps}} = T_a \omega_a \qquad (5.10)$$

$$\frac{\partial E_{ps}}{\partial t} = T_{ps} \omega_a \qquad (5.11)$$

$$P_{out_{ps}} = -P_{in_{ps}} + \frac{\partial E_{ps}}{\partial t} \qquad (5.12)$$

5.3.2 Gearbox

$$P_{in_{gb}} = (T_a - T_{ps})\omega_a \qquad (5.13)$$

$$P_{fr_{gb}} = -T_f \omega_a \qquad (5.14)$$

$$P_{out_{gb}} = -P_{in_{gb}} - P_{fr_{gb}} \qquad (5.15)$$

5.3.3 Camshaft and individual cams

$$P_{in_{cam\,shaft}} = (T_{c_{STANCE}} + T_{c_{PO}})\omega_c \qquad (5.16)$$

From this point on, the two cam-ram systems are dealt with separately. Therefore, the following equations apply:

$$P_{in_{cam}} = T_{c_{STANCE}}\omega_c \qquad \text{or} \qquad P_{in_{cam}} = T_{c_{PO}}\omega_c \tag{5.17}$$

$$P_{out_{cam}} = -P_{in_{cam}} \tag{5.18}$$

where the torque applied to the cam (T_c) by the camshaft has the opposite sign to the torque exerted on the cam profile by the roller (see equation (4.50)).

5.3.4 Rolling resistance element

$$P_{in_{rolres}} = F_n\dot{y}\cos\alpha + F_t(\dot{\beta}r + \dot{y}\sin\alpha) - M_{rolres}\omega_c \tag{5.19}$$

$$P_{fr_{rolres}} = -M_{rolres}\omega_{rel} = -M_{rolres}(\dot{\beta} - \omega_c) \tag{5.20}$$

$$P_{out_{rolres}} = -P_{in_{rolres}} - P_{fr_{rolres}} \tag{5.21}$$

This is not a real component, but a virtual one necessary to correctly describe the rolling resistance phenomenon between cam surface and roller (see Appendix A.2 for a complete explanation).

5.3.5 Roller

$$P_{in_{rol}} = F_n\dot{y}\cos\alpha + F_t(\dot{\beta}r + \dot{y}\sin\alpha) - M_{rolres}\dot{\beta} \tag{5.22}$$

$$P_{fr_{rol}} = -M_{brg}\dot{\beta} \tag{5.23}$$

$$\frac{\partial(ke)_{rol}}{\partial t} = \frac{\partial}{\partial t}\left(\frac{1}{2}m\dot{y}^2 + \frac{1}{2}I_{rol}\dot{\beta}^2\right) = m\dot{y}\ddot{y} + I_{rol}\dot{\beta}\ddot{\beta} \tag{5.24}$$

$$\frac{\partial(pe)_{rol}}{\partial t} = \frac{\partial}{\partial t}(mgy) = mg\dot{y} \tag{5.25}$$

$$P_{out_{rol}} = -P_{in_{rol}} - P_{fr_{rol}} + \frac{\partial(ke)_{rol}}{\partial t} + \frac{\partial(pe)_{rol}}{\partial t} \tag{5.26}$$

5.3.6 Follower

$$P_{in_{fol}} = R_V\dot{y} \tag{5.27}$$

$$P_{fr_{fol}} = -F_{fr_{guide}}\dot{y} \tag{5.28}$$

$$\frac{\partial(ke)_{fol}}{\partial t} = \frac{\partial}{\partial t}\left(\frac{1}{2}M\dot{y}^2\right) = M\dot{y}\ddot{y} \tag{5.29}$$

$$\frac{\partial(pe)_{fol}}{\partial t} = \frac{\partial}{\partial t}(Mgy) = Mg\dot{y} \tag{5.30}$$

$$\frac{\partial E_{rs}}{\partial t} = F_s\dot{y} = (ky + y_0)\dot{y} \tag{5.31}$$

$$P_{out_{fol}} = -P_{in_{fol}} - P_{fr_{fol}} + \frac{\partial(ke)_{fol}}{\partial t} + \frac{\partial(pe)_{fol}}{\partial t} + \frac{\partial E_{rs}}{\partial t} \tag{5.32}$$

where $F_{fr_{guide}} = F_{fr1} + F_{fr2}$ is the total friction at the follower guide, and $\frac{\partial E_{rs}}{\partial t}$ is the rate of change of energy stored in the follower return spring.

5.3.7 Cylinder (including pipes and discrete components)

$$P_{in_{cyl}} = (F_h + P_{atm}A)\dot{y} \tag{5.33}$$

$$P_{fr_{cyl}} = -F_{fr_{cyl}}\dot{y} \tag{5.34}$$

$$P_{losses_{cyl}} = -Q\Delta P =$$

$$= -Q\Delta P_{to\ acc} \quad \text{during working phases (WP)} \tag{5.35}$$

$$= -Q\Delta P_{to\ tank} \quad \text{during non-working phases (NWP)} \tag{5.36}$$

$$\frac{\partial E_{oil_{cyl}}}{\partial t} = -P_{cyl}\dot{V}_{\beta_{cyl}} =$$

$$= \begin{cases} 0 & \text{during load acceptance} \\ -\left(P_{cyl}\dot{V}_{\beta_{cyl}}\right)_{STANCE} & \text{during WP of the stance system} \\ -\left(P_{cyl}\dot{V}_{\beta_{cyl}}\right)_{PO} & \text{during WP of the push-off system} \\ 0 & \text{during swing} \end{cases} \tag{5.37}$$

$$P_{out_{cyl}} = -P_{in_{cyl}} - P_{fr_{cyl}} - P_{losses_{cyl}} + \frac{\partial E_{oil_{cyl}}}{\partial t} \tag{5.38}$$

where: $F_{fr_{cyl}}$ is the piston O-ring friction; ΔP is the pressure drop due to fluid friction in valves, pipes and fittings; and $\frac{\partial E_{oil_{cyl}}}{\partial t}$ is the rate of change of strain energy in the cylinder oil due to oil compressibility. The minus sign in the P_{losses} expression is necessary because the product $(Q\Delta P)$ is always positive, given the sign of ΔP (see equation (4.64)). The follower and piston are treated as a single body and, hence, their masses combined. For this reason, kinetic and

potential energy variations due to the piston translating inside the cylinder are taken into account in the follower power audit above.

5.3.8 Accumulator

$$P_{in_{acc}} = (Q + \dot{V}_{\beta_{cyl}})P_{acc} =$$

$$= \begin{cases} 0 & \text{during load acceptance} \\ (Q + \dot{V}_{\beta_{cyl}})_{STANCE}P_{acc} & \text{during WP of the stance system} \\ (Q + \dot{V}_{\beta_{cyl}})_{PO}P_{acc} & \text{during WP of the push-off system} \\ 0 & \text{during swing} \end{cases} \qquad (5.39)$$

$$P_{loss_{HEAT}} = h_{N_2}A_w(T_{wall} - T_{gas}) \qquad (5.40)$$

$$\frac{\partial E_{oil_{acc}}}{\partial t} = -P_{acc}\dot{V}_{\beta_{acc}} \qquad (5.41)$$

$$\frac{\partial E_{gas_{acc}}}{\partial t} = \frac{5}{2}nR\frac{dT}{dt} \qquad (5.42)$$

$$P_{in_{acc}} + P_{loss_{HEAT}} = \frac{\partial E_{oil_{acc}}}{\partial t} + \frac{\partial E_{gas_{acc}}}{\partial t} \qquad (5.43)$$

where: $P_{loss_{HEAT}}$ is the power lost due to heat transfer from the accumulator to the surrounding environment; h_{N_2} is the convection heat transfer coefficient for nitrogen; A_W the internal surface area of the accumulator exposed to gas for heat transfer (see Appendix A.5); $\frac{\partial E_{oil_{acc}}}{\partial t}$ is the rate of change of strain energy in the accumulator oil due to oil compressibility; and $\frac{5}{2}nRT$ is the energy stored in a diatomic gas such as nitrogen.

5.3.9 Tank

$$P_{in_{tank}} = QP_{atm} =$$

$$= \begin{cases} (Q_{STANCE} + Q_{PO})P_{atm} & \text{during load acceptance} \\ Q_{PO}P_{atm} & \text{during WP of the stance system} \\ Q_{STANCE}P_{atm} & \text{during WP of the push-off system} \\ (Q_{STANCE} + Q_{PO})P_{atm} & \text{during swing} \end{cases} \qquad (5.44)$$

$$P_{loss_{tank}} = -P_{in_{tank}} \qquad \text{when } P_{in_{tank}} \geq 0 \qquad (5.45)$$

$$P_{loss_{tank}} = 0 \qquad \text{when } P_{in_{tank}} < 0$$

5.3.10 Power residuals

If the whole system has been modelled correctly, obeying the laws of physics, over the whole gait cycle, then the power output from one component is equal to the power input to the next component. Specifically, given the sign convention adopted here (see equation (5.8) and Figure 5.7):

$$P_{in_k} = -P_{out_{k-1}} \tag{5.46}$$

Or to calculate the residual that should be very small:

$$residual = P_{in_k} + P_{out_{k-1}} \cong 0 \tag{5.47}$$

This leads to the following power residual equations for each component:

$$residual_{ps-gb} = P_{in_{gb}} + P_{out_{ps}} \tag{5.48}$$

$$residual_{gb-cam\ shaft} = P_{in_{cam\ shaft}} + P_{out_{gb}} \tag{5.49}$$

where: $\quad P_{in_{cam\ shaft}} = (T_{c_{STANCE}} + T_{c_{PO}})\omega_c$

$$residual_{cam-rolres} = P_{in_{rolres}} + P_{out_{cam}} \tag{5.50}$$

$$residual_{rolres-rol} = P_{in_{rol}} + P_{out_{rolres}} \tag{5.51}$$

$$residual_{rol-fol} = P_{in_{fol}} + P_{out_{rol}} \tag{5.52}$$

$$residual_{fol-cyl} = P_{in_{cyl}} - [(P_{atm}A)\dot{y}] + P_{out_{fol}} \tag{5.53}$$

$$residual_{cyl-acc} = P_{in_{acc}} + P_{out_{cyl}} \tag{5.54}$$

where: $P_{out_{cyl}} = \begin{cases} 0 & \text{during load acceptance} \\ P_{out_{cyl_{STANCE}}} & \text{during WP of the stance system} \\ P_{out_{cyl_{PO}}} & \text{during WP of the push-off system} \\ 0 & \text{during swing} \end{cases}$

$$residual_{cyl-tank} = P_{in_{tank}} + P_{out_{cyl}} \tag{5.55}$$

where:

$P_{out_{cyl}} = \begin{cases} P_{out_{cyl_{STANCE}}} + P_{out_{cyl_{PO}}} & \text{during load acceptance} \\ P_{out_{cyl_{PO}}} & \text{during WP of the stance system} \\ P_{out_{cyl_{STANCE}}} & \text{during WP of the push-off system} \\ P_{out_{cyl_{STANCE}}} + P_{out_{cyl_{PO}}} & \text{during swing} \end{cases}$

These residual equations and the individual power terms for each component were implemented in MATLAB. The cam-ram power equations in sections 5.3.3 to 5.3.7 and also equations (5.50) - (5.53) above were implemented twice for the stance and push-off systems.

Figure 5.8 to Figure 5.13 show the results derived from the power residual equations. Referring to Figure 5.3, to put these in perspective, the push-off peak power is about 190W. Therefore, these results confirm that the entire system has been modelled correctly over the whole gait cycle as they all show an order of magnitude of $1e-14$, except for the one between the two cylinders and the accumulator, the order of magnitude of which is $1e-6$.
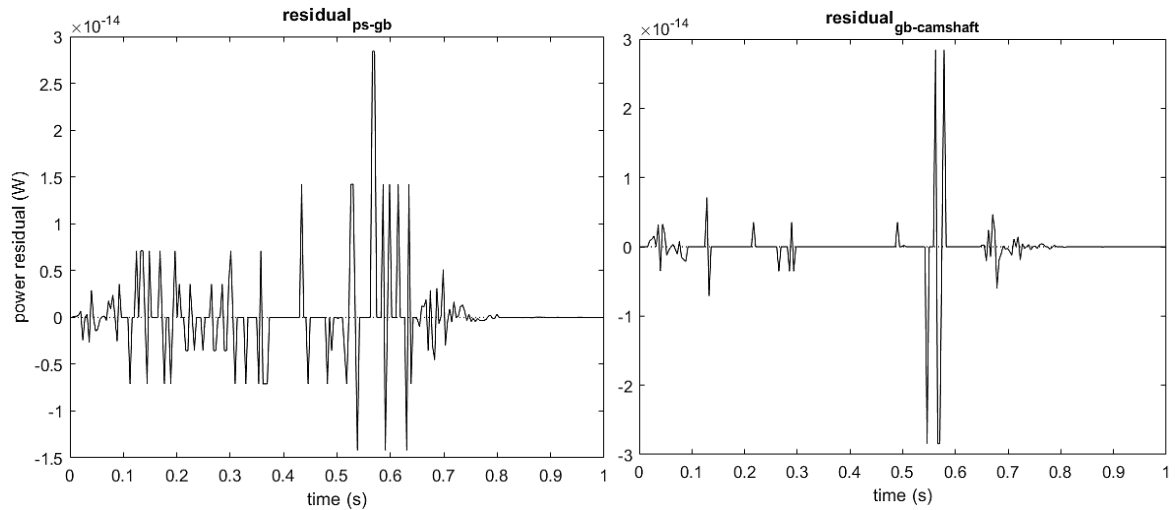
Figure 5.8 Power residuals between the parallel spring and the gearbox on the left, and between the gearbox and the camshaft on the right. Power in Watts.
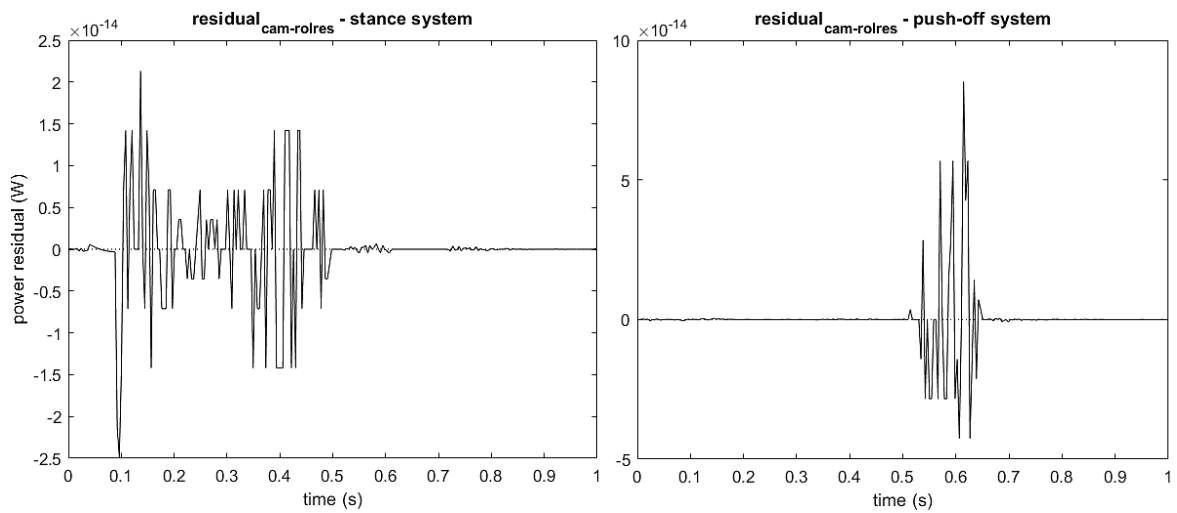
Figure 5.9 Power residuals between the cam and the rolling resistance element in the stance cam-ram system on the left, and in the push-off cam-ram system on the right. Power in Watts.
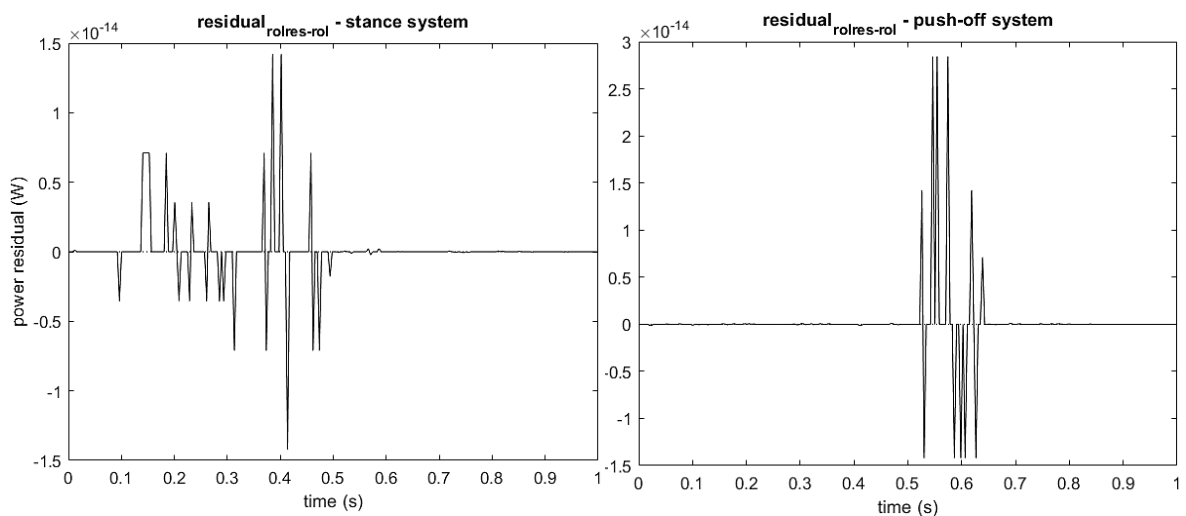
Figure 5.10 Power residuals between the rolling resistance element and the roller in the stance cam-ram system on the left, and in the push-off cam-ram system on the right. Power in Watts.

143
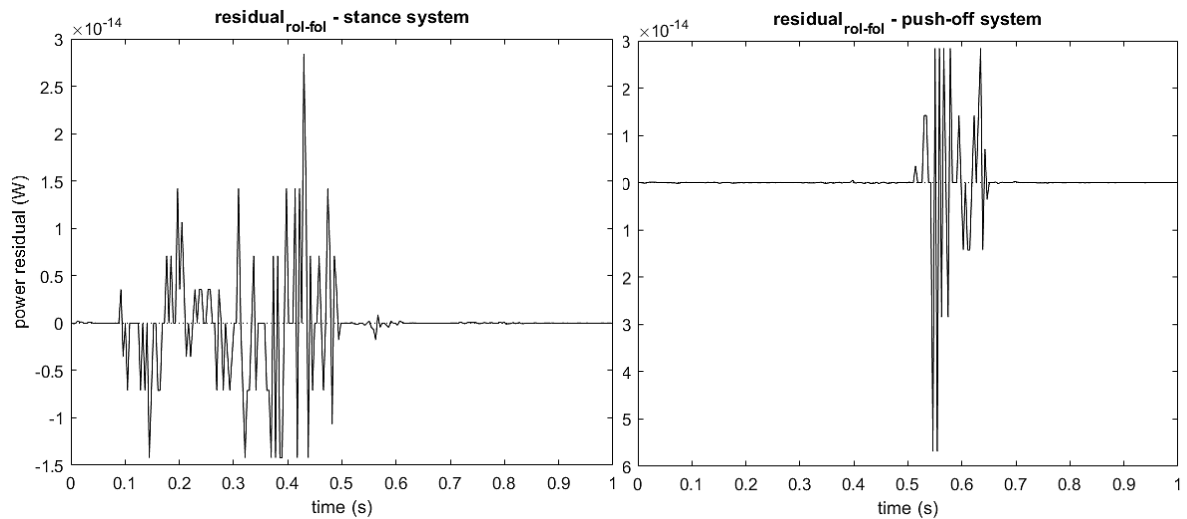
Figure 5.11 Power residuals between the roller and the follower in the stance cam-ram system on the left, and in the push-off cam-ram system on the right. Power in Watts.
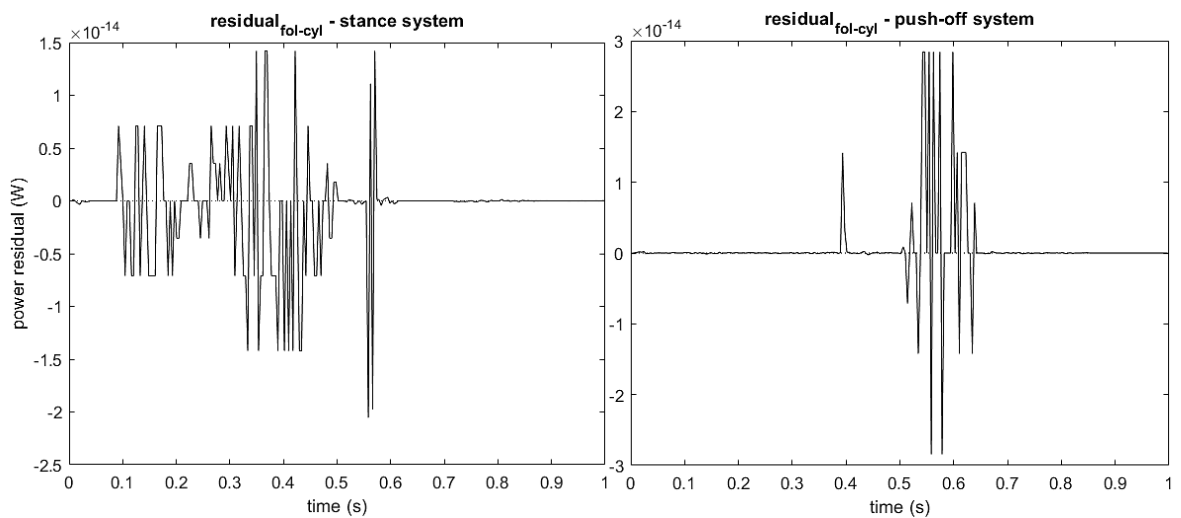
Figure 5.12 Power residuals between the follower and the cylinder in the stance cam-ram system on the left, and in the push-off cam-ram system on the right. Power in Watts.
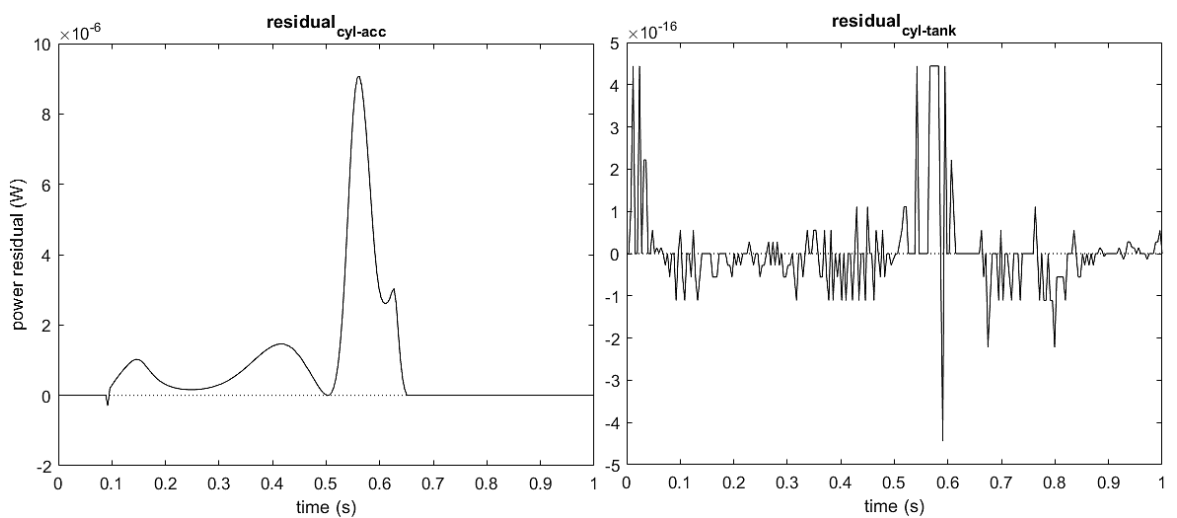
Figure 5.13 Power residuals between the two cylinders and the accumulator on the left, and the two cylinders and the tank on the right. Power in Watts.

144

6. Chapter 6: Cam-ram design
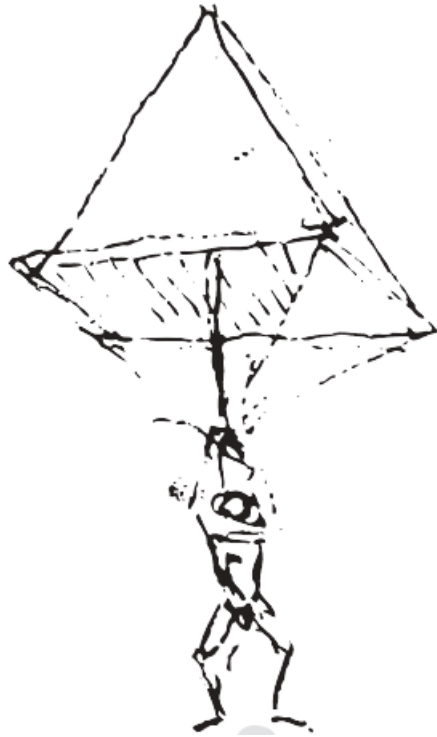
Leonardo da Vinci (c. 1485), Parachute, Codex Atlanticus

"No effect is in nature without reason;
you understand the reason and you don't need experience."

(Leonardo Da Vinci)

In this chapter, the process followed for the preliminary design of the two cam-ram systems is illustrated. It was assumed that the cam-ram performances in their working phases would dominate the design decisions because the power flows are much greater than in their non-working phases, when the cam-rams simply overcome frictional losses. Therefore, the two systems were designed to achieve good performances in their working phases only. In other words, the stance cam-ram system was designed for the stance phase prior to push-off (i.e. from foot flat to maximum dorsiflexion at the start of push-off), and the push-off cam-ram was designed for the push-off phase (i.e. from maximum dorsiflexion to toe-off prior to swing).

An early stage simulation model was used that only modelled the friction losses directly associated with the two cam-rams during their working phases. This model neglected the cam-ram losses in their non-working phases, major and minor flow losses, losses in the accumulator, and the two follower return springs, because it was assumed these would have little effect on the selected cam-ram design parameters.

In order to conduct the preliminary design, firstly, all of the design parameters were classified to identify the primary and secondary independent design variables. The following two sections cover categorisation of the design parameters and the preliminary design process respectively.

Note that, in this chapter, dimensions are shown in millimetres because of the qualitative nature of size related design decisions.

6.1   Categorisation of the design parameters

The various design parameters were divided into three categories: constants, *independent* variables, and *dependent* variables. The independent variables can be further split into "primary" and "secondary" independent variables. The primary ones are those which largely affect the magnitude of the forces acting on the cam-ram components, such as the cam, roller, follower, and the bearings associated with them, which in turn determines the selection of these components, and specifically their size, so that they can withstand those forces. Furthermore, because they determine the forces in the system, these primary independent

variables were also expected to have a major effect on the energy efficiency of the system. The secondary independent variables do not have a strong effect on the size of the cam-ram components, but were still expected to influence energy efficiency and, to a lesser extent, overall dimensions.

Through a process of brainstorming and with the aim of minimising the number of primary independent variables, to simplify the design investigation, three primary independent variables that most directly influence the forces acting on the cam-ram components were identified:

- Gearbox ratio.

- Maximum hydraulic pressure in the accumulator.

- Hydraulic ram bore.

The gearbox is placed in between the ankle and the cam-shaft, in parallel to the spring. Therefore, it determines the cam-shaft torque and changing its ratio has a direct effect on the forces acting on the cam-ram components. Similarly, the maximum hydraulic pressure and the ram bore determine the hydraulic force acting on the piston and, in turn, the forces acting on the other cam-ram components.

Possible values for these three variables were selected based on upper or lower limits that were thought to provide sensible constraints on the size of the components. A minimum gearbox ratio of one corresponds to having no gearbox in the system and, consequently, zero gearbox losses and a simpler design, which would be a significant advantage. Two higher ratios are included in case a ratio of one leads to forces and, hence, cam-ram component sizes that are too large. The ram bores were chosen to limit the size of the device, which should be part of a lower-limb prosthesis the size and weight of which is no more than an intact limb. Therefore, the maximum bore chosen was $20mm$. The minimum bore of $5mm$ was chosen to avoid the efficiency penalties associated with even smaller hydraulic rams (Durfee *et al.*, 2011; Xia *et al.*, 2011; Xia & Durfee, 2011a, 2011b, 2014). Neubauer *et al.* (2014) used a ram bore of approximately $13mm$ in their hydraulic ankle-foot orthosis. They also used pressures around $100bar$ demonstrating that this is practically feasible. Furthermore, industrial hydraulic systems typically operate at pressures of up to $200bar$. Hence, for this application, $100bar$

was set as the upper limit with two smaller values of $20bar$ and $50bar$. These values are summarised in Table 6.1.

gearbox ratio GR	max pressure P_{max} (bar)	ram bore D (mm)
1	20	5
3	50	10
5	100	20

Table 6.1 The alternative values chosen for each of the three primary independent variables.

Different combinations of these values of the three primary independent variables result in quite different configurations of the two cam-ram systems, which are investigated in detail in subsection 6.2.1.

The secondary independent variables include:
- Lowest position of the follower, a, as shown in Figure 4.3;
- Follower offset, e, as shown in Figure 4.3;
- Residual length $= 5mm$ (clearance) when the piston has completed its instroke;
- Diameter, $D_{pipe} = 5mm$, of the pipes connecting the hydraulic rams to the accumulator;
- Length, $L_{pipe} = 50mm$, of the pipes between the hydraulic rams and accumulator;
- Accumulator volume, $V_A = 250cc$.

Residual length has been given an arbitrary but realistic value of $5mm$ because it has no effect on system performance. Pipe diameter ($5mm$) and length ($50mm$) were considered realistic and it was also assumed that the flow losses would have a negligible effect on the working phase performances of the cam-rams, during which power flows are large. Therefore, their effect on performance over the whole gait cycle is studied in Chapter 7, where a sensitivity study for design parameters not considered here and physical constants is reported. The accumulator volume has been given an arbitrary but realistic value of $250cc$ (as explained in section 3.4.3). This is relatively small with respect to the pylon, its envisaged location, and was thought to be a realistic level of miniaturisation. This is also large enough to store energy over

many gait cycles, for later use when climbing a slope, but this has not been studied in this thesis.

Therefore, after reducing the number of possibilities for the primary variables (subsection 6.2.1), the two remaining secondary independent variables, a and e, that have an effect on the working phase performances of the two cam-rams, were investigated (subsection 6.2.3).

Appendix D shows the complete table of constants, *independen*t variables (primary and secondary), and *dependent* variables.

6.2   Preliminary design investigation

After categorising the design parameters, a preliminary design investigation was conducted, which included four main steps:

1.   Given the chosen set of values for the three primary independent variables (Table 6.1), a subset of feasible designs was identified by eliminating designs that are unrealistic in terms of size.

2.   For the feasible designs, roller diameters (i.e. a dependent variable) that can withstand the cam-roller contact forces were found.

3.   For the feasible designs, good values for the two secondary independent variables, a and e, were found.

4.   The feasible designs, with all independent variables determined, were compared in terms of their energy losses.

The following design constraints were defined for variables involved in the preliminary design investigation, noting that these should not be too small to avoid pre-empting the results of the design study:

•   To limit the overall size of the cam-rams to fit within the length of the pylon, the total length of the hydraulic ram when the piston is at the end of its outstroke should be no more than $150mm$. The total length is the sum of the ram length for zero stroke (i.e. the sum of the component lengths) and the piston stroke. Based on hydraulic cylinder catalogues (HYDAIRA (p. 13) for instance), a cylinder for pressures up to $100bar$ has a zero

stroke length of approximately $100mm$. Therefore, the maximum stroke was set to $50mm$.

- To limit the overall size of the cam-rams, the upper limit both for the offset e and the distance a (see Figure 4.3) was set to $a_{max} = e_{max} = 50mm$

- Given the above, it seemed reasonable to set a maximum roller diameter of $d_{roller_{max}} = 30mm$.

- To avoid high lateral forces and, hence, high follower friction, cam design handbooks generally suggest limiting the pressure angle to 30°, although with a rigid follower, strong follower bearings, and a small follower overhang, the maximum pressure angle may be increased (Rothbart, 2004). Also Realmuto *et al.* (2015) used the same 30° limit in the design of their powered ankle prosthesis. Therefore, in this work, the same maximum cam pressure angle was used ($|\alpha|_{max} = 30°$).

6.2.1   Step 1 – Determine a subset of feasible designs (primary independent variables)

The set of values for the three primary independent variables (Table 6.1) was used as starting point of the design investigation. Therefore, twenty-seven different combinations of the primary independent variables were possible. However, it seemed sensible to start with a gearbox ratio of $GR = 1$, corresponding to a system with no gearbox, to avoid energy losses due to gearbox friction and simplify the design. This reduced considerably the number of combinations to be analysed: from twenty-seven to nine.

For each one of the nine combinations, the length of the piston stroke was estimated for both cam-ram systems to exclude those combinations with a stroke greater than the $50mm$ upper limit. Neglecting all losses, the stroke length was estimated by considering the negative ankle work done during the working phase of the stance system and, hence, the corresponding energy to be stored in the accumulator; and also the positive ankle work done during the working phase of the push-off system and, hence, the corresponding energy to be released from the accumulator. The total work done by the hydraulic rams over their working phases is $W = F_{h_{nominal}} \cdot stroke_{nominal}$. Rearranging for piston stroke gives:

$$stroke_{nominal} = \frac{W}{F_{h_{nominal}}} \tag{6.1}$$

Where, assuming a constant accumulator pressure,

$$F_{h_{nominal}} = P_{max} * A = P_{max} * \pi \left(\frac{D}{2}\right)^2 \tag{6.2}$$

Firstly, considering the stance system in its working phase, the corresponding negative work done by an anatomically intact ankle (see Figure 2.2) was evaluated by numerically integrating ankle power based on the data collected by Bari (2013) for healthy level walking at a self-selected speed, which was also used as input to the simulation model described in the previous chapter. The energy stored during the working phase of the stance system amounts to approximately $18.9J$, and substituting this in equation (6.1) together with the maximum hydraulic pressure (P_{max}) and the ram bore (D), from Table 6.1, the results shown in Table 6.2 were obtained.

	P_{max} (bar)		
D (mm)	100	50	20
20	**6**	**12**	**30**
10	**24**	**48**	120
5	96	193	481

Table 6.2 Nominal stroke length (mm) for the piston of the stance system.

The same calculation was repeated for the push-off system. The energy released during the working phase of the push-off system amounts to approximately $11.9J$, and substituting this in equation (6.1) together with the maximum hydraulic pressure (P_{max}) and the ram bore (D), from Table 6.1, the results shown in Table 6.3 were obtained.

	P_{max} (bar)		
D (mm)	100	50	20
20	**4**	**8**	**19**
10	**15**	**30**	76
5	61	121	303

Table 6.3 Nominal stroke length (mm) for the piston of the push-off system.

The five bold values in Table 6.2 and Table 6.3 are those combinations with a stroke that is less than the maximum allowed (i.e. $50mm$). These combinations of the primary independent variables were carried forward for the following analyses.

6.2.2   Step 2 – Determine the roller diameters

For each of the five selected combinations, the nominal (maximum) hydraulic force ($F_{h_{nominal}}$) acting on the ram was calculated according to equation (6.2). It was then used as an input to the MATLAB simulation model described in Chapter 5 to obtain the corresponding maximum value of the normal force acting between the cam and the roller over the working phase ($F_{n_{nominal}}$). Then, from catalogues SKF (2013) for rollers with a diameter bigger than $16mm$; IKO (2016) and IKO (2017) for rollers with a diameter smaller than $16mm$), the minimum roller diameter able to withstand that force was identified, based on the quoted maximum dynamic radial loads. So, in this context, it should be noted that roller diameter is a dependent design variable.

To run the MATLAB simulation model for the first time (to get $F_{n_{nominal}}$), an initial roller diameter is required, which was set to $26mm$ because that was the largest available (SKF, 2013) that satisfied the constraint $d_{roller} \leq 30mm$. In addition, different stud diameters are offered for the same roller diameter and, therefore, the largest stud diameter was used to be conservative, because it generates the largest friction moment (see equation (4.35) in subsection 4.3.3). Also, arbitrary values for distance a ($40mm$) and offset e ($15mm$) were used at this stage. Moreover, to be conservative, the initial system pressure in these simulations was equal to the maximum pressure ($P_{start} = P_{max}$), instead of $P_{start} = 0.90 * P_{max}$.

Given the maximum value of the normal force during the working phase ($F_{n_{nominal}}$), the minimum roller diameter d_{roller} able to withstand that force is identified. If this minimum roller diameter d_{roller} exceeds the maximum available value ($26\,mm$) that satisfies the constraint ($d_{roller} \leq 30mm$), then the hydraulic ram force producing it would need to be decreased by decreasing either the maximum pressure P_{max} or the ram bore D (see equation (6.2)), before increasing the gearbox ratio to reduce camshaft torque. Once a satisfactory minimum roller diameter was found, it was used as input to the MATLAB simulation model, replacing $d_{roller} = 26mm$, to again evaluate $F_{n_{nominal}}$ acting between cam and roller over the working phase and, hence, check that the roller can withstand the recalculated load.

Table 6.4 shows the results of this process for both cam-ram systems, for the initial simulations (unbolded) and for the final simulations (bolded). In all cases, the roller diameter was decreased from the initial value of $26mm$ and the maximum normal force increased slightly, but this increase was not enough to require a change to the roller selection. There were negligible changes in the cam pressure angles and piston strokes, the latter being close to the approximate calculations in Table 6.2 and Table 6.3. All ten roller diameters are the same or smaller than the one used by Realmuto *et al.* (2015) for the cam-roller-follower system in their active ankle prosthesis: they used a roller with a diameter of $19mm$.

COMBINATIONS (primary indep. variables)	$F_{h_{nominal}}$ (N)	STANCE SYSTEM		PUSH-OFF SYSTEM	
		$F_{n_{nominal}}$ (N)	roller Ø (mm)	$F_{n_{nominal}}$ (N)	roller Ø (mm)
1. $GR = 1$, $P_{max} = 100bar$, $D = 20mm$	3141.59	3462.78	26	3373.79	26
		3506.82	**19**	**3409.62**	**19**
2. $GR = 1$, $P_{max} = 100bar$, $D = 10mm$	785.40	1735.32	26	1673.54	26
		1868.46	**16**	**1805.70**	**16**
3. $GR = 1$, $P_{max} = 50bar$, $D = 20mm$	1570.80	2301.52	26	2202.67	26
		2438.22	**16**	**2332.23**	**16**
4. $GR = 1$, $P_{max} = 50bar$, $D = 10mm$	392.70	1304.04	26	1260.70	26
		1391.51	**16**	**1344.50**	**16**
5. $GR = 1$, $P_{max} = 20bar$, $D = 20mm$	628.32	1624.37	26	1560.07	26
		1745.94	**16**	**1679.73**	**16**

Table 6.4 Determining roller diameters. Those combinations having a stroke length smaller than $50mm$ were analysed in terms of nominal hydraulic ram force and nominal normal force acting between the cam and the roller, and the roller diameter able to bear that force was found, both for the stance and the push-off system.

6.2.3   Step 3 – Determine the two secondary independent variables, a and e.

In this third step of the preliminary design investigation, the five feasible designs identified in the previous subsections ($stroke \leq 50mm$ and $d_{roller} \leq 30mm$) were further analysed to find good values for the two secondary independent variables, distance a and offset e. The main effect of these two variables is to change the geometry shown in Figure 4.3 and, hence, the cam pressure angle α (equation (4.31)). As stated at the beginning of this section, one of the design constraints is $|\alpha|_{max} = 30°$. Therefore the aim was to find values of a and e, with $a_{max} = e_{max} = 50mm$, which keep the cam pressure angle below 30° during the two cam-ram systems' working phases, while also reducing their dimensions as far as possible. All simulations in this third step use the correct roller diameter from the previous step.

The process implemented in MATLAB to identify good values for the two secondary independent variables a and e is as follows:

1. From the formula for cam pressure angle α (equation (4.31)), and given that a and y are always positive, it can be seen that increasing a has the effect of decreasing cam pressure angle α. Therefore, to minimise α and hence follower friction, initially the distance a was set to its upper limit ($a = a_{max} = 50mm$).

2. The offset e was adjusted to further minimise α. The following range of values for the offset e was considered:

$$e = [5, 10, 15, 20, 25, 30, 35, 40, 45, 50]\ (mm)$$

For each value of the offset e, the MATLAB simulation model was run to find the largest absolute value of the cam pressure angle, $\max(|\alpha|)$, during the working phase of the cam-ram. Closely spaced values of e were added near to the minimum for $\max(|\alpha|)$ to accurately determine the minimum and the corresponding optimum value of e.

3. Depending on the minimum value of $\max(|\alpha|)$, there were three options:

    i. If $\min(\max(|\alpha|)) \geq 30°$, that combination of the primary independent variables was eliminated.

    ii. If $\min(\max(|\alpha|))$ was close to $30°$ ($25° \leq \min(\max(|\alpha|)) < 30°$), that combination was considered acceptable with the current value of a and the optimum value of e.

    iii. If $\min(\max(|\alpha|)) \ll 30°$, smaller values of the distance a were tried to reduce the size of the cam-ram system. The MATLAB simulation model was run again with the new values of the distance a and for different values of the offset e to recalculate $\min(\max(|\alpha|))$ and the corresponding optimum value of e (i.e. stage 2 above was repeated for each new value of a).

STANCE SYSTEM

The stance system results of the first pass of the second stage described above (i.e. varying e with $a = a_{max} = 50mm$) are shown in Table 6.5. The first two columns show the design parameters inherited from the first two steps of the design investigation (sections 6.2.1 and

6.2.2). Columns 3 to 5 show the values of the distance a (always $50mm$ at this stage), the optimum offset e that minimises $\max(|\alpha|)$, and the corresponding minimum value of $\max(|\alpha|)$ respectively. The two rows with bold text (i.e. combinations 1 and 3) correspond to combinations of the primary independent variables that ensure $\max(|\alpha|) < 30°$, while the others do not and, therefore, they were excluded according to stage 3, rule i, above.

COMBINATION (primary indep. variables)	$roller\ Ø$ (mm)	$distance\ a$ (mm)	$offset\ e$ (mm)	$\mathbf{min(max(|\alpha|))}$ $(°)$
1. $\boldsymbol{GR = 1,}$ $\boldsymbol{P_{max} = 100bar,}$ $\boldsymbol{D = 20mm}$	**19**	**50**	**19**	**17.35**
2. $GR = 1$ $P_{max} = 100bar,$ $D = 10mm$	16	50	50	51.93
3. $\boldsymbol{GR = 1,}$ $\boldsymbol{P_{max} = 50bar,}$ $\boldsymbol{D = 20mm}$	**16**	**50**	**36**	**29.72**
4. $GR = 1,$ $P_{max} = 50bar,$ $D = 10mm$	16	50	50	67.18
5. $GR = 1,$ $P_{max} = 20bar,$ $D = 20mm$	16	50	50	55.97

Table 6.5 Optimising offset e – 1st pass. Stance system: those combinations having a stroke length smaller than $50mm$ were analysed with the correct roller diameter and for $\boldsymbol{a = 50mm}$. The offset $\boldsymbol{e}$ that minimises the maximum absolute cam pressure angle is shown (together with the pressure angle).

Combination 3 satisfied step 3, rule ii, and was therefore accepted for carrying forward to the final step of the design investigation (section 6.2.4). The results for this combination are summarised in Table 6.6, and Figure 6.1 shows the $\max(|\alpha|)$ trend when the offset e is varied, with the distance a fixed ($a = a_{max} = 50mm$). There is a clear minimum for $\max(|\alpha|)$ of 29.72°, which is just below the upper limit of 30°.

Combination 3:

	roller Ø (mm)	distance a (mm)	offset e (mm)	max(|α|) (°)
$GR = 1$, $P_{max} = 50bar$, $D = 20mm$	16	50	36	29.72

Table 6.6 Combination 3 for the stance system.
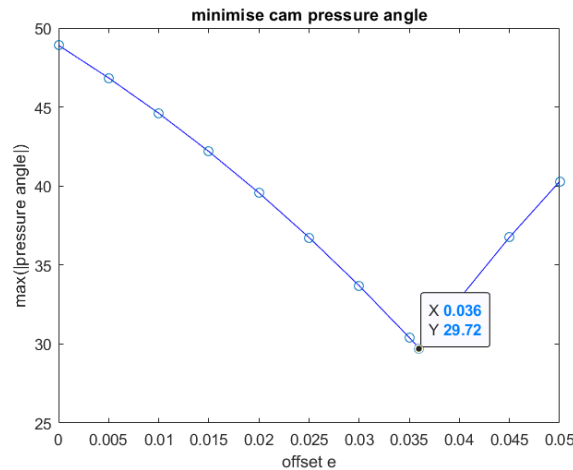
Figure 6.1 Combination 3 for the stance system: $\mathbf{max}(|\boldsymbol{\alpha}|)$ for different values of the offset $\boldsymbol{e}$ and for $\boldsymbol{a} = \mathbf{50mm}$.

Combination 1 resulted in a minimum for $max(|\alpha|)$ of 17.35° and, therefore, smaller values of the distance a were tried to reduce the size of the cam-ram system as dictated by stage 3, rule iii. This process is illustrated in Figure 6.2, with the numerical data for the successive minima shown in Table 6.7. To be conservative, $a = 26mm$ was eliminated and $a = 30mm, 40mm, 50mm$ were all carried forward to the final step of the design investigation (section 6.2.4) to see if there was a trade-off between size, specifically the distance a, and energy losses.
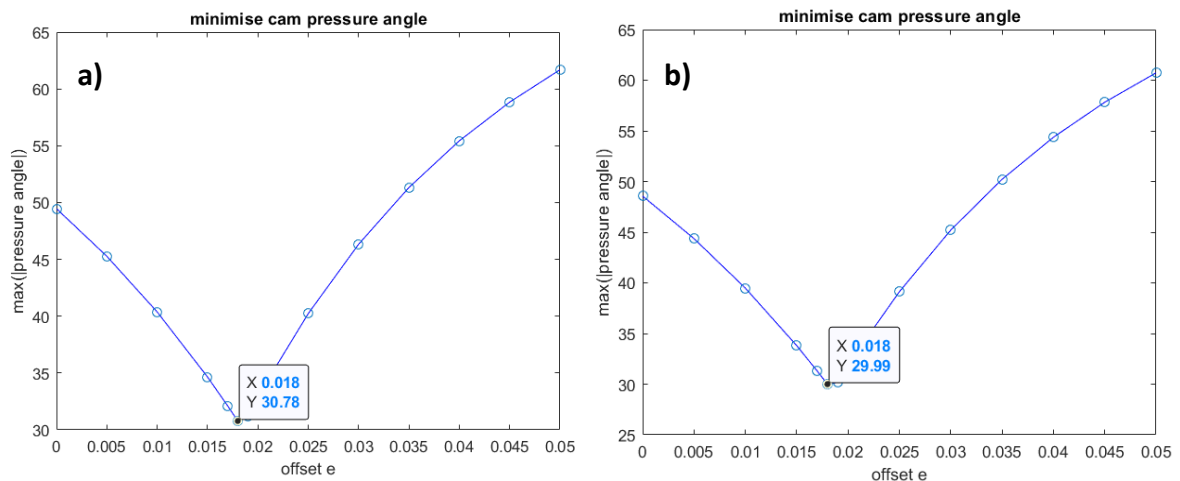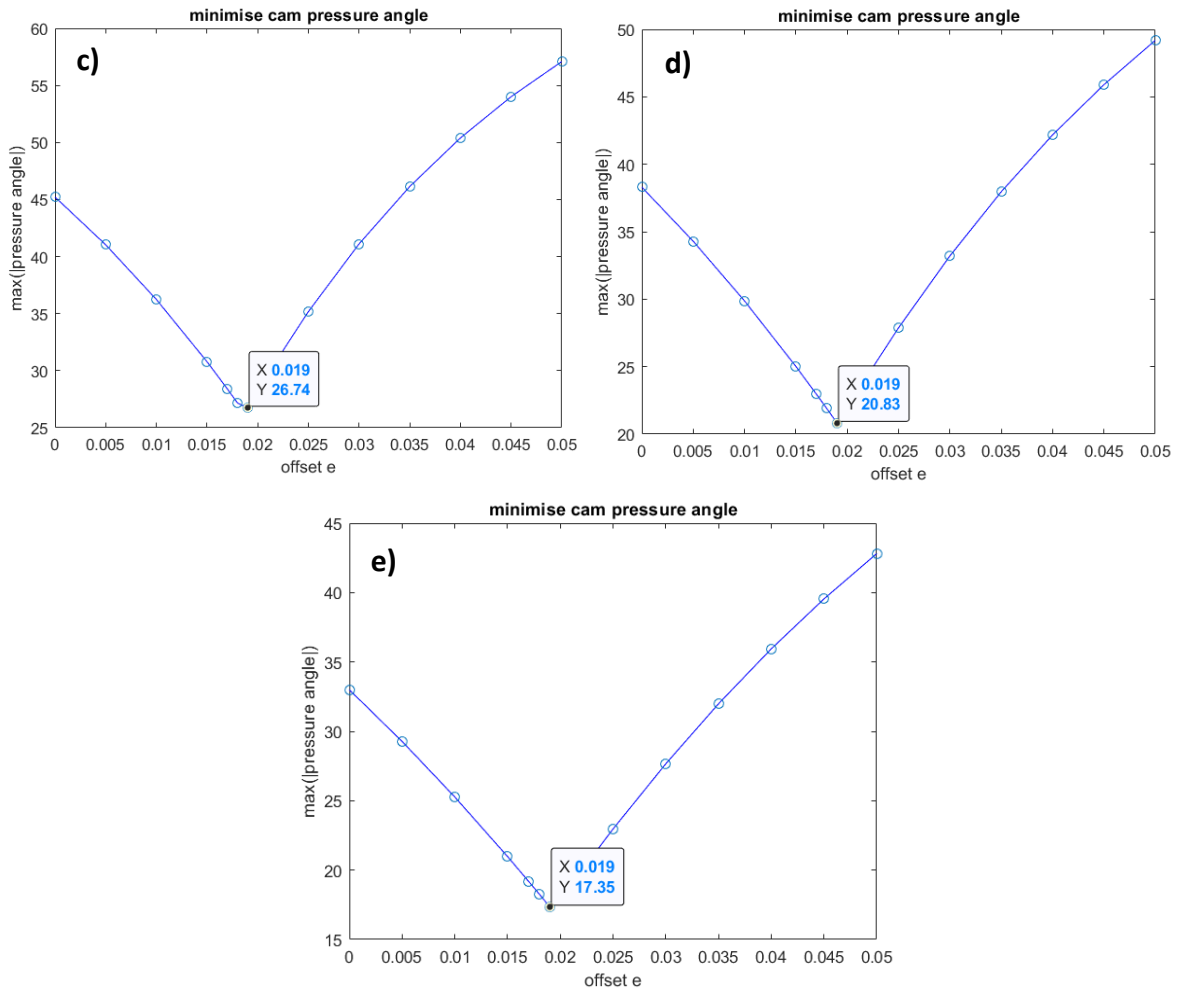
Figure 6.2 Combination 1 for the stance system: $\mathbf{max}(|\boldsymbol{\alpha}|)$ for different values of the offset $\boldsymbol{e}$ and for (a) $\boldsymbol{a} = \boldsymbol{25mm}$, (b) $\boldsymbol{a} = \boldsymbol{26mm}$, (c) $\boldsymbol{a} = \boldsymbol{30mm}$, (d) $\boldsymbol{a} = \boldsymbol{40mm}$, (e) $\boldsymbol{a} = \boldsymbol{50mm}$.

distance a (*mm*)	*offset e* (*mm*)	$\mathbf{max}(|\boldsymbol{\alpha}|)$ (°)
25	18	30.78
26	18	29.99
30	19	26.74
40	19	20.83
50	19	17.35

Table 6.7 Combination 1 for the stance system: how the offset $\boldsymbol{e}$ and $\mathbf{max}(|\boldsymbol{\alpha}|)$ vary when the distance $\boldsymbol{a}$ becomes smaller than $50mm$.

Interestingly, the results showed that the offset e that minimises $\max(|\alpha|)$ is $e = 19mm$, for $a = 30mm, 40mm, 50mm$. This trend is shown in the contour plot in Figure 6.3, with the

vertical band of dark blue illustrating that the optimum value for offset e is almost constant and just under $20mm$ for all values of distance a.
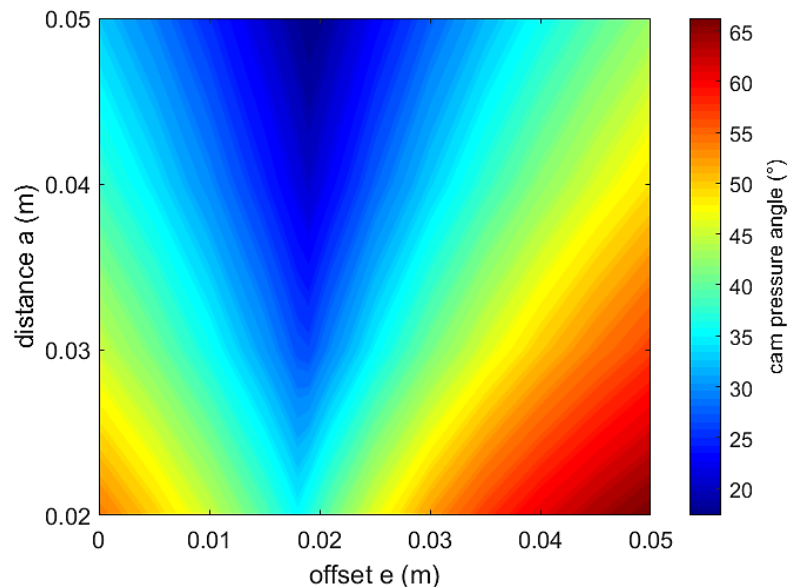
Figure 6.3 Combination 1 for the stance system: contour plot illustrating how $\mathbf{max}(|\boldsymbol{\alpha}|)$ varies when the offset e and the distance $\boldsymbol{a}$ change.

PUSH-OFF SYSTEM

The push-off system results of the first pass of the second stage described above (i.e. varying e with $a = a_{max} = 50mm$) are shown in Table 6.8. The first two columns show the design parameters inherited from the first two steps of the design investigation (sections 6.2.1 and 6.2.2). Columns 3 to 5 show the values of the distance a (always $50mm$ at this stage), the optimum offset e that minimises max($|\alpha|$), and the corresponding minimum value of max($|\alpha|$) respectively. The two rows with bold text (i.e. combinations 1 and 3) correspond to combinations of the primary independent variables that ensure max($|\alpha|$) < 30°, while the others do not and, therefore, they were excluded according to step 3, rule i, above.

COMBINATION (primary indep. variables)	$roller\ \emptyset$ (mm)	$distance\ a$ (mm)	$offset\ e$ (mm)	$\min(\max(|\alpha|))$ $(°)$
1. $GR=1,$ $P_{max}=100bar,$ $D=20mm$	**19**	**50**	**19**	**15.96**
2. $GR=1$ $P_{max}=100bar,$ $D=10mm$	16	50	50	52.78
3. $GR=1,$ $P_{max}=50bar,$ $D=20mm$	**16**	**50**	**37**	**28.56**
4. $GR=1,$ $P_{max}=50bar,$ $D=10mm$	16	50	50	69.98
5. $GR=1,$ $P_{max}=20bar,$ $D=20mm$	16	50	50	58.11

Table 6.8 Optimising offset e – 1st pass. Push-off system: those combinations having a stroke length smaller than $50mm$ were analysed with the correct roller diameter and for distance $a = 50mm$. The offset e that minimises the maximum absolute cam pressure angle is shown (together with the pressure angle).

Combination 3 satisfied step 3, rule ii, and was therefore accepted for carrying forward to the final step of the design investigation (section 6.2.4). The results for this combination are summarised in Table 6.9, and Figure 6.4 shows the $\max(|\alpha|)$ trend when the offset e is varied, with the distance a fixed ($a = a_{max} = 50mm$). There is a clear minimum for $\max(|\alpha|)$ of 28.56°, which is just below the upper limit of 30°.

Combination 3:

	$roller\ \emptyset$ (mm)	$distance\ a$ (mm)	$offset$ (mm)	$|\alpha|_{actual\ max}$ $(°)$
$GR=1,$ $P_{max}=50bar,$ $D=20mm$	16	50	37	28.56

Table 6.9 Combination 3 for the push-off system.
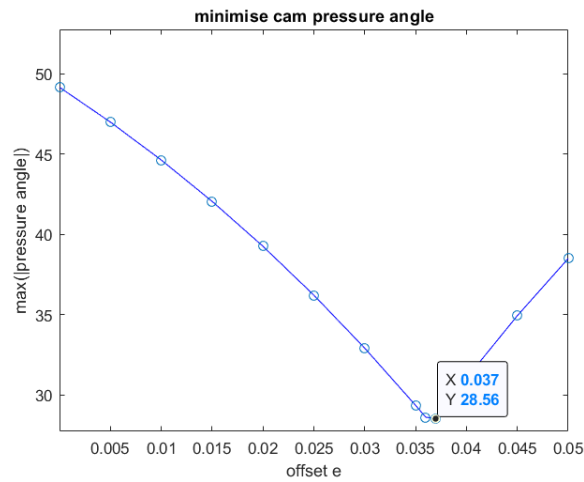
Figure 6.4 Combination 3 for the push-off system: $\mathbf{max}(|\boldsymbol{\alpha}|)$ for different values of the offset $\boldsymbol{e}$ and for $\boldsymbol{a} = \mathbf{50}\boldsymbol{mm}$.

Combination 1 resulted in a minimum for max($|\alpha|$) of 15.96° and, therefore, smaller values of the distance a were tried to reduce the size of the cam-ram system as dictated by stage 3, rule iii. This process is illustrated in Figure 6.5, with the numerical data for the successive minima shown in Table 6.10. To be conservative, $a = 23mm, 24mm, 25mm$ were eliminated and $a = 30mm, 40mm, 50mm$ were all carried forward to the final step of the design investigation (section 6.2.4) to see if there was a trade-off between size, specifically the distance a, and energy losses.
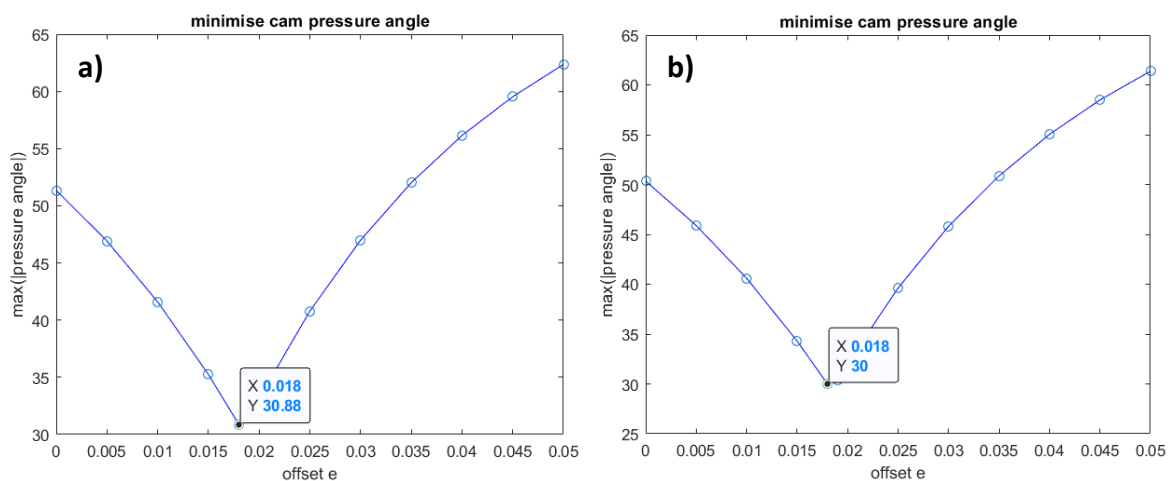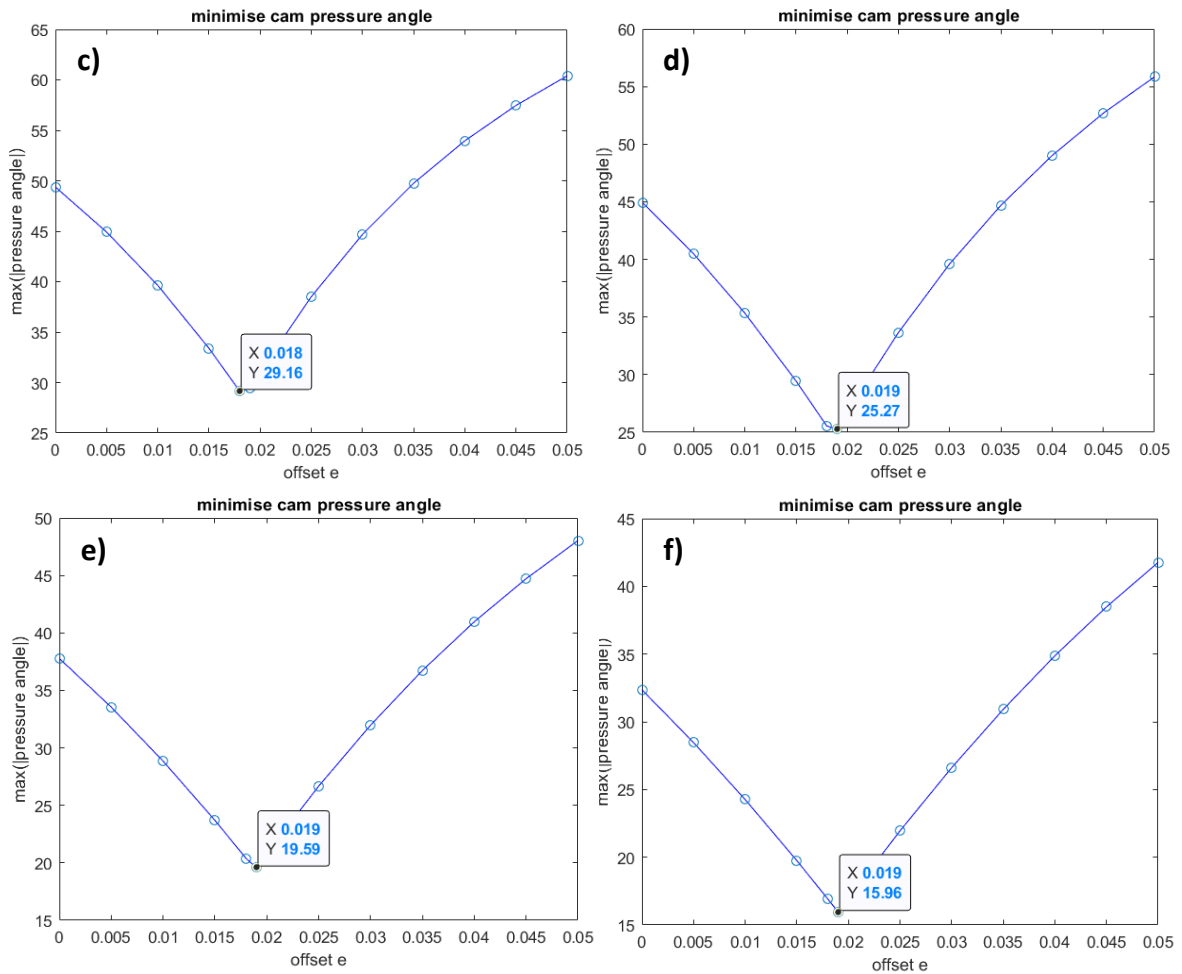
Figure 6.5 Combination 1 for the push-off system: $\max(|\alpha|)$ for different values of the offset e and for (a) $a = 23mm$, (b) $a = 24mm$, (c) $a = 25mm$, (d) $a = 30mm$, (e) $a = 40mm$, (f) $a = 50mm$.

distance a (mm)	offset e (mm)	$|\alpha|_{actual\ max}$ $(°)$
23	18	30.88
24	18	30
25	18	29.16
30	19	25.27
40	19	19.59
50	19	15.96

Table 6.10 Combination 1 for the push-off system: how the offset e and $\max(|\alpha|)$ vary when the distance a becomes smaller than $50mm$.

As was the case for the stance cam-ram, the results showed that the offset e that minimises $\max(|\alpha|)$ is $e = 19mm$, for $a = 30mm, 40mm, 50mm$. This trend is shown in the contour

162

plot in Figure 6.3, with the vertical band of dark blue illustrating that the optimum value for offset e is almost constant and just under $20mm$ for all values of distance a.
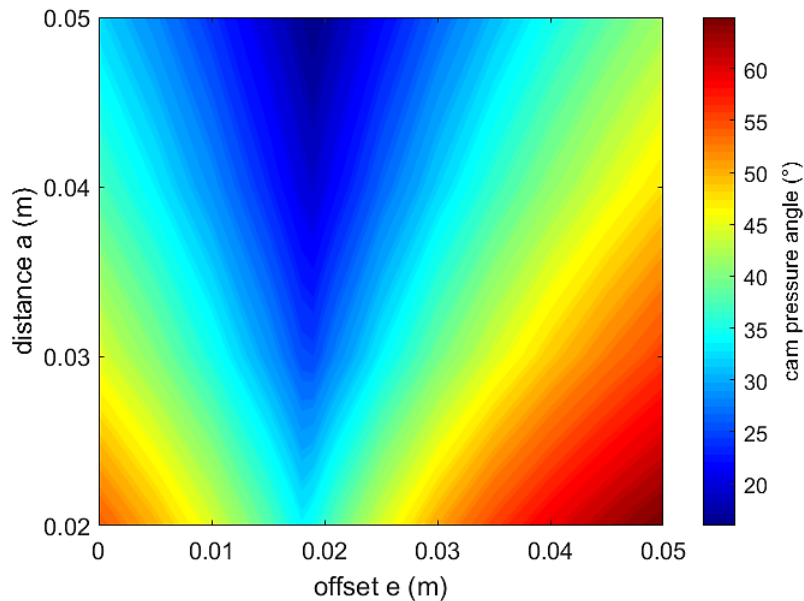
Figure 6.6 Combination 1 for the push-off system: contour plot illustrating how $\mathbf{max}(|\boldsymbol{\alpha}|)$ varies when the offset e and the distance $\boldsymbol{a}$ change.

6.2.4   Step 4 – Compare energy losses

To summarise the results of this design investigation so far:

Step 1 – For both cam-ram systems, the same five combinations of the primary independent variables were carried forward.

Step 2 – All five of these combinations were carried forward with roller diameters that satisfied the design constraint ($d_{roller} \leq 30mm$).

Step 3 – For both cam-ram systems, the same three combinations of the primary independent variables were eliminated because cam pressure angle was too large (i.e. $\min(\max(|\alpha|)) \geq 30°$). The two remaining combinations were carried forward with alternative values of a and e as shown in Table 6.11 below.

COMBINATION (primary indep. variables)	$roller\ Ø$ (mm)	$distance\ a$ (mm)	$offset\ e$ (mm)
$GR = 1,$ $P_{max} = 100bar,$ $D = 20mm$	19	50	19
$GR = 1,$ $P_{max} = 100bar,$ $D = 20mm$	19	40	19
$GR = 1,$ $P_{max} = 100bar,$ $D = 20mm$	19	30	19
$GR = 1,$ $P_{max} = 50bar,$ $D = 20mm$	16	50	36 (37 for push-off)

Table 6.11 Remaining design alternatives. The design parameters are the same for both cam-ram systems except for the offset *e* for the 4th design alternative.

In this final step of the design investigation, for each cam-ram system in turn, these four design alternatives were compared in terms of their energy losses. Power flows were calculated using the equations in section 5.3, and then the energy balance over the cam-ram's working phase was obtained by integration. For each design alternative, four energy terms were considered:

- The energy input – For the stance system, this is the energy input from the ankle. For the push-off system, this is the energy input from the accumulator.

- The energy output – For the stance system, this is the energy stored in the accumulator. For the push-off system, this is the energy output to the ankle.

- The energy lost because of friction in the cam rolling resistance element, in the roller, at the follower guide, and at the cylinder O-ring. Because the gearbox ratio is $GR = 1$, corresponding to no gearbox, in all cases the gearbox friction is zero.

- The energy stored in the mechanical components of the system, including strain energy in the parallel spring, and the kinetic and potential energies of the roller and follower.

As mentioned at the beginning of this chapter, the following terms were neglected:

- Losses in the two cam-ram systems during their non-working phases.

- Major and minor flow losses.

- Losses in the accumulator because of heat transfer.

- The two follower return springs.

STANCE SYSTEM

Tables 6.12 to 6.15 and Figures 6.7 to 6.10 show the energy balance over the working phase of the stance cam-ram system (i.e. mid and terminal stance, from foot flat to maximum dorsiflexion) for the four design alternatives.

1) $P_{max} = 100bar, D = 20mm, a = 50mm$ and $e = 19mm$:

	energy (J)	*corresponding* %
Energy input	18.91	100
Energy output	18.21	96.30
Energy lost	0.30	1.60
Energy stored in system	0.40	2.10

Table 6.12 Stance system: energy balance for $P_{max} = 100bar$, $D = 20mm$, $a = 50mm$ and $e = 19mm$.
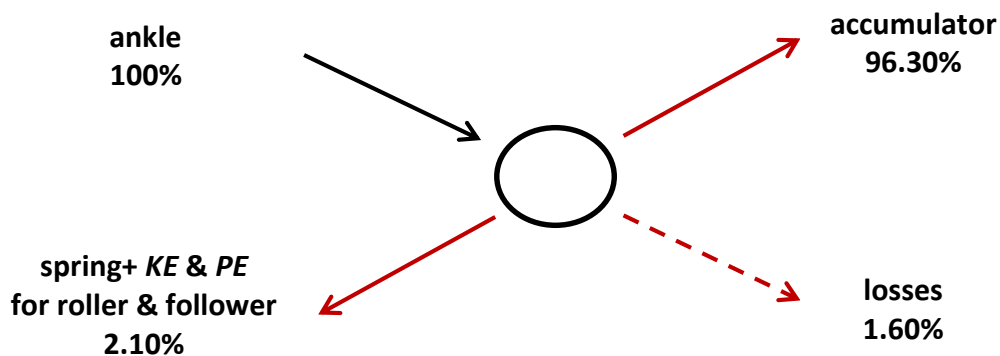
Figure 6.7 Stance system: energy balance (percentages) for $P_{max} = 100bar$, $D = 20mm$, $a = 50mm$ and $e = 19mm$.

2) $P_{max} = 100bar, D = 20mm, a = 40mm$ and $e = 19mm$:

	energy (J)	*corresponding* %
Energy input	18.91	100
Energy output	18.23	96.43
Energy lost	0.28	1.47
Energy stored in system	0.40	2.10

Table 6.13 Stance system: energy balance for $P_{max} = 100bar$, $D = 20mm$, $a = 40mm$ and $e = 19mm$.
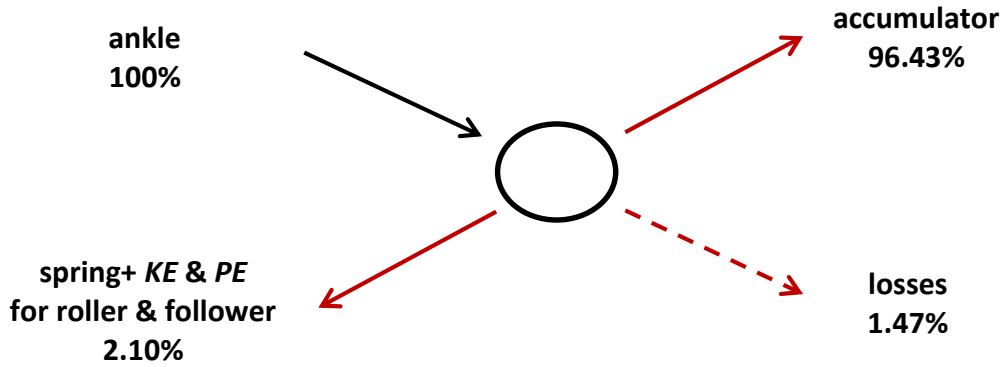
Figure 6.8 Stance system: energy balance (percentages) for $P_{max} = 100bar$, $D = 20mm$, $a = 40mm$ and $e = 19mm$.

3) $P_{max} = 100bar$, $D = 20mm$, $a = 30mm$ and $e = 19mm$:

	energy (J)	*corresponding* %
Energy input	18.91	100
Energy output	18.25	96.53
Energy lost	0.26	1.37
Energy stored in system	0.40	2.10

Table 6.14 Stance system: energy balance for $P_{max} = 100bar$, $D = 20mm$, $a = 30mm$ and $e = 19mm$.
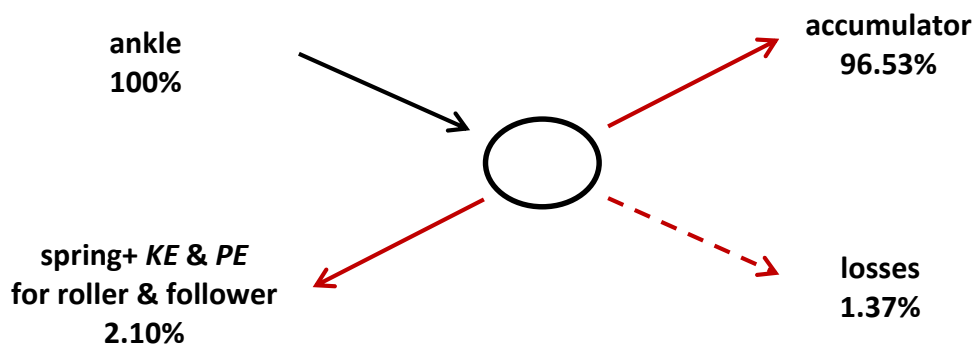
Figure 6.9 Stance system: energy balance (percentages) for $P_{max} = 100bar$, $D = 20mm$, $a = 30mm$ and $e = 19mm$.

4) $P_{max} = 50bar$, $D = 20mm$, $a = 50mm$ and $e = 36mm$:

	energy (J)	*corresponding* %
Energy input	18.91	100
Energy output	18.14	95.93
Energy lost	0.37	1.96
Energy stored in system	0.40	2.12

Table 6.15 Stance system: energy balance for $P_{max} = 50bar$, $D = 20mm$, $a = 50mm$ and $e = 36mm$.
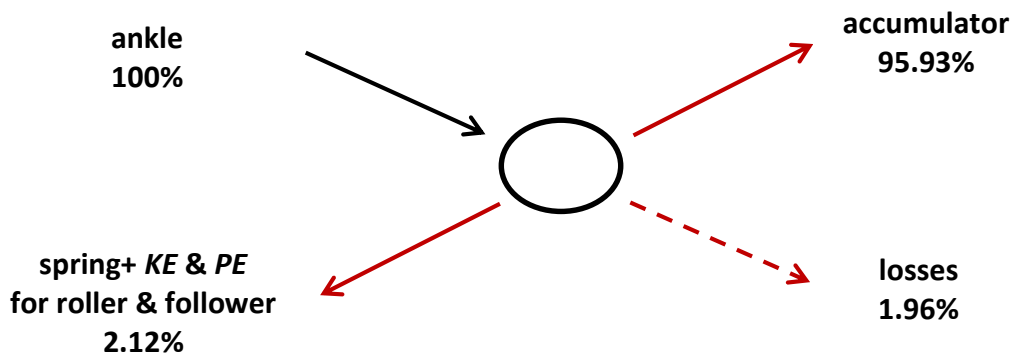
Figure 6.10 Stance system: energy balance (percentages) for $P_{max} = 50bar$, $D = 20mm$, $a = 50mm$ and $e = 36mm$.

Given the results shown above, it is clear that the third design alternative has both the smallest energy losses (1.37%) and the smallest value of distance a (30mm), which helps to minimise the size of the cam-ram system. Hence, the recommended design parameters for the stance cam-ram are as follows:

	roller Ø (*mm*)	*distance a* (*mm*)	*offset e* (*mm*)
$GR = 1$, $P_{max} = 100bar$, $D = 20mm$	19	30	19

Table 6.16 Final layout for the stance cam-ram system.

PUSH-OFF SYSTEM

Tables 6.17 to 6.20 and Figures 6.11 to 6.14 show the energy balance over the working phase of the push-off cam-ram system (i.e. push-off, from maximum dorsiflexion to toe-off) for the four design alternatives.

1) $P_{max} = 100bar$, $D = 20mm$, $a = 50mm$ and $e = 19mm$:

	energy (J)	*corresponding* %
Energy input	14.81	100
Energy output	11.88	80.23
Energy lost	0.36	2.45
Energy stored in system	2.56	17.31

Table 6.17 Push-off system: energy balance for $P_{max} = 100bar$, $D = 20mm$, $a = 50mm$ and $e = 19mm$.
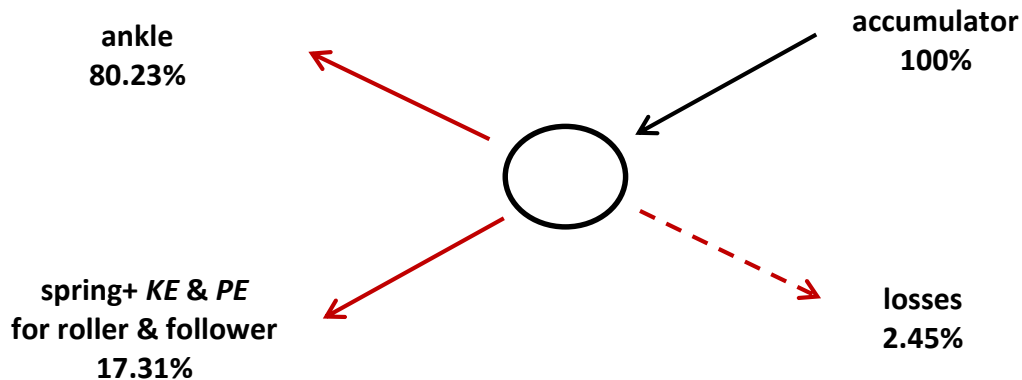
Figure 6.11 Push-off system: energy balance (percentages) for $P_{max} = 100bar$, $D = 20mm$, $a = 50mm$ and $e = 19mm$.

2) $P_{max} = 100bar$, $D = 20mm$, $a = 40mm$ and $e = 19mm$:

	energy (J)	*corresponding* %
Energy input	14.77	100
Energy output	11.88	80.46
Energy lost	0.32	2.18
Energy stored in system	2.56	17.36

Table 6.18 Push-off system: energy balance for $P_{max} = 100bar$, $D = 20mm$, $a = 40mm$ and $e = 19mm$.
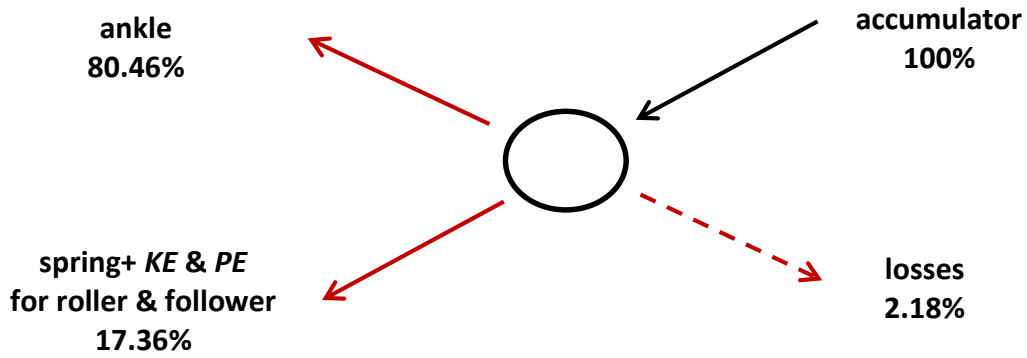
Figure 6.12 Push-off system: energy balance (percentages) for $P_{max} = 100bar$, $D = 20mm$, $a = 40mm$ and $e = 19mm$.

3) $P_{max} = 100bar$, $D = 20mm$, $a = 30mm$ and $e = 19mm$:

	energy (J)	*corresponding* %
Energy input	14.73	100
Energy output	11.88	80.65
Energy lost	0.29	1.95
Energy stored in system	2.56	17.40

Table 6.19 Push-off system: energy balance for $P_{max} = 100bar$, $D = 20mm$, $a = 30mm$ and $e = 19mm$.
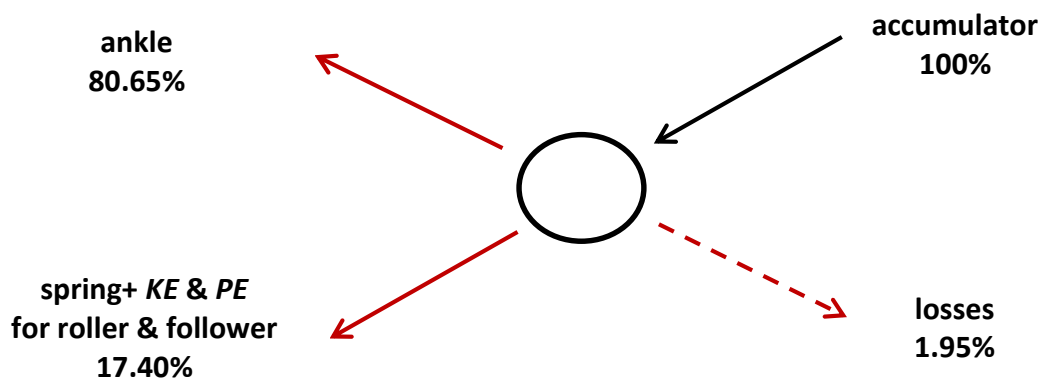
Figure 6.13 Push-off system: energy balance (percentages) for $P_{max} = 100bar$, $D = 20mm$, $a = 30mm$ and $e = 19mm$.

4) $\boldsymbol{P_{max} = 50bar, D = 20mm}$, $a = 50mm$ and $e = 37mm$:

	energy (J)	*corresponding* %
Energy input	14.81	100
Energy output	11.88	80.20
Energy lost	0.37	2.50
Energy stored in system	2.56	17.29

Table 6.20 Push-off system: energy balance for $\boldsymbol{P_{max} = 50bar, D = 20mm}$, $a = 50mm$ and $e = 37mm$.
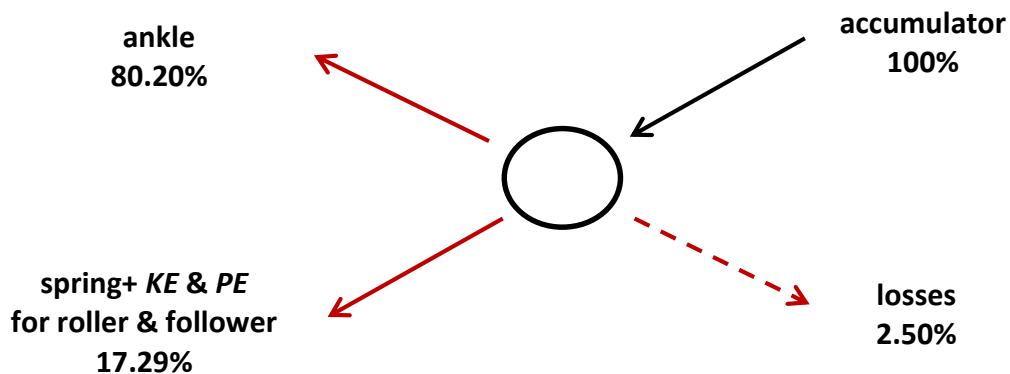
Figure 6.14 Push-off system: energy balance (percentages) for $\boldsymbol{P_{max} = 50bar, D = 20mm}$, $a = 50mm$ and $e = 37mm$.

As was the case for the stance cam-ram, it is clear that the third design alternative has both the smallest energy losses (1.95%) and the smallest value of distance a (30mm), which helps to minimise the size of the cam-ram system. Hence, the recommended design parameters for the push-off cam-ram are as follows:

	roller Ø (*mm*)	*distance a* (*mm*)	*offset e* (*mm*)
$GR = 1,$ $P_{max} = 100bar,$ $D = 20mm$	19	30	19

Table 6.21 Final layout for the push-off cam-ram system.

6.3   Conclusion

The results of this preliminary design investigation show that, when the gearbox is not included, the best designs for the two cam-ram systems are the same. They achieve the best performance, with lower energy losses and smaller dimensions, by using the following primary independent variables:

- Maximum hydraulic pressure $P_{max} = 100\ bar$;
- Ram bore $D = 20mm$.

Furthermore, to withstand the radial cam forces, both cam-ram systems need rollers with minimum diameters of $19mm$, which is the same as the diameter used by Realmuto *et al.* (2015) for the cam-roller-follower system in their active ankle prosthesis.

Finally, to ensure the cam pressure angle does not exceed $30°$ and also to help minimise the size of both cam-ram systems, the values chosen for the secondary independent variables are:

- Offset $e = 19mm$;
- Distance $a = 30mm$.

The energy balance results for this design alternative, during the working phases of the two cam-ram systems, are very promising. Specifically, the energy losses do not exceed 2% of the energy input to the system (i.e. from the ankle for the stance system and from the accumulator for the push-off system). However, an early stage simulation model was used for this design investigation, which only modelled the friction losses directly associated with the two cam-rams during their working phases. This model neglected the cam-ram losses in their non-working phases, major and minor flow losses, losses in the accumulator, and the two follower return springs, because it was assumed these would have little effect on the selected cam-ram design parameters. Therefore, the energy losses will certainly increase when all the significant sources of energy dissipation are considered and this is the subject of the next chapter, which investigates losses over the whole gait cycle, including those neglected here.

7.Chapter 7: System performance

Leonardo Da Vinci (c.1500-05), Sketches, Codex Arundel (folio 41r), British Library, London

"Those who fall in love with practice without science
are like the helmsman, who enters the ship without the helm or the compass,
and never knows where to go."

(Leonardo Da Vinci)

In this chapter, all of the modelled energy losses over the whole gait cycle are investigated, including those neglected in the preliminary design investigation of Chapter 6, which used an early stage simulation model including only the frictional losses directly associated with the two cam-ram systems in their working phases. For the investigations conducted in this chapter, the complete simulation model described in Chapter 5 was used to simulate the final design, established in Chapter 6, operating over the whole gait cycle. This included all the sources of energy dissipation as follows: frictional losses in both cam-ram systems associated with rolling resistance between rollers and cams, roller bearings, follower bearings (i.e. self-aligning linear ball bearings), and piston O-rings; flow losses in pipes and discrete components such as inlets, exits, bends and DCVs; and accumulator losses due to heat transfer.

Firstly, the different sources of energy loss are considered for the final design established in Chapter 6 to identify the most significant sources. Secondly, the results of a sensitivity study are presented, in which the values of the design parameters were varied over sensible ranges to establish where energy losses may be particularly sensitive to changes in the design parameters and, hence, strict constraints need to be imposed.

Note that, also in this chapter, dimensions are shown in millimetres.

7.1   Energy losses in the current system

In this section, the energy losses in the final design are broken down according to their sources. All design parameter values, including independent and dependant variables and constants, were those established in Chapters 4, 5 and 6. The energy losses were evaluated for each gait phase and over the whole gait cycle.

The energy losses considered are due to the following effects, with the parameter associated with each loss and a section reference displayed in brackets:

1. Rolling resistance between roller and cam for both cam-rams (μ_{rolres} ; section 4.3.3);
2. Friction in both roller bearings (μ_{brg} ; section 4.3.3);
3. Sliding friction in both follower bearings (μ_{sl} ; section 4.3.3);
4. Sliding friction at both piston O-rings (f$_C$; section 4.4.2);

5. Flow losses in the pipes connecting the two hydraulic rams and the accumulator (D_{pipe}, L_{pipe} ; section 4.5.1);

6. Flow losses in the discrete components connecting the two rams and the accumulator - one contraction at the exit of the ram (K_{exit}), one expansion at the inlet of the accumulator ($K_{entrance}$), one 90° elbow (K_{elbow}), and one DCV (section 4.5.2);

7. Flow losses in the discrete components connecting the two rams and the tank - one contraction at the exit of the ram (K_{exit}), one expansion at the inlet of the tank ($K_{entrance}$), and one DCV (section 4.5.2);

8. Heat transfer from the accumulator to the external environment (h_{N_2} ; section 5.3.8).

The values of the energy loss parameters were chosen conservatively or, where this wasn't appropriate, given sensible values. For example, when a typical range is given in the literature, the conservative end of the range was chosen, as explained in the corresponding modelling section. Flow losses in both pipes and discrete components depend on pipe diameter (D_{pipe}), according to equations (4.59), (4.60) and (4.62) in section 4.5. A diameter of $5 mm$ was chosen as it seemed realistic and yet not small enough to result in high flow losses. This is confirmed by the results below.

The values of the energy loss parameters are shown in Table 7.1, together with the corresponding energy loss in each phase (load acceptance, stance, push-off and swing) and over the whole gait cycle, evaluated by integration of the power losses (see equations in section 5.3). Moreover, the total energy lost over the whole gait cycle is also displayed as a percentage of the total eccentric work done by the prosthetic ankle throughout the gait cycle (almost $20.59 J$), which is the maximum amount of energy available to be stored in the system and returned. Although power losses have been defined as negative in earlier chapters, in this chapter the absolute values of the energy losses are shown.

	$E_{lost@LA}$ (J)	$E_{lost@STANCE}$ (J)	$E_{lost@PO}$ (J)	$E_{lost@SWING}$ (J)	$E_{lost@TOTAL}$ (J)	%eccentric work
$\mu_{rolres} = 0.002$ rolling resistance between cam and roller	0.0010	0.0819	0.1202	0.0022	0.2054	1
$\mu_{brg} = 0.002$ roller bearing friction	0.0004	0.0339	0.0501	0.0009	0.0854	0.41
$\mu_{sl} = 0.003$ follower sliding friction	0.0002	0.0256	0.0279	0.0005	0.0542	0.26
$f_C = 0.952$ O-ring friction	0.0243	0.4394	0.3875	0.0347	0.8859	4.30
$D_{pipe} = 5\ mm$ flow losses — *pipes* $L = 50\ mm$	0	0.0023	0.0047	0	0.0071	0.03
DCV	$0.0063e-03$	$0.0074e-03$	0.0001	$0.0010e-03$	0.0001	$0.49e-03$
fittings $K_{entrance} = 0.5$ $K_{exit} = 1$ $K_{elbow} = 0.9$	$0.1142e-03$	0.0002	0.0026	$0.0181e-03$	0.0029	0.01
total	0.0001	0.0025	0.0074	$0.0191e-03$	0.0101	0.05
$h_{N_2} = 25\,\dfrac{W}{m^2 \cdot K}$ accumulator heat losses	0	0.1904	0.0845	0.0537	0.3285	1.60
total over the whole gait cycle					1.57	7.62

Table 7.1 Sources of energy dissipation for the final design. From left to right: energy loss parameter values; energy loss in each phase (J); and energy loss over the whole gait cycle (J and as a percentage of the total eccentric work done by the prosthetic ankle).

The results of this breakdown of energy losses show that the largest energy loss is due to the O-ring friction in the two rams (4.3% of the total eccentric work), followed by heat transfer from the accumulator to the external environment (1.60% of the total eccentric work), and then losses associated with friction in the cam-roller-follower assemblies (rolling resistance 1%; roller bearings 0.41%; and follower bearings 0.26% of the total eccentric work). Conversely, flow losses are tiny (0.05% of the total eccentric work). Therefore, for the assumed pipe diameter and length, and realistic parameter values for fittings and DCVs, the flow losses seem to have a negligible effect on the performances of the two cam-ram systems, even during their working phases when power flows are large. On the contrary, mechanical friction phenomena and heat losses from the accumulator should be minimised to increase the efficiency of the system. Indeed, significant improvements could be achieved by reducing

O-ring friction and heat loss from the accumulator. The effects of changing the values of the energy loss parameters are considered in the next section.

In summary, Figure 7.1 and Table 7.2 show the energy flows in the new design, over the whole gait cycle, including: the eccentric work done, corresponding to the external energy input; the concentric work done, mainly during push-off; energy losses; and the net energy stored and carried forward for future gait cycles (e.g. for ascending slopes). Energy losses include all sources of energy dissipation that were modelled: those shown in Table 7.1 and also compressibility losses at valve transitions, which amount to no more than 0.6% of the total eccentric work. The latter were estimated based on the connections of the two rams to the tank at the end of their respective working phases, which is when the strain energy stored in the cylinder oil during the two working phases is lost. Trapezoidal integration was used for the estimate, neglecting major and minor losses. Therefore, the energy lost due to oil compressibility at valve transition at the end of the stance working phase is:

$$\Delta E_{\beta cyl\ STANCE} = \Delta V_{\beta cyl\ STANCE} \frac{\left(P_{atm_{gauge}} + P_{cyl\ STANCE_{gauge}}\right)}{2} =$$

$$= \Delta V_{\beta cyl\ STANCE} \frac{\left((P_{atm} - P_{atm}) + (P_{cyl\ STANCE} - P_{atm})\right)}{2} = \quad (7.1)$$

$$= \Delta V_{\beta cyl\ STANCE} \frac{\left(P_{cyl\ STANCE} - P_{atm}\right)}{2} = 0.042J =$$

$$= 0.2\%\ of\ the\ eccentric\ work$$

where $\Delta V_{\beta cyl\ STANCE} = -V_{cyl\ STANCE} \frac{(P_{atm} - P_{cyl\ STANCE})}{\beta} = -V_{cyl\ STANCE} \frac{(P_{atm} - P_{acc})}{\beta} =$ $9.169e - 9\ m^3$, with $\beta = 1.657e + 09\ Pa$, $V_{cyl\ STANCE} = 0.1671e - 05\ m^3$, and $P_{cyl\ STANCE} = P_{acc} = 9.194e + 06\ Pa$ (data from MATLAB simulation model). The energy lost due to oil compressibility at valve transition at the end of the push-off working phase is:

$$\Delta E_{\beta cyl\ PO} = \Delta V_{\beta cyl\ PO} \frac{\left(P_{atm_{gauge}} + P_{cyl\ PO_{gauge}}\right)}{2} =$$

$$= \Delta V_{\beta cyl\ PO} \frac{\left((P_{atm} - P_{atm}) + (P_{cyl\ PO} - P_{atm})\right)}{2} = \quad (7.2)$$

$$= \Delta V_{\beta cyl\,PO} \frac{\left(P_{cyl\,PO} - P_{atm}\right)}{2} = 0.078J =$$

$$= 0.4\% \ of \ the \ eccentric \ work$$

where $\quad \Delta V_{\beta cyl\,PO} = -V_{cyl\,PO} \frac{\left(P_{atm} - P_{cyl\,PO}\right)}{\beta} = -V_{cyl\,PO} \frac{\left(P_{atm} - P_{acc}\right)}{\beta} = 1.747e - 8 \ m^3, \quad$ with $V_{cyl\,PO} = 0.3242e - 05 \ m^3$, and $P_{cyl\,PO} = P_{acc} = 9.032e + 06 \ Pa.$

The primary contribution to the net energy stored and carried forward is the change in energy stored in the accumulator, estimated from equation (5.43) rearranged for $\frac{\partial E_{gas\,acc}}{\partial t}$: the energy stored during mid and terminal stance in the accumulator amounts to approximately $17.29J$, while the energy released during push-off amounts to $14.32J$. Theoretically, for periodic ankle kinematics, the net changes over the whole gait cycle in strain energy stored in the parallel spring and the two follower return springs, and potential and kinetic energy of the rollers and followers, should be zero. Nevertheless, in the MATLAB simulations this change in stored energy turns out to be approximately $0.0025 \ J$, and is included in the net energy stored and carried forward (Figure 7.1 and Table 7.2). The sum of these energy flows for the whole system differs from zero: it is approximately -0.83% of the total eccentric work done, which represents the accuracy of the simulation model developed in this PhD work.
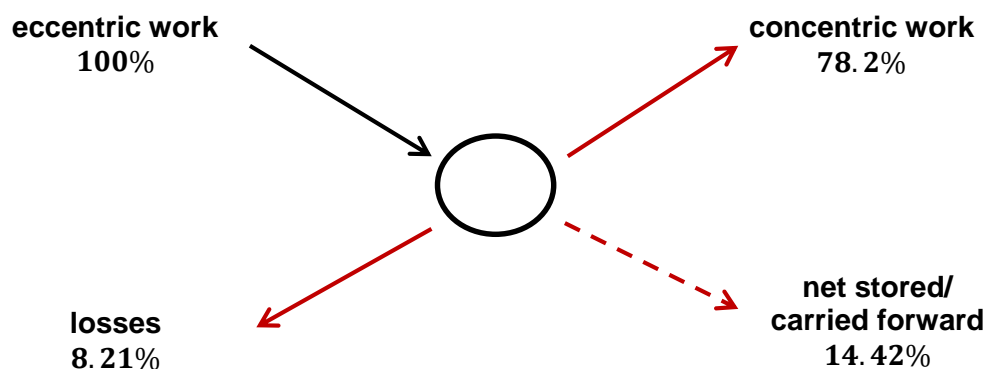
Figure 7.1 Energy flows (percentages) in the new hydraulic ankle over the whole gait cycle.

	$abs(energy)$ (J)	$\%\ eccentric\ work$
eccentric work	20.59	100%
concentric work	16.10	78.2%
energy lost	1.69	8.21%
energy stored and carried forward	2.97	14.42%
residual (simulation's accuracy)	$-\mathbf{0.17}$	$-\mathbf{0.83}\%$

Table 7.2 Energy flows in the new hydraulic ankle over the whole gait cycle (*J* and as a percentage of the total eccentric work done by the prosthetic ankle).

7.2 Sensitivity study

A sensitivity study was undertaken to establish where energy losses may be particularly sensitive to changes in the design parameters and, hence, strict constraints need to be imposed. For each parameter associated with a source of energy loss (see Table 7.1), a range of values that goes beyond the typical ranges found in the literature was chosen to conduct this sensitivity study. To be consistent, this was done by multiplying the chosen values for the final design by 0.25, 0.5, 2 and 4. However, where this led to unrealistic values or it was useful to extend the range, an alternative range was chosen.

The MATLAB code was further modified in order to re-run the design program for each parameter value from the chosen range. This meant adding a fourth *for* loop, which steps through the sequence of parameter values and, for each value, executes the three nested loops already making up the design program (see section 5.2). In this way, the cam profiles and return springs are re-evaluated for each parameter value.

The following sub-sections show the changes in energy lost when a particular energy loss parameter is varied. Tables 7.3 – 7.9 and Figures 7.2 – 7.10 display the energy lost in each gait phase (J) and the total energy lost over the whole the gait cycle (J and also as a percentage of the total eccentric work over the gait cycle). The highlighted rows in the tables correspond to the parameter values in the final design, that is the energy losses already listed in Table 7.1.

7.2.1 Rolling resistance (μ_{rolres})

The moment describing the rolling resistance between cam and roller (M_{rolres}) is given by equation (4.36). Typical values for the coefficient of rolling friction (μ_{rolres}) from the literature are between 0.001 and 0.002 (see section 4.3.3). For the final design, the chosen value of μ_{rolres} is 0.002 (see Table 7.1), and the range chosen for the sensitivity study is shown in the first column of Table 7.3. The energy lost was evaluated by integration of the rolling resistance power ($P_{fr_{rolres}}$) (equation (5.20) in section 5.3) and is shown in Table 7.3 and Figure 7.2.

$\boldsymbol{\mu_{rolres}}$	$\boldsymbol{E_{lost@LA}(J)}$	$\boldsymbol{E_{lost@STANCE}(J)}$	$\boldsymbol{E_{lost@PO}(J)}$	$\boldsymbol{E_{lost@SWING}(J)}$	$\boldsymbol{E_{lost@TOTAL}(J)}$	% eccentric work
0.002/4	0.0002	0.0205	0.0301	0.0006	0.0514	0.25
0.002/2	0.0005	0.0410	0.0601	0.0011	0.1027	0.50
0.002	0.0010	0.0819	0.1202	0.0022	0.2054	1
0.002 ∗ 2	0.0020	0.1638	0.2404	0.0045	0.4106	1.99
0.002 ∗ 4	0.0040	0.3274	0.4804	0.0089	0.8207	3.99

Table 7.3 Sensitivity of energy lost because of rolling resistance to changes in μ_{rolres}. From left to right: values of μ_{rolres}; energy loss in each phase (J); and energy loss over the whole gait cycle (J and as a percentage of the total eccentric work done by the prosthetic ankle).

The energy lost over the gait cycle increases almost linearly as the rolling friction coefficient increases. A coefficient of $\mu_{rolres} \leq 0.002$ guarantees that the rolling resistance energy losses are no more than 1% of the total eccentric work. Given that this was chosen as a conservative value, it may be possible to achieve $\mu_{rolres} = 0.001$ and, hence, reduce this energy loss to 0.50% of the total eccentric work.
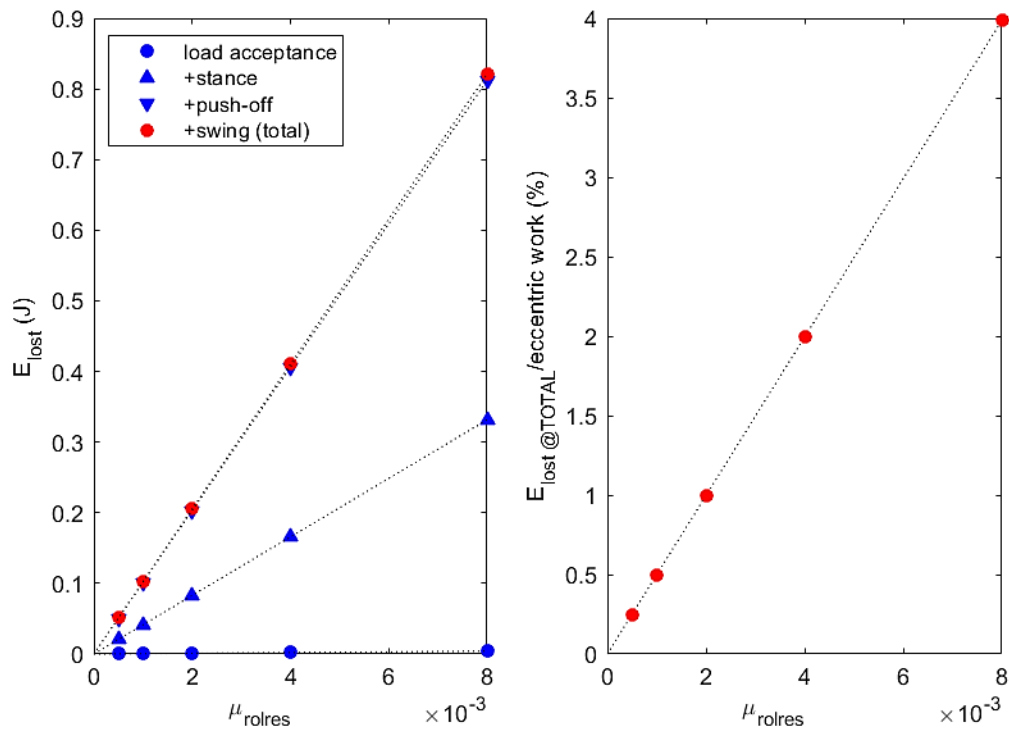
Figure 7.2 Sensitivity of energy lost because of rolling resistance to changes in μ_{rolres}. The plot on the left shows how the phase losses accumulate to give the total loss over the whole gait cycle (J). The plot on the right shows the total energy loss as a percentage of the total eccentric work done by the prosthetic ankle.

7.2.2   Roller bearing friction (μ_{brg})

The moment describing friction at the roller bearing (M_{brg}) is given by equation (4.35). For the final design, the chosen value of μ_{brg} is 0.002 (see Table 7.1), which is the worst case coefficient of friction found in the literature for both needle roller bearings and for cylindrical roller bearings (SKF, 2013). The lowest value reported in SKF (2013) is $\mu_{brg} = 0.0011$ for cylindrical roller bearings with a cage. These values apply when the force acting on the roller is only radial (the axial force is zero). The range chosen for the sensitivity study is shown in the first column of Table 7.4. The energy lost was evaluated by integration of the roller bearing friction power ($P_{fr_{rol}}$) (equation (5.23) in section 5.3) and is shown in Table 7.4 and Figure 7.3.

μ_{brg}	$E_{lost@LA}(J)$	$E_{lost@STANCE}(J)$	$E_{lost@PO}(J)$	$E_{lost@SWING}(J)$	$E_{lost@TOTAL}(J)$	% eccentric work
0.002/4	0.0001	0.0085	0.0125	0.0002	0.0214	0.10
0.002/2	0.0002	0.0170	0.0251	0.0005	0.0427	0.21
0.002	0.0004	0.0339	0.0501	0.0009	0.0854	0.41
0.002 ∗ 2	0.0008	0.0679	0.1002	0.0019	0.1708	0.83
0.002 ∗ 4	0.0017	0.1357	0.2004	0.0037	0.3415	1.66

Table 7.4 Sensitivity of energy lost because of roller bearing friction to changes in μ_{brg}. From left to right: values of μ_{brg}; energy loss in each phase (J); and energy loss over the whole gait cycle (J and as a percentage of the total eccentric work done by the prosthetic ankle).

The energy lost over the gait cycle increases almost linearly as the roller bearing coefficient of friction increases. A coefficient of $\mu_{brg} \leq \sim 0.006$ guarantees the roller bearing energy losses are less than 1% of the total eccentric work. Given that $\mu_{brg} = 0.002$ was chosen as a conservative value, it may be possible to achieve $\mu_{brg} = 0.001$ and, hence, reduce this energy loss to 0.21% of the total eccentric work.

Figure 7.3 Sensitivity of energy lost because of roller bearing friction to changes in μ_{brg}. The plot on the left shows how the phase losses accumulate to give the total loss over the whole gait cycle (J). The plot on the right shows the total energy loss as a percentage of the total eccentric work done by the prosthetic ankle.

7.2.3   Sliding friction at the follower (μ_{sl})

The two sliding friction forces (F_{fr1} and F_{fr2}) at both follower bearings (each consisting of 2 self-aligning linear ball bearings) are given by equations (4.42) and (4.43). Typical values from the literature for the coefficient of friction (μ_{sl}) of lubricated linear ball bearings are between 0,0015 for heavy loads and 0,005 for light loads. For the final design, the chosen value of μ_{sl} is 0.003 (see Table 7.1) because the energy lost is likely to be highest when the forces are high and, hence, it would be unrealistic to use the light load μ_{sl}. The range chosen for the sensitivity study is shown in the first column of Table 7.5. The energy lost was evaluated by integration of the sliding friction power ($P_{fr_{fol}}$) (equation (5.28) in section 5.3) and shown in Table 7.5 and Figure 7.4.

μ_{sl}	$E_{lost@LA}(J)$	$E_{lost@STANCE}(J)$	$E_{lost@PO}(J)$	$E_{lost@SWING}(J)$	$E_{lost@TOTAL}(J)$	% eccentric work
0.005/4	0.0001	0.0106	0.0116	0.0002	0.0226	0.11
0.005/2	0.0002	0.0213	0.0233	0.0004	0.0452	0.22
0.003	0.0002	0.0256	0.0279	0.0005	0.0542	0.26
0.005	0.0003	0.0426	0.0465	0.0009	0.0903	0.44
0.005 * 2	0.0007	0.0855	0.0927	0.0017	0.1806	0.88
0.005 * 4	0.0014	0.1714	0.1844	0.0035	0.3607	1.75

Table 7.5 Sensitivity of energy lost because of sliding friction to changes in μ_{sl}. From left to right: values of μ_{sl}; energy loss in each phase (J); and energy loss over the whole gait cycle (J and as a percentage of the total eccentric work done by the prosthetic ankle).

The energy lost over the gait cycle increases almost linearly as the coefficient of sliding friction increases. A coefficient of $\mu_{sl} \leq 0.11$ guarantees the sliding friction energy losses are less than 1% of the total eccentric work. The value chosen for the final design is $\mu_{sl} = 0.003$ and this already leads to relatively low sliding friction losses of 0.26% of the total eccentric work.
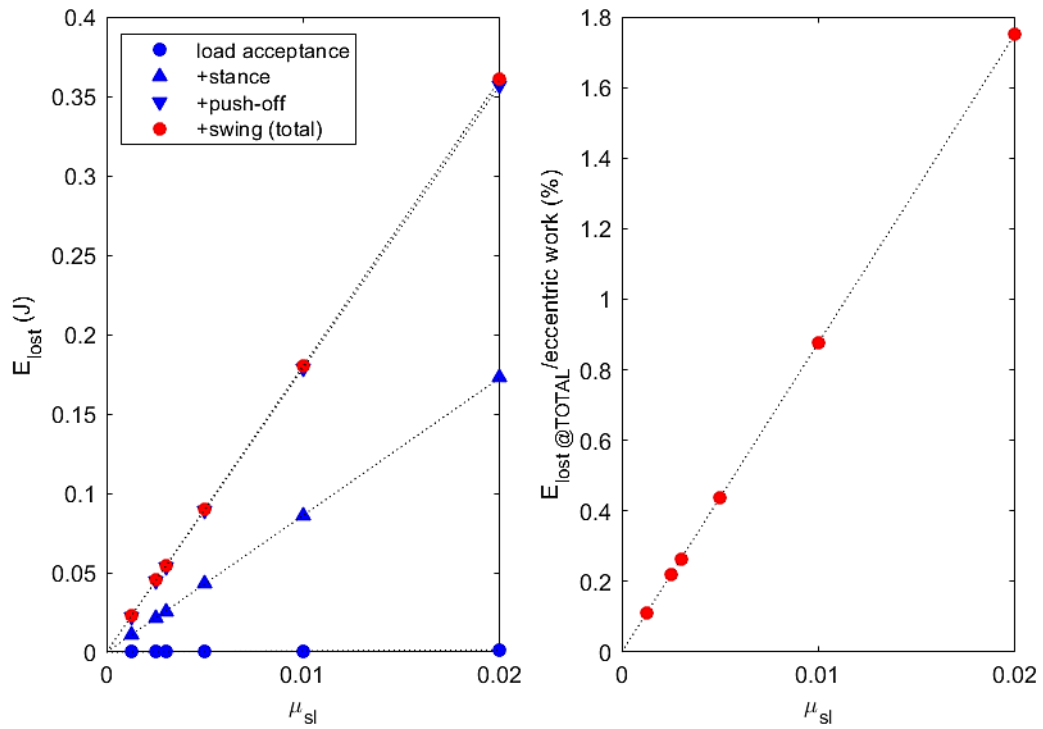
Figure 7.4 Sensitivity of energy lost because of sliding friction to changes in μ_{sl}. The plot on the left shows how the phase losses accumulate to give the total loss over the whole gait cycle (J). The plot on the right shows the total energy loss as a percentage of the total eccentric work done by the prosthetic ankle.

7.2.4   O-ring friction (f_C)

The friction at the hydraulic cylinder O-ring ($F_{fr_{cyl}}$) is given by Martini's O-ring model (see section 4.4.2). As equation (4.54) shows, the friction formula contains a pressure-dependent term and a cross-sectional squeeze dependent term. The first term only depends on given geometry and the pressure across the O-ring and, therefore, is not considered in the sensitivity study. The second term includes a friction parameter f_C that depends on the rubber hardness and the squeeze ratio and, therefore, this is considered in the sensitivity study. For the final design, a specific O-ring with a given hardness was selected and a squeeze ratio of $\varepsilon = 0.14$ was assumed, which led to $f_C = 0.952$. The range chosen for the sensitivity study is shown in the first column of Table 7.6. The energy lost is evaluated by integration of the O-ring friction power ($P_{fr_{cyl}}$) (equation (5.34) in section 5.3) and shown in Table 7.6 and Figure 7.5.

f_C	$E_{lost@LA}(J)$	$E_{lost@STANCE}(J)$	$E_{lost@PO}(J)$	$E_{lost@SWING}(J)$	$E_{lost@TOTAL}(J)$	% eccentric work
$f_C/4$	0.0062	0.3634	0.3018	0.0087	0.6801	3.30
$f_C/2$	0.0122	0.3886	0.3302	0.0174	0.7485	3.64
f_C	0.0243	0.4394	0.3875	0.0347	0.8859	4.30
$f_C * 2$	0.0481	0.5388	0.4997	0.0688	1.1553	5.61
$f_C * 4$	0.0947	0.7333	0.7197	0.1360	1.6837	8.18

Table 7.6 Sensitivity of energy lost because of O-ring friction to changes in f_C. From left to right: values of f_C; energy loss in each phase (*J*); and energy loss over the whole gait cycle (*J* and as a percentage of the total eccentric work done by the prosthetic ankle).

The energy lost over the gait cycle increases almost linearly as f_C increases. Unfortunately, even the smallest coefficient tested ($\frac{f_C}{4} = \frac{0.952}{4} = 0.238$) generates energy losses of over 3% of the total eccentric work and is the largest source of energy loss in the system. Furthermore, with the selected O-ring of given hardness, the minimum value of f_C consistent with a realistic but low squeeze ratio (for instance $\varepsilon = 0.07$ (Xia & Durfee, 2011b, 2014)) is $f_C = 0.476$, which generates energy losses of over 3.64% of the total eccentric work.
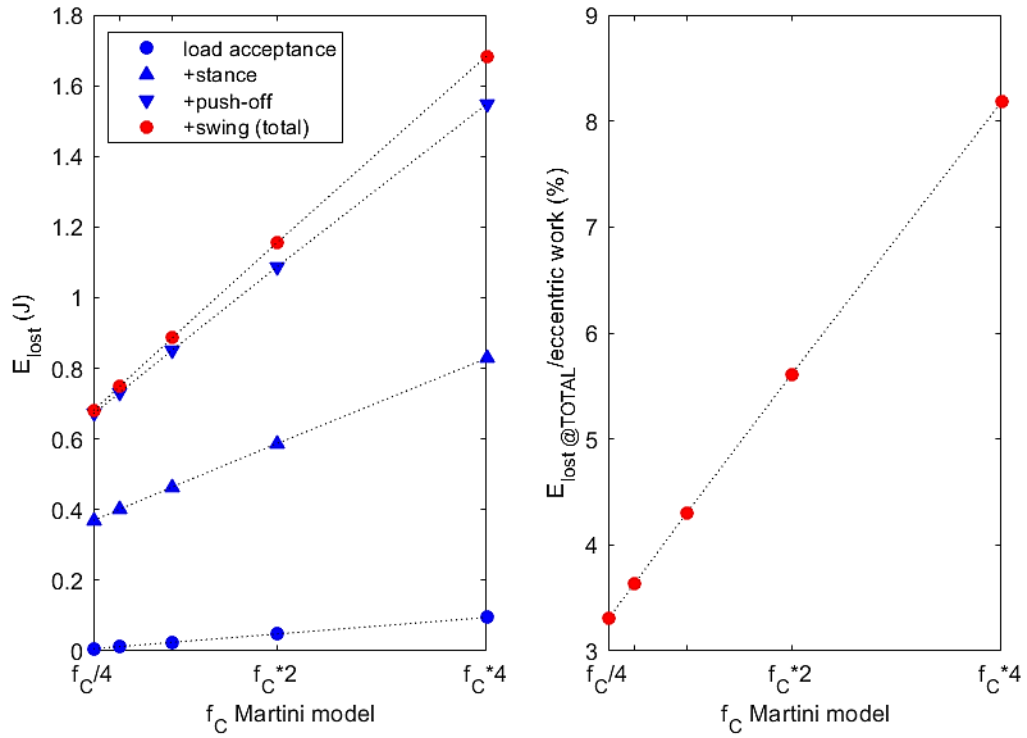
Figure 7.5 Sensitivity of energy lost because of O-ring friction to changes in f_C. The plot on the left shows how the phase losses accumulate to give the total loss over the whole gait cycle (J). The plot on the right shows the total energy loss as a percentage of the total eccentric work done by the prosthetic ankle.

7.2.5 Flow losses

7.2.5.1 Varying pipe diameter (D_{pipe})

Pipe diameter (D_{pipe}) is a secondary independent variable whose value affects not only major flow losses in pipes, according to equation (4.60) (see section 4.5.1), but also minor flow losses in discrete components such as inlets, exits, bends and DCVs, as equations (4.61) and (4.63) show (see section 4.5.2). For the final design, the chosen value of D_{pipe} is $5mm$ (see Table 7.1), and the range used for the sensitivity study is shown in the first column of Table 7.7. Specifically, the upper ($10mm$) and lower ($2mm$) limits of this range were considered to be realistic. Given that a change in D_{pipe} leads to a change in the pressure drops across pipes and also discrete components, Table 7.7 displays the energy losses attributed to pipes, DCVs and "fittings" (i.e. inlets, exits and 90° elbows), and the total (sum of these three terms), when only D_{pipe} varies. The energy lost (Table 7.7 and Figure 7.6) is evaluated by integration of the flow loss powers (equations (5.35) and (5.36) in section 5.3.7).

D_{pipe} (mm)	$E_{lost@TOTAL}(J)$				% eccentric work
	pipes	*DCVs*	*fittings*	*total*	*total*
2	0.2782	0.0054	0.1117	0.3953	1.92
3	0.0546	0.0011	0.0223	0.0780	0.38
4	0.0173	0.0003	0.0071	0.0247	0.12
5	0.0071	0.0001	0.0029	0.0101	0.05
6	0.0034	$0.0673e - 03$	0.0014	0.0049	0.02
7	0.0018	$0.0364e - 03$	0.0008	0.0026	0.01
8	0.0011	$0.0213e - 03$	0.0004	0.0015	$7e - 03$
9	0.0007	$0.0133e - 03$	0.0003	0.0010	$5e - 03$
10	0.0004	$0.0087e - 03$	0.0002	0.0006	$3e - 03$

Table 7.7 Sensitivity of energy lost across pipes, DCVs and fittings to changes in D_{pipe}. From left to right: values of D_{pipe}; energy losses over the whole gait cycle across pipes, DCVs and fittings (J); and total energy loss over the whole gait cycle (J and as a percentage of the total eccentric work done by the prosthetic ankle).

Major and minor losses over the gait cycle increase as the pipe diameter decreases. Specifically, for very small values of D_{pipe} ($< 3mm$), the total energy lost across pipes, inlets,

exits, 90° elbows and DCVs exceeds 1% of the total eccentric work, primarily because of the major flow losses across pipes. In particular, it can be seen from Figure 7.6 that the relationship is very non-linear and there are diminishing returns if the pipe diameter is increased above $5mm$. So, by chance, the "realistic" pipe diameter selected for the final design is a good choice, leading to very small flow losses of 0.05% of the total eccentric work done by the prosthetic ankle.
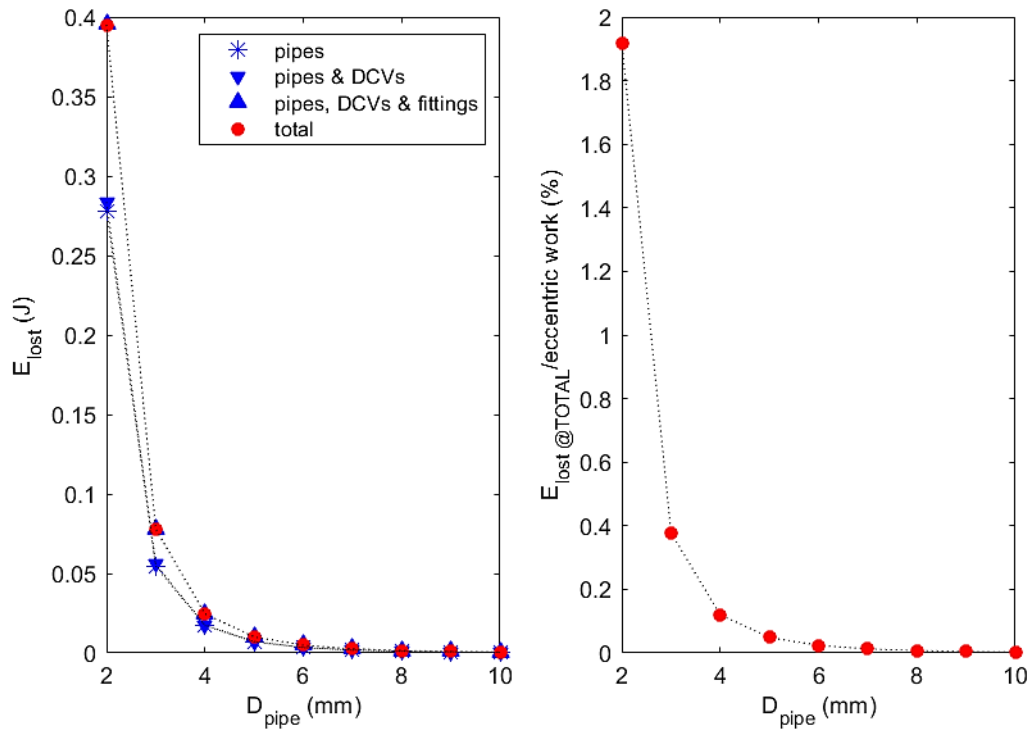
Figure 7.6 Sensitivity of energy lost across pipes, DCVs and fittings to changes in D_{pipe}. The plot on the left shows how the losses across pipes, DCVs and fittings accumulate over the whole gait cycle to give the total loss (J). The plot on the right shows the total energy loss over the whole gait cycle as a percentage of the total eccentric work done by the prosthetic ankle.

7.2.5.2 Varying pipe length (L_{pipe})

Unlike pipe diameter, pipe length (L_{pipe}) is a secondary independent variable whose value affects only major flow losses in the pipes between the two rams and the accumulator (there are no pipes between the rams and tank), according to equation (4.60) (section 4.5.1). For the final design, the chosen value of L_{pipe} is $50mm$ (see Table 7.1), and the range chosen for the sensitivity study is shown in the first column of Table 7.8. Specifically, the upper ($150mm$) and lower ($10mm$) limits of this range were considered to be realistic. For $5mm$ diameter pipes, Table 7.8 and Figure 7.7 display the energy losses across the pipes evaluated by integration of the flow loss power (equations (5.35) and (5.36) in section 5.3.7), but considering only the pressure drops across pipes.

L_{pipe} (mm)	$E_{lost@LA}(J)$	$E_{lost@STANCE}(J)$	$E_{lost@PO}(J)$	$E_{lost@SWING}(J)$	$E_{lost@TOTAL}(J)$	%eccentric work
10	0	0.0005	0.0009	0	0.0014	$6.80e-03$
30	0	0.0014	0.0028	0	0.0042	0.02
50	0	0.0023	0.0047	0	0.0071	0.03
70	0	0.0033	0.0066	0	0.0099	0.05
90	0	0.0042	0.0085	0	0.0127	0.06
110	0	0.0052	0.0104	0	0.0155	0.08
130	0	0.0061	0.0123	0	0.0184	0.09
150	0	0.0070	0.0142	0	0.0212	0.10

Table 7.8 Sensitivity of energy lost because of pipe flow losses to changes in L_{pipe}. From left to right: values of L_{pipe}; energy loss in each phase (J); and energy loss over the whole gait cycle (J and as a percentage of the total eccentric work done by the prosthetic ankle).

Pipe flow losses over the gait cycle increase almost linearly as the pipe length increases. For $5mm$ diameter pipes, the energy lost across the pipes is negligible: 0.1% of the total eccentric work for $L_{pipe} = 150mm$.
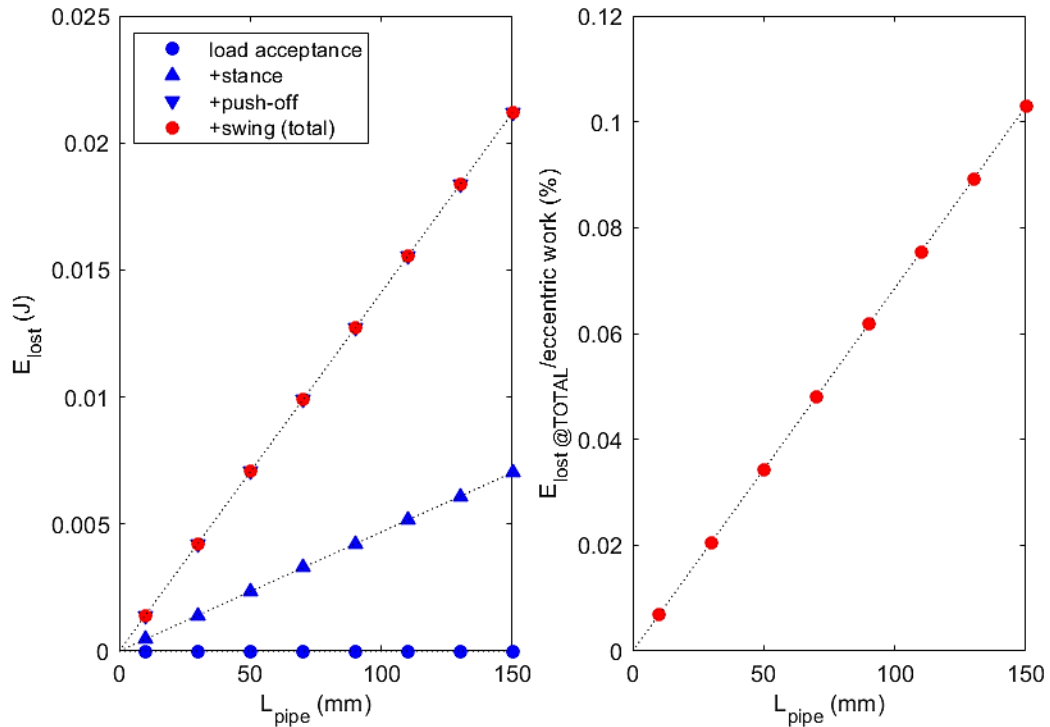
Figure 7.7 Sensitivity of energy lost because of pipe flow losses to changes in L_{pipe}. The plot on the left shows how the phase losses accumulate to give the total loss over the whole gait cycle (J), noting that the pipe flow losses are zero during load acceptance and swing because both rams are connected to tank. The plot on the right shows the total energy loss as a percentage of the total eccentric work done by the prosthetic ankle.

The contour plot below (Figure 7.8) shows how pipe flow losses vary with both pipe length and diameter. As expected from equation (4.60) (section 4.5.1), a larger pipe diameter and shorter pipe length reduce the energy lost. Pipes longer than $40mm$ combined with very small diameters ($D_{pipe} \leq 3mm$), generate energy losses larger than 1% of the total eccentric work. In conclusion, the pipe diameter selected for the final design is a good choice, leading to very small flow losses even when the pipe length is $150mm$ (i.e. 0.1% of the total eccentric work done by the prosthetic ankle).
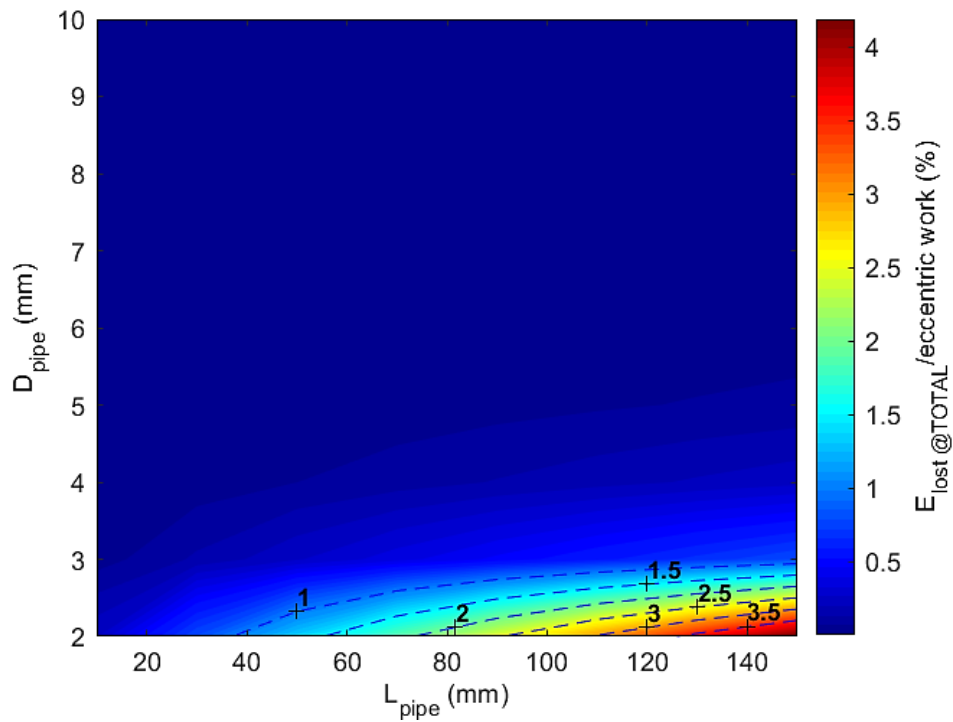
Figure 7.8 Sensitivity of energy lost because of pipe flow losses to changes in L_{pipe} and D_{pipe}. The energy loss is displayed as a percentage of the total eccentric work done by the prosthetic ankle.

7.2.5.3 Varying discrete components parameters ($K_{entrance}$, K_{elbow})

Minor flow losses across the discrete components (i.e. inlets, exits and 90° elbows) depend not only on D_{pipe} (see section 7.2.5.1), but also on the dimensionless loss coefficients K for each discrete component, as equation (4.60) (section 4.5.2) shows. Typical values of these loss coefficients found in the literature are: $K_{entrance}$ varies between 0.05 for a rounded entrance and 0.5 for a sharp-edged entrance (Durfee *et al.*, 2015), $K_{exit} = 1$ for both a sharp-edged and a rounded exit (Durfee *et al.*, 2015), and K_{elbow} varies between 0.2 (Durfee *et al.*, 2015) and 0.9 (Cundiff, 2002). For the final design, the chosen values of K (see Table 7.1) coincide with the conservative end of the ranges found in literature, generating the largest pressure drops (e.g. $K_{entrance} = 0.5$ is the maximum value for a sharp-edged entrance). The ranges considered for the sensitivity study are based on the values quoted in Figure 4.10: K_{exit} remains equal to 1; $K_{entrance}$ is varied between 0.05 and 1 in increments of 0.15; and K_{elbow} is varied between 0.2 and 1 in increments of 0.1.

The MATLAB code used so far was revised to add a fifth *for* loop so that, for each value of $K_{entrance}$, K_{elbow} is varied over the chosen range, and the cam profiles and return springs are re-evaluated for each combination of $K_{entrance}$ and K_{elbow}. Figure 7.9 shows the total energy lost across inlets, exits and 90° elbows, evaluated using equations (5.35) and (5.36) (section 5.3.7), but considering only the pressure drops across these three discrete components as follows:

$$P_{fittings} = -Q\Delta P_{fittings\ to\ tank} \qquad \text{during non-working phases}$$
$$P_{fittings} = -Q\Delta P_{fittings\ to\ acc} \qquad \text{during working phases}$$

Referring to Figure 7.9, as expected, the total energy lost across inlets, exits and 90° elbows over the gait cycle increases as both of the loss coefficients increase. However, even when $K_{entrance} = K_{elbow} = K_{exit} = 1$, the energy losses are very small (approximately 0.02% of the total eccentric work). In conclusion, the flow losses across the discrete components are unlikely to be an issue unless the hydraulic circuit becomes very tortuous with many changes of direction (i.e. elbows).
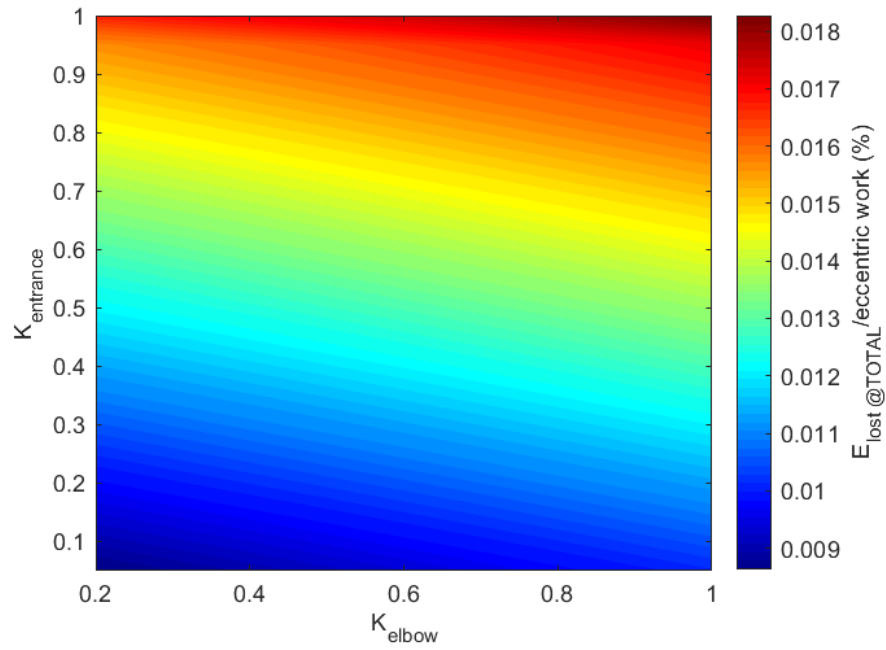
Figure 7.9 Sensitivity of energy lost because of flow losses in discrete components to changes in $K_{entrance}$ and K_{elbow} (K_{exit} always equals 1). The energy loss is displayed as a percentage of the total eccentric work done by the prosthetic ankle.

7.2.6   Heat losses from the accumulator

Over the short duration of the gait cycle, the charge and discharge of the accumulator is assumed to be approximately adiabatic. However, over many gait cycles, heat losses from the gas to the surroundings through the accumulator wall ($T_{wall} = T_{env} = 293K$) need to be taken into account, which is based on Newton's law of cooling (see equation (5.40) in section 5.3). These losses are modelled using the heat transfer model described by Pourmovahed and Otis (1990) based on the thermal time-constant (τ) (see equation (A.17) in Appendix A.5), so that the gas temperature changes are evaluated at each instant of the gait cycle using equation (4.79) (section 4.6.3). The thermal time constant includes the convection heat transfer coefficient (h_{N_2}), whose typical values for gases involved in a free convection process are between $2\frac{W}{m^2 \cdot K}$ and $25\frac{W}{m^2 \cdot K}$ (e.g. $h_{air} = 10\frac{W}{m^2 \cdot K}$) (Bergman *et al.*, 2011, p. 8). The conservative end of this range was chosen ($h_{N_2} = 25\frac{W}{m^2 \cdot K}$, see Table 7.1), and the range considered for the sensitivity study is shown in the first column of Table 7.9. The energy lost (Table 7.9 and Figure 7.10) is evaluated by integration of the heat transfer power ($P_{loss_{HEAT}}$) (equation (5.40) in section 5.3).

h_{N_2} $(\frac{W}{m^2 \cdot K})$	$E_{lost@LA}(J)$	$E_{lost@STANCE}(J)$	$E_{lost@PO}(J)$	$E_{lost@SWING}(J)$	$E_{lost@TOTAL}(J)$	%eccentric work
0.5	0	0.0038	0.0017	0.0011	0.0066	0.03
1	0	0.0076	0.0034	0.0021	0.0131	0.06
2	0	0.0152	0.0068	0.0043	0.0263	0.13
4	0	0.0305	0.0135	0.0086	0.0526	0.26
6.25	0	0.0476	0.0211	0.0134	0.0821	0.40
8	0	0.0609	0.0270	0.0172	0.1051	0.51
12.5	0	0.0952	0.0422	0.0268	0.1643	0.80
25	0	0.1904	0.0845	0.0537	0.3285	1.60
50	0	0.3808	0.1689	0.1073	0.6571	3.19
100	0	0.7617	0.3379	0.2146	1.3142	6.38

Table 7.9 Sensitivity of energy lost because of heat transfer to changes in h_{N_2}. From left to right: values of h_{N_2}; energy loss in each phase (*J*); and energy loss over the whole gait cycle (*J* and as a percentage of the total eccentric work done by the prosthetic ankle).
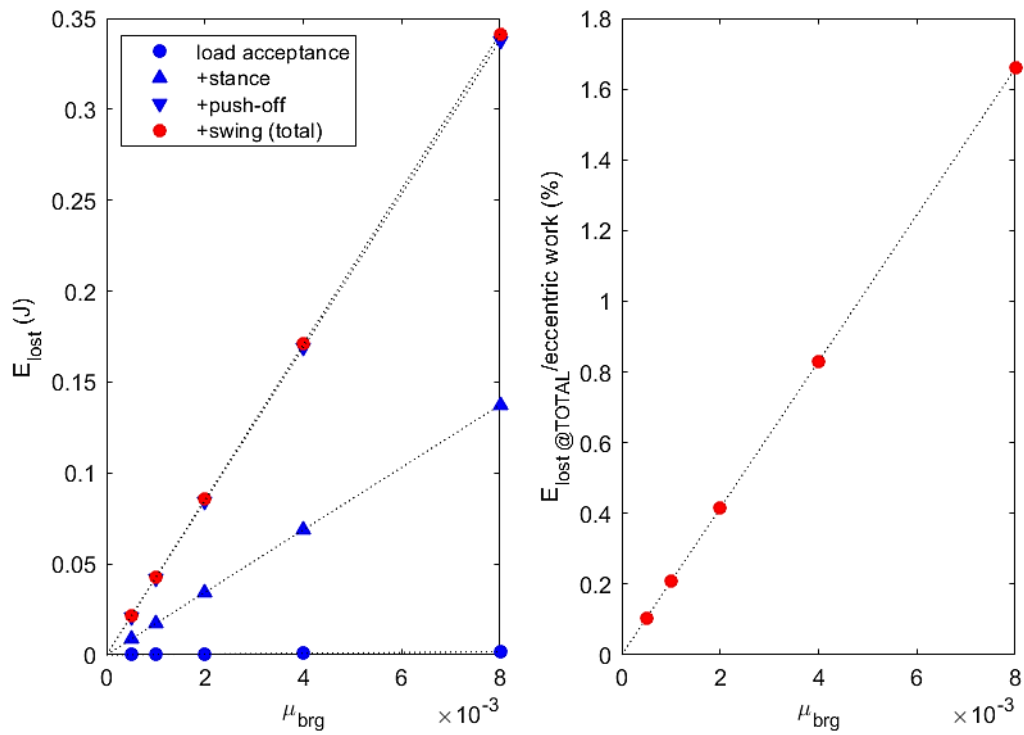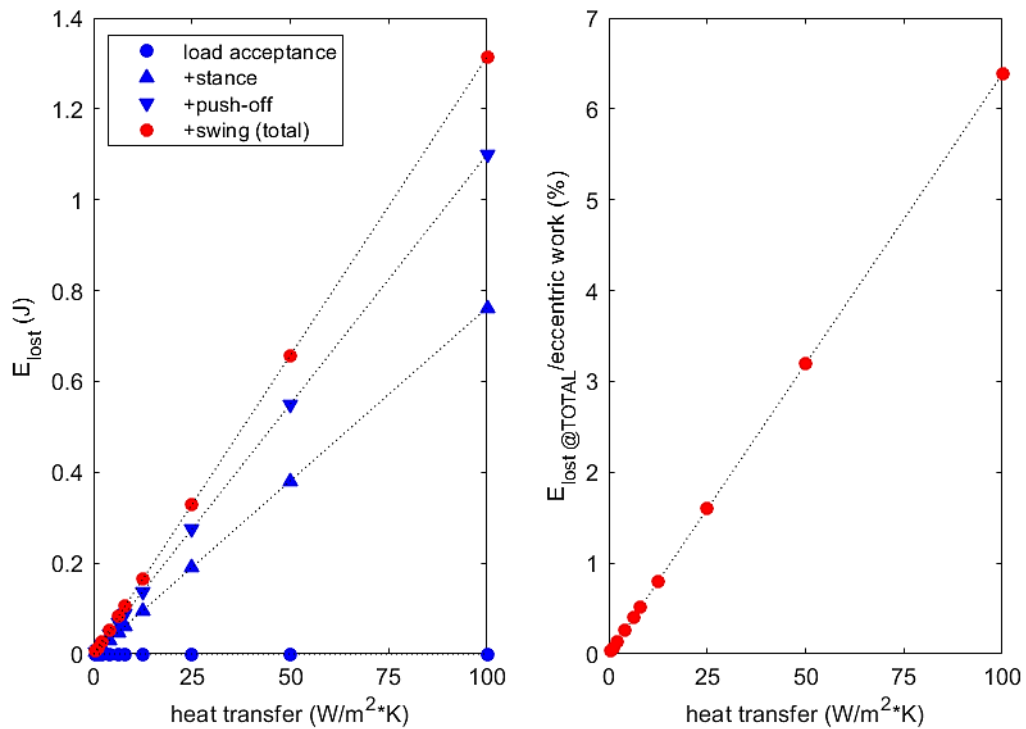
Figure 7.10 Sensitivity of energy lost because of heat transfer to changes in h_{N_2}. The plot on the left shows how the phase losses accumulate to give the total loss over the whole gait cycle (J). The plot on the right shows the total energy loss as a percentage of the total eccentric work done by the prosthetic ankle.

The energy lost from the accumulator because of heat transfer over the gait cycle increases almost linearly as the convection heat transfer coefficient (h_{N_2}) increases. The value chosen for the final design ($h_{N_2} = 25\frac{W}{m^2 \cdot K}$) is at the conservative end of the typical range of heat transfer coefficients for gases involved in a free convection process. This generates an energy loss of 1.60% of the total eccentric work and, as a result, heat transfer is the second largest energy loss in the system.

To reduce the heat losses, the accumulator could be insulated so that the inside surface of the accumulator wall is no longer at $T_{env} = 293K$. Indeed, in this case, it could be assumed the inside surface of the wall is at the gas temperature and heat transfer occurs through conduction, where the convective heat transfer coefficient (h_{N_2}) is replaced by k/s, where k is the thermal conductivity of the wall material and s is the wall thickness. For illustration only, for a composite wall with thermal conductivity of $0.045 \frac{W}{m \cdot K}$ (2020) and a wall thickness of

$0.005m$, the convective heat transfer coefficient is replaced by $k/_S = 9\frac{W}{m^2 \cdot K}$, which would reduce the heat losses to approximately 0.58% of the total eccentric work.

7.3   Conclusions

The energy losses in the final design are summarised in Figure 7.1 and Table 7.2. The total energy lost over the gait cycle is 8.21% of the total eccentric work. Compressibility losses at valve transitions are no more than 0.6% of the total eccentric work, but it would be sensible to continue to model them in case that figure increases in future designs. The sensitivity study reported in section 7.2 provides some insight into how these losses might be reduced and where strict design constraints are necessary to avoid higher losses.

The largest source of energy loss in the final design is O-ring friction (4.30% of the total eccentric work). To reduce this, a lower O-ring squeeze ratio could be used. With the selected O-ring of given hardness, the minimum value of f_C consistent with a realistic but low squeeze ratio ($\varepsilon = 0.07$) is $f_C = 0.476$, which generates energy losses of over 3.64% of the total eccentric work.

The second largest source of energy loss in the final design is heat loss from the accumulator (1.60% of the total eccentric work). However, this is based on a convective model of heat transfer that assumes the accumulator wall provides no insulation. Conversely and for illustration only, if the accumulator is insulated, so that heat transfer occurs through conduction, using a composite accumulator wall of thickness $0.005m$ would reduce the heat losses to approximately 0.58% of the total eccentric work.

The three sources of friction in the cam-roller-follower assemblies also result in significant energy losses in the final design. Rolling resistance between cam and roller contributes 1% of the total eccentric work, which was based on a conservative value for the coefficient of rolling resistance of $\mu_{rolres} = 0.002$. It may be possible to achieve $\mu_{rolres} = 0.001$ and, hence, reduce this energy loss to 0.50% of the total eccentric work. Similarly, if the roller bearing coefficient of friction (μ_{brg}) could be reduced from 0.002 to 0.001, then roller bearing friction

losses could be reduced from 0.41% to 0.21% of the total eccentric work. The value chosen for the follower bearing coefficient of friction is $\mu_{sl} = 0.003$ and this already leads to relatively low sliding friction losses of 0.26% of the total eccentric work.

The flow losses in the final design are negligible, being 0.05% of the total eccentric work. The sensitivity study confirmed that, as long as the pipe diameter is not reduced below $5mm$, even with $L_{pipe} = 150mm$ and $K = 1$ for all fittings, they are unlikely to exceed 0.2% of the total eccentric work.

In conclusion, if the changes suggested above could be implemented, then it may be possible to reduce the total energy losses over the gait cycle, associated with the parameters listed in Table 7.1, by almost a third to 5.83% of the total eccentric work.

8. Chapter 8: Conclusions

Image from the "The Creation of Adam",
a fresco by Michelangelo Buonarroti (c. 1508-1512)
in the Sistine Chapel (Rome)

"Do not merely practice your art,

but force your way into its secrets;

it deserves that, for only art and science can exalt man to divinity"

(Ludwig Van Beethoven (1812), Letter to Emilie)

The overarching aim of this work was to design a novel prosthetic ankle based on simple miniature hydraulic components, including an accumulator for energy storage and return, to imitate the behaviour of an intact ankle. To achieve this, two objectives were defined, namely to develop the concept design and to demonstrate through simulations that the expected performance of the new design justifies physical prototyping in the future. The work undertaken to achieve these two objectives and related conclusions are reviewed in the following two sections.

8.1   The new design

A concept design (Figure 3.3) has been developed for a new hydraulic prosthetic ankle. The ankle joint drives two cams, which in turn drive two hydraulic rams. A "stance cam-ram system" captures the eccentric (negative) work done from foot flat until maximum dorsiflexion, by pumping oil into the accumulator. A "push-off cam-ram system" returns concentric (positive) work during push-off to provide forward propulsion through fluid flowing from the accumulator to the ram. Each hydraulic ram is connected to the tank, so that its ram force is negligible, during the other ram's working phase, load acceptance and swing. The torsional spring, which works in parallel to the two cam-ram systems, is an approximate fit to ankle torque during load acceptance, thereby providing good load acceptance, ground clearance during swing, and contributing to standing stability.

The cams convert ankle rotation into linear motion of the hydraulic rams and vice versa. The cam profiles are designed to replicate an intact ankle's torque-versus-angle curve over their working phases. Taking into account other sources of torque such as the torsional spring, the stance cam's profile ensures that the ankle torque during mid and terminal stance (i.e. ankle dorsiflexion) mimics that of an intact ankle. Similarly, the push-off cam's profile ensures that the ankle torque during push-off (i.e. ankle plantarflexion) mimics that of an intact ankle.

Using two cam-rams means it is possible to store and return different amounts of energy during their two working phases. In this way, during level and downhill walking, the energy stored can exceed the energy returned. In other words, the excess eccentric work associated with the torque-versus-angle hysteresis loop can be captured. This excess energy can then be

carried forward to assist with short periods of uphill walking. Furthermore, even when the accumulator is full and, thus, it has reached maximum pressure, the ankle joint will continue to provide the necessary braking during downhill walking by using a pressure relief valve to dissipate eccentric work in the form of heat.

Although the work described in this thesis was limited to the design of the prosthetic ankle joint, the use of a single accumulator as a common energy store would allow a multi-joint version of the design to transfer energy between the knee and the ankle joints. For example, a cam-rams based device at the knee joint, similar to the one developed for this PhD work, could be connected to the same accumulator. In this way, it would be possible to store eccentric work done at the knee joint and return it at the ankle joint during push-off.

To estimate the size, particularly the height, of the new device, a solid model of the main components affecting height has been created in SolidWorks (v. 2014; Dassault Systemes Solidworks Corp.). This also serves as an illustration of how the components might be physically assembled. As explained in Chapter 3, the available height for the new prosthesis assembly, from the ground to the distal connection with the socket, is $28.38\,cm$, corresponding to a missing anatomy mass of approximately $2.43\,kg$. Keeping within this height would ensure the device is suitable for over 97% of transtibial amputees.

Referring to Figure 8.1, the new prosthetic ankle is envisioned as a modular component placed between a typical low-profile ESR foot, made of two carbon fibre laminates, and an integrated pylon-accumulator component not shown. The cams are part of the foot assembly, rotating with it relative to the shank, and the roller-follower-ram assembly is part of the shank. In this way, ankle joint rotation leads to the cams rotating relative to the roller-followers, converting ankle rotation into linear motion of the hydraulic rams and, hence, fluid flow between the rams and the accumulator or tank (Figure 8.2). The latter would be in the space surrounding the hydraulic rams. Components not shown include the parallel spring, the self-aligning linear ball bearings guiding the followers, DCVs, and other hydraulic components. The connection between the prosthetic ankle and the distal end of the pylon is realised through the male adapter on the top of the ankle unit, and the pipes connecting the rams to the accumulator

pass through the adapter. The proximal end of the pylon is then connected to the distal end of the socket through a male adapter.

male adapter

novel hydraulic ankle prosthesis with aesthetic cover

typical low-profile ESR foot
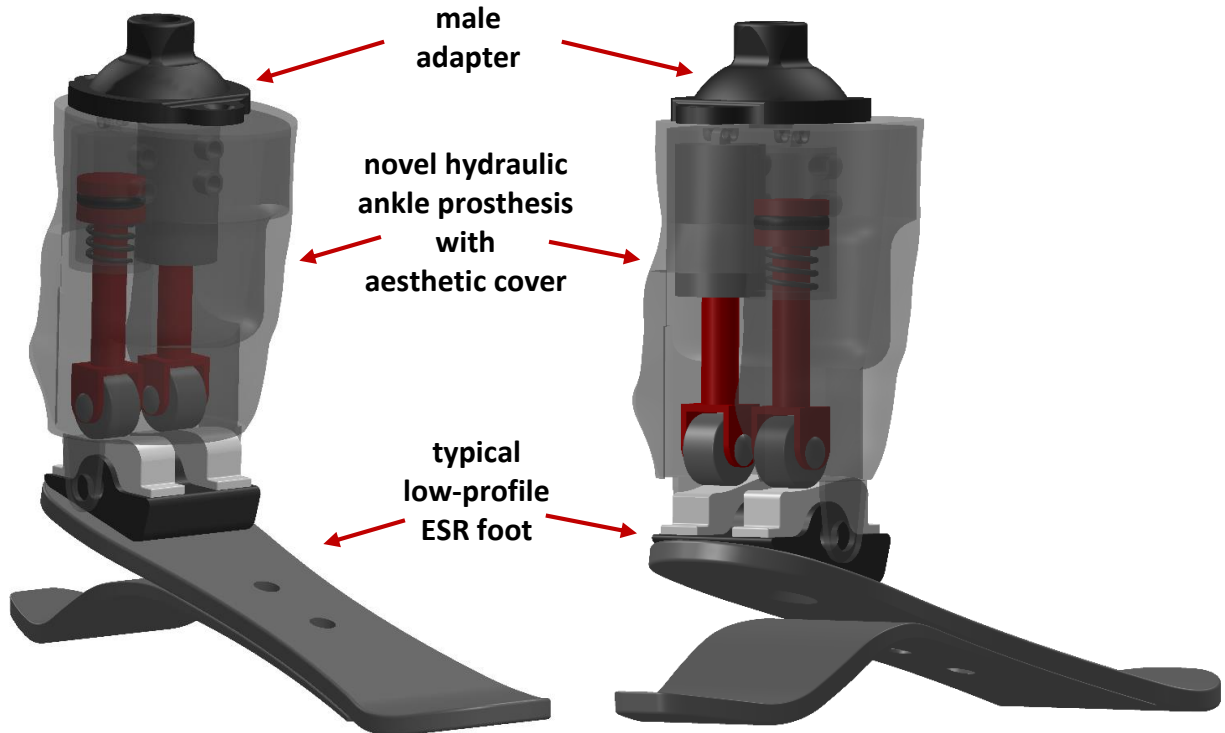
Figure 8.1 Solid model of the main components of the novel hydraulic ankle prosthesis (cams, rollers, followers, rams) enclosed in an aesthetic cover and connected to a typical low-profile ESR foot (two carbon fibre laminates). Data for the two cam profiles (the two white components) were exported to Solidworks from the MATLAB design program and automatically fitted to splines. The 2D cam profiles are shown in Appendix B.1.

To / From the ACCUMULATOR via pipes

Oil flow from the stance ram to store energy

Oil flow to the push-off ram to return energy

STANCE ram

PUSH-OFF ram

follower return spring

STANCE roller

PUSH-OFF roller

STANCE cam

PUSH-OFF cam

ankle joint rotation axis
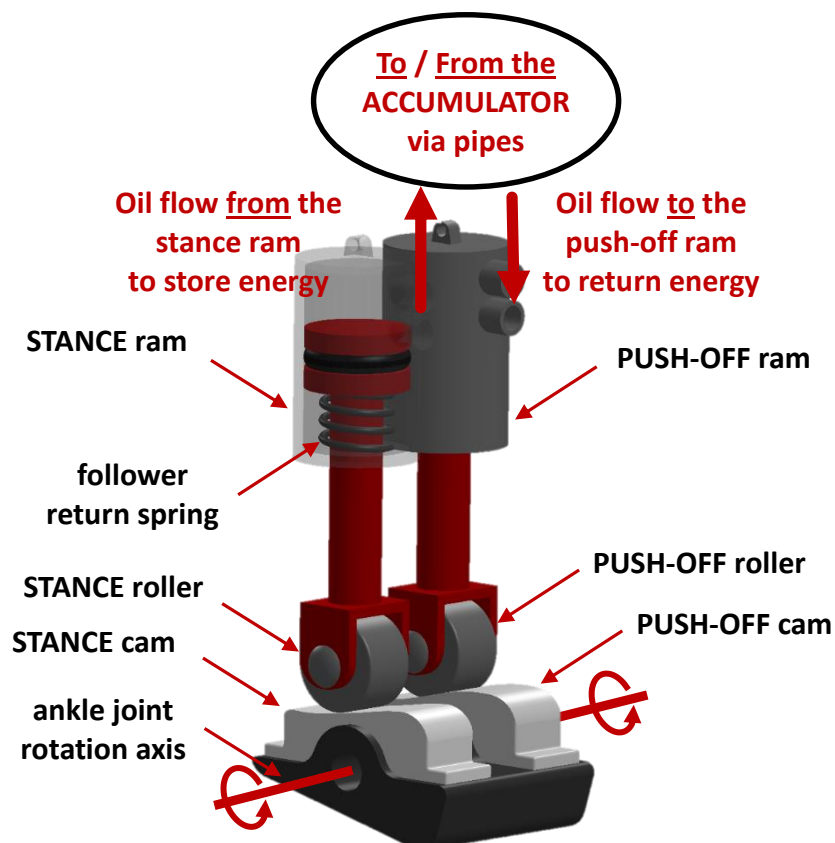
Figure 8.2 Exploded view of the main components of the novel hydraulic ankle prosthesis: cams, rollers, followers, and hydraulic rams.

A rough estimate of the height of the whole prosthesis is obtained as follows:

- Approximately $16\,cm$ from the ground to the base of the male adapter pyramid, corresponding to the distal end of the pylon, as shown in Figure 8.3 with the pistons in full outstroke.

- The bespoke accumulator is envisioned as a cylinder with a base radius of approximately $3\,cm$ and a height of $10\,cm$ (Appendix A.5). This is integrated with the prosthesis pylon, which will therefore have a $6\,cm$ internal diameter, whereas $3\,cm$ is a typical pylon internal diameter. The pylon height, including the two tubular adapters at its ends, needs to include the accumulator and to allow connection with the ankle unit and the distal end of the socket. Thus, a total pylon height of $12\,cm$ is estimated, from the base of the male adapter pyramid up to the distal end of the socket.

Therefore, the estimated prosthesis height from the ground to the distal end of the socket is approximately $28\,cm$, which is within the available height of $28.38\,cm$ for the whole assembly. A rough estimate of the mass of the prosthesis is derived in Appendix E. Using conservative assumptions, the estimated mass is $2.35\,kg$, which is comparable with the missing anatomy mass of approximately $2.43\,kg$.

In conclusion, it has been shown that the main components of the system – cams, rams, and accumulator - could be physically realistic, matching the size and the mass of the missing anatomy.
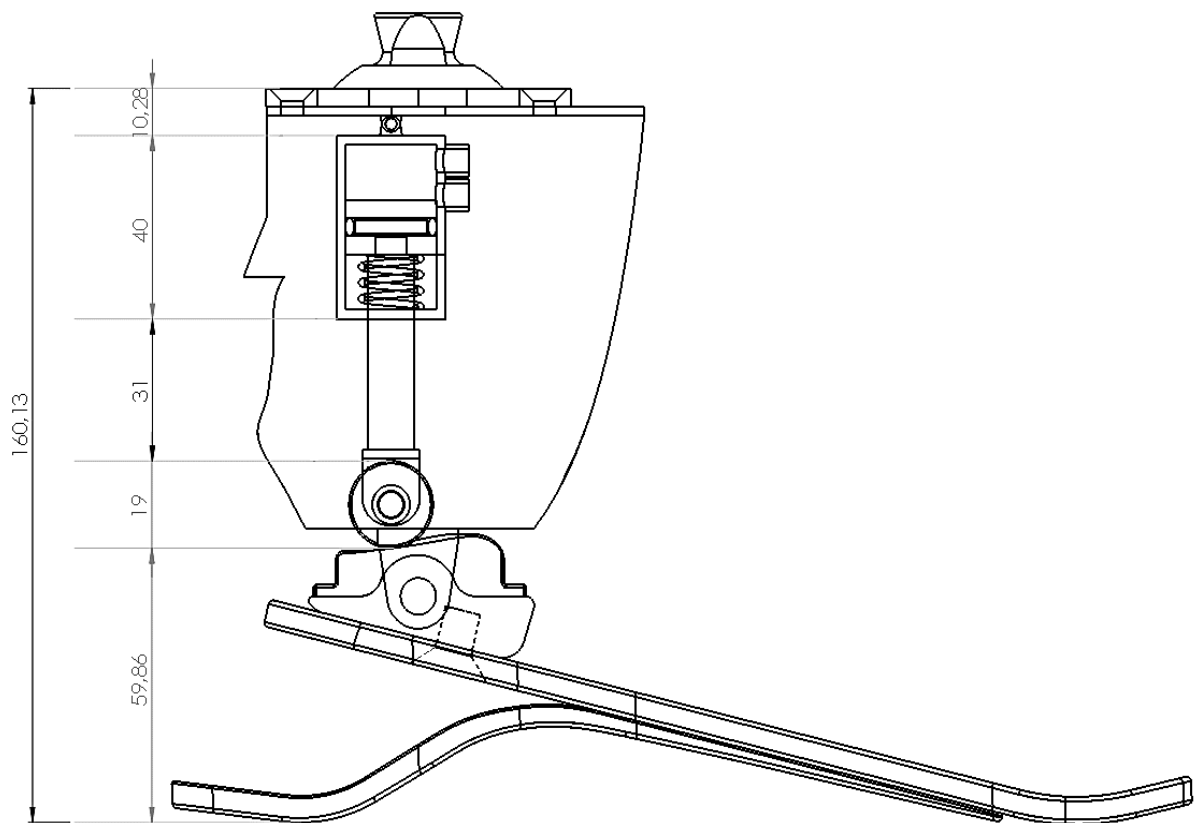
Figure 8.3 Lateral view of the prosthetic foot and novel hydraulic ankle (derived from the solid model in Figure 8.1). The height of selected components and the total height are shown in mm.

8.2   Simulated performance

A mathematical model of the new hydraulic prosthetic ankle was defined (Chapter 4), including each of its components and considering all significant sources of energy loss, in order to obtain a realistic estimate of the performance of the new device and its efficiency. Based on this mathematical model, a simulation model of the whole system was implemented in MATLAB (Chapter 5), which simulates its operation over the whole gait cycle, as it stores and returns energy at the ankle joint. A design program, based upon the simulation model, was used to design the profiles of the two cams to replicate the intact ankle torque, and to specify the two follower return springs (Chapters 5 and 6).

The two cam-ram systems were designed to achieve good performances in their working phases only (Chapter 6). Energy losses not directly associated with the two cam-rams in their working phases were neglected, because it was assumed these would have little effect on the selected cam-ram design parameters. Maximum hydraulic pressure, ram bore, and cam-follower configuration were optimised based on the results of multiple MATLAB simulations to minimise energy losses while achieving realistic overall dimensions.

Figure 8.4 shows that, with the input ankle angle curve being that of a particular intact ankle, the system almost perfectly replicates the torque and power curves of this intact ankle during the two working phases (i.e. from foot flat to toe-off). This differs from simulations and in-vivo testing results of unpowered and powered clutch-and-spring devices (see Figure 2.17 and Figure 2.33 for a comparison), while it confirms the good results that can be obtained using hydraulics (see Figure 2.35 for the simulation results of a hydraulic prosthetic knee developed at Cleveland State University by van den Bogert et al. (2012)). However, because the torsional spring is only an approximate fit to the ankle torque during load acceptance, the match is less good during load acceptance and swing. The disadvantage of using the same spring to bring the ankle back to neutral during swing is that, during push-off plantarflexion, the spring stores more energy than needed to return the foot to neutral during swing. This energy corresponds to the smaller peak in power straight after the push-off peak and is wasted (dissipated) during swing (Figure 8.4, black solid line in right hand plot).
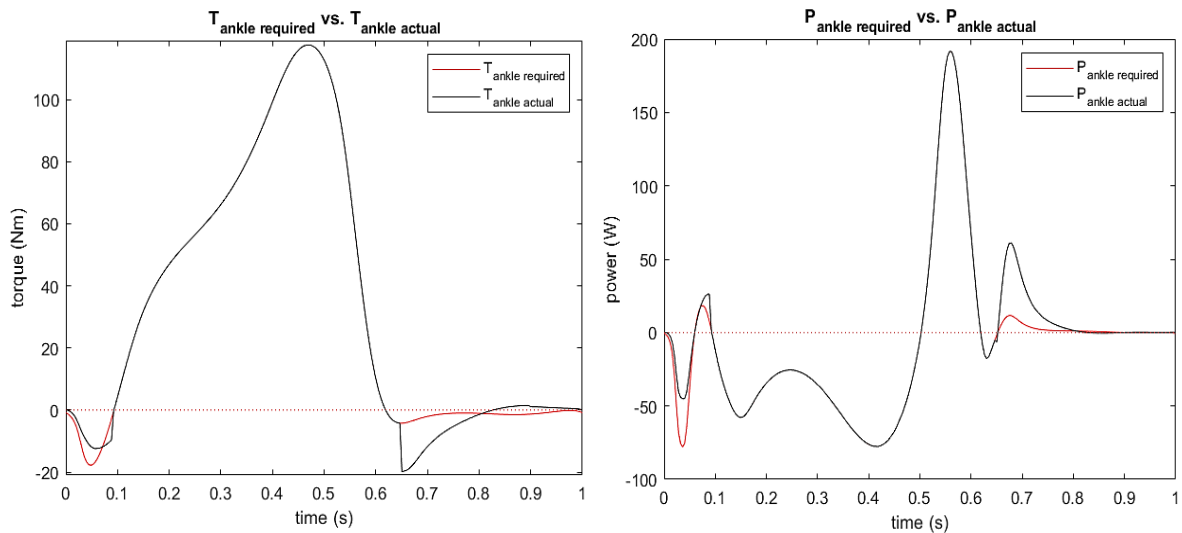
Figure 8.4 Torque (on the left) and power (on the right) at the prosthetic ankle joint; providing a comparison between the required (red solid line) – from an anatomically intact subject - and the actual (black solid line) over the gait cycle.

In Chapter 7, firstly, the different sources of energy loss in the final design established in Chapter 6 are considered to identify the most significant sources. Chapter 7 then presents the results of a sensitivity study, in which the values of the design parameters were varied over sensible ranges to establish where energy losses may be particularly sensitive to changes in the design parameters and, hence, strict constraints need to be imposed.

Figure 8.5 shows the energy flows in the new design, over the whole gait cycle, including: the eccentric work done, corresponding to the external energy input; the concentric work done, mainly during push-off; energy losses; and the net energy stored and carried forward for future gait cycles (e.g. for ascending slopes). The energy losses over the whole gait cycle are 8.21% of the total eccentric work done by the prosthetic ankle.
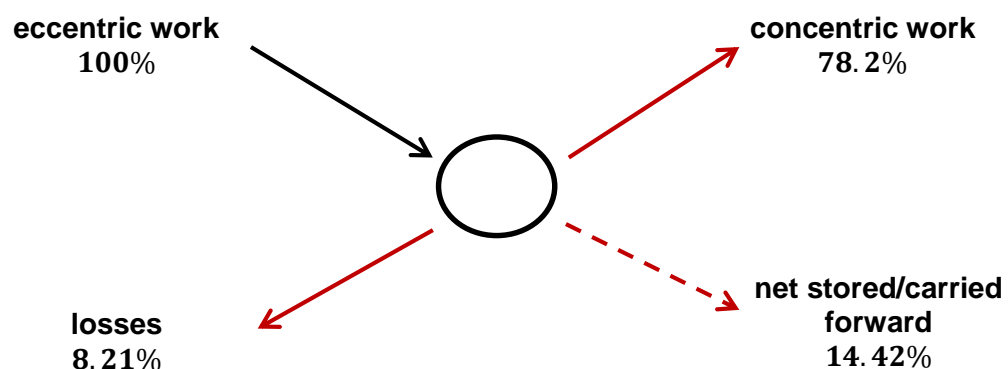
Figure 8.5 Energy flows (percentages) in the new hydraulic ankle over the whole gait cycle.

The largest source of energy loss in the final design is O-ring friction (4.30% of the total eccentric work), followed by heat loss from the accumulator (1.60%) and friction in the cam-roller-follower assemblies (1.67% in total). The compressibility losses amount to 0.6% of the total eccentric work, while flow losses are negligible (0.05%) and, as long as the pipe diameter is not reduced below $5mm$, they are unlikely to exceed 0.2%. With the changes suggested in Chapter 7, it may be possible to reduce the total energy lost over the gait cycle to 5.83% of the total eccentric work.

This device, therefore, is far more efficient than, for instance, the hydraulic orthosis designed by Kangude *et al.* (2009) : the energy stored in the accumulator during mid and terminal stance amounts to approximately $17.29J$, corresponding to almost 84% of the total eccentric ankle work, and $14.32J$ are then released from the accumulator during push-off, of which $11.90J$ are available at the ankle joint, corresponding to almost 69% of the total stored energy in the accumulator, as compared with only 7.40% in Kangude's orthosis.

8.3 Novel contributions

The novel contributions of this PhD work fall into two groups, namely: those related to the novelty of the new design; and those related to the modelling, simulation and design methods.

a) Novelty of the new design:
- The use of cams enables biomimetic joint-torque curves to be reproduced.
- By using two cam-rams, it is possible to follow different joint-torque versus joint-angle curves during different phases of the gait cycle, which is a feature of normal gait. In other words, hysteresis like curves can be followed.
- By using two cam-rams, it is possible to store and return different amounts of energy during different phases of the gait cycle. In this way, during level and downhill walking, the energy stored can exceed the energy returned, and the excess energy can be carried forward to assist with short periods of uphill walking.
- In multi-joint systems (e.g. trans-femoral prostheses and exoskeletons), the use of a single energy store (i.e. an accumulator) means that energy can be transferred

between joints. For example, higher level amputees would benefit if the excess of eccentric work at the knee could be stored and used in a controlled manner at the ankle for push-off. Hydraulic actuation is ideally suited for transferring energy between joints because the transfer mechanism involves only pipes and fluid, rather than gears and linkages.

- The design could be combined with a battery-powered system to reduce the energy storage and recharge requirements. For example, an electrically driven pump could be used to recharge the accumulator. This could be useful for extended periods of uphill walking. Alternatively, a hand driven pump could be used to recharge the accumulator.

b) Novelty of the modelling, simulation and design methods:

- A comprehensive mathematical model, which includes all significant sources of energy loss, has been defined and, based upon it, a simulation model implemented in MATLAB.

- A novel design program has been created, which uses the simulation model to design the profiles of the two cams to replicate the intact ankle torque, and to specify the two follower return springs.

- Design and sensitivity studies have been undertaken to establish a set of design parameters that minimise energy losses while achieving realistic overall dimensions.

8.4 Limitations and recommendations for future work

a) The main inputs to the simulation-based design program are the ankle angle and torque over the gait cycle. Experimental averaged data from anatomically intact subjects walking at self-selected speed on level ground, from Bari (2013), were used. Although it is within the range of data seen in healthy gait, this input data is optimistic with respect to the amount of eccentric work done. Optimistic data were used because it is believed that amputees could benefit from walking in a manner that provides good push-off if it reduces their metabolic cost of walking. Therefore, the clinical feasibility of the new design will depend on whether the eccentric ankle work needed prior to push-off is justified by the

benefits of a more normal push-off, which can only be investigated by in-vivo testing with amputees (Gardiner *et al.*, 2017).

b) The cam profiles are specified according to the required ankle torque-versus-angle curve used as input to the design program. This means that cam profiles could be unique to the amputee, providing a personalised prosthesis. Indeed the cams could be manufactured in the prosthetics clinic using a rapid manufacturing technique such as 3D printing or CNC machining. To achieve this, methods could be developed for basing the required ankle torque-versus-angle curve for first prescription on the amputee's anthropometric, health, fitness and activity characteristics. According to the principle of prioritising design simplicity, cams will be the only components that the prosthetist needs to manufacture in clinic, while all the other components will be standardised.

c) The new device comprises two cam-ram systems designed for their respective working phases only, during which they are connected to the accumulator, and they are otherwise connected to the tank. The parallel spring is an approximate fit to the ankle torque during load acceptance only. The disadvantage is that, during push-off plantarflexion, the spring stores more energy than needed to return the foot to neutral during swing and this excess energy is lost (dissipated). Therefore, it may be worthwhile to consider design changes to reduce the energy lost in this way. This could potentially increase the stored energy carried forward by $2.6\,J$ per gait cycle.

The parallel spring is also designed to contribute to standing stability. However, according to the literature, the quasi-stiffness of the ankle joint during standing is much larger than during stance (Figure 8.6). It has been estimated that the prosthetic ankle stiffness for standing should be three times higher than for walking (Shepherd & Rouse, 2017), which is itself considerably higher than that needed for load acceptance. So it may also be useful to consider design changes to better support standing.
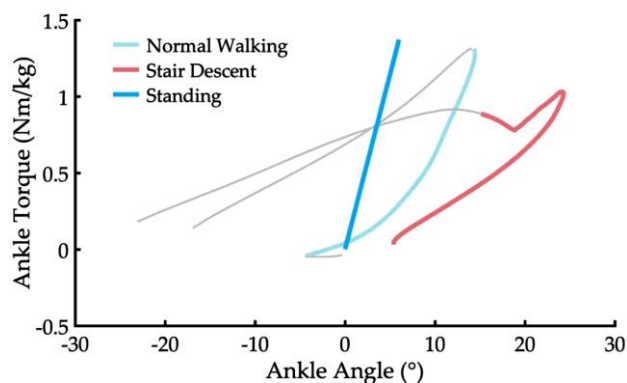
Figure 8.6 Torque-versus-angle curve for an anatomically intact ankle joint during normal walking, stair descent and standing. The coloured portions correspond to dorsiflexion during stance for normal walking, and to heel strike to toe-off for stair descent. Positive angles correspond to dorsiflexion and positive torque to an internal plantarflexion moment. Image source: Shepherd and Rouse (2017).

In principle, the four phases of gait that are clearly visible in the ankle torque-versus-angle curve (i.e. load acceptance, foot flat to heel lift, push-off, and swing) and standing could all have a dedicated cam-ram system. However, this would require further miniaturisation and probably the inclusion of a gearbox to increase the rotation of the cam-shaft.

d) The novel hydraulic ankle has been designed for level walking only. Therefore, future work should investigate the feasibility of including real-time adaptation to different slopes, stairs and walking speed, possibly through the use of 3D cams so that the effective 2D cam could be changed to suit the conditions.

e) Two key assumptions made in the simulation model are that: a) the new prosthetic ankle operates with "perfect control", meaning that valve transitions are instantaneous and occur at the ideal moments; and b) the cam profiles are ideal so that, in the two cam-ram working phases, the required ankle torque is achieved. Furthermore, the electrical power required by the control system has not been considered. Although this would be primarily for control, not for propulsion, the required battery size still needs to be established.

Hence, future work should develop and test a control architecture for detecting gait events, driving valve transitions, and adjusting 3D cam-follower configuration for terrain and speed adaptation. Clearly, this is as big a challenge as the mechanical design.

f) Once the mechanical and control issues described above have been satisfactorily resolved, the research should move on to design for manufacture, physical prototyping, and in-vivo testing with amputees. This will raise many practical issues that cannot be studied through modelling and simulation.

As previously mentioned, the use of cams with subject-specific profiles will allow for a personalised lower-limb prosthesis. Cam profiles for first prescription would be manufactured based on ankle torque-versus-ankle angle curves for both level and slope walking and over a range of walking speeds averaged over a number of anatomically intact subjects with similar anthropometric, health, fitness and activity characteristics.

Then in vivo-testing will disclose the ankle response for different walking conditions in terms of speed and slope. This will allow, in turn, further optimisation to accommodate variations in individual ankle response detected through gait analysis. Specifically, a second prescription with optimised 3D cam profiles will follow to match subject-specific ankle torque-versus-ankle angle curves for both level and slope walking averaged over a range of walking speeds. A second gait analysis will provide a check that the prosthesis ankle response is correct over different walking conditions, promoting lower-limbs walking symmetry and reducing compensatory mechanisms at the lower-limb joints.

g) While this PhD work covers the design of a prosthetic ankle joint aimed mainly at transtibial amputees, a similar design for a prosthetic knee together with an energy transfer system between the knee and the ankle joints is envisioned in future work on a system for transfemoral amputees.

The design of a hydraulic knee would be based on the knee's torque-versus-angle curve (Figure 8.7). Specifically, two cam-ram systems could be used to replicate the large hysteresis loop associated with swing. These would produce biomimetic knee torques during swing and store the excess of eccentric work at the knee that is dissipated in commercially available devices. The steeper loop associated with stance could be achieved in the conventional way with a knee lock and a spring to provide stance phase knee flexion.

211
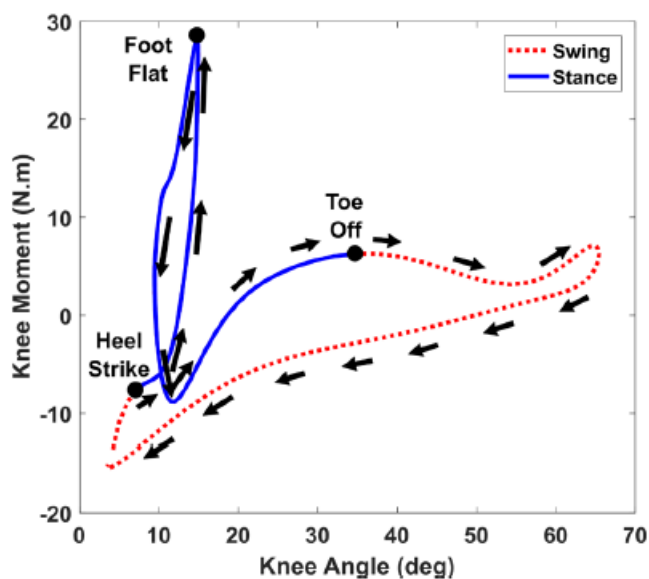
Figure 8.7 Torque-versus-angle curve for an anatomically intact knee joint during a complete gait cycle of level walking. Figure adapted from Saivimal et al. (2018).

Transfemoral amputees could benefit from energy transfer between the knee and the ankle joints, with a single accumulator and cam-ram based joints at the knee and ankle. The use of a single accumulator as a common energy store means that there is no need to explicitly provide for synchronisation between joints. In other words, apart from sharing the accumulator, the two joints can operate independently. In this way, eccentric work at both ankle and knee could be captured, increasing the stored energy carried forward to assist with short periods of uphill walking. This stored energy could be returned either at the ankle for push-off or at the knee for climbing stairs or slopes or for other demanding tasks, although the latter would need a system that could adapt to different terrains as mentioned above. Once the feasibility of a multi-joint system for transfemoral amputees has been demonstrated, future work could investigate the feasibility of using a similar approach for exoskeletons.

Appendix A:

More about the physics of the system

A.1 Roller radial load

For the roller, the equivalent dynamic bearing load is equal to the radial load acting on the bearing: $P = F_{rad}$ (SKF, 2013, p. 1117).
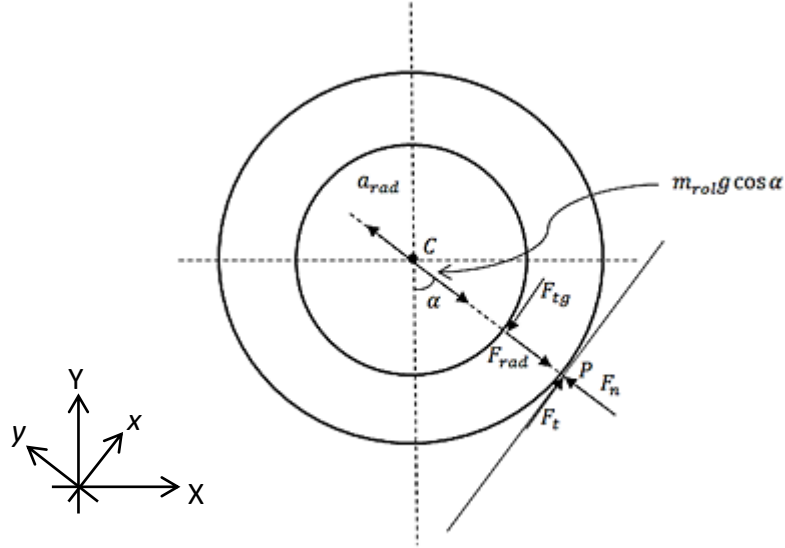
Figure A. 1 Free-body diagram of the roller-follower, highlighting the presence of the bearing and considering the forces acting on it.

Applying Newton's 2nd law in the direction normal to cam surface (considering the *xy*-plane in Figure A. 1), the radial load F_{rad} acting on the bearing is calculated as follows:

$$\sum F_y = m_{rol} a_{rad} \qquad F_n - F_{rad} - m_{rol} g \cos \alpha = m_{rol} a_{rad} \qquad \text{(A. 1)}$$

with $a_{rad} = \ddot{y} \cos \alpha$ (i.e. acceleration of the roller in the radial direction), and m_{rol} the mass of the rotating outer part of the roller. So, the complete expression for the radial load is:

$$F_{rad} = F_n - m_{rol} \cos \alpha \, (g + \ddot{y}) \qquad \text{(A. 2)}$$

At this stage, it is important to understand how much F_{rad} might differ from the normal force F_n acting on cam profile, so as to consider a possible approximation of F_{rad} to F_n. To do this, the mass of the rotating outer part of the roller (m_{rol}) needs to be estimated.

For the purpose of this estimation, a reasonable value for the roller-follower radius r was used: $r = \frac{0.019}{2}$ m. Starting from this, the other dimensions of the cam follower derived from SKF catalogue (SKF, 2013, pp. 1140-1141) (Figure A. 2):

$$B \quad = \quad 0.032 \; m;$$

$$B_1 \quad = \quad 0.020 \; m;$$

$$C \quad = \quad 0.011 \; m;$$

$$d_1 \quad = \quad 0.015 \; m;$$

$$d_{brg} \quad = \quad 0.011 \; m \text{ (bearing bore diameter)};$$

$$D \quad = \quad 0.019 \; m;$$

$$m \quad = \quad 0.032 \; kg \text{ (average roller mass value)};$$

$$m_{rol} \quad = \quad \rho_{ss} V_{rol} = 7700 \, \frac{kg}{m^3} \cdot \pi \cdot 6.6e - 07 \; m^3 \cong 0.016 \; kg \tag{A. 3}$$
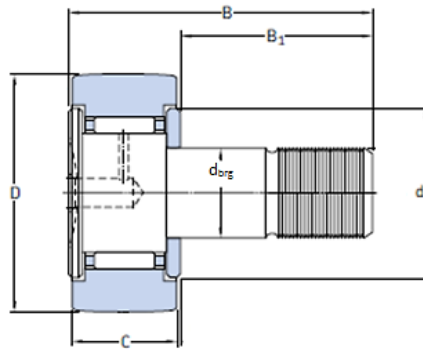
Figure A. 2 Engineering drawing of a cam follower (SKF, 2013, p. 1140).

Assuming that the whole cam follower is made of stainless steel, $\rho_{ss} = 7700 \, \frac{kg}{m^3}$ (The Physics Factbook); and the approximate volume of the rotating outer part of the roller (V_{rol}) is calculated as follows:

$$V_{rol} = C\pi \left((\frac{D}{2})^2 - (\frac{d_{brg}}{2})^2 \right) = \pi \cdot 6.6e - 07 \; m^3 \tag{A. 4}$$

The previously calculated mass m_{rol} is close to the mass of a "support roller" - the most similar component to the rolling part of a cam follower from catalogue, which is included between

0.019 kg and 0.021 kg (SKF, 2013, p. 1134). This means that the estimation of the mass of the rotating outer part of the roller is correct. Therefore, the moment of inertia of the rotating outer part of the roller is evaluated as follows:

$$I_{rol} = \frac{1}{2}m_{rol}\left(\left(\frac{D}{2}\right)^2 + \left(\frac{d_{brg}}{2}\right)^2\right) = 9.62e - 07 \; kg \cdot m^2 \qquad \text{(A. 5)}$$

Going back to equation (A. 2), the maximum percentage error between the two forces F_{rad} and F_n along the whole gait cycle is evaluated as follows:

$$percentage \; error = \left\|\frac{F_{rad} - F_n}{F_{rad}}\right\| \times 100 \qquad \text{(A. 6)}$$

The maximum percentage error is approximately equal to 0.0053% during the working phase of the stance system and to 0.0057% during the working phase of the push-off system. This means that, from now on, it is reasonable to assume $F_{rad} \cong F_n$, neglecting the other term in equation (A. 2). Thus, equation (4.35) becomes:

$$M_{brg} = sign(\dot{\beta}) \cdot \mu_{brg} \cdot \frac{d_{brg}}{2} \cdot |F_n| \; (Nm) \qquad \text{(A. 7)}$$

A.2 Rolling resistance element in the power audit

This appendix explains the reason for the introduction of a rolling resistance element between cam and roller in the power audit.

The contact point P on cam surface is the same as point P on the roller, as well as the translation of point P on cam is the same as the one of point P on the roller. Therefore, there aren't relative translations between P on the cam and P on the roller: they remain coincident. However, cam and roller have different angular velocities – respectively ω_C and $\dot{\beta}$, so that the angular velocity of the same point P on the two surfaces is different. Consequently, the power generated by the cam and transmitted to the roller due to the translational velocity of P is the same, whereas the power generated by the cam and transmitted to the roller due to the angular velocity of P is different. For this reason, it is necessary to introduce a third mechanical component between cam and roller to model properly the contact region (schematic in Figure A. 3) and the power loss existing there because of the rolling resistance and the different angular velocities. It is possible to model the contact region as a damper (see Figure A. 4), since this is a well-known mechanical element to dissipate energy in a system.
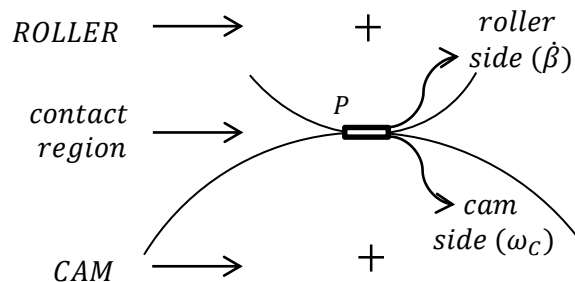
Figure A. 3 Schematic of the contact region between cam and roller.

As Figure A. 4 shows, the rolling resistance M_{rolres} is acting on the roller in the opposite direction to the angular velocity $\dot{\beta}$ – i.e. the clockwise direction; therefore, it will act on the cam in the opposite direction – i.e. anticlockwise, which is the same direction of the rotation of the cam. At the same time, it will act on the two sides of the rolling resistance element – cam side and roller side – with opposite directions to those of the two respective adjacent components. Moreover, each side of the rolling resistance element is characterised by the same angular velocity of the adjacent component. It follows that:

- The power generated by the cam is equal to the one transmitted to the next element - i.e. the rolling resistance element, the damper – and it is given by the sum of the positive power due to F_n and F_t and the negative term given by M_{rolres}. Here, M_{rolres} is multiplied by ω_C since this is the angular velocity characterising the next element, which is the cam side of the rolling resistance element. They have opposite direction, so that M_{rolres} generates negative power into the damper.

- The power generated by the damper is equal to the one transmitted to the roller and it is given by the sum of the positive power acting on the roller due to F_n and F_t and the negative term given by M_{rolres}. Here, M_{rolres} is multiplied by $\dot{\beta}$ as this is the angular velocity characterising the next element, which is the roller. They have opposite direction, so that M_{rolres} generates negative power into the roller.
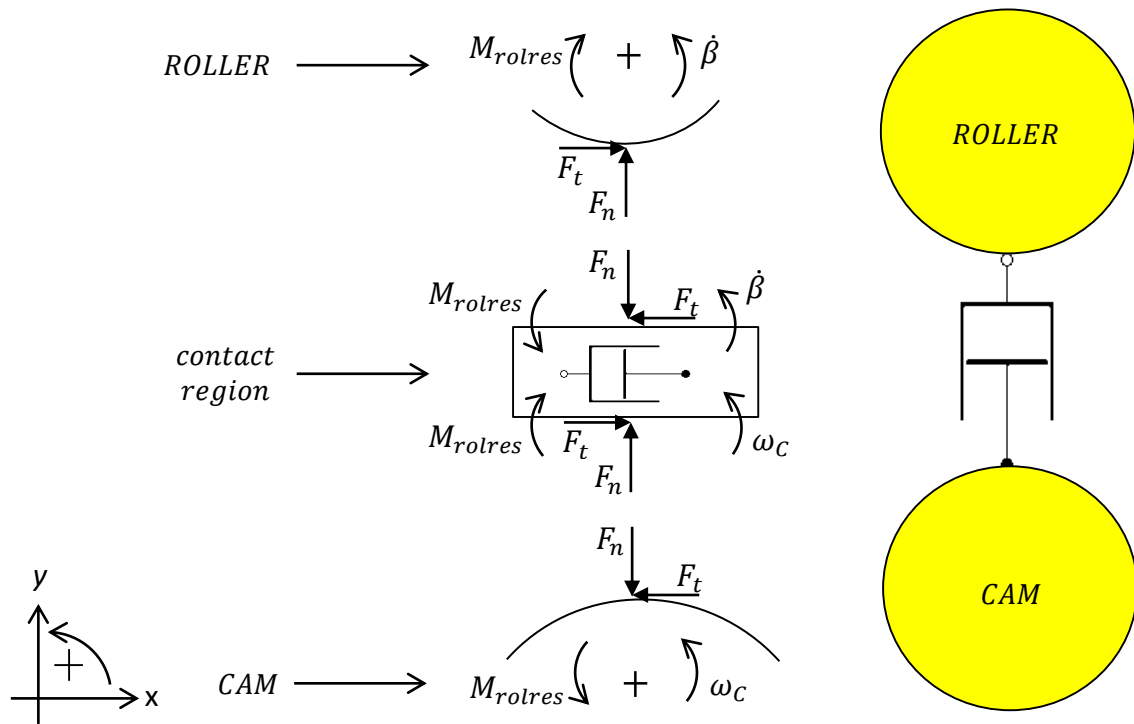
Figure A. 4 Schematic of the cam, the roller and the rolling resistance at the contact region modelled as a mechanical element – damper – to properly define energy dissipation between cam and roller.

The difference between the power transmitted to and generated by the damper represents, precisely, the power loss due to rolling resistance:

$$P_{fr_{rolres}} = M_{rolres}\omega_{rel} = M_{rolres}(\dot{\beta} - \omega_C) \tag{A. 8}$$

A.3 Xia et al.'s friction model vs. Martini's friction model

The comparison between the two friction models was conducted considering a ram bore diameter equals to $20\ mm$. Specifically, looking at Parker 's O-ring catalogue (Parker Hannifin, 2007b), the closest dimension for the bore diameter is $0.812\ in$, equal to $20.62\ mm$, for an O-ring 2-207. The section below shows the calculations of the frictional forces at the piston O-ring with the two models: Xia et al.'s friction model (Xia & Durfee, 2011b), and Martini's friction model (Martini, 1984).

Xia &Durfee's model

The total frictional force at the cylinder O-ring is defined as follows:

$$F_{fr_{cyl}} = \pi \mu_f D d_{O-ring} E \varepsilon \sqrt{2\varepsilon - \varepsilon^2} =$$

$$= \pi \cdot 0.4 \cdot 0.02062 \cdot \frac{0.139}{39.3701} \cdot 10^7 \cdot 0.07144 \cong 65.37 N$$

(A. 9)

where $D = \frac{0.812 \text{in}}{39.3701 \frac{\text{in}}{m}} \cong 0.02062 m$ is the ram bore and $d_{O-ring} = \frac{0.139 \text{in}}{39.3701 \frac{\text{in}}{m}} \cong 0.00353 m$ the O-ring cross-section diameter.

Martini's model

The total dynamic frictional force is defined as $F_{fr_{cyl}} = F_H + F_C$ where F_H is the friction due to differential pressure across O-ring cross section, while F_C is the friction due to O-ring cross-sectional squeeze. All the values in Martini's formulae are expressed according to the British Imperial system of units. According to what explained in section 4.4.2, the pressure dependent term of the frictional force is evaluated as follows:

$$F_{H_{cyl}} = \text{A}f_H = 0.299 \cdot 43.64 \cong 13.05 lb \cong 58.05 N$$

(A. 10)

where $d_{O-ring\_OUT} = 0.824 in$

$$d_{O-ring} = 0.139in$$

$$D_m = (d_{O-ring\_OUT} - d_{O-ring}) = 0.824 - 0.139 = 0.685in$$

$$A = \pi D_m d_{O-ring} = 0.299in^2$$

$$f_H = 0.545(\Delta P)^{0.61} = 0.545(P_{cyl} - P_{atm})^{0.61} =$$

$$= 0.545\left((92 \cdot 10^5 Pa - 101325Pa) \cdot 0.000145038\frac{psi}{Pa}\right)^{0.61}$$

$$= 0.545(1319.65)^{0.61} = 43.64psi$$

Considering the maximum pressure achievable in the accumulator ($P_{max} = 100bar$), the cross-sectional squeeze dependent term of the frictional force is evaluated as follows:

$$F_{C_{cyl}} = L_0 f_C = 2.58 \cdot 0.952 = 2.46lb \cong 10.96N \tag{A. 11}$$

where $L_0 = \pi d_{O-ring\_OUT} = 2.58in$

$$f_C = (-0.884 + 0.0206H_S - 0.0001H_S{}^2)S_W =$$

$$= (-0.884 + 0.0206 \cdot 70 - 0.0001 \cdot 70^2) \cdot (100 * \varepsilon) =$$

$$= (-0.884 + 0.0206 \cdot 70 - 0.0001 \cdot 70^2) \cdot (100 * 0.14) = 0.952$$

Therefore, the resulting total frictional force at the O-ring is:

$$F_{fr_{cyl}} = F_{H_{cyl}} + F_{C_{cyl}} = 13.05lb + 2.46lb = 15.51lb \cong 69N \tag{A. 12}$$

In conclusion, Martini's model turned out to be the most conservative (i.e. characterised by the highest friction losses) and it also properly accounts for the differential pressure across the O-ring.

A.4 Working fluid

Neubauer (2017), in his PhD Thesis entitled "Principles of Small-Scale Hydraulic Systems for Human Assistive Machines", defines mineral oil as the preferred working fluid for use in human assistive hydraulic machines. Water based fluids are generally used in applications with elevated working temperatures due to the risk of ignition. This is not the case of human assistive machines, where operating temperatures of the fluid along with the surface temperatures of the machinery must remain low as it directly interfaces the human body. Moreover, mineral oils are non-toxic, they have a low chemical reactivity and low density making the system lighter than a system where water based working fluid are used.

Usually, the type of mineral oil to be used for a specific hydraulic application is given by the same manufacturers of hydraulic components. Looking at catalogues of hydraulic cylinders for big industrial application, they suggest using a mineral oil ISO VG 80-100, where VG specifies the "viscosity grade" of the oil, defined as the average viscosity in $\frac{mm^2}{s}$ at 40°C (see Figure A.5). An oil ISO VG 80-100 may be appropriate for big hydraulic components, but it may be too viscous for miniaturised hydraulics and really small pipes with a working temperature of approximately 20°C.
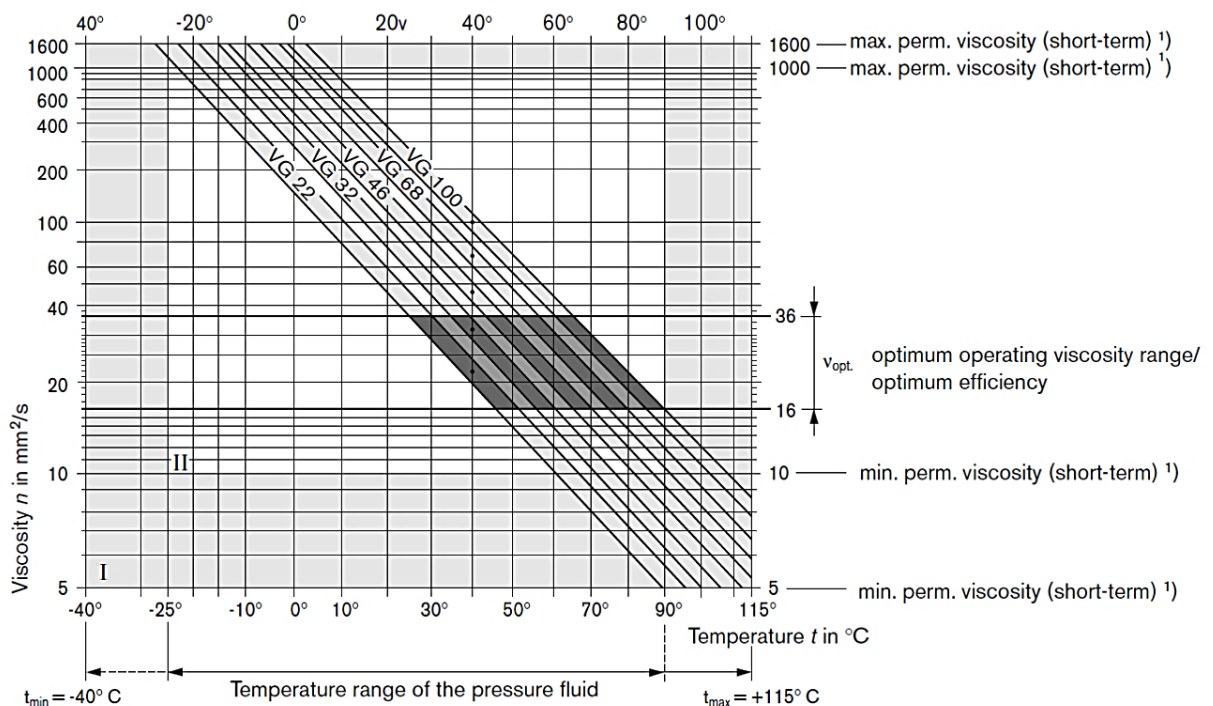
Figure A. 5 Selection chart of mineral-oil based fluids suitable for use with axial piston pumps and axial piston motors (Bosch Rexroth AG).

Looking at Bosch Rexroth AG (pp. 1-4) catalogue, $v_{operating} = 16 - 100 \frac{mm^2}{s}$ is defined as

the viscosity range for use with 100% operating time and $v_{optimum} = 16 - 36 \frac{mm^2}{s}$ as the

viscosity range for optimum efficiency. Hence, an oil in between an ISO VG 32 – recommended

for winter condition - and an ISO VG 46 – recommended for summer conditions or enclosed

spaces- should be considered. The chart in Figure A. 6 shows that, as the temperature

decreases from the 40°C of the viscosity grade definition to a normal operating temperature

(20°C), the viscosity will increase reaching values in between $80 - 100 \frac{mm^2}{s}$.
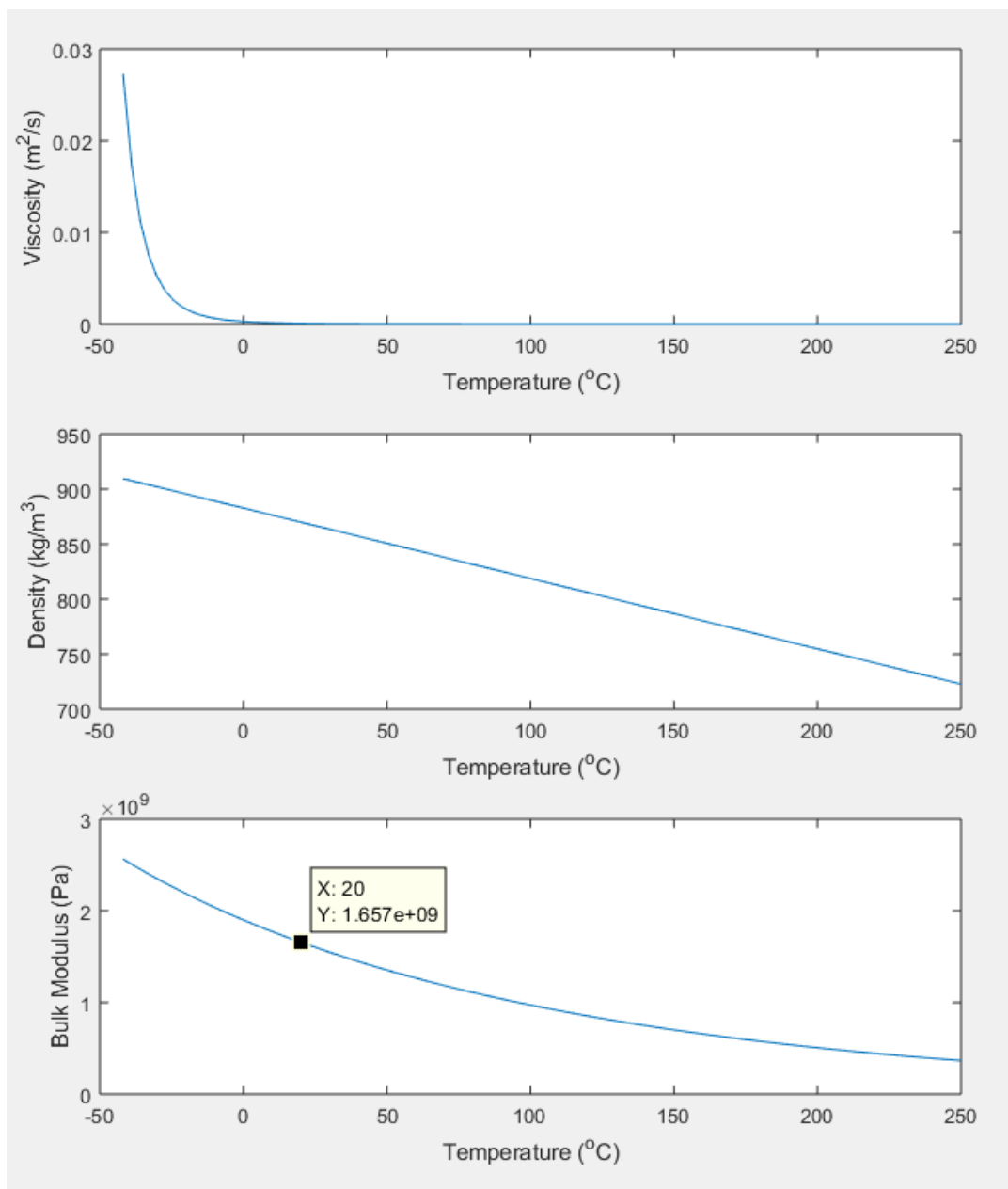
Figure A. 6 Properties of a mineral oil ISO VG 32 (ESSO UNIVIS N32) from the library "Hydraulics Utilities" of Simscape Fluids (Simulink, MathWorks, Massachusetts, USA.): kinematic viscosity (v), density (ρ) and bulk modulus (β).

A mineral oil ISO VG 32 was chosen. It is characterised by a kinematic viscosity $v = 32 \frac{mm^2}{s}$ at $40°C$, which increases when temperature decreases. The average density of these oils is $\rho = 870 \frac{kg}{m^3}$ (Neubauer, 2017, p. 17) and the bulk modulus is $\beta = 1.9e + 09\ Pa$. The library "Hydraulics Utilities" of Simscape Fluids (Simulink, The MathWorks Inc., Massachusetts, USA) contains the properties of different hydraulic fluids: for a mineral oil ISO VG 32 (ESSO UNIVIS N32) at $20°C$, the density is equal to the above-mentioned one ($\rho = 870 \frac{kg}{m^3}$), the kinematic viscosity is equal to $v = 79.87 \frac{mm^2}{s} \cong 80 \frac{mm^2}{s}$, and the bulk modulus is $\beta = 1.657e + 09\ Pa$ (Figure A. 6). Fluid properties in Simscape Fluids comes from the Skydrol family of hydraulic fluids, obtained from literature provided by the manufacturer Eastman Chemical Company (The MathWorks Inc., 2018).

In summary, the hydraulic fluid used for this specific application is characterised by: kinematic viscosity $v \cong 80 \frac{mm^2}{s}$, density $\rho = 870 \frac{kg}{m^3}$, $\beta = 1.657e + 09\ Pa$ (ISO VG 32 mineral oils have, usually, a relatively high bulk modulus, but smaller than water), and the resulting dynamic viscosity $u = v \cdot \rho = 80 \frac{mm^2}{s} \cdot 870 \frac{kg}{m^3} = 0.0696 Pa \cdot s \cong 0.07 Pa \cdot s$.

A check was done about the nature of the flow in pipes to appropriately estimate the pressure drop across them. To guarantee a laminar flow inside the pipes, the Reynolds' number should be less than 2300:

$$Re = \frac{4Q_{max}}{\pi D v_{f_{min}}} \leq 2300 \tag{A. 13}$$

The maximum flow obtained from MATLAB simulations during the two working phases of the system is approximately $Q_{max} = 7.50 \cdot 10^{-6} \frac{m^3}{s}$ (considering the best designs for the two cam-ram systems from Chapter 6 with $P_{max} = 100\ bar$ and ram bore $D = 0.020 m$). Considering also pipe diameter $D_{pipe} = 0.005\ m$ (as showed in section 4.5), equation (A. 13) can be rearranged to get the minimum viscosity to guarantee a laminar flow:

$$v_{f\,min} \geq \frac{4Q_{max}}{2300\pi D_{pipe}} = \frac{4 \cdot 7.50 \cdot 10^{-6}\frac{m^3}{s}}{2300\pi \cdot 0.005m} = 8.30 \cdot 10^{-7}\frac{m^2}{s}$$

$$v_{f\,min} \geq 0.830\frac{mm^2}{s} = 0.830cSt \tag{A. 14}$$

This is a tiny value for the kinematic viscosity of the fluid. This means that a mineral oil ISO VG 32 satisfies the condition of a laminar flow.

If pipe diameter decreases, for instance $D_{pipe} = 0.002\ m$, it yields:

$$v_{f\,min} \geq 2.08\frac{mm^2}{s} = 2.08cSt \tag{A. 15}$$

which is still a very small value in comparison with the kinematic viscosity of the selected mineral oil ISO VG 32.

Finally, considering the properties of the selected mineral oil, the maximum flow Q_{max} (from MATLAB), and $D_{pipe} = 0.005m$, Reynolds number was evaluated.

$$\mathrm{Re} = \frac{4Q_{max}}{\pi D_{pipe} v_f} = \frac{4 \cdot 7.50 \cdot 10^{-6}\frac{m^3}{s}}{\pi \cdot 0.005m \cdot 80 \cdot 10^{-6}\frac{m^2}{s}} \cong 23.87 \tag{A. 16}$$

The Reynolds' number is still smaller than 2300, so that the flow is laminar.

A.5 Thermal time constant calculation

The thermal time-constant τ described by Pourmovahed and Otis (1990) and used to model the relaxation process of the gas after a rapid compression or expansion in a gas-charged accumulator is defined as follows:

$$\tau = \frac{m_{N_2} C_V}{h_{N_2} A_W} \tag{A. 17}$$

where C_V is the specific heat at constant volume, h_{N_2} is the value of the convection heat transfer coefficient for nitrogen, and A_W is the effective area of the accumulator for heat convection (i.e. the total internal surface area exposed to gas). The thermal time constant (τ) represents the time needed by the gas pressure (or gas temperature) to drop by 63.2%. It was experimentally determined looking at a constant-volume pressure relaxation in response to a change in the gas volume. The worst situation is the one with a quick temperature decay, so with a very small τ. For this reason, to estimate the heat loss from the accumulator to the surroundings, conservative values of the parameters involved in equation (A. 17) were selected.

For a diatomic gas such as N_2, the specific heat at constant value is evaluated as follows:

$$C_V = \frac{5}{2} R = \frac{5}{2} \cdot 8.314 \frac{J}{mol \cdot K}$$
$$C_V = \frac{5}{2} \cdot 8.314 \frac{J}{mol \cdot K} \cdot \frac{1}{0.028014 \, ^{kg}/_{mol}} \cong 741.95 \frac{J}{kg \cdot K} \tag{A. 18}$$

Otherwise, directly from The Engineering ToolBox (2003): $C_V = 743 \frac{J}{kg \cdot K}$. To be conservative, the smallest value of C_V ($C_V \cong 741.95 \frac{J}{kg \cdot K}$) was used.

Likewise for A_w, according to a conservative approach, the total internal surface area exposed to gas in a diaphragm accumulator was considered to be equal to the total internal surface area of the accumulator. Considering $V_A = 250e - 06 \, m^3$ and the accumulator as a cylinder,

the total internal surface was evaluated as follows: $A_w = 2\pi r h_{acc} + 2 \cdot \pi r^2 = 2\pi r(h_{acc} + r)$, where r is the radius of the base of the accumulator and h_{acc} its height. Some trials were done to estimate reasonable values for r and h_{acc}. Using the volume formula $V_A = \pi r^2 h_{acc}$ and selecting different values of h_{acc}, the corresponding radii are:

$$1) \; h_{acc} = 0.050m \;\; \rightarrow \;\; r = \sqrt{\frac{V_A}{\pi h_{acc}}} = \sqrt{\frac{250e{-}06 \; m^3}{\pi 0.050m}} \cong 0.040m \tag{A. 19}$$

$$2) \; h_{acc} = 0.080m \;\; \rightarrow \;\; r = \sqrt{\frac{V_A}{\pi h_{acc}}} = \sqrt{\frac{250e{-}06 \; m^3}{\pi 0.080m}} \cong 0.031m \tag{A. 20}$$

$$3) \; h_{acc} = 0.100m \;\; \rightarrow \;\; r = \sqrt{\frac{V_A}{\pi h_{acc}}} = \sqrt{\frac{250e{-}06 \; m^3}{\pi 0.100m}} \cong 0.028m \tag{A. 21}$$

Given that the accumulator is envisioned to be integrated with the pylon of the prosthesis and, thus, reasonable sizes should be considered for its height and diameter, the third option was selected. Therefore, $A_w = 2\pi r(h_{acc} + r) = 2\pi \cdot 0.028m(0.100m + 0.028m) = 0.0225m^2$.

It is not easy to find an accurate value for h_{N_2}, since most of the times it refers to liquid nitrogen. Typical values of h_{N_2} for gases involved in a free convection process are included between $2 \frac{W}{m^2 \cdot K}$ and $25 \frac{W}{m^2 \cdot K}$ (Bergman *et al.*, 2011, p. 8), and $h_{N_2} = 25 \frac{W}{m^2 \cdot K}$ was chosen to be conservative.

As a result, the time-constant τ is evaluated as follows:

$$\tau = \frac{m_{N_2} C_V}{h_{N_2} A_W} = \frac{0.012942 \; kg \cdot 741.95 \frac{J}{kg \cdot K}}{25 \; W/_{m^2 \cdot K} \cdot 0.0225m^2} \cong 17.07s \tag{A. 22}$$

It is possible to evaluate the heat transfer between the gas and the surroundings (Q_{heat}) using the Newton's law of cooling as follows (Pourmovahed & Otis, 1990):

$$\frac{dQ_{heat}}{dt} = hA_w(T_w - T_{gas}) \tag{A. 23}$$

where T_w is defined as the "spatially averaged wall temperature" ($T_w = T_{env} = 293K$), T_{gas} as the bulk gas temperature, h as "the overall heat transfer coefficient" from the gas to the surrounds, and A_w as "the total internal surface area exposed to gas". In the same paper, h is defined also as the "convection heat transfer coefficient", being ($\frac{W}{m^2 \cdot K}$) its unit of measurement, so that $h = h_{N_2}$. Pourmovahed and Otis (1990) specified that it is not a real constant since it varies during the cooling process of the gas, but in many cases it is possible to consider it as constant without decreasing the accuracy of the calculations. Nevertheless, given the uncertainties about the value of h_{N_2}, a sensitivity study is conducted in Chapter 7 to check the sensitivity of the model - in terms of heat losses - with respect to changes in this design parameter.

Appendix B:

Test results and checks for the working phases

B.1 Cam profiles

Cam profile is designed in MATLAB using the mapping method described in section 4.3.1. Figure B. 1 shows the 2D profiles of the stance and the push-off cams.
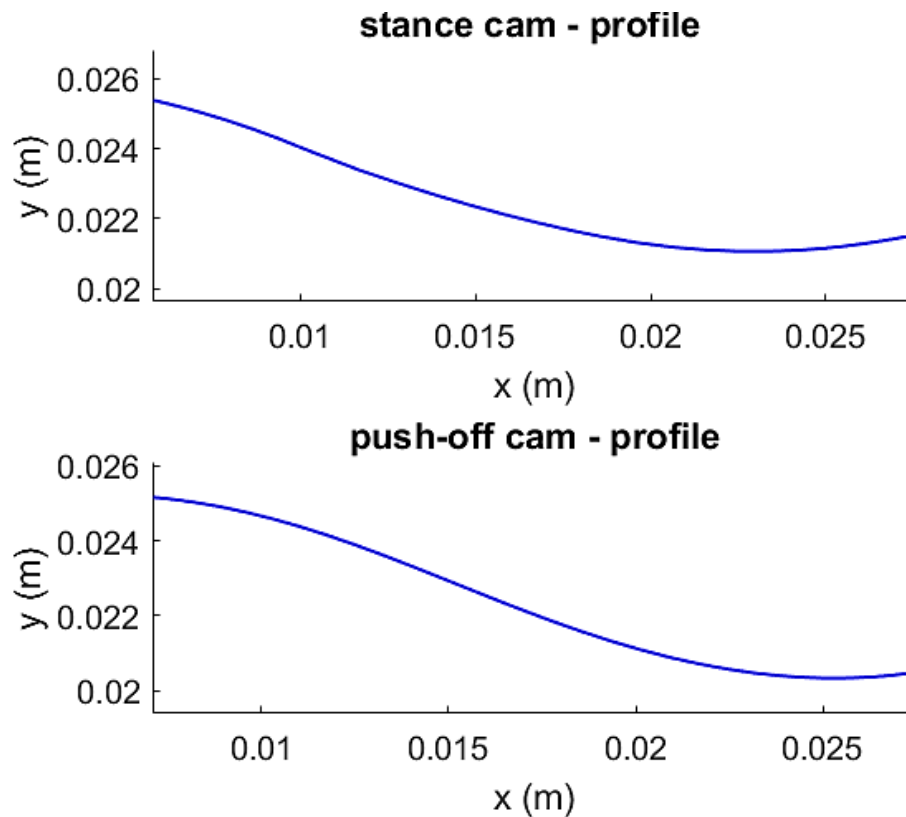
Figure B. 1 Cam profile of the stance (top) and of the push-off (bottom) cam-ram system, drawn in Matlab using the mapping method and shown in the cam reference frame.

All the geometry, kinematic and dynamic checks below were conducted both for the stance and the push-off cam - ram system but, for the sake of simplicity, the results showed in the plots below refer just to the stance system.

B.2 Geometry check: Cam design

1. In addition to the mapping method, an alternative method commonly used in cam profile design is the one named "inversion". For example, in a disk cam with a translating follower mechanism, the follower translates when the cam turns. This means that the relative motion between them is a combination of a relative turning motion and a relative

translating motion. Without changing this feature of their relative motion, the "inverted mechanism" is now considered: the cam remains fixed and the follower performs both the relative turning and translating motions. The follower is moving along cam profile to those positions corresponding to the angles of rotation of the cam, so it presents the same relative motion. Considering a roller-follower, the problem of designing cam profile becomes a problem of calculating the inner envelope of the roller profile as the follower is positioned around the cam. Figure B. 2 shows the fixed cam and the roller-follower turning and translating around it, in the inverted configuration.
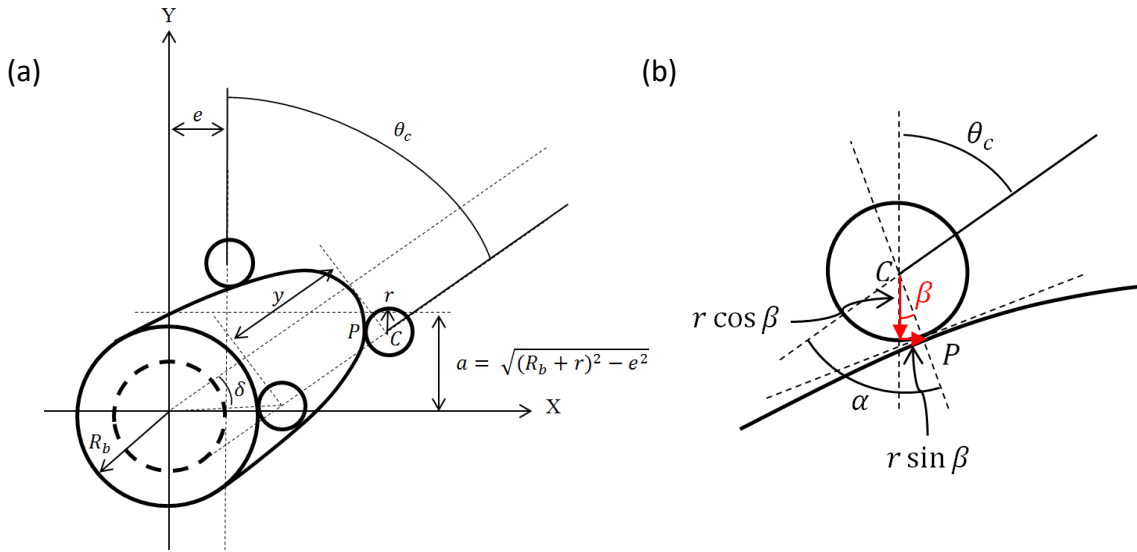
Figure B. 2 Cam system in the "inverted configuration" (a) and zoom in on the roller-follower (b).

The coordinates of the roller centre in the XY-plane, when the follower is vertical (that is its real position in the normal configuration), are: $(x_C, y_C) = (e, a + y)$, where a is an arbitrary constant. The rotation of the follower around the centre of the fixed cam in the clockwise direction (same angle of rotation θ_c but in the opposite direction with respect to cam rotation) can be represented by an anticlockwise rotation of the coordinate system through the same angle θ_c. Hence, the coordinates of the centre of the roller in its new position (after rotation) can be computed as follows, considering the initial ones and applying the rotation matrix for an anticlockwise rotation of the coordinate system:

$$\begin{bmatrix} x_C' \\ y_C' \end{bmatrix} = \begin{bmatrix} \cos\theta_c & \sin\theta_c \\ -\sin\theta_c & \cos\theta_c \end{bmatrix} \begin{bmatrix} e \\ (a + y) \end{bmatrix} \tag{B. 1}$$

Therefore, looking at Figure B. 2 (b), the coordinates of the contact points are obtained from those of the roller centre:

$$x_P = x_C' + r \sin \beta = x_C' + r \sin(\alpha - \theta_c)$$
$$y_P = y_C' - r \cos \beta = y_C' - r \cos(\alpha - \theta_c)$$

(B. 2)

since $\beta = (\alpha - \theta_c)$ as Figure B. 2 (b) shows.

2. The geometry of cam and roller-follower was checked in an early-stage simulation model (for this reason cam profiles in the plots below differ from the final ones showed in Figure B. 1). Given the positive anticlockwise rotation of the cam θ_C, to get the corresponding position of the follower in the inverted configuration, this component is turned around the centre of the cam in the reverse direction (clockwise) through the same angle θ_C as explained at point (2). The pressure angle (α) is always defined, at any point, as the angle between the normal to cam profile and the instantaneous direction of the follower motion. The line passing through the roller centre C and representing the instantaneous direction of the follower (line 1 in Figure B. 3) is defined as follows:

$$y - y_C = m(x - x_C)$$

(B. 3)

with $m = tan(90° - \theta_C) = cot(\theta_C) = \frac{1}{tan \theta_C}$. The line passing through the roller centre C and normal to cam profile at contact point P (line 2 in Figure B. 3) is defined as follows:

$$y - y_C = n(x - x_C)$$

(B. 4)

with the slope $n = tan(90° - \theta_C + \alpha) = tan(90° - (\theta_C - \alpha)) = cot(\theta_C - \alpha) = \frac{1}{tan(\theta_C - \alpha)}$. Implementing equations (B. 3) and (B. 4) in MATLAB, if cam pressure angle is correctly evaluated, line 2 drawn in accordance with equation (B. 4) should coincide with the one connecting the two points P and C and calculated as follows (equation of a line passing through two points):

$$\frac{(x - x_P)}{(x_C - x_P)} = \frac{(y - y_P)}{(y_C - y_P)}$$

(B. 5)
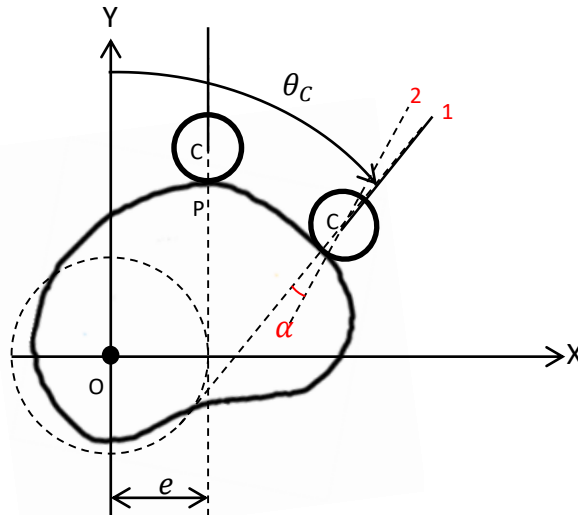
Figure B. 3 Roller rolling on cam surface when the cam is fixed (inverted configuration". Line 1 represents the instantaneous direction of the follower, while line 2 represents the normal to cam profile at contact point P.

Figure B. 4 shows that results are consistent with theory: the green line obtained implementing equation (B. 5) coincides with the line connecting the roller centre C to the contact point P.
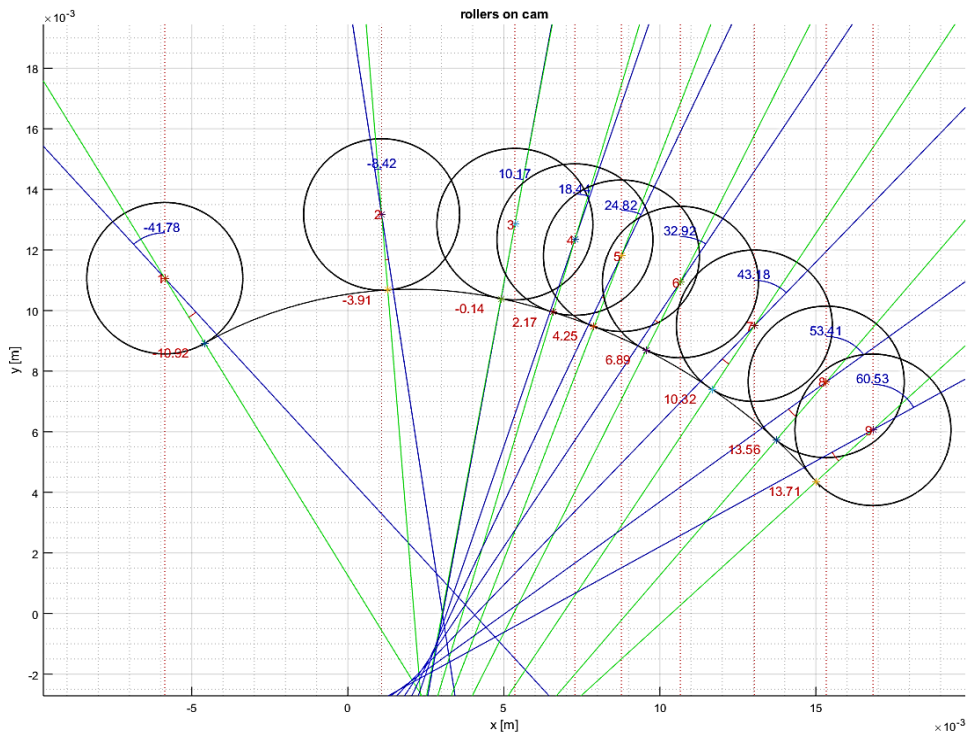
Figure B. 4 In the inverted configuration, the follower is moving along cam profile to those positions corresponding to a number of selected cam angles θ_C during the working phase of the stance cam-ram system. The blue line represents the instantaneous direction of the follower (line 1 in Figure B.2) characterised by a rotation around the centre of the cam in the reverse direction through the same angle θ_C. The green line, instead, represents the normal to cam profile at contact point P (line 2 in Figure B.2). The angles between the normal to cam profile and the instantaneous direction of the follower motion – i.e. the ones labelled with red values –are cam pressure angles, while those angles labelled in blue corresponds to cam rotation θ_C.

The same geometry check was repeated using the rotation matrix. The follower direction is given by the line connecting the centre of the roller C and the midpoint H between the lines of action of the two constraining reactions at the follower guide (N_1, N_2), while the normal to cam profile is given by the line passing through the centre of the roller C and the contact point P. The coordinates of the three points P, C and H are evaluated by mapping them between the fixed frame and the cam frame, as done previously for the design of cam profile (see equation (4.10)(4.12)):

$$\begin{bmatrix} x_C \\ y_C \end{bmatrix}_{cam} = \begin{bmatrix} \cos\theta_c & \sin\theta_c \\ -\sin\theta_c & \cos\theta_c \end{bmatrix} \begin{bmatrix} x_C \\ y_C \end{bmatrix}_{fix} = \begin{bmatrix} \cos\theta_c & \sin\theta_c \\ -\sin\theta_c & \cos\theta_c \end{bmatrix} \begin{bmatrix} e \\ (a+y) \end{bmatrix} \qquad \text{(B. 6)}$$

$$\begin{bmatrix} x_P \\ y_P \end{bmatrix}_{cam} = \begin{bmatrix} \cos\theta_c & \sin\theta_c \\ -\sin\theta_c & \cos\theta_c \end{bmatrix} \begin{bmatrix} x_P \\ y_P \end{bmatrix}_{fix} = \begin{bmatrix} \cos\theta_c & \sin\theta_c \\ -\sin\theta_c & \cos\theta_c \end{bmatrix} \begin{bmatrix} e + r\sin\alpha \\ (a+y) - r\cos\alpha \end{bmatrix} \qquad \text{(B. 7)}$$

$$\begin{bmatrix} x_H \\ y_H \end{bmatrix}_{cam} = \begin{bmatrix} \cos\theta_c & \sin\theta_c \\ -\sin\theta_c & \cos\theta_c \end{bmatrix} \begin{bmatrix} x_H \\ y_H \end{bmatrix}_{fix} = \begin{bmatrix} \cos\theta_c & \sin\theta_c \\ -\sin\theta_c & \cos\theta_c \end{bmatrix} \begin{bmatrix} e \\ (a+y) + c + \dfrac{l}{2} \end{bmatrix} \qquad \text{(B. 8)}$$

The coordinates of these three points in the cam frame are evaluated in MATLAB for some values of the cam angle of rotation θ_C, and the segment connecting point C to point H, representing the follower, is plotted together with that one connecting point C to point P, representing the normal to cam profile (Figure B. 5).
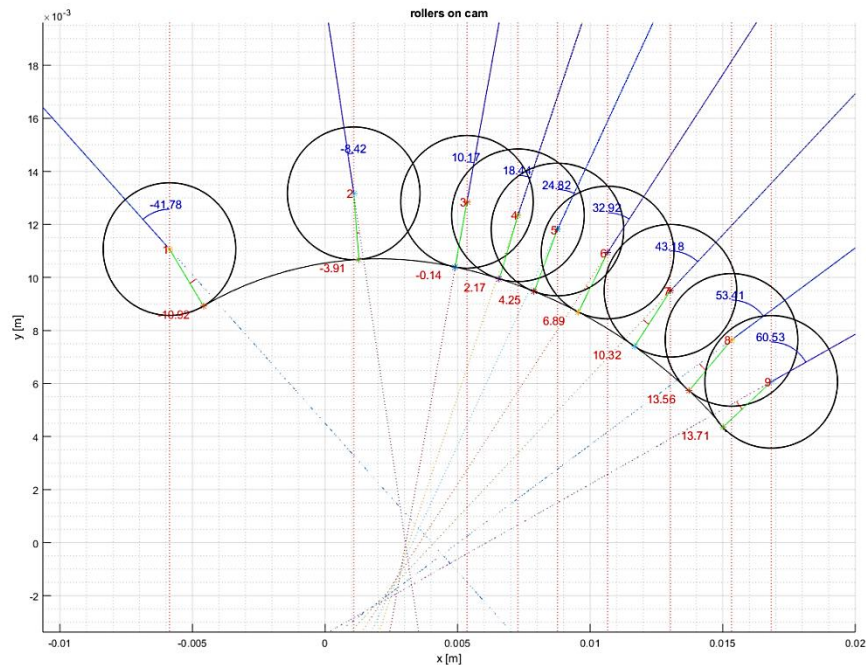
Figure B. 5 Geometry check in Matlab when cam is fixed and the follower is moving along cam profile to those positions corresponding to a number of selected cam angles θ_C, using the mapping method. The blue line connects the centre of the roller C to the midpoint H between the lines of action of the two constraining reactions (N_1, N_2) at the follower guide and represents the instantaneous direction of the follower. The green line connects the centre of the roller C and the contact point P, and represents the normal to cam profile at contact point P. Cam pressure angles are those between the normal to cam profile and the instantaneous direction of the follower motion –labelled with red values, while the angles of rotation of the cam θ_C are labelled in blue.

3. The geometry was checked also considering the real scam-ram system, in which cam is rotating anticlockwise and the follower moves upward. A kind of animation was developed in MATLAB using the mapping method to show how the system works. Cam profile is turning about its centre – the origin O of the fixed frame - through the angle θ_c in the anticlockwise direction during the working phase of the stance system, mimicking ankle dorsiflexion (defined as an anticlockwise rotation). Therefore, cam profile coordinates for each anticlockwise rotation are obtained mapping cam profile coordinates previously calculated from the cam frame to the fixed frame, which is exactly the opposite of what was done before to obtain cam profile (equation (4.12)). So, the following calculations were implemented in MATLAB for each cam angle θ_c in the stance working phases.

$$\begin{bmatrix} x_P \\ y_P \end{bmatrix}_{fix} = \begin{bmatrix} \cos\theta_c & -\sin\theta_c \\ \sin\theta_c & \cos\theta_c \end{bmatrix} \begin{bmatrix} x_P \\ y_P \end{bmatrix}_{cam} \tag{B. 9}$$

Figure B. 6 shows the result of this check with the respective positions of cam and roller for a number of selected cam angles θ_c.
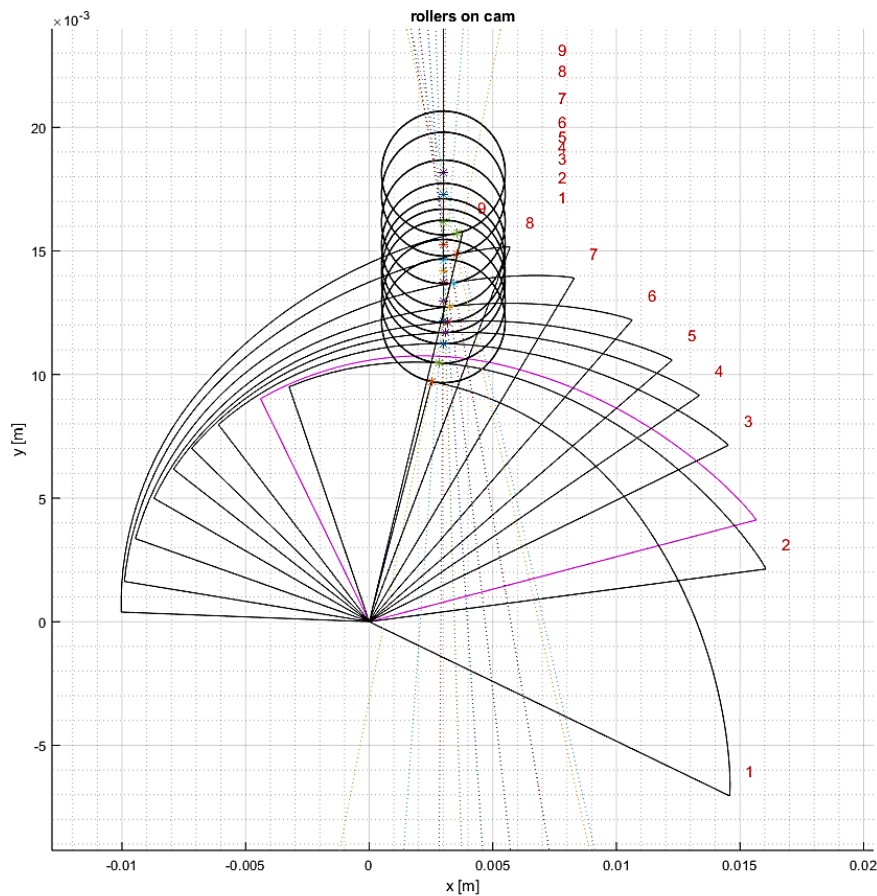
Figure B. 6 Geometry check in Matlab considering the stance cam-ram system in its working phase, when cam is rotating anticlockwise and the follower moves upward. The curvilinear part of each cam section represents cam profile for the working phase, while the two edges connect the first and the last point of cam profile to the centre of the cam (i.e. the origin (0, 0) of the fixed frame). The magenta section represents cam position at the beginning of the gait cycle (i.e. when $\theta_c \simeq 0$). Asterisks represent the contact point P between cam and roller for the selected cam angles of rotation θ_c.

Figure B. 6 shows as the stance cam, at the beginning of the gait cycle, rotates clockwise with respect to its initial position (i.e. the magenta section, when $\theta_C \simeq 0$), corresponding exactly to negative values of θ_C (i.e. initial plantarflexion). Then, as θ_C goes towards positive values (corresponding to dorsiflexion) during stance, cam rotates anticlockwise, pushing the piston upwards. The nine plots in Figure B. 7 show exactly the same relative positions between roller-follower and cam for nine angles of rotation θ_C of the working phase, while the piston moves up.
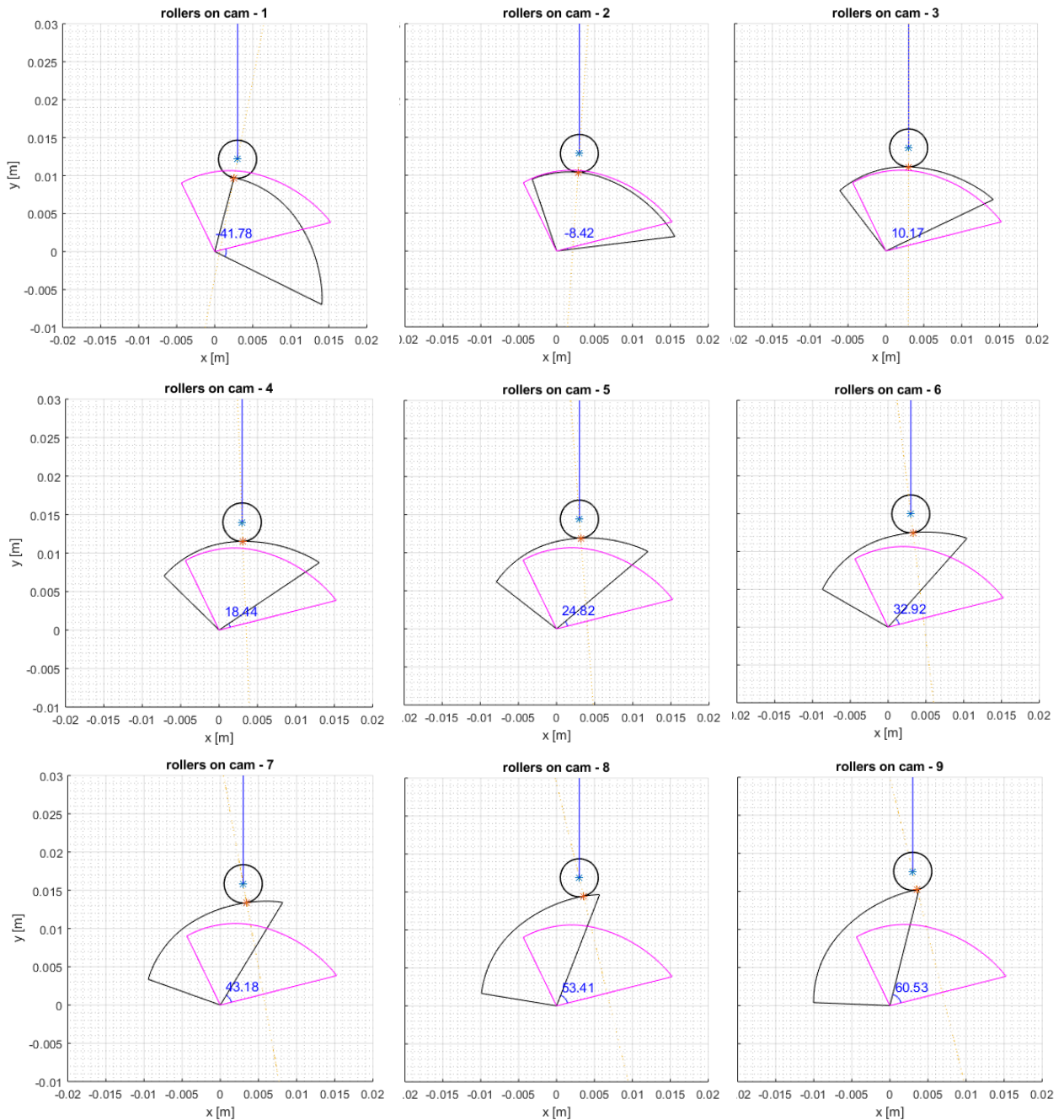
Figure B. 7 Relative positions between roller-follower and cam for nine angles of rotation θ_C during the working phase of the stance cam-ram system: cam rotates anticlockwise while the piston moves up. Cam angles θ_C, representing the rotation of the cam from its initial position (magenta section), are labelled in blue.

B.3 Kinematic check: Roller kinematics

1. A check was conducted to ensure that the contact point P between cam and roller rolls the same distance both on roller and on cam surface during the same time interval. S_{rol} and S_C are the displacements of the contact point P respectively on roller and on cam surface. Following the sign convention used so far (i.e. angles positive if anticlockwise (ACW)), also cam length is assumed as positive when the rotation of the cam is ACW (working phase of the stance cam), and as negative when cam rotates CW (working phase of the push-off cam). Below, four cases were analysed corresponding to the four possible combinations for the stance cam and the push-off cam in their working phase, when cam is rotating in the first quadrant.

STANCE cam-ram system
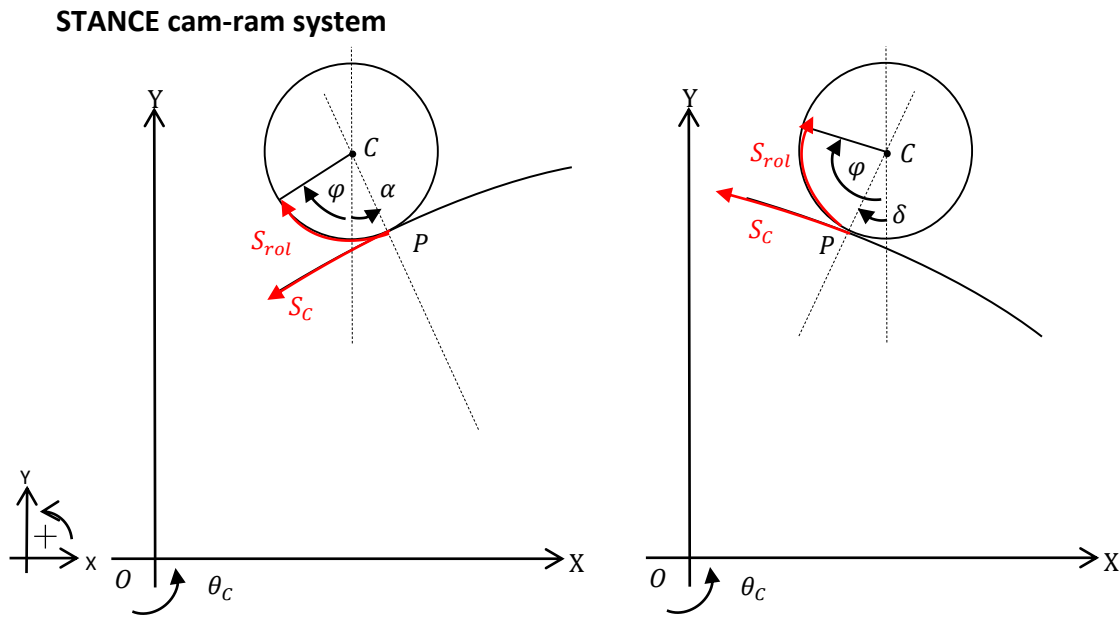
Figure B. 8 Cam-roller configuration for the stance cam-ram system when $\theta_C > 0$, while $\alpha > 0$ (on the left) and $\alpha < 0$ (on the right).

$$\theta_C > 0 \rightarrow S_C > 0 \qquad\qquad \theta_C > 0 \rightarrow S_C > 0$$

$$\alpha > 0,\ \beta < 0\ (\varphi = -\beta) \qquad \alpha < 0\ (\delta = -\alpha),\ \beta < 0\ (\varphi = -\beta)$$

$$\text{with } \alpha < |\varphi| \qquad\qquad \text{with } \varphi > \delta$$

$$S_C = S_{rol} = (\varphi + \alpha)r = (-\beta + \alpha)r \qquad S_C = S_{rol} = (\varphi - \delta)r = (-\beta + \alpha)r$$

$$\boldsymbol{\beta = \alpha - \frac{S_C}{r}} \quad \text{(B. 10)} \qquad\qquad \boldsymbol{\beta = \alpha - \frac{S_C}{r}} \quad \text{(B. 11)}$$

PUSH-OFF cam-ram system
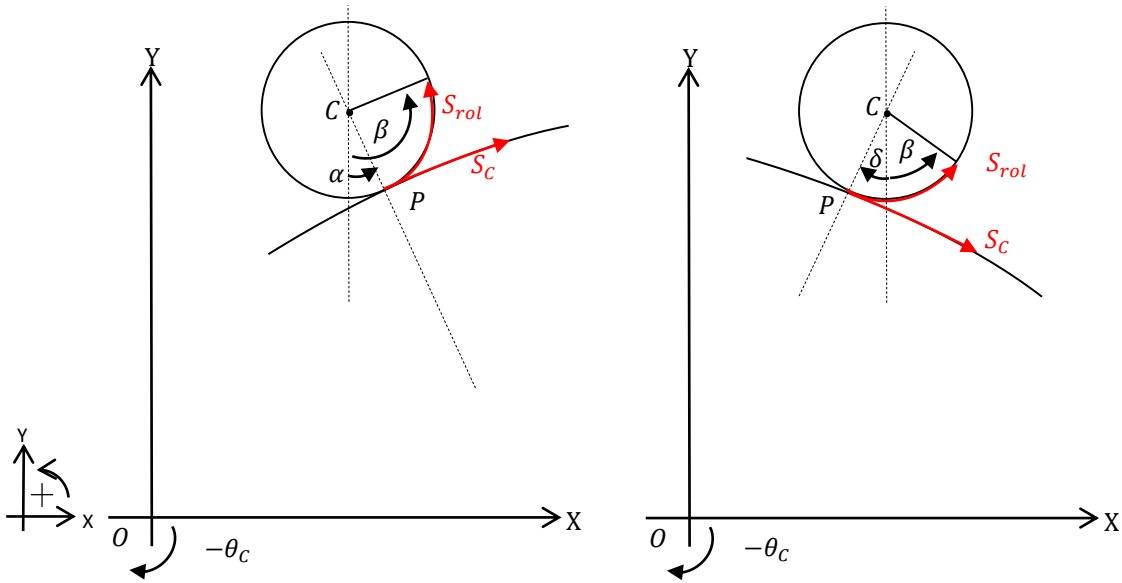
Figure B. 9 Cam-roller configuration for the push-off cam-ram system when $\theta_C < 0$, while $\alpha > 0$ (on the left) and $\alpha < 0$ (on the right).

$\theta_C < 0 \rightarrow S_C < 0$ $\theta_C < 0 \rightarrow S_C < 0$

$\alpha > 0, \beta > 0$ $\alpha < 0 \ (\delta = -\alpha), \beta > 0$

with $\beta > \alpha$ with $\delta < |\beta|$

$S_C = S_{rol} = -(\beta - \alpha)r$ $S_C = S_{rol} = (\beta + \delta)r = (\beta - \alpha)r$

$\boldsymbol{\beta = \alpha + \dfrac{S_C}{r}}$ (B. 12) $\boldsymbol{\beta = \alpha + \dfrac{S_C}{r}}$ (B. 13)

Despite there are four different equations for the four different cases, it is possible to consider just one equation to describe all the previous case:

$$S_C = -(\beta - \alpha)r \tag{B. 14}$$

where the $(-)$ sign highlights that S_C is negative when $\theta_C < 0$. Equation (B. 14) works for all the cases replacing the different values of angles in it. From this equation, it follows:

$$\beta = \alpha - \frac{S_C}{r} \tag{B. 15}$$

For a small S_C, there are other two possible cases:

a) **PUSH-OFF cam-ram system**

when $\alpha < 0$ $(\delta = -\alpha)$,

$\beta < 0$ $(\varphi = -\beta)$

and $\delta > |\beta|$

b) **STANCE cam-ram system**

when $\alpha > 0$

$\beta > 0$

and $\alpha > |\varphi|$
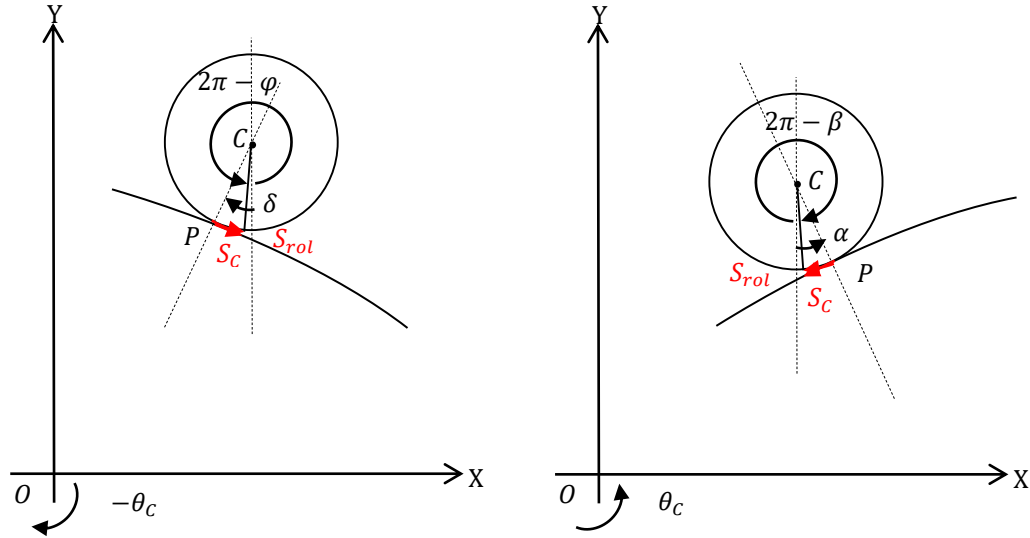
Figure B. 10 Cam-roller configuration for a small S_C, for the push-off (a) and the stance (b) cam-ram system.

Also in these two cases, equation (B. 14) works. To use the right value for each variable in equation (B. 14), it was chosen to consider all the variables on time intervals rather than on the time instants. For this reason, the following equation was used:

$$\Delta S_C = -(\Delta\beta - \Delta\alpha)r \tag{B. 16}$$

that yields

$$\Delta\beta = \Delta\alpha - \frac{\Delta S_C}{r} \tag{B. 17}$$

with $\Delta S_C = \left(\sqrt{diff(x)^2 + diff(y)^2}\right)$, being $diff(x)$ and $diff(y)$ the differences between adjacent coordinates x and y of cam profile, and $\Delta\alpha = diff(\alpha)$. This means, for instance, that ΔS_{C_1} is the distance between the first and the second point of cam profile, as well as $\Delta\alpha_1 = \alpha_2 - \alpha_1$ and $\Delta\beta_1 = \beta_2 - \beta_1$. Then, the indices coincide. Implementing equation (B. 17) in MATLAB, $\Delta\beta$ was evaluated, β obtained and then derived to get $\dot{\beta}$ using "*gradient*" (preferred to "*diff*", which is characterised by poor performance), and $\dot{\beta}$ was compared to $\dot{\beta}$ evaluated in equation (4.29). To be consistent with theory, a sign was

assigned to cam length S_C for stance cam and push-off cam in MATLAB. Figure B. 11 shows results of the angular velocity comparison.
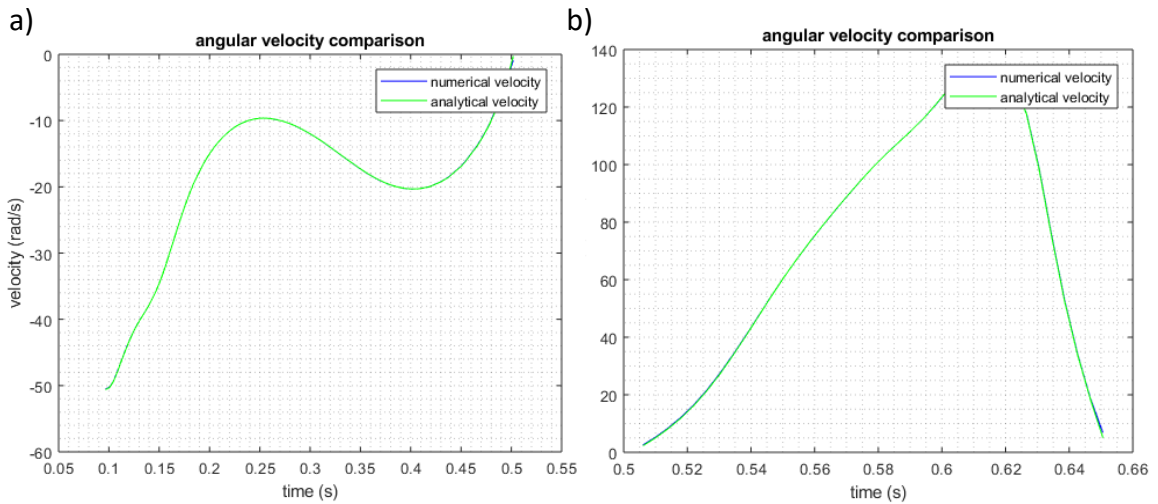
Figure B. 11 Comparison between $\dot{\beta}$ evaluated in equation (4.29) (green line) and $\dot{\beta}$ evaluated applying "*gradient*" to β (blue line), both for the stance (a) and the push-off (b) cam-ram system. The angular velocity β is obtained by $\Delta\beta$ (equation B.17).

The previously evaluated value of $\dot{\beta}$ was derived again using "*gradient*" to obtain $\ddot{\beta}$ and to compare it with $\ddot{\beta}$ previously evaluated equation (4.24). Figure B. 12 shows results of the angular acceleration comparison. The difference existing at the last time instant of the working phase is due to a numerical error generated in MATLAB at the extremities of the interval considered for calculation.
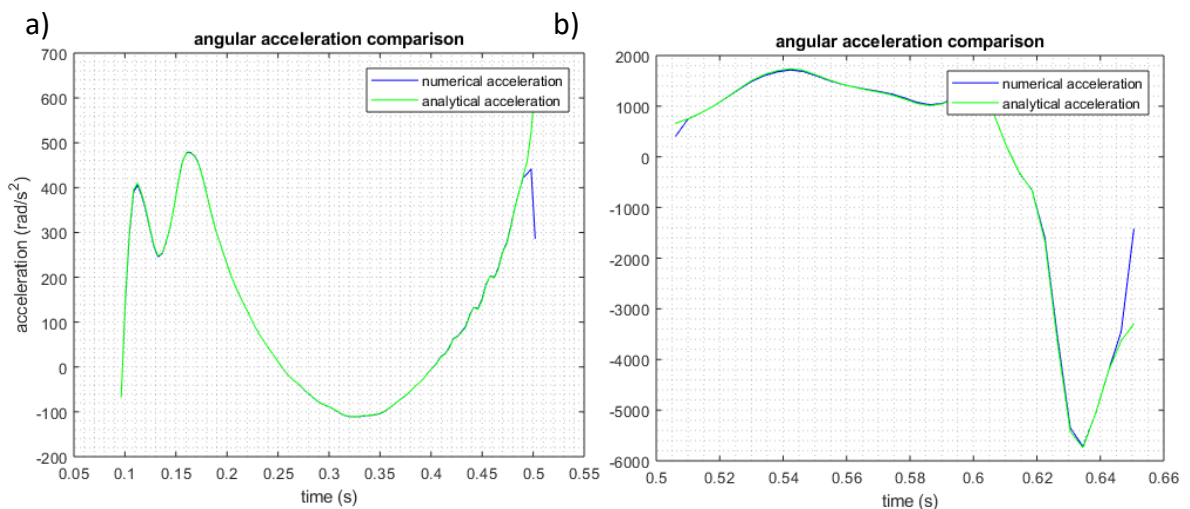
Figure B. 12 Comparison between $\ddot{\beta}$ evaluated in equation (4.24) (green line) and $\ddot{\beta}$ evaluated from $\Delta\beta$ applying "*gradient*" to $\dot{\beta}$.

2. For the roller kinematics evaluation, just the first quadrant was considered for the reasons explained in section 4.3.2 and with a positive slope of cam surface. Nevertheless, the signs of calculations should take care of themselves both with a positive and a negative slope of cam surface. A check was conducted considering both cases to guarantee the correctness of previous calculations.

A negative slope of cam surface corresponds to a negative cam pressure angle α (see Figure B. 13 (b): $0° \leq \delta \leq 90°$, with $\delta = -\alpha$ and $-90° \leq \alpha \leq 0°$). Everything respects the signs convention specified.

a) $0° \leq \alpha \leq 90°$ b) $0° \leq \delta \leq 90°$,

$\delta = -\alpha$ and $-90° \leq \alpha \leq 0°$
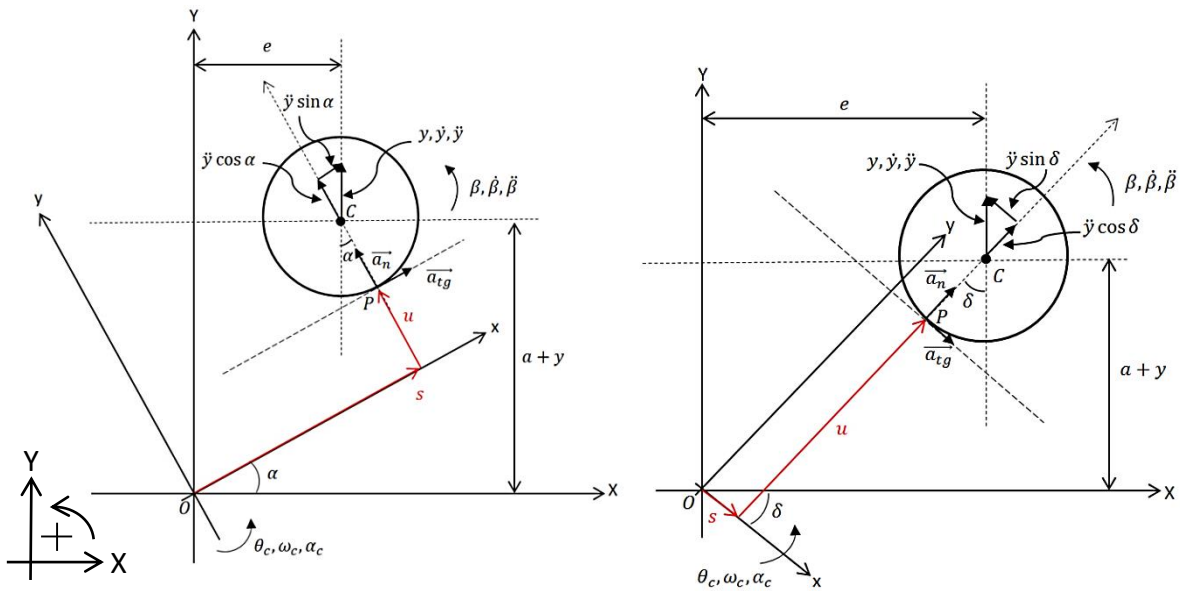
Figure B. 13 Roller on cam surface in case of positive (a) and negative slope (b).

The two vectors $\vec{s}$ and $\vec{u}$ are calculated in equation (4.17) looking at the geometry when cam surface presents a positive slope at the contact point. Here, the two vectors are evaluated also looking at the geometry when cam surface presents a negative slope at the contact point and δ is the pressure angle.

$$\overrightarrow{OP} = \begin{bmatrix} s \\ u \\ 0 \end{bmatrix} \qquad\qquad \overrightarrow{OP} = \begin{bmatrix} s \\ u \\ 0 \end{bmatrix}$$

$$s = [e + (a + y)\tan\alpha]\cos\alpha \qquad\qquad s = [e - (a + y)\tan\delta]\cos\delta$$

$$u = (a + y)\cos\alpha - r - e\sin\alpha \quad \text{(B. 18)} \qquad u = (a + y)\cos\delta - r + e\sin\delta \quad \text{(B. 19)}$$

Substituting $\delta = -\alpha$ in the equations of $\vec{s}$ and $\vec{u}$ in case of negative slope, they result to be the same equations used for a positive slope, so that mathematics is identical in both cases.

This guarantees that equation (4.17) is valid in both cases and, consequently, all the kinematics previously evaluated is correct.

B.4 Dynamic check: Dynamic analysis

The six simultaneous non-linear equations coming from the dynamic analysis (equations (4.32) - (4.34) and (4.39) - (4.41)) were implemented and solved in MATLAB. This included, at the beginning, a study of how best to solve the six simultaneous non-linear equations. Using an early-stage simulation model, the issue was understanding the difference in computational speed between:

a) the use of a MATLAB non-linear solver (i.e. *"fsolve"*);
b) the evaluation of different systems of six linear equations, given by considering in turn positive or negative signs where absolute values and sign functions exist.

In addition, the residuals of the six equations were evaluated throughout the gait cycle to validate the correctness of the dynamic model. They were calculated moving all the terms of each one of the six equations on the left of the equal, and normalising them by the hydraulic force at the start $F_h|_0 = P_0 \cdot A$ (where P_0 is the pressure inside the cylinder at the beginning of the gait cycle).

$$\sum F_x = m\ddot{x} = 0 \quad F_t \cos\alpha - F_n \sin\alpha + R_H = 0$$

$$residual\ 1 = (F_t \cos\alpha - F_n \sin\alpha + R_H)/F_h|_0 \tag{B. 20}$$

$$\sum F_y = m\ddot{y} \quad F_t \sin\alpha + F_n \cos\alpha - R_V - mg = m\ddot{y}$$

$$residual\ 2 = (F_t \sin\alpha + F_n \cos\alpha - R_V - mg - m\ddot{y})/F_h|_0 \tag{B. 21}$$

$$\sum M_C = I_{rol}\ddot{\beta} \quad F_t r - M_{rolres} - M_{brg} = I_{rol}\ddot{\beta}$$

$$residual\ 3 = (F_t r - M_{rolres} - M_{brg} - I_{rol}\ddot{\beta})/F_h|_0 \tag{B. 22}$$

$$\sum F_x = M\ddot{x} = 0 \quad N_2 - R_H - N_1 = 0$$

$$residual\ 4 = (N_2 - R_H - N_1)/F_h|_0 \tag{B. 23}$$

$$\sum F_y = M\ddot{y} \quad R_V - F_h - Mg - F_{fr1} - F_{fr2} = M\ddot{y}$$

$$residual\ 5 = (R_V - F_h - Mg - F_{fr1} - F_{fr2} - M\ddot{y})/F_h|_0 \tag{B. 24}$$

$$\sum M_H = 0 \quad M_{brg} - R_H\left(c + \frac{l}{2}\right) + N_1\frac{l}{2} + N_2\frac{l}{2} - M_{fr1} + M_{fr2} = 0$$

$$residual\ 6 = (M_{brg} - R_H \left(c + \frac{l}{2}\right) + N_1 \frac{l}{2} + N_2 \frac{l}{2} - M_{fr1} +$$
$$+ M_{fr2})/F_h|_0 \qquad \text{(B. 25)}$$

The force F_n results to be positive during the working phase of the two cam-ram systems. Therefore, M_{brg} (equation (4.35)) and M_{rolres} (equation (4.36)) become:

$$M_{brg} = sign(\dot{\beta}) \cdot \mu_{brg} \cdot \frac{d_{brg}}{2} \cdot F_n \qquad \text{(B. 26)}$$

$$M_{rolres} = sign(\omega_{rel}) \cdot \mu_{rolres} \cdot F_n \cdot r \qquad \text{(B. 27)}$$

so that

$$M_{brg} + M_{rolres} = \left(sign(\omega_{rel})\mu_{rolres} + sign(\dot{\beta})\mu_{brg} \cdot \frac{d_{brg}}{2r}\right) \cdot r \cdot F_n \qquad \text{(B. 28)}$$

In MATLAB is possible to implement directly the six simultaneous equations according to the expression "$A * x = b$", where "A" is the coefficient matrix, "x" is the vector of the unknowns, and "b" is the vector of the constant terms. The matrix below derives from the six equations of the dynamic analysis, when all the absolute values are considered as positive (just to show how the equations should be sorted to be solved in MATLAB). Therefore, the unknowns can be evaluated using the specific MATLAB command to solve a system of linear equations "$x = A \backslash b$".

$$\underbrace{\begin{bmatrix} -\sin\alpha & \cos\alpha & 0 & 0 & 0 & 1 \\ \cos\alpha & \sin\alpha & 0 & 0 & -1 & 0 \\ -\left(\begin{matrix} sign(\omega_{rel})\mu_{rolres} + \\ +sign(\dot{\beta})\mu_{brg} \cdot \frac{d_{brg}}{2r} \end{matrix}\right)r & r & 0 & 0 & 0 & 0 \\ 0 & 0 & -1 & 1 & 0 & -1 \\ 0 & 0 & -sign(\dot{y})\mu_{sl} & -sign(\dot{y})\mu_{sl} & 1 & 0 \\ sign(\dot{\beta})\mu_{brg}\frac{d_{brg}}{2} & 0 & \left(\frac{l}{2} - sign(\dot{y})\frac{d}{2}\mu_{sl}\right) & \left(\frac{l}{2} + sign(\dot{y})\frac{d}{2}\mu_{sl}\right) & 0 & -\left(c + \frac{l}{2}\right) \end{bmatrix}}_{A} \cdot \underbrace{\begin{bmatrix} F_n \\ F_t \\ N_1 \\ N_2 \\ R_V \\ R_H \end{bmatrix}}_{x} =$$

$$
= \begin{bmatrix} 0 \\ mg + m\ddot{y} \\ I_{rol}\ddot{\beta} \\ 0 \\ Mg + M\ddot{y} + F_h + F_s \\ 0 \end{bmatrix}
$$

$$
= \qquad b
$$

In this case, with F_n always positive, four cases exist according to the signs of N_1 and N_2. Table B. 1 Changes in the *A* matrix, when F_n is positive, while N_1 and N_2 change their sign. For each instant of the gait cycle, only one valid solution of the six simultaneous equations exists, corresponding to one of the four matrices.Table B. 1 shows the changes in the *A* matrix for the four cases, leading to four different matrices corresponding to four systems of linear equations. For each instant of the gait cycle, there is only one valid solution of the six simultaneous equations, corresponding to one of the four matrices.

The other way to solve the six non-linear equations ((4.32) - (4.34) and (4.39) - (4.41) (i.e. equations (B. 20) - (B. 25))) in MATLAB is using directly the command "*fsolve*".

Despite the higher computational cost, the command "*fsolve*" was used since it takes care by itself of absolute values and sign functions.

The residuals of the six equations were evaluated in MATLAB, substituting all the unknowns with the values previously obtained from solving the six equations. They result to be tiny, with an order of magnitude of 10e-16 (see Figure B. 14), corresponding to MATLAB floating-point relative accuracy. This means that everything that follows equations (4.32) - (4.34) and (4.39) - (4.41) is correct.
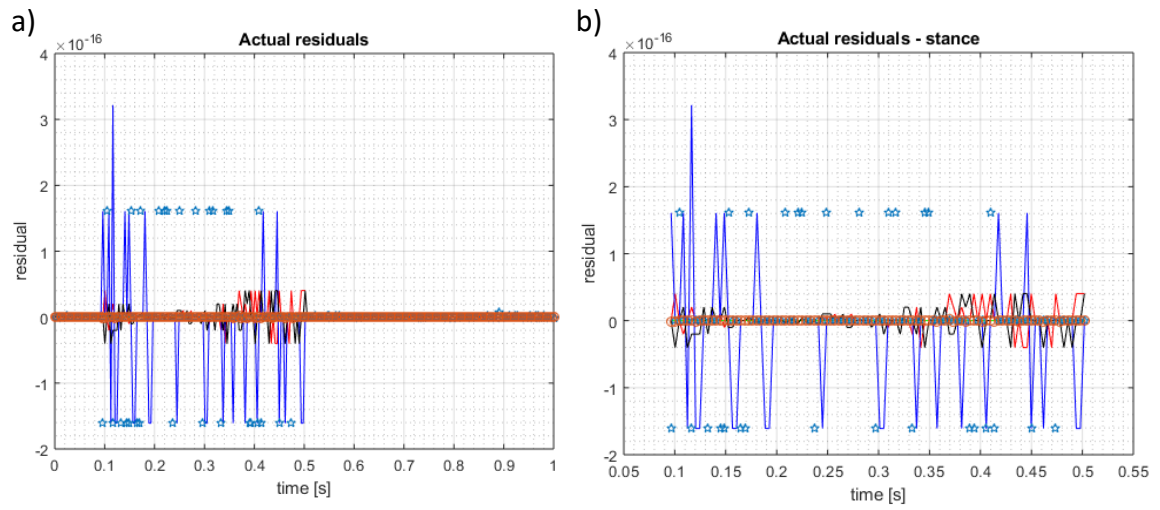
Figure B. 14 Sum of the residuals of the 6 equations, evaluated as shown previously (equations (B. 20) - (B. 25)): throughout the gait cycle (a) and just during the working phase of the stance cam-ram system (b).

	N_1	N_2	F_{fr1}	F_{fr2}	M_{fr1}, M_{fr2}
I	**+ve**	**+ve**	$sign(\dot{y})\mu_{sl}N_1$	$sign(\dot{y})\mu_{sl}N_2$	$\frac{d}{2}sign(\dot{y})\mu_{sl}N_1, \frac{d}{2}sign(\dot{y})\mu_{sl}N_2$

$$\begin{bmatrix} -\sin\alpha & \cos\alpha & 0 & 0 & 0 & 1 \\ \cos\alpha & \sin\alpha & 0 & 0 & -1 & 0 \\ -\left(\begin{matrix}sign(\omega_{rel})\mu_{rolres} + \\ +sign(\dot{\beta})\mu_{brg}\cdot\frac{d_{brg}}{2r}\end{matrix}\right)r & r & 0 & 0 & 0 & 0 \\ 0 & 0 & -1 & 1 & 0 & -1 \\ 0 & 0 & \boldsymbol{-sign(\dot{y})\mu_{sl}} & \boldsymbol{-sign(\dot{y})\mu_{sl}} & 1 & 0 \\ sign(\dot{\beta})\mu_{brg}\frac{d_{brg}}{2} & 0 & \left(\frac{l}{2}-sign(\dot{y})\frac{d}{2}\mu_{sl}\right) & \left(\frac{l}{2}+sign(\dot{y})\frac{d}{2}\mu_{sl}\right) & 0 & -\left(c+\frac{l}{2}\right) \end{bmatrix} \cdot \begin{bmatrix} F_n \\ F_t \\ N_1 \\ N_2 \\ R_V \\ R_H \end{bmatrix} = \begin{bmatrix} 0 \\ mg+m\ddot{y} \\ I_{rol}\ddot{\beta} \\ 0 \\ Mg+M\ddot{y}+F_h+F_s \\ 0 \end{bmatrix}$$

	N_1	N_2	F_{fr1}	F_{fr2}	M_{fr1}, M_{fr2}
II	**−ve**	**−ve**	$-sign(\dot{y})\mu_{sl}N_1$	$-sign(\dot{y})\mu_{sl}N_2$	$\frac{d}{2}sign(\dot{y})\mu_{sl}N_1, \frac{d}{2}sign(\dot{y})\mu_{sl}N_2$

$$\begin{bmatrix} -\sin\alpha & \cos\alpha & 0 & 0 & 0 & 1 \\ \cos\alpha & \sin\alpha & 0 & 0 & -1 & 0 \\ -\left(\begin{matrix}sign(\omega_{rel})\mu_{rolres} + \\ +sign(\dot{\beta})\mu_{brg}\cdot\frac{d_{brg}}{2r}\end{matrix}\right)r & r & 0 & 0 & 0 & 0 \\ 0 & 0 & -1 & 1 & 0 & -1 \\ 0 & 0 & \boldsymbol{sign(\dot{y})\mu_{sl}} & \boldsymbol{sign(\dot{y})\mu_{sl}} & 1 & 0 \\ sign(\dot{\beta})\mu_{brg}\frac{d_{brg}}{2} & 0 & \left(\frac{l}{2}-sign(\dot{y})\frac{d}{2}\mu_{sl}\right) & \left(\frac{l}{2}+sign(\dot{y})\frac{d}{2}\mu_{sl}\right) & 0 & -\left(c+\frac{l}{2}\right) \end{bmatrix} \cdot \begin{bmatrix} F_n \\ F_t \\ N_1 \\ N_2 \\ R_V \\ R_H \end{bmatrix} = \begin{bmatrix} 0 \\ mg+m\ddot{y} \\ I_{rol}\ddot{\beta} \\ 0 \\ Mg+M\ddot{y}+F_h+F_s \\ 0 \end{bmatrix}$$

	N_1	N_2	F_{fr1}	F_{fr2}	M_{fr1}, M_{fr2}
III	**+ve**	**−ve**	$sign(\dot{y})\mu_{sl}N_1$	$-sign(\dot{y})\mu_{sl}N_2$	$\frac{d}{2}sign(\dot{y})\mu_{sl}N_1, \frac{d}{2}sign(\dot{y})\mu_{sl}N_2$

$$\begin{bmatrix} -\sin\alpha & \cos\alpha & 0 & 0 & 0 & 1 \\ \cos\alpha & \sin\alpha & 0 & 0 & -1 & 0 \\ -\left(\begin{matrix}sign(\omega_{rel})\mu_{rolres} + \\ +sign(\dot{\beta})\mu_{brg}\cdot\frac{d_{brg}}{2r}\end{matrix}\right)r & r & 0 & 0 & 0 & 0 \\ 0 & 0 & -1 & 1 & 0 & -1 \\ 0 & 0 & \boldsymbol{-sign(\dot{y})\mu_{sl}} & \boldsymbol{sign(\dot{y})\mu_{sl}} & 1 & 0 \\ sign(\dot{\beta})\mu_{brg}\frac{d_{brg}}{2} & 0 & \left(\frac{l}{2}-sign(\dot{y})\frac{d}{2}\mu_{sl}\right) & \left(\frac{l}{2}+sign(\dot{y})\frac{d}{2}\mu_{sl}\right) & 0 & -\left(c+\frac{l}{2}\right) \end{bmatrix} \cdot \begin{bmatrix} F_n \\ F_t \\ N_1 \\ N_2 \\ R_V \\ R_H \end{bmatrix} = \begin{bmatrix} 0 \\ mg+m\ddot{y} \\ I_{rol}\ddot{\beta} \\ 0 \\ Mg+M\ddot{y}+F_h+F_s \\ 0 \end{bmatrix}$$

$-\textbf{ve}$	$+\textbf{ve}$	$-sign(\dot{y})\mu_{sl}N_1$	$sign(\dot{y})\mu_{sl}N_2$	$\frac{d}{2}sign(\dot{y})\mu_{sl}N_1,\ \frac{d}{2}sign(\dot{y})\mu_{sl}N_2$

$$
IV \quad
\begin{bmatrix}
-\sin\alpha & \cos\alpha & 0 & 0 & 0 & 1 \\
\cos\alpha & \sin\alpha & 0 & 0 & -1 & 0 \\
-\left(\begin{array}{c}sign(\omega_{rel})\mu_{rolres}+\\+sign(\dot{\beta})\mu_{brg}\cdot\frac{d_{brg}}{2r}\end{array}\right)r & r & 0 & 0 & 0 & 0 \\
0 & 0 & -1 & 1 & 0 & -1 \\
0 & 0 & \boldsymbol{sign(\dot{y})\mu_{sl}} & \boldsymbol{-sign(\dot{y})\mu_{sl}} & 1 & 0 \\
sign(\dot{\beta})\mu_{brg}\frac{d_{brg}}{2} & 0 & \left(\frac{l}{2}-sign(\dot{y})\frac{d}{2}\mu_{sl}\right) & \left(\frac{l}{2}+sign(\dot{y})\frac{d}{2}\mu_{sl}\right) & 0 & -\left(c+\frac{l}{2}\right)
\end{bmatrix}
\cdot
\begin{bmatrix}
F_n \\ F_t \\ N_1 \\ N_2 \\ R_V \\ R_H
\end{bmatrix}
=
\begin{bmatrix}
0 \\ mg+m\ddot{y} \\ I_{rol}\ddot{\beta} \\ 0 \\ Mg+M\ddot{y}+F_h++F_s \\ 0
\end{bmatrix}
$$

Table B. 1 Changes in the *A* matrix, when F_n is positive, while N_1 and N_2 change their sign. For each instant of the gait cycle, only one valid solution of the six simultaneous equations exists, corresponding to one of the four matrices.

Appendix C: MATLAB pseudo-code

C.1 Notes on MATLAB operations and variables calculations

It is fundamental to remind the reader of this pseudo-code some simple rules about operations in MATLAB. While a unique way exists to solve additions and subtractions, in case of multiplications, divisions or powers, involving both arrays and matrices, it is possible to perform element-by-element operations (referred to as "array operations" and indicated by placing a dot before the corresponding operation symbol – respectively ".*",".",".^") or according to the rules of matrix algebra (referred to as "matrix operations"). In the current pseudo-code, all the operations are supposed to be element-wise and they involve scalars and arrays. When a scalar operates on a vector, the scalar is always applied to each vector element. This is valid for multiplications and divisions, so that there are no needs to specify the type of operation with the corresponding specific operator. When multiplications and divisions involve two or more vectors, instead, and the element-wise operation needs to be performed, it is necessary to use the specific operators: respectively ".*" and "./".When an array is raised to a power that is a scalar, MATLAB evaluates the element-wise power, and in this case the operator ".^" is needed.

Therefore, if not explicitly specified, all the operations described in the "HIGH-LEVEL PSEUDO-CODE" and in the "MATHEMATICAL PSEUDO-CODE" are element-wise operations (i.e. "array-based calculations"), so that the previous directions need to be followed. Also, many "for loops" are defined in the "HIGH-LEVEL PSEUDO-CODE" and in the "MATHEMATICAL PSEUDO-CODE", which execute the same block of code a specific number of times, keeping track of each iteration with an incrementing index variable. All the calculations performed in these loops on arrays involve just that element of each array having that specific index (specified both in the "HIGH-LEVEL PSEUDO-CODE" and in the "MATHEMATICAL PSEUDO-CODE" with the subscript n referred to the nth -element of the array). Hence, they are all scalar values: the dot before multiplication or division operator is not needed.

C.2 HIGH-LEVEL PSEUDO-CODE

C.2.1 Design program

Some of the functions called in the script below are the same called also in the script "**C.2.2 Simulation model**" because, as explained in Chapter 5, the inner time-stepping loop is almost identical in the simulation model and in the design program and other parts of the code are also adapted from that of the simulation model.

1. Define a variable ("$gait\ cycle$") and set it as equal to "$design$" to recognise that some of the tasks included in the functions below are valid just when the same function is called in the below script for cam design (and not in "**C.2.2 Simulation model**").
2. Set the slope and intercept of the characteristics of the two return springs as equal to zero.
3. **RETURN SPRING SIZING** - enter the **FOR loop** that runs the code two times: a first time to size the two return springs, and a second time to design cams profiles when the two sized springs are included in the system.

FOR $spring = 1:2$

4. Import data (experimental data collected by (Bari, 2013) for healthy level walking at self-selected speed) from Excel file: time instants for a full gait cycle and corresponding values of ankle angle and ankle torque (changing its sign to have positive ankle power in input to the device and negative ankle power in output from the device)
5. Define the time interval Δt between each instant of the gait cycle as the mean value of all the intervals coming from data (i.e. mean value of the vector resulting from applying the command "$diff$" to the time imported before).
6. Calculate the ankle angular velocity at each instant of the gait cycle inside a for loop:

$$\omega_{a_n} = \frac{\Delta\theta_{a_{n-1}} + \Delta\theta_{a_n}}{2\Delta t}$$

with $2 \leq n \leq (end - 1)$. For $n = 1$ and $n = end$: $\omega_{a_1} = \frac{\Delta\theta_{a_1}}{\Delta t}$ and $\omega_{a_{end}} = \frac{\Delta\theta_{a(end)}}{\Delta t}$.

7. Calculate the ankle angular acceleration at each instant of the gait cycle inside a for loop:

$$\alpha_{a_n} = \frac{\Delta\omega_{a_{n-1}} + \Delta\omega_{a_n}}{2\Delta t}$$

with $2 \le n \le (end - 1)$. For $n = 1$ and $n = end$: $\alpha_{a_1} = \frac{\Delta\omega_{a_1}}{\Delta t}$ and $\alpha_{a_{end}} = \frac{\Delta\omega_{a_{(end)}}}{\Delta t}$.

8. Identify important gait events:

- **Positive torque:** the time instant right before that one at which the ankle torque becomes positive.

- **Maximum dorsiflexion**: the time instant of the maximum ankle angle in the used convention.

- **Maximum plantarflexion:** the time instant of the minimum ankle angle in the used convention.

9. Identify four phases of the gait cycle and gather them in the structure "$gait\_phase$":

- **Load acceptance:** despite the theoretical definition of this phase of the gait, in the actual code this name refers to the phase going from the initial contact of the foot with the ground at the beginning of the gait cycle to the instant right before that one of "Positive torque".

- **Stance**: from the time instant of "Positive torque" to the instant right before the one of maximum dorsiflexion.

- **Push-off**: from the time instant of maximum dorsiflexion to the instant right before the one of maximum plantarflexion.

- **Swing**: from the time instant of maximum plantarflexion to the end of the gait cycle.

10. Pre-allocate the maximum amount of space required for all the arrays used in the code downstream to speed up the code execution time. In case of a loop, indeed, the size of arrays incrementally increases each time through the loop, and this can adversely affect performance and memory use. The variables need to be pre-allocated for both systems, and the space required for each variable is that one of a vector with a length equal to the number of time instants of the considered gait cycle. The arrays considered are those changing size in the inner for loop: Q, $F_{fr_{cyl}}$, F_h, T_{gas}, P_{acc}, V_{acc}, V_{gas}, $T_{c_{actual}}$, $\Delta P_{to\ acc}$, $\Delta P_{to\ tank}$.

11. Define pressure and temperature of the surroundings: $T_{env} = 293K$, $P_{atm} = 101325\ Pa$.

12. Call section "**C.3.1 Accumulator, gas and oil properties**" to get the properties of the diaphragm accumulator.

13. Call section "**C.3.2 Hydraulic cylinders properties**" to get the properties of the two hydraulic cylinders of the stance and the push-off system.

14. Call section "**C.3.3 Major and minor losses properties**", where the properties of pipes, inlets/exits, fittings and DCVs for the two systems are defined.

15. Call section "**C.3.4 Geometry, masses, coefficients of friction**" where the size of cam, roller and follower, and the masses of the two systems are defined, together with the coefficients of friction.

16. Define accumulator P, V and T at the first time instant ($n = 1$) of the gait cycle:

$$P_{acc_{n=1}} = 0.90 * P_{max}$$

$$V_{acc_{n=1}} = V_A - (V_A - V_{acc_{pre-charge}})\left(\frac{P_{pre-charge}}{P_{acc_{n=1}}}\right); \text{ %oil volume - isothermal process}$$

$$V_{gas_{n=1}} = V_A - V_{acc_{n=1}} \text{ % gas volume into the accumulator}$$

$$T_{gas_{n=1}} = T_{env}$$

17. Evaluate the working of the parallel spring:

- Call function "**C.3.5 Parallel linear spring**" containing the spring model (with its constants) to calculate the torque provided by the parallel spring and the torque acting on the system.

18. Evaluate the working of the gearbox:

- Set the gearbox ratio.

- Define the "capacity" of the gearbox (i.e. its size) as $T_{capacity} = \max\left|T_{in_{gb}}\right|$, where $T_{in_{gb}}$ is the torque in input to the gearbox, which is the ankle torque minus the spring torque.

- Call function "**C.3.6 Gearbox**" containing the gearbox model to calculate angle, velocity and acceleration of the cam, the losses due to the friction torque, and the output torque acting on the rest of the system as the gearbox ideal output torque minus friction.

Get ready for the iteration loop

19. Set the number of main iterations to converge on a solution: 5 (see section 5.2).

20. Call section "**C.3.16 Variables initialisation**" to define the variables needed to enter the main outer loop.

21. **ITERATIVE CALCULATION of CAM PROFILES** (referred to as outer iteration loop):

FOR each iteration

- Call section "**C.3.17 Kinematics**" to evaluate all the kinematic variables of the two systems necessary to enter further on the inner for loop.

- Calculate the two return spring forces ($F_{s_{STANCE}}$ and $F_{s_{PO}}$) considering the displacement of the pistons from the previous bullet, and the slope and intercept of the two springs characteristics previously defined (see step (2) if "*spring*"=1 or step (22) if "*spring*"=2).

- Calculate the flow in the two systems (Q_{STANCE}, Q_{PO}) given by piston velocity times the ram bore area.

- Call function "**C.3.18 Major and minor losses evaluation**" to evaluate the pressure drop in the pipework of the stance system - both from ram to accumulator ($\Delta P_{to\ acc_{STANCE}}$) and from ram to tank ($\Delta P_{to\ tank_{STANCE}}$).

- Call function "**C.3.18 Major and minor losses evaluation**" to evaluate the pressure drop in the pipework of the push-off system - both from ram to accumulator ($\Delta P_{to\ acc_{PO}}$) and from ram to tank ($\Delta P_{to\ tank_{PO}}$).

- Initialise the pressure in the two cylinders:

$$P_{cyl_{STANCE}} = P_{atm} + \Delta P_{to\ tank_{STANCE}}$$

$$P_{cyl_{PO}} = P_{atm} + \Delta P_{to\ tank_{PO}}$$

These values will be overwritten during the two working phases of the gait cycle.

- Initialise the oil volume in the two cylinders:

$$V_{cyl_{STANCE}} = \frac{\pi D_{STANCE}^2}{4} \cdot \left(residual\ length + (\max(y_{STANCE}) - y_{STANCE})\right)$$

$$V_{cyl_{PO}} = \frac{\pi D_{PO}^2}{4} \cdot \left(residual\ length + (\max(y_{PO}) - y_{PO})\right)$$

- Define the vector *guess* containing six initial guesses for the six unknowns of the dynamic analysis. The same values are used for both systems.

- **TIME STEPPING LOOP** for each time instant of the gait cycle (referred to as inner loop).

FOR each time-instant n of the ankle data

1) Check the opening of the two DCVs and the possible changes in V, P and T in the accumulator due to oil compressibility:

    IF LOAD ACCEPTANCE

        ➤ 2 DCVs OPEN TO TANK.

    ELSE IF STANCE

        ➤ STANCE DCV OPEN TO ACCUMULATOR:

        IF n is time instant 1 of stance

            Call function "**C.3.8 Connect to accumulator**" to evaluate the changes in V, P and T in the accumulator due to oil compressibility, occurring when the DCV connects the stance ram to the accumulator. The values in input to the function are those referred to the STANCE system.

        END IF

        ➤ PUSH-OFF DCV OPEN TO TANK.

    ELSE IF PUSH-OFF

        ➤ STANCE DCV OPEN TO TANK:

        IF n is time instant 1 of push-off

$$P_{cyl_{STANCE_n}} = P_{atm} + \Delta P_{to\ tank_{STANCE_n}}$$

        END IF

        ➤ PUSH-OFF DCV OPEN TO ACCUMULATOR:

IF n is time instant 1 of push-off

Call function "**C.3.8 Connect to accumulator**" to evaluate the changes in V, P and T in the accumulator due to oil compressibility, occurring when the DCV connects the push-off ram to the accumulator. The values in input to the function are those referred to the PUSH-OFF system.

END IF

ELSE IF SWING

➢ 2 DCVs OPEN TO TANK:

IF n is time instant 1 of SWING

$$P_{cyl_{PO_n}} = P_{atm} + \Delta P_{to\ tank_{PO_n}}$$

END IF

END IF

2) STANCE CAM-RAM DYNAMIC ANALYSIS:

➢ Call function "**C.3.10 Friction at O-ring**" to evaluate the friction force $F_{fr_{cyl\_STANCE_n}}$ at the internal sealed element in the stance cylinder.

➢ Evaluate the actual hydraulic ram force in the stance system:

$$F_{h_{STANCE_n}} = \left(P_{cyl_{STANCE_n}} - P_{atm}\right) A_{STANCE} + F_{fr_{cyl\_STANCE_n}}$$

➢ Call function "**C.3.11 Dynamic analysis**", which in turn calls "**C.3.12 Dynamic analysis fsolve**", to run the dynamic analysis for the time instant n in order to evaluate all the forces acting on the stance system and the resulting actual cam torque $T_{c_{STANCE_n}}$.

3) PUSH-OFF CAM-RAM DYNAMIC ANALYSIS:

> Call function "**C.3.10 Friction at O-ring**" to evaluate the friction force $F_{fr_{cyl\_PO_n}}$ at the internal sealed element in the push-off cylinder.

> Evaluate the actual hydraulic ram force in the push-off system:

$$F_{h_{PO_n}} = \left(P_{cyl_{PO_n}} - P_{atm}\right) A_{PO} + F_{fr_{cyl\_PO_n}}$$

> Call function "**C.3.11 Dynamic analysis**", which in turn calls "**C.3.12 Dynamic analysis fsolve**", to run the dynamic analysis for the time instant n in order to evaluate all the forces acting on the push-off system and the resulting actual cam torque $T_{c_{PO_n}}$.

4) Evaluate the total torque in output from the two cams of the two systems:

$$T_{c_{TOT_n}} = T_{c_{STANCE_n}} + T_{c_{PO_n}}$$

5) Evaluate the values of V, P and T in the accumulator at the next time instant ($n + 1$), due to the fluid flow from the ram to the accumulator, and adjust the value of $\left(\frac{dy}{d\theta_c}\right)_n$ to be used in the next iteration.

IF LOAD ACCEPTANCE or SWING

> Call function "**C.3.9 Incremental accumulator changes**": the ACCUMULATOR is isolated, but heat transfer may still exist from the accumulator to the surroundings.

ELSE IF STANCE

➢ Call function "**C.3.9 Incremental accumulator changes**": the ACCUMULATOR is connected to the stance ram. The function's inputs referred to the cylinder are those of the stance cylinder.

➢ Adjust $\left(\frac{dy}{d\theta_c}\right)_n$ for the stance system as the stance ram is connected to the accumulator. The new value of $\left(\left(\frac{dy}{d\theta_c}\right)_{STANCE}\right)_n$ (see equation (5.5) in section 5.2.1) will be used in the next iteration.

$$\left(\left(\frac{dy}{d\theta_c}\right)_{STANCE}\right)_{NEW_n} = \frac{\left(T_{c_{r_n}} - T_{c_{TOT_n}}\right) + \left(\left(\frac{dy}{d\theta_c}\right)_{STANCE}\right)_n F_{h_{STANCE_n}}}{F_{h_{STANCE_n}}}$$

ELSE IF PUSH-OFF

➢ Call function "**C.3.9 Incremental accumulator changes**": the ACCUMULATOR is connected to the push-off ram. The function's inputs referred to the cylinder are those of the push-off cylinder.

➢ Adjust $\left(\frac{dy}{d\theta_c}\right)_n$ for the push-off system as the push-off ram is connected to the accumulator. The new value of $\left(\left(\frac{dy}{d\theta_c}\right)_{PO}\right)_n$ (see equation (5.5) in section 5.2.1) will be used in the next iteration.

$$\left(\left(\frac{dy}{d\theta_c}\right)_{PO}\right)_{NEW_n} = \frac{\left(T_{c_{r_n}} - T_{c_{TOT_n}}\right) + \left(\left(\frac{dy}{d\theta_c}\right)_{PO}\right)_n F_{h_{PO_n}}}{F_{h_{PO_n}}}$$

END IF

END FOR (inner loop)

• SET the initial ratio $\left(\frac{dy}{d\theta_c}\right)_{initial}$ for the two systems (see step (20)) in the next iteration of the outer loop as equal to the new ones just evaluated:

$$\left(\frac{dy}{d\theta_c}\right)_{STANCE_{initial}} = \left(\left(\frac{dy}{d\theta_c}\right)_{STANCE}\right)_{NEW}$$

$$\left(\frac{dy}{d\theta_c}\right)_{PO_{initial}} = \left(\left(\frac{dy}{d\theta_c}\right)_{PO}\right)_{NEW}$$

END FOR (outer loop)

22. If the upstream code has been run just once (i.e. $spring = 1$), the normal force acting between cam and roller is known for both systems, so that it is used to size the two return springs:

   IF $spring = 1$

   ➤ Defined a desired minimum value for the normal force between cam and roller of the two systems ($F_{n_{desired\_STANCE}}, F_{n_{desired\_PO}}$).

   ➤ Evaluate the corresponding required spring force for the two systems as the difference between the desired and the actual normal force ($F_{s_{required\_STANCE}} = F_{n_{desired\_STANCE}} - F_{n_{STANCE}}, F_{s_{required\_PO}} = F_{n_{desired\_PO}} - F_{n_{PO}}$).

   ➤ Call function "**C.3.13 Return spring sizing**" to get the slope and intercept of the stance spring characteristic.

   ➤ Call function "**C.3.13 Return spring sizing**" to get the slope and intercept of the push-off spring characteristic.

   ➤ Clear all the variables except the two slops and the two intercepts of the springs, the variable "$spring$" and the variable "$gait\ cycle$".

   END IF

   END FOR ("spring" loop)

23. Call function "**C.3.7 Gearbox backwards**" to evaluate the actual ankle torque as the sum of the parallel spring torque and the gearbox input (ankle side) torque.

24. Memorise the values of $\left(\frac{dy}{d\theta_c}\right)_{STANCE}$ and $\left(\frac{dy}{d\theta_c}\right)_{PO}$ used during the last iteration of the outer iteration loop to converge to the solution: they guarantee that the cam profiles here defined are used then for the gait cycles simulation in the script "**C.2.2 Simulation model**". Memorise also the gear ratio, the gearbox capacity, the characteristics of the two return springs, and the actual ankle torque to be used in the simulation of the first gait cycle (see "**C.2.2 Simulation model**") to detect gait phases and events. They may be all memorised in a structure array in MATLAB and saved as a *.mat* file.

25. Draw the two cam profiles running the script named "**C.3.14 Cam profile**", which calculates the coordinates of the contact points between cam and roller throughout the gait cycle for the two systems, using as input piston displacement and cam angle of rotation from the last iteration of the iteration loop to converge to the solution.

    * Specifically, the function "**C.3.15 Mapping fix to body**" – called inside a for loop - maps the coordinates of the contact point for each time instant n of the gait cycle from fixed frame to cam frame by applying a transformation matrix.

    * The obtained coordinates of the contact points for the two systems are then plotted: they constitute the two cam profiles (y coordinates against x coordinates) in the cam frame.

26. Run the post-model code **"C.3.19 Power audit"** to calculate the power in input/output/lost for each component of the system, and the power residuals between each component of the system and the following one, plotting the results.

C.2.2 Simulation model

1. Set the variable ("*gait cycle*") as equal to 1 to count the gait cycles.

2. Define a variable ("*continue simulating*") to stop the gait cycles simulations as the user requires. If set as equal to 1, it indicates that the simulation must continue to the next gait cycle.

3. Import the variables memorised in a *.mat* file at step (24) of the script "**C.2.1 Design program**": $\left(\frac{dy}{d\theta_c}\right)_{STANCE}$ and $\left(\frac{dy}{d\theta_c}\right)_{PO}$, which define cams profiles; the gear ratio; the gearbox capacity; the characteristics of the two return springs; and the actual ankle torque to be used in the simulation of the first gait cycle below to detect gait phases and events.

4. Enter the while loop to simulate as many gait cycles as the user requires:

   WHILE *continue simulating* $== 1$

   Steps (5) to (15) of the below numbered list are the same as steps (5) to (15) in "**C.2.1 Design program**".

5. Import data from Excel file: time instants for a full gait cycle and corresponding values of ankle angle.

6. Define the time interval Δt between each instant of the gait cycle as the mean value of all the intervals coming from data (i.e. mean value of the vector resulting from applying the command "*diff*" to the time imported before).

7. Calculate the ankle angular velocity at each instant of the gait cycle inside a for loop:

$$\omega_{a_n} = \frac{\Delta\theta_{a_{n-1}} + \Delta\theta_{a_n}}{2\Delta t}$$

   with $2 \leq n \leq (end - 1)$. For $n = 1$ and $n = end$: $\omega_{a_1} = \frac{\Delta\theta_{a_1}}{\Delta t}$ and $\omega_{a\,end} = \frac{\Delta\theta_{a(end-1)}}{\Delta t}$.

8. Calculate the ankle angular acceleration at each instant of the gait cycle inside a for loop:

$$\alpha_{a_n} = \frac{\Delta\omega_{a_{n-1}} + \Delta\omega_{a_n}}{2\Delta t}$$

with $2 \leq n \leq (end - 1)$. For $n = 1$ and $n = end$: $\alpha_{a_1} = \frac{\Delta \omega_{a_1}}{\Delta t}$ and $\alpha_{a\,end} = \frac{\Delta \omega_{a(end)}}{\Delta t}$.

9. Identify important gait events:

    - **Positive torque:** the time instant right before that one at which the ankle torque (the one imported at step (3) above, otherwise the one resulting from the previous gait cycle) becomes positive.

    - **Maximum dorsiflexion**: the time instant of the maximum ankle angle in the used convention.

    - **Maximum plantarflexion:** the time instant of the minimum ankle angle in the used convention.

10. Identify four phases of the gait cycle and gather them in the structure "$gait\_phase$":

    - **Load acceptance:** despite the theoretical definition of this phase of the gait, in the actual code this name is referred to the phase going from the initial contact of the foot with the ground at the beginning of the gait cycle to the instant right before that one of "Positive torque".

    - **Stance**: from the time instant of "Positive torque" to the instant right before the one of maximum dorsiflexion.

    - **Push-off**: from the time instant of maximum dorsiflexion to the instant right before the one of maximum plantarflexion.

    - **Swing**: from the time instant of maximum plantarflexion to the end of the gait cycle.

11. Pre-allocate those variables used in the downstream code (Q, $F_{fr_{cyl}}$, F_h, T_{gas}, P_{acc}, V_{acc}, V_{gas}, $T_{c\,actual}$, $\Delta P_{to\ acc}$, $\Delta P_{to\ tank}$): they are arrays whose length is equal to the number of time instants of the gait cycle.

12. Define pressure and temperature of the surroundings: $T_{env} = 293K$, $P_{atm} = 101325\ Pa$.

13. Call section "**C.3.1 Accumulator, gas and oil properties**" to get the properties of the diaphragm accumulator.

14. Call section "**C.3.2 Hydraulic cylinders properties**" to get the properties of the two hydraulic cylinders of respectively the stance and the push-off system.

15. Call section "**C.3.3 Major and minor losses properties**", where the properties of pipes, inlets/exits, fittings and DCVs for the two systems are defined.

16. Call section "**C.3.4 Geometry, masses, coefficients of friction**" where the size of cam, roller and follower, and the masses of the two systems are defined, together with the coefficients of friction.

17. Define accumulator P, V and T at the first time instant ($n = 1$) of the gait cycle:

IF $gait\ cycle == 1$

$$P_{acc_{n=1}} = 0.90 * P_{max}$$

$$V_{acc_{n=1}} = V_A - (V_A - V_{acc_{pre-charge}}) \left(\frac{P_{pre-charge}}{P_{acc_{n=1}}}\right); \%\text{oil volume - isothermal process}$$

$$V_{gas_{n=1}} = V_A - V_{acc_{n=1}} \% \text{ gas volume into the accumulator}$$

$$T_{gas_{n=1}} = T_{env};$$

ELSE

$$P_{acc_{n=1}} = P_{acc}@END\ of\ SWING\ previous\ gait\ cycle$$

$$V_{acc_{n=1}} = V_{acc}\ @END\ of\ SWING\ previous\ gait\ cycle \quad \% \text{ accumulator oil volume}$$

$$V_{gas_{n=1}} = V_{gas}\ @END\ of\ SWING\ previous\ gait\ cycle \quad \% \text{ accumulator gas volume}$$

$$T_{gas_{n=1}} = T_{gas}\ @END\ of\ SWINGprevious\ gait\ cycle$$

END IF

18. Call function "**C.3.5 Parallel linear spring**" containing the spring model to calculate the torque provided by the parallel spring.

19. Call function "**C.3.6 Gearbox**" containing the gearbox model to calculate angle, velocity and acceleration of the cam.

20. Call section "**C.3.16 Variables initialisation**" to define some of the variables needed further on.

21. Call section "**C.3.17 Kinematics**" to evaluate all the kinematic variables of the two systems necessary to enter further on the for loop.

22. Calculate the two return spring forces ($F_{S_{STANCE}}$ and $F_{S_{PO}}$) considering the displacement of the pistons from the previous step, and the slope and intercept of the two springs imported at step (3).

23. Calculate the flow in the two systems (Q_{STANCE}, Q_{PO}) given by piston velocity times ram bore area.

24. Call function "**C.3.18 Major and minor losses evaluation**" to evaluate the total pressure drop in the pipework of the stance system - both from ram to accumulator ($\Delta P_{to\ acc_{STANCE}}$) and from ram to tank ($\Delta P_{to\ tank_{STANCE}}$).

25. Call function "**C.3.18 Major and minor losses evaluation**" to evaluate the total pressure drop in the pipework of the push-off system - both from ram to accumulator ($\Delta P_{to\ acc_{PO}}$) and from ram to tank ($\Delta P_{to\ tank_{PO}}$).

26. Initialise the pressure in the two cylinders (which will be overwritten during the two working phases):

$$P_{cyl_{STANCE}} = P_{atm} + \Delta P_{to\ tank_{STANCE}}$$

$$P_{cyl_{PO}} = P_{atm} + \Delta P_{to\ tank_{PO}}$$

27. Initialise the volume of oil in the two cylinders:

$$V_{cyl_{STANCE}} = \frac{\pi D^2}{4} \cdot \left(residual\ length + (\max(y_{STANCE}) - y_{STANCE})\right)$$

$$V_{cyl_{PO}} = \frac{\pi D^2}{4} \cdot \left(residual\ length + (\max(y_{PO}) - y_{PO})\right)$$

28. Define the vector $guess$ containing six initial guesses for the six unknowns of the dynamic analysis. The same is used for both systems.

29. **TIME STEPPING LOOP** for each time instant of the gait cycle:

   <u>**FOR each time-instant n of the ankle data**</u>

   1) Check the opening of the two DCVs and the possible changes in V, P and T in the accumulator due to oil compressibility:

      IF LOAD ACCEPTANCE

         ➢ 2 DCVs OPEN TO TANK.

ELSE IF STANCE

> STANCE DCV OPEN TO ACCUMULATOR:

IF n time instant 1 of stance

Call function "**C.3.8 Connect to accumulator**" to evaluate the changes in V, P and T in the accumulator due to oil compressibility, occurring when the DCV connects the stance ram to the accumulator. The values in input to the function are those referred to the STANCE system.

END IF

> PUSH-OFF DCV OPEN TO TANK.

ELSE IF PUSH-OFF

> STANCE DCV OPEN TO TANK:

IF n is time instant 1 of push-off

$$P_{cyl_{STANCE_n}} = P_{atm} + \Delta P_{to\ tank_{STANCE_n}}$$

END IF

> PUSH-OFF DCV OPEN TO ACCUMULATOR:

IF time instant 1 of push-off

Call function "**C.3.8 Connect to accumulator**" to evaluate the changes in V, P and T in the accumulator due to oil compressibility, occurring when the DCV connects the push-off ram to the accumulator. The values in input to the function are those referred to the PUSH-OFF system.

END IF

264

ELSE IF SWING

> ➤ 2 DCVs OPEN TO TANK:

IF n is time instant 1 of SWING

$$P_{cyl_{PO_n}} = P_{atm} + \Delta P_{to\ tank_{PO_n}}$$

END IF

END IF

2) STANCE CAM-RAM DYNAMIC ANALYSIS:

> ➤ Call function "**C.3.10 Friction at O-ring**" to evaluate the friction force $F_{fr_{cyl\_STANCE_n}}$ at the internal sealed element in the stance cylinder.

> ➤ Evaluate the actual hydraulic ram force in the stance system:

$$F_{h_{STANCE_n}} = \left(P_{cyl_{STANCE_n}} - P_{atm}\right)A + F_{fr_{cyl\_STANCE_n}}$$

> ➤ Call function "**C.3.11 Dynamic analysis**", which in turn calls "**C.3.12 Dynamic analysis fsolve**", to run the dynamic analysis for the time instant n in order to evaluate all the forces acting on the stance system and the resulting actual cam torque $T_{c_{STANCE_n}}$.

3) PUSH-OFF CAM-RAM DYNAMIC ANALYSIS:

> ➤ Call function "**C.3.10 Friction at O-ring**" to evaluate the friction force $F_{fr_{cyl\_PO_n}}$ at the internal sealed element in the push-off cylinder.

> ➤ Evaluate the actual hydraulic ram force in the push-off system:

$$F_{h_{PO_n}} = \left(P_{cyl_{PO_n}} - P_{atm}\right)A + F_{fr_{cyl\_PO_n}}$$

➢ Call function "**C.3.11 Dynamic analysis**", which in turn calls "**C.3.12 Dynamic analysis fsolve**", to run the dynamic analysis for the time instant n in order to evaluate all the forces acting on the push-off system and the resulting actual cam torque $T_{c_{PO_n}}$.

4) Evaluate the values of V, P and T in the accumulator for the next time instant ($n + 1$) due to the fluid flow from the ram to the accumulator.

IF LOAD ACCEPTANCE or SWING

➢ Call function "**C.3.9 Incremental accumulator changes**": the ACCUMULATOR is isolated but heat transfer may still exist from the accumulator to the surroundings.

ELSE IF STANCE

➢ Call function "**C.3.9 Incremental accumulator changes**": the ACCUMULATOR is connected to the stance ram. The function's inputs referred to the cylinder are those of the stance cylinder.

ELSE IF PUSH-OFF

➢ Call function "**C.3.9 Incremental accumulator changes**": the ACCUMULATOR is connected to the push-off ram. The function's inputs referred to the cylinder are those of the push-off cylinder.

END IF

END FOR (TIME STEPPING LOOP)

29. Evaluate the total torque in output from the two cams of the two systems:

$$T_{c_{TOT_n}} = T_{c_{STANCE_n}} + T_{c_{PO_n}}$$

30. Call function "**C.3.7 Gearbox backwards**" to evaluate the actual ankle torque as the sum of the parallel spring torque and the gearbox input (ankle side) torque.

31. Delete the last final value of the following vectors: pressure (P_{acc}), oil volume (V_{acc}), temperature (T_{gas}) and gas volume (V_{gas}), inside the accumulator, as actually they corresponds to the time instant 251 that does not exist (they are the outputs of the function **"C.3.9 Incremental accumulator changes"** when called at the last instant of the swing phase).

32. Ask the user if he/she wants to continue modelling **another gait cycle**:

    IF yes:

    a. Increase the variable that counts gait cycles (i.e. "$gait\ cycle$").
    b. Memorise the values of pressure (P_{acc}), oil volume (V_{acc}), gas volume (V_{gas}), and temperature (T_{gas}) inside the accumulator at the last time instant of the gait cycle (see step (31)) to be used as initial values for the next gait cycle (see step (17) above).
    c. Clear all the variables except: the values memorised at the previous bullet; $\left(\frac{dy}{d\theta_C}\right)_{STANCE}$ and $\left(\frac{dy}{d\theta_C}\right)_{PO}$ to guarantee that the cam profile is always the same throughout the simulation; the number of gait cycles run so far; the gear ratio; the gearbox capacity; the characteristics of the two return springs; and the actual ankle torque to be used in the next gait cycle to detect gait phases and events.

    ELSE

    Change the value of the variable that stops the gait cycles simulation: $continue\ simulating = 2$.

    END IF

    END WHILE loop

C.3 MATHEMATICAL PSEUDO-CODE

C.3.1 Accumulator, gas and oil properties

- Set the maximum pressure and volume of the accumulator:

$P_{max} = 100 bar$

$V_A = 250e - 06 \ m^3 = 250cc$

$A_W = 0.0225 m^2$ effective area of the accumulator for heat convection (i.e. the total internal surface area exposed to gas) with $h_{acc} = 0.100m$ and $r_{acc} = 0.028m$ (accumulator with cylindrical shape)

- Evaluate minimum pressure, pre-charge pressure and volume:

$P_{min} = 0.50 * P_{max}$

$P_{pre-charge} = 0.90 * P_{min}$

$V_{acc_{pre-charge}} = 0m^3$ oil volume at pre-charge pressure in the accumulator

$V_{gas_{pre-charge}} = V_A$ gas volume at pre-charge pressure in the accumulator

- Define the structure "oil" with the properties of the used oil (ISO VG 32):

$\rho = 870 \frac{kg}{m^3}$ $\mu = 0.07 Pa \cdot s$

$v = 80 \frac{mm^2}{s}$ $\beta = 1.657e + 09 \ Pa$

- Define the structure "gas" with the properties of the considered gas (N_2):

$k = 1.4$ index of the polytropic equation

$R = 8.314 \frac{J}{mol \cdot K}$ ideal gas constant

$C_{V N_2} = 741.95 \frac{J}{kg \cdot K}$ gas specific heat at constant volume for N_2

$h_{N_2} = 25 \frac{W}{m^2 \cdot K}$ overall heat transfer coefficient for N_2

$n_{N_2} = \frac{P_{pre-charge} V_{GAS\_pre-charge}}{R T_{pre-charge}}$ required number of moles of N_2 ($T_{pre-charge} = T_{env}$)

$m_{N_2} = n_{N_2} \cdot M_{N_2}$ required mass of N_2

$\tau = \frac{m_{N_2} C_{V N_2}}{h_{N_2} A_W}$ thermal time-constant

C.3.2 Hydraulic cylinders properties

$residual\ length = 0.005m$ distance between the inner head of the ram and the piston head, when the piston has completed its instroke

$\varepsilon = 0.14$ O-ring squeeze ratio

$E = 10e + 06Pa$ O-ring Young modulus

$H = 70$ O-ring shore hardness (for Martini's model)

- Stance hydraulic cylinder:

$D_{STANCE} = 0.02062m$ ram bore diameter

$A_{STANCE} = \pi \dfrac{D_{STANCE}^2}{4}$ ram bore area - oil side

$stroke\ length_{STANCE} = 0.006m$

$d_{O-ring_{STANCE}} = \dfrac{0.139\text{in}}{39.3701\frac{\text{in}}{m}} \cong 0.00353m$ O-ring cross-sectional diameter

$d_{\ O-ring\_OUT_{STANCE}} = \dfrac{0.824\text{in}}{39.3701\frac{\text{in}}{m}} \cong 0.02093m$ O-ring outside diameter (just for Martini's

model)

- Push-off hydraulic cylinder

$D_{PO} = 0.02062m$

$A_{PO} = \pi \dfrac{D_{PO}^2}{4}$

$stroke\ length_{PO} = 0.004m$

$d_{O-ring_{PO}} = \dfrac{0.139\text{in}}{39.3701\frac{\text{in}}{m}} \cong 0.00353m$

$d_{\ O-ring\_OUT_{PO}} = \dfrac{0.824\text{in}}{39.3701\frac{\text{in}}{m}} \cong 0.0209m$

C.3.3 Major and minor losses properties

- Define the structure *"pipes"* with the parameters necessary to evaluate the pressure drop due to friction inside the pipework:

  $D_{pipe} = 0.005m$ conduit internal diameter (hydraulic diameter)

  $L_{pipe} = 0.050m$ max length of the conduit

- Define the structure *"inlets_exits"* with the parameters necessary to evaluate the pressure drop at inlets/exits:

  $K_{exit} = 1$ loss coefficient for abrupt exit

  $K_{entrance} = 0.5$ loss coefficient for an entrance with a square-edged entrance

- Define the structure *"fitting"* with the parameters necessary to evaluate the pressure drop at the fittings:

  $K_{elbow} = 0.9$ loss coefficient for a standard elbow

- Define the structure *"DCV"* with the parameters necessary to evaluate the pressure drop at the DCV:

  $C_d = 0.62$ orifice discharge coefficient

  $d_{valve\_external} = D_{pipe} = 0.005\ m$ diameter of the ports of the valve

  $D_{valve\_internal} = 1.4 d_{valve_{external}} = 0.007\ m$ internal diameter of the valve

  $A_{orifice} = \pi D_{valve\_internal} d_{valve\_external}$ orifice cross-section

  $K_{eq\_DCV} = \dfrac{1}{\left(C_d A_{orifice} \sqrt{2/\rho} \right)^2}$ equivalent loss coefficient

C.3.4 Geometry, masses, coefficients of friction

- Define the structure "*stance geometry*" containing the values of cam, roller and follower geometry for the stance system.

  $a = 0.030\ m$ independent variable included in cam pressure angle evaluation

  $e = 0.019\ m$ cam offset

  $r = \dfrac{0.019}{2}\ m$ roller radius

  $d_{stud} = 0.011\ m$ diameter of the stud of the roller

  $d_{follower} = 0.5 d_{piston\ head_{STANCE}}$ follower diameter ($d_{piston\ head_{STANCE}} = 0.02055m$)

  $c = r + stroke\ length + safety\ margin$

                             initial follower overhang ($safety\ margin = \dfrac{r}{3}$)

  $l = 2r + safety\ margin$ length of the follower guide

  $l_{follower} = c + l$ follower length

  $V_{follower} = \pi \dfrac{d_{follower}^2}{4} \cdot l_{follower}$ follower volume

- Define the structure "*stance masses*" containing the values of masses for the stance system.

  $m = 0.032\ kg$ mass of roller

  $m_{rol} = 0.016\ kg$ mass of the outer rolling part of the roller

  $M = V_{follower} \cdot \rho_{SS}$ mass of the follower, with $\rho_{SS} = 7700 \dfrac{kg}{m^3}$ density of stainless steel

- Define the structure "*push $-$ off geometry*" containing values of cam, roller and follower geometry for the push-off system.

  $a = 0.030\ m$ independent variable included in cam pressure angle evaluation

  $e = 0.019\ m$ cam offset

  $r = \dfrac{0.019}{2}m$ roller radius

  $d_{stud} = 0.011\ m$ diameter of the stud of the roller

  $d_{follower} = 0.5 d_{piston\ head_{PO}}$ follower diameter ($d_{piston\ head_{PO}} = 0.02055m$)

  $c = r + stroke\ length + safety\ margin$

                             initial follower overhang with $safety\ margin = \dfrac{r}{3}$

  $l = 2r + safety\ margin$ length of the guide at the follower

$$l_{follower} = c + l \qquad\qquad \text{length of the follower}$$

$$V_{follower} = \pi \frac{d_{follower}^2}{4} \cdot l_{follower} \qquad\qquad \text{follower volume}$$

- Define the structure "$push - off\ masses$" containing the values of masses for the push-off system.

  $m = 0.032kg$ mass of roller

  $m_{rol} = 0.016kg$ mass of the outer rolling part of the roller

  $M = V_{follower} \cdot \rho_{SS}$ mass of the follower, with $\rho_{SS} = 7700 \frac{kg}{m^3}$ density of stainless

                                          steel

- Define the structure "c$oefficients\ of\ friction$" for both systems.

  $\mu_{brg} = 0.002$ coefficient of friction associated to the bearing placed into the

                                          roller

  $\mu_{rolres} = 0.002$ coefficient of friction associated to the rolling between roller

                                          and cam surface

  $\mu_{sl} = 0.003$ coefficient of friction associated to the sliding at the follower

                                          guide

C.3.5 Parallel linear spring

To evaluate the torque of the torsional spring placed in parallel with the two cam-ram systems.

Inputs:

θ_a	ankle angle
$m = 58.4038 \; N \cdot m/rad$	slope of the spring characteristic
$c = 0 \; N \cdot m$	intercept of the spring characteristic
T_a	ankle torque

Output:

T_{ps}	torque provided by the parallel spring
$T_{out_{ps}}$	torque acting on the system

Method:

- $T_{ps} = m\theta_a + c$
- $T_{out_{ps}} = T_a - T_{ps}$

C.3.6 Gearbox

To evaluate angle and velocity of the cam, the losses due to the friction torque, and the output torque acting on the rest of the system as the gearbox ideal output torque minus friction. The below function is used for each gait cycle with the only difference that, from the second gait cycle onward, just the kinematic input and output need to be considered.

Inputs:

GR	gearbox ratio
$T_{in_{gb}} = T_{out_{ps}}$	torque in input to the gearbox
θ_a	rotation angle of the ankle
ω_a	angular velocity of the ankle
α_a	angular acceleration of the ankle
$T_{capacity}$	gearbox "size"

Output:

T_f	frictional torque
T_{c_r}	total required camshaft torque
θ_c	rotation angle of the cam
ω_c	angular velocity of the cam
α_c	angular velocity of the cam

Method:

- $\theta_c = \theta_a GR$
- $\omega_c = \omega_a GR$
- $\alpha_c = \alpha_a GR$
- $\eta_g = 100 - (GR - 1)^{k_g}$ efficiency (i.e. a percentage), with k_g a coefficient to fit data
- $T_f = sign(\omega_a) \cdot T_{capacity} \frac{(100 - \eta_g)}{100}$
- $T_{c_r} = \left(\frac{T_{in_{gb}} - T_f}{GR} \right)$

C.3.7 Gearbox backwards

This function evaluates the gearbox input (ankle side) torque once the cam profiles are given.

Inputs:

GR gearbox ratio

$T_{out_{gb}} = T_c$ gearbox output (accumulator side) torque, corresponding to the total

         actual camshaft torque

$T_{capacity}$ gearbox size

Output:

T_f frictional torque

$T_{in_{gb}}$ gearbox input (ankle side) torque

Method:

- $\eta_g = 100 - (GR - 1)^{k_g}$

- $T_f = sign(\omega_c) \cdot T_{capacity} \dfrac{(100 - \eta_g)}{100}$

- $T_{in_{gb}} = T_{out_{gb}} \cdot GR + T_f$

C.3.8 Connect to accumulator

To evaluate the changes in P, V and T in the accumulator occurring when the DCV connects the cylinder to the accumulator – i.e. initial oil compressibility at the first time instant of the working phase of the two systems.

<u>Inputs</u>:

$P_{acc_{pre}} = P_{acc_n}$	accumulator pressure <u>before</u> connecting
$T_{gas_{pre}} = T_{gas_n}$	gas temperature <u>before</u> connecting
$V_{acc_{pre}} = V_{acc_n}$	oil volume in the accumulator <u>before</u> connecting
$P_{cyl_{pre}} = P_{cyl_n}$	cylinder pressure <u>before</u> connecting
$V_{cyl_{pre}} = V_{cyl_n}$	oil volume in the cylinder <u>before</u> connecting
$V_{gas_{pre}} = V_{gas_n}$	gas volume <u>before</u> connecting
$\Delta P_{to\ acc} = \Delta P_{to\ acc_n}$	total pressure drop between the cylinder and the accumulator
V_A	maximum accumulator volume
oil	structure containing the properties of the oil
gas	structure containing the properties of the gas

<u>Outputs</u>:

$V_{acc_{post}}$	oil volume in accumulator <u>after</u> connecting
$P_{acc_{post}}$	accumulator pressure <u>after</u> connecting
$T_{gas_{post}}$	gas temperature <u>after</u> connecting
$V_{gas_{post}}$	gas volume <u>after</u> connecting
$P_{cyl_{post}}$	cylinder pressure <u>after</u> connecting

All the "post" values, when they are returned from this function, they are used to update all the corresponding values for the same time instant n (V_{acc_n}, P_{acc_n}, T_{gas_n}, V_{gas_n}, P_{cyl_n}).

<u>Method (if 1st time instant of the WP)</u>:

residual = 10000;   initial value of residual to enter the while loop below (Pa)

$$P_{acc_{post\_est}} = P_{acc_{pre}}$$ initial estimate of the accumulator pressure <u>after</u> connecting

WHILE *residual > 1Pa*

$$P_{cyl_{post}} = P_{acc_{post\_est}} + \Delta P_{to\ acc}$$

$$\Delta V_{\beta_{acc}} = -V_{acc_{pre}} \frac{\left(P_{acc_{post\_est}} - P_{acc_{pre}}\right)}{\beta}$$ -ve if oil volume increases

$$\Delta V_{\beta_{cyl}} = -V_{cyl_{pre}} \frac{\left(P_{cyl_{post}} - P_{cyl_{pre}}\right)}{\beta}$$ +ve if oil volume increases

$$\Delta V_\beta = \Delta V_{\beta_{acc}} + \Delta V_{\beta_{cyl}}$$

$$V_{gas_{post}} = V_{gas_{pre}} - \Delta V_\beta$$

$$T_{gas_{post}} = T_{gas_{pre}} \left(\frac{V_{gas_{pre}}}{V_{gas_{post}}}\right)^{k-1}$$

$$P_{acc_{post}} = P_{acc_{pre}} \left(\frac{V_{gas_{pre}}}{V_{gas_{post}}}\right)^{k}$$

$$residual = \left|P_{acc_{post\_est}} - P_{acc_{post}}\right|$$

$$P_{acc_{post\_est}} = P_{acc_{post}}$$

END WHILE

$$V_{acc_{post}} = V_A - V_{gas_{post}}$$

C.3.9 Incremental accumulator changes

To evaluate the changes in V, P and T in the accumulator for each incremental change in piston displacement ($\Delta y_n = y_{n+1} - y_n$).

Inputs:

n	time instant at which the present function is called
$gait\_phase$	structure containing the definition of the different gait phases for the currently simulated gait cycle
$\Delta y = \Delta y_n$	incremental change in piston displacement
$\Delta t = \Delta t_n$	time interval
$P_{acc_{pre}} = P_{acc_n}$	accumulator pressure <u>before</u> Δy_n
$P_{cyl_{pre}} = P_{cyl_n}$	cylinder pressure <u>before</u> Δy_n
$T_{gas_{pre}} = T_{gas_n}$	gas temperature <u>before</u> Δy_n
$V_{acc_{pre}} = V_{acc_n}$	oil volume in accumulator <u>before</u> Δy_n
$V_{cyl_{pre}} = V_{cyl_n}$	oil volume in cylinder <u>before</u> Δy_n
$V_{gas_{pre}} = V_{gas_n}$	gas volume <u>before</u> Δy_n
$\Delta P_{to\ acc_{post}} = \Delta P_{to\ acc_{n+1}}$	pressure drop across DCV and pipework to accumulator <u>after</u> i.e. at time instant $(n+1)$
V_A	maximum accumulator volume
A	ram bore area
oil	structure containing the properties of the oil
gas	structure containing the properties of the gas
T_{env}	temperature of the surroundings

Outputs:

$P_{acc_{post}}$	accumulator pressure <u>after</u> Δy_n
$P_{cyl_{post}}$	cylinder pressure <u>after</u> Δy_n
$T_{gas_{post}}$	gas temperature <u>after</u> Δy_n
$V_{acc_{post}}$	oil volume in accumulator <u>after</u> Δy_n
$V_{gas_{post}}$	gas volume <u>after</u> Δy_n

All the "post" values, when returned from this function, are used to update all the corresponding values for the time instant $(n + 1)$ $(P_{acc_{n+1}}, P_{cyl_{n+1}}, T_{gas_{n+1}}, V_{acc_{n+1}}, V_{gas_{n+1}})$.

Method:

residual = 10000;   initial value of residual to enter the while loop below (Pa)

$P_{acc_{post\_est}} = P_{acc_{pre}}$ initial estimate of the accumulator pressure <u>after</u> Δy_n

IF STANCE or PUSH-OFF (i.e. WP of the 2 SYSTEMS: the accumulator is connected respectively to the stance and the push-off ram)

      WHILE *residual > 1Pa*

$$P_{cyl_{post}} = P_{acc_{post\_est}} + \Delta P_{to\ acc_{post}}$$

$$\Delta V_{\beta_{acc}} = -V_{acc_{pre}} \frac{\left(P_{acc_{post\_est}} - P_{acc_{pre}}\right)}{\beta}$$

$$\Delta V_{\beta_{cyl}} = -V_{cyl\_pre} \frac{\left(P_{cyl_{post}} - P_{cyl_{pre}}\right)}{\beta}$$

$$\Delta V_{\beta} = \Delta V_{\beta_{acc}} + \Delta V_{\beta_{cyl}}$$

$$\Delta V_{oil\ flow} = \Delta y A + \Delta V_{\beta}$$

$$V_{acc_{post}} = V_{acc_{pre}} + \Delta V_{oil\ flow}$$

$$V_{gas_{post}} = V_A - V_{acc_{post}}$$

$$T_{gas_{post\_poly}} = T_{gas_{pre}} \left(\frac{V_{gas_{pre}}}{V_{gas_{post}}}\right)^{k-1}$$

$$\Delta T_{poly} = T_{gas_{post\_poly}} - T_{gas_{pre}}$$

$$T_{gas_{post\_transfer}} = \left[T_{gas_{pre}} - T_{env}\right] e^{-\frac{\Delta t}{\tau}} + T_{env}$$

$$\Delta T_{transfer} = T_{gas_{post\_transfer}} - T_{gas_{pre}}$$

$$\Delta T_{total} = \Delta T_{poly} + \Delta T_{transfer}$$

$$T_{gas_{post}} = T_{gas_{pre}} + \Delta T_{total}$$

$$P_{acc_{post}} = nR \frac{T_{gas_{post}}}{V_{gas_{post}}}$$

$$residual = \left| P_{acc_{post\_est}} - P_{acc_{post}} \right|$$

$$P_{acc_{post\_est}} = P_{acc_{post}}$$

END WHILE

ELSE IF LOAD ACCEPTANCE or SWING (i.e. NWP for both the 2 SYSTEMS: the accumulator is isolated but there is still heat transfer)

WHILE *residual > 1Pa*

$$\Delta V_{\beta\,acc} = -V_{acc_{pre}} \frac{\left(P_{acc_{post\_est}} - P_{acc_{pre}} \right)}{\beta}$$

$$V_{acc_{post}} = V_{acc_{pre}} + \Delta V_{\beta\,acc}$$

$$V_{gas_{post}} = V_A - V_{acc_{post}}$$

$$T_{gas_{post\_poly}} = T_{gas_{pre}} \left(\frac{V_{gas_{pre}}}{V_{gas_{post}}} \right)^{k-1}$$

$$\Delta T_{poly} = T_{gas_{post\_poly}} - T_{gas_{pre}}$$

$$T_{gas_{post\_transfer}} = \left[T_{gas_{pre}} - T_{env} \right] e^{-\frac{\Delta t}{\tau}} + T_{env}$$

$$\Delta T_{transfer} = T_{gas_{post\_transfer}} - T_{gas_{pre}}$$

$$\Delta T_{total} = \Delta T_{poly} + \Delta T_{transfer}$$

$$T_{gas_{post}} = T_{gas_{pre}} + \Delta T_{total}$$

$$P_{acc_{post}} = nR \frac{T_{gas_{post}}}{V_{gas_{post}}}$$

$$residual = \left| P_{acc_{post\_est}} - P_{acc_{post}} \right|$$

$$P_{acc_{post\_est}} = P_{acc_{post}}$$

END WHILE

END IF

C.3.10 Friction at O-ring

To evaluate friction at the internal sealed element – the piston head - (with O-ring) in the cylinder. Martini's model is used as it is more conservative than Xia's model - i.e. characterised by the highest friction losses. Note that all the values used by Martini are expressed in the British Imperial system of units

Inputs:

$\dot{y} = \dot{y}_n$ piston velocity <u>at time instant</u> n (<u>before</u> Δy_n)

P pressure in the rod-less side of the piston

d_{O-ring} O-ring cross-sectional diameter for both pistons

d_{O-ring_OUT} O-ring outside diameter for both pistons

$\varepsilon = 0.14$ O-ring squeeze ratio

$H_S = 70°$ O-ring shore hardness

Output:

$F_{fr_{cyl}}$ friction for O-ring sealed cylinder model <u>at time instant</u> n

The values $(F_{fr_{cyl_n}})$ returned in output from this function corresponds to the same time instant n of the input.

Method:

- $P_{atm} = 101325 Pa * 0.000145038$ to convert P_{atm} in psi

- $P_{psi} = P * 0.000145038$ to convert the system pressure P in psi

- $\Delta P = abs(P_{psi} - P_{atm})$

- $L_0 = \pi d_{O-ring\_OUT}$

- $S_W = 100\varepsilon$ actual squeeze of the O-ring cross section

- $f_C = (-0.884 + 0.0206 H_S - 0.0001 H_S{}^2) S_W$

- $F_C = sign(\dot{y}) L_0 f_C$

- $D_m = d_{O-ring\_OUT} - d_{O-ring}$ O-ring mean diameter

- $A = \pi D_m d_{O-ring}$

- $f_H = 0.545 (\Delta P)^{0.61}$

- $F_H = sign(\dot{y}) A f_H$

- Conversion back from the British Imperial System of unit to the International System of units:

$$F_{fr_{cyl}} = \frac{F_C + F_H}{0.2248}$$

C.3.11 Dynamic analysis

To evaluate all the forces acting on the roller-follower and the follower system at each time instant n of the gait cycle. The six simultaneous non-linear equations coming from the dynamic analysis are implemented and solved using the specific MATLAB command "fsolve".

Inputs:

n	time instant at which the present function is called
$F_h = F_{h_n}$	hydraulic ram force (including friction inside the ram) <u>at time instant n</u>
$F_s = F_{s_n}$	return spring force <u>at time instant n</u>
$\dot{y} = \dot{y}_n$	piston velocity <u>at time instant n</u>
$\ddot{y} = \ddot{y}_n$	piston acceleration <u>at time instant n</u>
$guess$	vector of initial guesses for the six unknowns of the dynamic analysis: the software starts from them to solve the non-linear system
$coefficients\ of\ friction$	structure containing the frictional coefficients for the whole system
$masses$	structure containing the masses of all the components of the system
$geometry$	structure containing the geometric parameters of cam, roller and follower
$vectors\ \vec{s}\ \&\ \vec{u}$	vectors defining the position of the contact point between cam and roller with respect to cam centre for Δy_n
$pressure\ angle\ (\alpha)$	pressure angle of the cam <u>at time instant n</u>
$\omega_c = \omega_{c_n}$	cam angular velocity <u>at time instant n</u>
$\alpha_c = \alpha_{c_n}$	cam angular acceleration <u>at time instant n</u>
$\dot{\beta} = \dot{\beta}_n$	roller angular velocity <u>at time instant n</u>
$\ddot{\beta} = \ddot{\beta}_n$	angular acceleration <u>at time instant n</u>
$\omega_{rel} = \omega_{rel_n}$	relative velocity between cam and roller <u>at time instant n</u>

Outputs:

F_n	unknown I: normal force acting on cam profile <u>at time instant n</u>
F_t	unknown II: tangential force acting on cam profile <u>at time instant n</u>
N_1	unknown III: constraining reaction at the follower guide <u>at time instant n</u>

N_2 unknown IV: constraining reaction at the follower guide <u>at time instant n</u>

R_V unknown V: vertical constraining reaction between roller and follower <u>at time instant n</u>

R_H unknown VI: horizontal constraining reaction between roller and follower <u>at time instant n</u>

F_{fr1} frictional force at the follower guide <u>at time instant n</u>

F_{fr2} frictional force at the follower guide <u>at time instant n</u>

M_{brg} frictional at the bearing placed into the roller <u>at time instant n</u>

M_{rolres} rolling resistance between cam and roller <u>at time instant n</u>

$T_{c_{actual}}$ actual cam torque <u>at time instant n</u>

$residuals$ residuals of the six equations <u>at time instant n</u>

The values returned in output from this function are used for the same time instant n of the input.

Method:

- $g = 9.81 \frac{m}{s^2}$ gravitational acceleration

- $I_{rol} = \frac{1}{2} m_{rol} \left(r^2 + \left(\frac{d_{brg}}{2} \right)^2 \right)$

- $x = fsolve(\textbf{``Dynamic analysis fsolve''}, guess, options)$

  MATLAB command "$fsolve$" starts from the values specified in $guess$ to solve the problem specified by $F(x) = 0$ for x, and it considers the optimization options specified in $options$.

  Command INPUT: the function "**C.3.12 Dynamic analysis fsolve**", which contains the function $F(x)$, constituted by the six simultaneous equations.

  Command OUTPUT: x, which is the vector of the six unknowns.

- $M_{brg} = sign(\dot{\beta}) \cdot \mu_{brg} \cdot \frac{d_{brg}}{2} \cdot |F_n|$

- $M_{rolres} = sign(\omega_{rel}) \cdot \mu_{rolres} \cdot |F_n| \cdot r$

- $F_{fr1} = sign(\dot{y}) \cdot \mu_{sl} |N_1|$

- $F_{fr2} = sign(\dot{y}) \cdot \mu_{sl} |N_2|$

- $residuals$ evaluation: all the terms of each one of the six equations are moved on the left side of the equal and normalised by the hydraulic force at the start.

- $T_{c_{camram}} = s \cdot F_n - u \cdot F_t - M_{rolres}$ torque applied to the cam according to equation (4.50) in section 4.3.4, where the subscript "*camram*" stands for either the stance or the push-off ram.

$T_{c_{camram}} = s \cdot F_n - u \cdot F_t - M_{rolres}$

C.3.12 Dynamic analysis fsolve

It contains the six simultaneous equations in six unknowns that command "fsolve" solves in MATLAB.

Inputs:

x	the vector of the six unknown which the command "fsolve" solves the problem specified by $F(x) = 0$ for
n	time instant at which the present function is called
$F_h = F_{h_n}$	hydraulic ram force (including friction inside the ram) <u>at time instant n</u>
$F_s = F_{s_n}$	return spring force <u>at time instant n</u>
$\dot{y} = \dot{y}_n$	piston velocity <u>at time instant n</u>
$\ddot{y} = \ddot{y}_n$	piston acceleration <u>at time instant n</u>
$\dot{\beta} = \dot{\beta}_n$	angular velocity of the roller-follower <u>at time instant n</u>
$\ddot{\beta} = \ddot{\beta}_n$	angular acceleration of the roller-follower <u>at time instant n</u>
$\omega_{rel} = \omega_{rel_n}$	relative angular velocity between cam and roller <u>at time instant n</u>
$coefficients\ of\ friction$	structure containing the frictional coefficients for all the system
$masses$	structure containing the masses of all the components of the system
$geometry$	structure containing the geometric parameters of cam, roller and follower.
$pressure\ angle\ (\alpha)$	pressure angle of the cam <u>at time instant n</u>
g	gravitational acceleration
I_{rol}	moment of inertia of the rotating outer part of the roller-follower

Outputs:

$F(x)$	function constituted by the six simultaneous equations <u>at time instant n</u> with $x = [F_n, F_t, N_1, N_2, R_V, R_H]$.

Method:

- As F is a function of x, to continue to use the real name of the unknowns in the downstream calculations, the following step is necessary:

$$F_n = x(1), F_t = x(2), N_1 = x(3), N_2 = x(4), R_V = x(5), R_H = x(6)$$

- $F_{fr1} = sign(\dot{y}) \cdot \mu_{sl}|N_1|$

- $F_{fr2} = sign(\dot{y}) \cdot \mu_{sl}|N_2|$

- $M_{fr1} = sign(N_1) \cdot \frac{d}{2}F_{fr1}$

- $M_{fr2} = sign(N_2) \cdot \frac{d}{2}F_{fr2}$

- $M_{brg} = sign(\dot{\beta}) \cdot \mu_{brg} \cdot \frac{d_{brg}}{2} \cdot |F_n|$

- $M_{rolres} = sign(\omega_{rel}) \cdot \mu_{rolres} \cdot |F_n| \cdot r$

- $F = \begin{bmatrix} F_t \cos\alpha - F_n \sin\alpha + R_H = 0 \\ F_t \sin\alpha + F_n \cos\alpha - R_V - mg = m\ddot{y} \\ F_t r - M_{rolres} - M_{brg} = I_{rol}\ddot{\beta} \\ N_2 - R_H - N_1 = 0 \\ R_V - F_h - Mg - F_{fr1} - F_{fr2} - F_s = M\ddot{y} \\ M_{brg} - R_H \left(c + \frac{l}{2}\right) + N_1\frac{l}{2} + N_2\frac{l}{2} - M_{fr1} + M_{fr2} = 0 \end{bmatrix}$

All the values in input and in output from this function are referred to the same time instant n, as this block of code is called inside the previous function ("**C.3.11 Dynamic analysis**").

C.3.13 Return spring sizing

To size the return spring to make F_n always positive (the roller-follower should always be in contact with the cam).

Inputs:

$F_{s_{required}}$ required spring force: difference between the desired and the actual normal

           force

y piston displacement throughout the gait cycle

Outputs:

k slope of the spring characteristic (N/m)

y_0 intercept of the spring characteristic (N)

Method:

1. Define the maximum slope allowable for the linear return spring (see section 5.2.2):

$$k_{max} = 500{,}000 \, \frac{N}{m}$$

2. Find the minimum value of piston displacement.
3. Find the corresponding indices of this minimum value in the array of the piston displacement.
4. Identify the value/s of $F_{s_{required}}$ corresponding to the minimum value of piston displacement.
5. Find the maximum value of those identified at the previous bullet.
6. Define a new array $(F_{s_{selected}})$ made of a range of values going from the value found at the previous bullet to the maximum value of $F_{s_{required}}$ (with $F_{s_{selected}} < max(F_{s_{required}})$) with an increment of $0.1N$.
7. Enter a FOR loop to identify all the pairs of slope (k) and the intercept (y_0) that make the spring characteristic always larger than the required spring force:

FOR $i = 1: length(F_{s_{selected}})$

- Set the value of the intercept: $y_0 = F_{s_{selected}}(i)$.

288

- Define a variable (*"differences"*) that will contain the differences between the resulting spring characteristics and $F_{s_{required}}$. It is initially set to an array of (-1), with a length equal to that of $F_{s_{required}}$.

- Set the initial value of the slope: $k = 0.1 \frac{N}{m}$.

- Set a while loop that, for each value of the intercept (y_0) defined at the first bullet, increases the value of the slope (k) until the difference between each element of the resulting spring force array (F_s) and the corresponding one of the required spring force array is positive ($differences = F_s - F_{s_{required}} \geq 0 \rightarrow F_s \geq F_{s_{required}}$ at each time instant):

WHILE $differences < 0$

  ➢ Evaluate the resulting spring force: $F_s = ky + y_0$.
  ➢ Recalculate the array of the difference: $differences = F_s - F_{s_{required}}$.

  ➢ **IF** $differences \geq 0$

  　　Terminate the WHILE loop (*"break"*).

  　　ELSE

  　　　Increase the value of the slope of $0.1 \frac{N}{m}$

  　　　IF the value of the slope is bigger than the maximum slope (see step (1) above)

  　　　　Terminate the WHILE loop (*"break"*).

  　　　END IF

  　　　Set again $differences$ to an array of (-1).

        END IF

    END WHILE

- Define an array with all those values of slope (k) that make the resulting spring characteristic (F_s) always bigger than $F_{s_{required}}$ ($differences \geq 0$).
- Memorise the corresponding values of the intercept (y_0).

END FOR

8. **FOR** all the combinations (k, y_0) previously memorised:

- Calculate the resulting spring characteristic: $F_s = ky + y_0$.
- Calculate the corresponding integral of the spring characteristic (using MATLAB command "$trapz$"): $area = trapz(y, F_s)$.

    END FOR

9. Identify the combination of k and y_0 of that spring characteristic with the minimum absolute value of the integral (i.e. that combination minimising $\int (F_s - F_{s_{required}}) dy$).

C.3.14 Cam profile

To obtain the two cam profiles mapping the coordinates of the contact points P between cam and roller from the fixed frame to the cam frame.

- **For** each time instant n, the coordinates of the contact point P between cam and roller are evaluated in the cam-based reference frame:

  FOR each time instant n

      Call the Function **"C.3.15 Mapping fix to body"**

  END FOR

- Plot the obtained coordinates of the cam profiles.

C.3.15 Mapping fix to body

Inputs:

$y = y_n$ piston displacement <u>at time instant n</u>

$\theta_c = \theta_{c_n}$ cam angle of rotation <u>at time instant n</u>

$geometry$ structure containing the geometric parameters of cam, roller and follower

$pressure\ angle\ (\alpha)$ pressure angle of the cam <u>at time instant n</u>

Output:

$\begin{bmatrix} x_P \\ y_P \end{bmatrix}_{cam}$ coordinates of the contact point $P(x_P, y_P)$ in the cam frame <u>at time instant n</u>

Method:

- $^{cam}_{fix}R = {}^{fix}_{cam}R^T = \begin{bmatrix} cos\theta_c & -sin\theta_c \\ sin\theta_c & cos\theta_c \end{bmatrix}^T = \begin{bmatrix} cos\theta_c & sin\theta_c \\ -sin\theta_c & cos\theta_c \end{bmatrix}$

- $\begin{bmatrix} x_P \\ y_P \end{bmatrix}_{fix} = \begin{bmatrix} geometry.cam\_offset + geometry.roller\_radius \cdot sin(\alpha) \\ (geometry.a + y) - geometry.roller\_radius \cdot cos(\alpha) \end{bmatrix}$

- $\begin{bmatrix} x_P \\ y_P \end{bmatrix}_{cam} = {}^{cam}_{fix}R \begin{bmatrix} x_P \\ y_P \end{bmatrix}_{fix}$ Matrix operation according to matrix algebra to get the coordinates of the contact point P mapped from the fixed to the cam frame.

C.3.16 Variables initialisation

- $\Delta\theta_c = diff(\theta_c)$ incremental changes in cam angle
- Evaluate the angle of the cam at the start and at the end of stance and push-off $(\theta_{c_{positive\_torque}}, \theta_{c_{\max DF}}, \theta_{c_{\max PF}})$ to evaluate further on $\frac{dy}{d\theta_c}$ for full gait cycle through interpolation.
- Pre-allocate the maximum amount of space required for all the forces (F_n, F_t, N_1, N_2, R_V, R_H, F_{fr1}, F_{fr2}) and moments (M_{brg}, M_{rolres}, T_c) in output from the dynamic analysis for both system in two structures called respectively *"dynamic_analysis_stance"* and *"dynamic_analysis_push − off"*. Those variables are arrays with a length equal to the number of time instants of the considered gait cycle.

- **IF $gait\ cycle\ == "design"$**

   - For both system, define an approximation of the hydraulic force – without friction and pressure drops- to start the simulation by multiplying the ram bore area by the difference between the starting cylinder pressure and the atmospheric pressure: $(P_{cyl_{STANCE}} − P_{atm})A_{STANCE}$ and $(P_{cyl_{PO}} − P_{atm})A_{PO}$. For this approximation, $P_{cyl_{STANCE}} = P_{cyl_{PO}} = P_{acc_{n=1}}$ because the flow necessary to evaluate major and minor losses is still unknown.

   - Pre-allocate the amount of space required from the hydraulic ram forces in the two systems ($F_{h_{STANCE}}$ and $F_{h_{PO}}$) - arrays with a length equal to the number of time instants of the gait cycle, and initialise the two forces to the hydraulic forces evaluated at the previous bullet.

   - Initialise the ratio of the incremental changes in length of the piston to the incremental changes in cam angle $\left(\frac{dy}{d\theta_c}\right)_{initial}$ to the ratio of the cam torque to the hydraulic force (see equation (5.4) in section 5.2) for the first iteration only:

$$\left(\frac{dy}{d\theta_c}\right)_{STANCE_{initial}} = \frac{T_{c_r}}{F_{h_{STANCE}}}$$

$$\left(\frac{dy}{d\theta_c}\right)_{PO_{initial}} = \frac{T_{c_r}}{F_{h_{PO}}}$$

ENDIF

C.3.17 Kinematics

- Pre-allocate the variables used in this block of code (Δy_{STANCE}, Δy_{PO}, y_{STANCE}, y_{PO}, $\dot{y}_{STANCE}$, $\dot{y}_{PO}$, $\ddot{y}_{STANCE}$, $\ddot{y}_{PO}$): Δy_{STANCE} and Δy_{PO} are arrays with a length equal to the number of time intervals of the gait cycle, while all the other variables are arrays with a length equal to the number of time instants of the gait cycle.

- **IF** $gait\ cycle\ ==\ "design"$

    - Pre-allocate $\left(\frac{dy}{d\theta_c}\right)_{STANCE}$ and $\left(\frac{dy}{d\theta_c}\right)_{PO}$ - arrays with a length equal to the number of time instants of the gait cycle.

    - Define $\left(\frac{dy}{d\theta_c}\right)_{STANCE}$ and $\left(\frac{dy}{d\theta_c}\right)_{PO}$ over the whole gait cycle using interpolation based on the relationship between respectively $\left(\frac{dy}{d\theta_c}\right)_{STANCE_{initial}}$ and $\left(\frac{dy}{d\theta_c}\right)_{PO_{initial}}$ and cam angle (θ_c) during the two working phases. Specifically, the values of the ratio $\frac{dy}{d\theta_c}$ outside of the working phases are overwritten with corrected values based on the relationship between $\frac{dy}{d\theta_c}$ and cam angle θ_c during the working phase (using MATLAB command for interpolation "*interp1*", which also performs extrapolation). This allows not to have sudden changes in cam profile shape and, thus, discontinuities in the results of the simulation.

        FOR each time instant n of the ankle data

            STANCE CAM-RAM system

            IF θ_{c_n} < angle of cam at start of stance ($\theta_{c_{positive\_torque_n}}$) **THEN**

            $$\left(\frac{dy}{d\theta_c}\right)_{STANCE_n} = 0$$

            ELSE

$\left(\frac{dy}{d\theta_c}\right)_{STANCE_n}$ is the result of the interpolation of $\left(\frac{dy}{d\theta_c}\right)_{STANCE}$ based on the

relationship between θ_c and $\left(\frac{dy}{d\theta_c}\right)_{STANCE_{initial}}\bigg|_{during\ STANCE}$, using MATLAB

command *"interp1"*.

END IF

PUSH-OFF CAM-RAM system

$\left(\frac{dy}{d\theta_c}\right)_{PO_n}$ is the result of the interpolation of $\left(\frac{dy}{d\theta_c}\right)_{PO}$ based on the relationship

between θ_c and $\left(\frac{dy}{d\theta_c}\right)_{PO_{initial}}\bigg|_{during\ PO}$, using MATLAB command *"interp1"*.

END FOR

END IF

- Evaluate the incremental changes in displacements of the two pistons in a for loop:

$$\Delta y_{STANCE_n} = \frac{\left(\left(\frac{dy}{d\theta_c}\right)_{STANCE_n} + \left(\frac{dy}{d\theta_c}\right)_{STANCE_{n+1}}\right)}{2} \cdot \Delta\theta_{c_n}$$

$$\Delta y_{PO_n} = \frac{\left(\left(\frac{dy}{d\theta_c}\right)_{PO_n} + \left(\frac{dy}{d\theta_c}\right)_{PO_{n+1}}\right)}{2} \cdot \Delta\theta_{c_n}$$

- Evaluate the overall displacement of the pistons throughout the gait cycle.

  - Set $y_{STANCE_{n=1}}$ and $y_{PO_{n=1}}$ as equal to 0.

  - **FOR** n=1 : length(Δy_{STANCE})

$$y_{STANCE_{n+1}} = y_{STANCE_n} + \Delta y_{STANCE_n}$$

END FOR

- **FOR** n=1 : length(Δy_{PO})

$$y_{PO_{n+1}} = y_{PO_n} + \Delta y_{PO_n}$$

END FOR

- In case negative values of piston displacement exist, shift the whole piston displacement curve in the direction of positive displacements:

IF $\min(y_{STANCE}) < 0$

$$y_{STANCE} = y_{STANCE} + |\min(y_{STANCE})|$$

END IF

IF $\min(y_{PO}) < 0$

$$y_{PO} = y_{PO} + |\min(y_{PO})|$$

END IF

- Evaluate cam pressure angle (using equation (4.31) in section 4.3.2) for both systems throwing an error if it is either smaller or larger than 90°**.**
- Evaluate the two vectors s and u for both systems (using equation (4.17) in section 4.3.2), throwing an error if u vector is negative during the working phase.
- Evaluate the velocity of the two pistons of the two systems follows:

$$\dot{y}_{STANCE} = \left(\frac{dy}{d\theta_c}\right)_{STANCE} \omega_c$$

$$\dot{y}_{PO} = \left(\frac{dy}{d\theta_c}\right)_{PO} \omega_c$$

- Evaluate angular velocity of the roller $\dot{\beta}$ according to equation (4.29) in section 4.3.2 ($\dot{\beta} = \frac{1}{r}[-u\omega_c - \dot{y}\sin\alpha]$).

- Evaluate the acceleration of the two pistons ($\ddot{y}_{STANCE}$ and $\ddot{y}_{PO}$) according to equation (4.23) in section 4.3.2.

- Evaluate the angular acceleration of the roller $\ddot{\beta}$ according to equation (4.24) in section 4.3.2 ($\ddot{\beta} = \frac{1}{r}[-u\alpha_c - s\omega_c{}^2 - \ddot{y}\sin\alpha]$).

- Evaluate the relative velocity between cam and roller ($\omega_{rel} = \dot{\beta} - \omega_c$).

- Update the length of the follower overhang for the two followers:

$c_{STANCE} = c_{STANCE_{initial}} - y_{STANCE}$

$c_{PO} = c_{PO_{initial}} - y_{PO}$

C.3.18 Major and minor losses evaluation

To calculate the pressure drops due to major and minor losses in the pipework both between the ram and the accumulator and between the ram and the tank.

Inputs:

$pipes$	structure containing the parameters describing the pipes
$inlets\_exits$	structure containing the parameters describing the inlets/exits
$fitting$	structure containing the parameters describing the fittings
DCV	structure containing the parameters describing the DCV
oil	structure containing the properties of the used oil (ISO VG 32)
Q	flow throughout the gait cycle

Outputs:

$\Delta P_{to\ acc}$	total pressure drop in the pipework between the ram and the accumulator
$\Delta P_{to\ tank}$	total pressure drop in the pipework between the ram and the tank

Method:

- Evaluate pipe area:

$$A_{pipe} = \pi \frac{D_{pipe}^{2}}{4}$$

- Using equation (4.63) in section 4.5.3, evaluate the pressure drop across the DCV.
- Using equation (4.61) in section 4.5.3, evaluate the pressure drop across fittings between the ram and the accumulator (exit, entrance and one elbow).
- Using equation (4.60) in section 4.5.1, evaluate the pressure drop across pipes.
- Evaluate the total pressure drop in the pipework between the ram and the accumulator by summing up the three previous pressure drops.

- Using the same equation (4.61) in section 4.5.3, evaluate the pressure drop across fittings between the ram and the tank (exit and entrance).

- Evaluate the total pressure drop in the pipework between the ram and the tank by summing up the pressure drop calculated at the previous bullet and that one across the DCV.

C.3.19 Power audit

Equations (5.10) - (5.45) in section 5.3 are implemented in this script, together with equations (5.48) - (5.55) for power residuals. Specifically, the cam-ram power equations in sections 5.3.3 to 5.3.7 and also equations (5.50) - (5.53) are implemented twice for the stance and push-off systems.

Appendix D:

Categorisation of the design parameters

Tables D. 1 – D. 7 below show all design parameters of the system divided into three categories: constants, *independent* variables (primary (in red) and secondary, as explained in section 6.1), and *dependent* variables.

Gearbox

Design parameters	Constants	*Primary independent variables*	*Secondary independent variables*	*Dependent variables*
GR (*dimensionless*) gearbox ratio	-	$1, 3, 5$	-	-
η_g (%) gearbox efficiency	-	-	-	$\eta_g = 100 - (GR - 1)^{k_g}$ with k_g= coefficient to fit data (Gardiner *et al.*, 2017)

Table D. 1 Parameters defining the gearbox.

Cam

Design parameters	Constants	*Primary independent variables*	*Secondary independent variables*	*Dependent variables*
a (m) starting position of the follower in the vertical direction (see Figure 4.3)	-	-	It can be varied to optimise the design (reducing the pressure angle α) $a_{max} = 50mm$	-

Design parameters	Constants	Primary independent variables	Secondary independent variables	Dependent variables
e (m) follower offset (or eccentricity) defining the distance between the centre line of the follower and the cam centre (see Figure 4.3)	-	-	It can be varied to optimise the design (reducing the pressure angle α) $e_{max} = 50mm$	-
α $(°)$ cam pressure angle (see Figure 4.3)	-	-	-	Calculated using equation (4.31) in section 4.3.2, and $|\alpha| \leq |\alpha|_{max} = 30°$

Table D. 2 Parameters defining the cam.

Roller

Design parameters	Constants	Primary independent variables	Secondary independent variables	Dependent variables
d_{roller} (m) roller diameter	-	-	-	It depends on the applied hydraulic ram force ($F_{h\,nominal}$) and, thus, on the generated $F_{n\,nominal}$. It is selected from catalogues according to the maximum allowable dynamic load in the radial direction that a roller can withstand. $d_{roller} \leq 30mm$
r (m) roller radius	-	-	-	$r = \dfrac{d_{roller}}{2}$

Design parameters	Constants	Primary independent variables	Secondary independent variables	Dependent variables
m (kg) roller mass	-	-	-	Depending on the selected d_{roller}, it comes from catalogues
m_{rol} (kg) mass of the rotating outer part of the roller	-	-	-	$m_{rol} = \rho_{roller} V_{rol}$ where V_{rol} is the volume of the outer rolling part of the roller (estimated from roller dimensions from catalogues). It mainly depends on d_{roller}
d_{brg} (m) stud diameter	-	-	-	It depends on d_{roller}
μ_{brg} $(dimensionless)$ coefficient of friction of roller-follower bearings	$\mu_{brg} = 0.002$ (SKF, 2013) for cylindrical roller bearings and needle roller bearings with cage	-	-	-
μ_{rolres} $(dimensionless)$ coefficient of rolling friction	$\mu_{rolres} = 0.002$ (steel on steel) It depends on the selected material for cam and roller	-	-	-

Table D. 3 Parameters defining the roller.

Follower

Design parameters	Constants	Primary independent variables	Secondary independent variables	Dependent variables

M (kg) follower mass	-	-	-	$M = \rho_{follower}V_{follower}$ with $V_{follower}$ evaluated from follower dimensions and considering it like a cylinder
$d_{follower}$ (m) follower diameter	-	-	-	Same value of the diameter of the piston rod (d), since they constitute one body
c (m) follower overhang	-	-	-	It should be kept small according to cam design suggestions (Rothbart, 2004). It changes with piston displacement y. Its initial value (when $y = 0m$) is set as: $c = stroke\ length + r +$ $safety\ margin$, with $safety\ margin = r/3$ and $stroke\ length$ estimated from theory. For each instant t of the gait cycle, its value for the next time instant $(t + 1)$ is evaluated as: $c_{t+1} = c_{initial} - y_t$
l (m) distance between the 2 lines of action of the two normal forces at the follower guide (N_1, N_2)	-	-	-	Assumed to be approximately $l = 2r + safety\ margin$

Design parameters	Constants	*Primary independent variables*	*Secondary independent variables*	*Dependent variables*
$l_{follower}$ (m) follower length	-	-	-	It depends on the value of c when the piston is at rest and on l: $l_{follower} = c + l$
μ_{sl} $(dimensionless)$ coefficient of friction of the bearings at the follower	$\mu_{sl} = 0.003$ (SKF, 2013) for self-aligning ball bearing	-	-	-

Table D. 4 Parameters defining the follower.

Cylinder & hydraulic oil

Design parameters	Constants	*Primary independent variables*	*Secondary independent variables*	*Dependent variables*
D (m) hydraulic ram bore	-	0.020, 0.010, 0.005	-	-
d (m) piston rod diameter	-	-	-	It depends on D. Analysing the relationship d/D for off-the-shelf hydraulic cylinders from catalogues (HYDAIRA; Hydraulics, 2018; RAMKO; STEERFORTH), generally $d = (0.44 - 0.66)D$. Hence, $d = 0.5D$ was chosen
$residual\ length$ (m) when the piston has completed its instroke, residual distance between piston head and the inner head of the ram	-	-	0.005	-

d_{O-ring} (m) O-ring cross-sectional diameter	-	-	-	It depends on the chosen D (from O-ring catalogues (Parker Hannifin, 2007a))
E (Pa) O-ring Young modulus	$E = 10e06$ typical modulus for elastomeric seals (Xia & Durfee, 2011a)	-	-	-
ε $(dimensionless)$ O-ring squeeze ratio	$\varepsilon = 0.14$ is the value used by Xia and Durfee (2014) to make sure friction was measurable in their experiments	-	-	-
μ_f $(dimensionless)$ friction coefficient between the O-ring and the cylinder-wall	$\mu_f = 0.4$ for O-ring seals ($\mu_f = 0.3 - 0.5$ for well finished and sufficiently lubricated sealed surfaces (Xia & Durfee, 2011b, 2014))	-	-	-
β (Pa) oil bulk modulus	$\beta = 1.657e + 09$ for an ISO VG 32 mineral oil (see Appendix A.4)	-	-	-
ρ $\left(\frac{kg}{m^3}\right)$ oil density	$\rho = 870$ for an ISO VG 32 mineral oil (see Appendix A.4)	-	-	-
v $\left(\frac{mm^2}{s}\right)$ oil kinematic viscosity	$v = 80$ for an ISO VG 32 mineral oil (see Appendix A.4)	-	-	-

Design parameters	Constants	Primary independent variables	Secondary independent variables	Dependent variables
μ $(Pa \cdot s)$ oil dynamic viscosity	$\mu = 0.07$ for an ISO VG 32 mineral oil (see Appendix A.4)	-	-	-

Table D. 5 Parameters defining the cylinder and the hydraulic oil.

Pipes & discrete components

Design parameters	Constants	Primary independent variables	Secondary independent variables	Dependent variables
D_{pipe} (m) pipe internal diameter (hydraulic diameter)	-	-	$0.005 m$	-
L_{pipe} (m) pipe length	-	-	$L_{pipe} = 0.050\ m$ from ram to accumulator. $L_{pipe} = 0\ m$ from ram to tank, as the DCV is mounted directly onto the ram and surrounded by the tank at atmospheric pressure	-
K_{exit} $(dimensionless)$ loss coefficient for sharp-edged exit	$K_{exp} = 1$ (Durfee et al., 2015)	-	-	-
$K_{entrance}$ $(dimensionless)$ loss coefficient for sharp-edged entrance	$K_{cont} = 0.5$ (Durfee et al., 2015)	-	-	-

K_{elbow} $(dimensionless)$ loss coefficient for a 90° elbow	$K_{elbow} = 0.9$ (Cundiff, 2002)	-	-	-
C_d $(dimensionless)$ orifice discharge coefficient	$C_d = 0.62$ (Durfee *et al.*, 2015, p. 27)	-	-	-
$d_{valve\_external}$ (m) diameter of the ports of the valve	-	-	-	It depends on pipe dimeter. It is assumed to be: $d_{valve\ external} = D_{pipe}$
$D_{valve\_internal}$ (m) internal diameter of the valve	-	-	-	It depends on $d_{valve\_external}$ and it is slightly bigger than that. It is assumed to be: $D_{valve_{internal}} = 1.4 d_{valve\_external}$
A_{orif} (m^2) orifice cross-sectional area	-	-	-	$A_{orif} =$ $= \pi D_{valve\ internal} d_{valve\ external}$
K_{orif} orifice equivalent loss coefficient	-	-	-	$K_{orif} = C_d A_{orif} \sqrt{2/\rho}$

Table D. 6 Parameters defining pipes and discrete components.

Accumulator & gas

Design parameters	Constants	*Primary independent variables*	*Secondary independent variables*	*Dependent variables*
P_{max} (Pa) maximum hydraulic pressure in the accumulator	-	$100 \cdot 10^5$, $50 \cdot 10^5$, $20 \cdot 10^5$	-	-

P_{min} (Pa) minimum rated pressure in the accumulator	-	-	-	$P_{min} = 0.5 \cdot P_{max}$ given the compression ration $\frac{P_{max}}{P_{min}} = 2$ (as recommended by some suppliers (HYDAC, 2015, p. 80))
$P_{pre-charge}(Pa)$ accumulator pre-charge pressure	-	-	-	$P_{pre-charge} = 0.90 \cdot P_{min}$ $= 0.45 \cdot P_{max}$
V_A (m^3) nominal volume of the accumulator	-	-	$V_A = 250cc$ This size was chosen for the reasons explained in section 3.4.3	-
$V_{acc_{pre-charge}}$ (m^3) oil volume at pre-charge in the accumulator	$V_{acc_{pre-charge}} = 0m^3$ There is no fluid in the accumulator at pre-charge	-	-	-
$V_{gas_{pre-charge}}(m^3)$ gas volume at pre-charge in the accumulator	-	-	-	$V_{gas_{pre-charge}} = V_A$ It corresponds to the nominal volume of the diaphragm accumulator (HYDAC, 2013, 2017)
k $(dimensionless)$ polytropic index	$k = 1.4$ for adiabatic process	-	-	-
R $\left(\frac{J}{mol \cdot K}\right)$ ideal gas constant	$R = 8.314$	-	-	-
$C_{V\,N_2}$ $\left(\frac{J}{kg \cdot K}\right)$ gas specific heat at constant volume for N_2	$C_{V\,N_2} = 741.95$	-	-	-

$h_{N_2}\left(\frac{W}{m^2 \cdot K}\right)$ convection heat transfer coefficient for N_2	$h_{N_2} = 25$	-	-	-
$n_{N_2}\ (mol)$ required number of moles of N_2 in the accumulator	-	-	-	$n_{N_2} = \dfrac{P_{pre-charge}V_{gas_{pre-charge}}}{RT_{pre-charge}}$ (with $T_{pre-charge} = T_{env} = 293K$)
$M_{N_2}\left(\frac{g}{mol}\right)$ molecular weight of N_2	$M_{N_2} = 28.014$	-	-	-
$m_{N_2}\ (kg)$ required mass of N_2	-	-	-	$m_{N_2} = n_{N_2} \cdot M_{N_2}$
$\tau\ (s)$ thermal time-constant	-	-	-	$\tau = \dfrac{m_{N_2}C_{V\,N_2}}{h_{N_2}A_W}$ with A_W total internal surface area of the accumulator exposed to gas (see Appendix A.5)

Table D. 7 Parameters defining the accumulator and the gas.

Appendix E:

Novel prosthesis - mass estimate

Table E. 1 shows a rough estimate of the mass of the whole prosthesis. The material of each components was selected according to what is reported for off-the-shelf components when possible, otherwise a reasonable material was chosen. The exact mass of the components is reported, sourced directly from catalogues, or estimated based on the proportion of off-the-shelf components, or evaluated directly in Solidworks (once the material is selected).

COMPONENT		MATERIAL	DENSITY ($\frac{kg}{m^3}$)	MASS (kg)	SOURCE
foot	inferior laminate	twill carbon fibre	1520	0.05874	material properties from Pace (2015), mass calculation in Solidworks
	superior laminate			0.09359	
ankle connection (between foot laminates and cams)		stainless steel	7700	0.16311	material properties and mass calculation in Solidworks
cams	stance	stainless steel	7700	0.03179	material properties and mass calculation in Solidworks
	push-off			0.03363	
roller: 19 mm diameter, 11 mm height (to be considered twice)		steel	-	0.021 (2x)	mass from catalogue (SKF, 2013, p. 1134)
roller pin (to be considered twice)		stainless steel	7700	0.00390 (2x)	material properties and mass calculation in Solidworks
two self-aligning linear ball bearings: 10 mm height, 10 mm internal diameter, 16 mm external diameter (to be considered twice)		-	-	approximately 2 x 0.0027 (2x)	estimate based on the proportion of those ones with a plastic cage and steel raceway segments by SKF (2014, p. 13): 10 mm height, 3 mm internal diameter, 7 mm external diameter, 0.0007 kg
piston (to be considered twice)	rod	stainless steel 1.4305	7900	0.03712 (2x)	same material used for pistons in HYDAIRA (p. 5), mass calculation in Solidworks
	head			0.02654 (2x)	

cylinder (to be considered twice)	stainless steel 1.4301	7900	0.05540 (2x)	same material used for cylinders in HYDAIRA (p. 5), mass calculation in Solidworks
follower return spring (to be considered twice)	stainless steel 1.4310	7900	0.00192 (2x)	same material used for springs in LESJOFORS (p. 12), mass calculation in Solidworks
O-ring (to be considered twice)	nitril (NBR)	1150	0.00040 (2x)	same material used for O-rings in HYDAIRA (p. 12), mass calculation in Solidworks
aesthetic cover	aluminium alloy 7075	2810	0.24090	material properties and mass calculation in Solidworks
male adapter	titanium alloy	4428,78	0.06481	material properties form Pace (2015), mass calculation in Solidworks
Total weight (excluding the pylon with the integrated accumulator)			0.98993	-
Total weight (with the $0.557\ kg$ pylon included)			**1.54693**	-

Table E. 1 Estimate of the mass of the components included in the novel hydraulic ankle, together with the two carbon fibre laminates, the ankle connection, the aesthetic cover and the male adapter depicted in Figure 8.1

The approximate mass of the pylon is $0.557\ kg$, as mentioned in Table E. 1, estimated as follows:

- Approximately $0{,}077\ kg$ for a carbon fibre pylon with a $6\ cm$ internal diameter, $11\ cm$ length ($12\ cm$ if the two tubular adapters at its ends are considered), and $2{,}5\ mm$ thickness (based on the proportion of a $50\ cm$ length, $3\ cm$ internal diameter, and $0.180\ kg$ pylon from http://www.roadrunnerfoot.com/eng/prodotti/tubi.html).

- Approximately $0.115\ kg$ for each one of the two aluminium alloy (7075) tubular adapters placed at the two pylon ends, with a $6\ cm$ internal diameter, a hypothesised $4\ cm$ height and $2\ mm$ thickness (based on the weight of a $3\ cm$ internal diameter and $0.075\ kg$ tubular adapter from http://www.roadrunnerfoot.com/eng/prodotti/attacchi.html). Thus $0.230\ kg$ in total.
- Approximately $0.250\ kg$ for a $250\ cc$ carbon-composite accumulator (see section 3.4.3).

For the other components missing, the mass is estimated as follows:

- An approximate mass of $0.050\ kg$ for the parallel torsional spring and $0.400\ kg$ for two miniaturised DCVs (estimated from https://nem-hydraulics.com/wp-content/uploads/2018/11/DT001GB001_IR02-Cartridge_CoverCatalogue.pdf).
- An estimate of $0.152\ kg$ for a total oil volume in the system of $175\ cc$. The oil volume in the $0.25\ l$ accumulator is estimated to be equal to $125\ cc$ when the accumulator is installed in the hydraulic circuit with a desired initial pressure at the beginning of the gait cycle ($P_{start} = 90\ bar$, section 4.6.4). A roughly $50\ cc$ are added for the oil in the rest of the system (i.e. in the tank and in the $1.96\ cc$ pipes between rams and the accumulator, with $L_{pipe} = 50mm$ and $D_{pipe} = 5mm$). The density of the selected mineral oil is $\rho = 870\frac{kg}{m^3}$ (see Appendix A.4).
- A tank surrounding the hydraulic rams with a mass perhaps as low as $0.200\ kg$. A $0.5\ l$ stainless steel low-pressure accumulator compatible with mineral oils weighs $1.2\ kg$ (Parker Hannifin, 2018, p. 35). However, the bespoke tank would be smaller (maybe $0.1\ l$) and, thus, its mass reduced, also thanks to the use of composite materials (mass reduced by around 75% (Crompton Technology Group Ltd, 2020)).

Therefore, the estimated total mass of the whole assembly is approximately $2.35\ kg$, which seems to match the mass corresponding to the $28.38\ cm$ distance from the ground to the distal connection with the socket (approximately $2.43\ kg$).

References

Ai, J., Chen, J.-F., Rotter, J. M., & Ooi, J. Y. (2011). Assessment of rolling resistance models in discrete element simulations. *Powder Technology*(206), 269-282. doi:10.1016/j.powtec.2010.09.030

Ansari, A., Atkeson, C. G., Choset, H., & Travers, M. (2015). *A Survey of Current Exoskeletons and Their Control Architectures and Algorithms (Draft 4.0)*. Retrieved from http://www.cs.cmu.edu/~cga/exo/survey.pdf

Au, S. K., Dilworth, P., & Herr, H. (2006, May). *An Ankle-Foot Emulation System for the Study of Human Walking Biomechanics.* Paper presented at the IEEE International Conference on Robotics and Automation (ICRA), Orlando, Florida.

Au, S. K., Herr, H., Weber, J., & Martinez-Villalpando, E. C. (2007, August 23-26,2007). *Powered Ankle-Foot Prosthesis for the Improvement of Amputee Ambulation.* Paper presented at the 29th Annual International Conference of the IEEE EMBS, Cité Internationale, Lyon, France.

Bari, A. Z. (2013). *An efficient energy storage and return prosthesis.* (PhD). University of Salford,

Behrens, S. M., Unal, R., Hekman, E. E., Carloni, R., Stramigioli, S., & Koopman, H. F. (2011). Design of a fully-passive transfemoral prosthesis prototype. *Conf Proc IEEE Eng Med Biol Soc, 2011*, 591-594. doi:10.1109/iembs.2011.6090111

Bellman, R. D., Holgate, M. A., & Sugar, T. G. (2008, 19-22 Oct. 2008). *SPARKy 3: Design of an active robotic ankle prosthesis with two actuated degrees of freedom using regenerative kinetics.* Paper presented at the 2008 2nd IEEE RAS & EMBS International Conference on Biomedical Robotics and Biomechatronics.

Bergelin, B. J., & Voglewede, P. A. (2012). Design of an Active Ankle-Foot Prosthesis Utilizing a Four-Bar Mechanism. *Journal of Mechanical Design, 134*(6). doi:10.1115/1.4006436

Bergman, T. L., Lavine, A. S., Incropera, F. P., & Dewitt, D. P. (2011). *Fundamentals of Heat and Mass Transfer* (SEVENTH EDITION ed.): JOHN WILEY & SONS.

Bosch Rexroth AG, M. H. Mineral-oil Based Pressure Fluids for axial piston units. In.

Brackx, B., Van Damme, M., Matthys, A., Vanderborght, B., & Lefeber, D. (2013). Passive Ankle-Foot Prosthesis Prototype with Extended Push-Off. *International Journal of Advanced Robotic Systems, 10*(2), 101. doi:10.5772/55170

Campos, A., & Durfee, W. K. (2015). *Experimental validation of an analytical model for o-ring friction and leakage at high pressure*. Department of Mechanical Engineering. University of Minnesota. Minneapolis, MN, 55455 USA.

Cao, H., Zhu, J., Xia, C., Zhou, H., Chen, X., & Wang, Y. (2010). *Design and Control of a Hydraulic-Actuated Leg Exoskeleton for Load-Carrying Augmentation*, Berlin, Heidelberg.

Caputo, J. M., Adamczyk, P. G., & Collins, S. H. (2015). *Informing Ankle-Foot Prosthesis Prescription through Haptic Emulation of Candidate Devices*. Paper presented at the IEEE International Conference on Robotics and Automation (ICRA), Washington State Convention Center, Seattle, Washington.

Caputo, J. M., & Collins, S. H. (2014). Prosthetic ankle push-off work reduces metabolic rate but not collision work in non-amputee walking. *Scientific Reports, 4:7213*. doi:10.1038/srep07213

Cherelle, P., Grosu, V., Cestari, M., Vanderborght, B., & Lefeber, D. (2016). The AMP-Foot 3, new generation propulsive prosthetic feet with explosive motion characteristics: design and validation. *BioMedical Engineering OnLine*.

Cherelle, P., Mathijssen, G., Wang, Q., Vanderborght, B., & Lefeber, D. (2014). Advances in Propulsive Bionic Feet and Their Actuation Principles. *Advances in Mechanical Engineering, 6*, 984046. doi:10.1155/2014/984046

Chin, R., Hsiao-Wecksler, E. T., & Loth, E. (2012). Fluid-Power Harvesting by Under-Foot Bellows During Human Gait. *Journal of Fluids Engineering, 134*(8). doi:10.1115/1.4005725

Collins, S. H., & Kuo, A. D. (2010). Recycling Energy to Restore Impaired Ankle Function during Human Walking. *Plos ONE, 5*(2, e9307). doi:10.1371/journal

10.1371/journal.pone.0009307.g001

Craig, J. J. (2005). *Introduction to Robotics: Mechanics & Control*: Pearson Education International.

Crompton Technology Group Ltd. (2020).

Cundiff, J. S. (2002). *Fluid Power Circuits and Control. Fundamentals and Applications*. Blacksburg, Virginia USA: CRC Press.

Dedić, R., & Dindo, H. (2011, 27-29 Oct. 2011). *SmartLeg: An intelligent active robotic prosthesis for lower-limb amputees.* Paper presented at the 2011 XXIII International Symposium on Information, Communication and Automation Technologies.

Durfee, W. K., Sun, Z., & Van de Ven, J. (2015). *Fluid Power System Dynamics*.

Durfee, W. K., Xia, J., & Hsiao-Wecksler, E. (2011). *Tiny Hydraulics for Powered Orthotics*. Paper presented at the IEEE International Conference on Rehabilitation Robotics (ICRR), Rehab Week Zurich, ETH Zurich Science City, Switzerland.

Elliott, S. B. (2014). *The SYMBIONIC® LEG: A synergy of intelligent knee and ankle functions*. Retrieved from https://assets.ossur.com/library/34727

Engineering-abc.com. (n.d.). Coefficient of friction, Rolling resistance and Aerodynamics. Retrieved from http://www.tribology-abc.com/abc/cof.htm

Epe Italiana Srl. (2012). Hydropneumatic Accumulators and Components. In.

Everarts, C., Dehez, B., & Ronsse, R. (2012, 7-12 Oct. 2012). *Variable Stiffness Actuator applied to an active ankle prosthesis: Principle, energy-efficiency, and control.* Paper presented at the 2012 IEEE/RSJ International Conference on Intelligent Robots and Systems.

Everarts, C., Dehez, B., & Ronsse, R. (2015, 28 Sept.-2 Oct. 2015). *Novel infinitely Variable Transmission allowing efficient transmission ratio variations at rest.* Paper presented at the 2015 IEEE/RSJ International Conference on Intelligent Robots and Systems (IROS).

Everarts, C., Thissen, A. J. C., Dehez, B., Ijspeert, A. J., & Ronsse, R. (2011). *Control and Design of an Active Prosthesis Based on Adaptive Oscillators.* Paper presented at the 10th Belgian Day on Biomedical Engineering – joint meeting with IEEE EMBS Benelux Chapter.

Ferris, A. E., Aldridge, J. M., Rabago, C. A., & Wilken, J. M. (2012). Evaluation of a powered ankle-foot prosthetic system during walking. *Arch Phys Med Rehabil, 93*(11), 1911-1918. doi:10.1016/j.apmr.2012.06.009

Flowers, W. C., & Mann, R. W. (1977). An Electrohydraulic Knee-Torque Controller for a Prosthesis Simulator. *Journal of Biomechanical Engineering, 99*(1), 3-8. doi:10.1115/1.3426266

Flynn, L., Geeroms, J., Jimenez-Fabian, R., Vanderborght, B., & Lefeber, D. (2015, 11-14 Aug. 2015). *CYBERLEGS Beta-Prosthesis active knee system.* Paper presented at the 2015 IEEE International Conference on Rehabilitation Robotics (ICORR).

Flynn, L., Geeroms, J., Jimenez-Fabian, R., Vanderborght, B., Vitiello, N., & Lefeber, D. (2014). Ankle–knee prosthesis with active ankle and energy transfer: Development of the CYBERLEGs Alpha-Prosthesis. *Robotics and Autonomous Systems, 73*, 4-15. doi:10.1016/j.robot.2014.12.013

Gao, F., Liao, W., Chen, B., Ma, H., & Qin, L. (2015, 11-14 Aug. 2015). *Design of powered ankle-foot prosthesis driven by parallel elastic actuator.* Paper presented at the 2015 IEEE International Conference on Rehabilitation Robotics (ICORR).

Gardiner, J. (2017). *Modelling small hydraulic cylinders*. Retrieved from

Gardiner, J., Bari, A. Z., Howard, D., & Kenney, L. (2016). Transtibial amputee gait efficiency: Energy storage and return versus solid ankle cushioned heel prosthetic feet. *Journal of Rehabilitation Research & Development, 53*(6), 1133-1138. doi:10.1682/JRRD.2015.04.0066

Gardiner, J., Bari, A. Z., Kenney, L., Twiste, M., Moser, D., Zahedi, S., & Howard, D. (2017). Performance of optimised prosthetic ankle designs that are based on a hydraulic variable displacement actuator (VDA). *IEEE Transactions on Neural Systems and Rehabilitation Engineering, 25*(12), 2418 - 2426. doi:10.1109/TNSRE.2017.2763999

Gardiner, J., & Howard, D. (2016). *Novel ESR and powered prosthetic joints*. Retrieved from

Geeroms, J., Flynn, L., Jimenez-Fabian, R., Vanderborght, B., & Lefeber, D. (2013). *Ankle-Knee Prosthesis with Powered Ankle and Energy Transfer for CYBERLEGs α-Prototype.* Paper presented at the 2013 IEEE International Conference on Rehabilitation Robotics, Seattle, Washington USA.

Genin, J. J., Bastien, G. J., Franck, B., Detrembleur, C., & Willems, P. A. (2008). Effect of speed on the energy cost of walking in unilateral traumatic lower limb amputees. *European Journal of Applied Physiology, 103*(6), 655. doi:10.1007/s00421-008-0764-0

Gitter, A., Czerniecki, J. M., & DeGroot, D. M. (1991). Biomechanical analysis of the influence of prosthetic feet on below-knee amputee walking. *Am J Phys Med Rehabil, 70*(3), 142-148. doi:10.1097/00002060-199106000-00006

Grabowski, A. M., D'Andrea, S. E., & Herr, H. M. (2011, March). *BIONIC LEG PROSTHESIS EMULATES BIOLOGICAL ANKLE JOINT DURING WALKING.* Paper presented at the Annual Meeting of the American Society of Biomechanics, Long Beach, CA, USA.

Grimmer, M., Eslamy, M., & Seyfarth, A. (2014). *Energetic and Peak Power Advantages of Series Elastic Actuators in an Actuated Prosthetic Leg for Walking and Running*.

Grimmer, M., Holgate, M., Holgate, R., Boehler, A., Ward, J., Hollander, K., . . . Seyfarth, A. (2016). A powered prosthetic ankle joint for walking and running. *Biomed Eng Online, 15*(Suppl 3), 141. doi:10.1186/s12938-016-0286-7

Guglielmino, E., Semini, C., Kogler, H., Scheidl, R., & Caldwell, D. G. (2010, 18-22 Oct. 2010). *Power hydraulics - switched mode control of hydraulic actuation.* Paper presented at the 2010 IEEE/RSJ International Conference on Intelligent Robots and Systems.

Han, X., Lu, L., Zheng, Y., Feng, X., Li, Z., Li, J., & Ouyang, M. (2019). A review on the key issues of the lithium ion battery degradation among the whole life cycle. *eTransportation, 1*, 100005. doi:https://doi.org/10.1016/j.etran.2019.100005

Hansen, A. H., Childress, D. S., Miff, S. C., Gard, S. A., & Mesplay, K. P. (2004). The human ankle during walking: implications for design of biomimetic ankle prostheses. *Journal of Biomechanics, 37*(10), 1467-1474. doi:https://doi.org/10.1016/j.jbiomech.2004.01.017

Herr, H., & Grabowski, A. M. (2012, 13 Jul). *Bionic ankle–foot prosthesis normalizes walking gait for persons with leg amputation.* Paper presented at the Proceeding of the Royal Society B.

Hitt, J. K., Bellman, R., Holgate, M., Sugar, T. G., & Hollander, K. W. (2007). *The SPARKy (Spring Ankle With Regenerative Kinetics) Project: Design and Analysis of a Robotic Transtibial Prosthesis With Regenerative Kinetics.* Paper presented at the ASME 2007 International Design Engineering Technical Conferences and Computers and Information in Engineering Conference.

Hitt, J. K., Merlo, J. L., & Johnston, J. D. (2010). *BIONIC RUNNING FOR UNILATERAL TRANSTIBIAL MILITARY AMPUTEES*.

Hitt, J. K., Sugar, T. G., Holgate, M., & Bellman, R. (2010). An Active Foot-Ankle Prosthesis With Biomechanical Energy Regeneration. *Journal of Medical Devices, 4*(1). doi:10.1115/1.4001139

Holgate, M., & Sugar, T. G. (2014). *Active Compliant Parallel Mechanisms.* Paper presented at the ASME 2014 International Design Engineering Technical Conferences and Computers and Information in Engineering Conference.

Hollander, K. W., Ilg, R., Sugar, T. G., & Herring, D. (2006). An efficient robotic tendon for gait assistance. *J Biomech Eng, 128*(5), 788-791. doi:10.1115/1.2264391

Hollander, K. W., Sugar, T. G., & Herring, D. E. (2005, 28 June-1 July 2005). *Adjustable robotic tendon using a 'Jack Spring'.* Paper presented at the 9th International Conference on Rehabilitation Robotics, 2005. ICORR 2005.

Hsu, M., Nielsen, D. H., Lin-Chan, S., & Shurr, D. (2006). The Effects of Prosthetic Foot Design on Physiologic Measurements, Self-Selected Walking Velocity, and Physical Activity in People With Transtibial Amputation. *Archives of Physical Medicine and Rehabilitation, 87*(1), 123-129. doi:https://doi.org/10.1016/j.apmr.2005.07.310

Huang, T. P., Shorter, K. A., Adamczyk, P. G., & Kuo, A. D. (2015). Mechanical and energetic consequences of reduced ankle plantar-flexion in human walking. *The Journal of Experimental Biology, 218*(22), 3541-3550. doi:10.1242/jeb.113910

Huo, W., Mohammed, S., Moreno, J. C., & Amirat, Y. (2016). Lower Limb Wearable Robots for Assistance and Rehabilitation: A State of the Art. *IEEE Systems Journal, 10*(3), 1068-1081. doi:10.1109/JSYST.2014.2351491

HYDAC, T. C. (2013). Sizing Accumulators. In.

HYDAC, T. C. (2015). Accumulators: Bladder, Piston, Diaphragm. In.

HYDAC, T. C. (2017). Diaphragm Accumulators. In.

HYDAIRA. Hydraulic Cylinders. In.

Hydraulics, I. (2018). Standard Hydraulic Cylinder Range. In.

HYDRO LEDUC. (2010). Hydro-pneumatic accumulators. In.

IKO. (2016). Cam Followers & Roller Followers. In.

IKO. (2017). CAM FOLLOWERS. In.

Isakov, E., Burger, H., Gregoric, M., & Marincek, C. (1996). Stump length as related to atrophy and strength of the thigh muscles in trans-tibial amputees. *Prosthetics and Orthotics International, 20*(2), 96-100.

Ishikawa, M., Komi, P. V., Grey, M. J., Lepola, V., & Bruggemann, G. P. (2005). Muscle-tendon interaction and elastic energy usage in human walking. *Journal of Applied Physiology, 99*(2), 603-608. doi:10.1152/japplphysiol.00189.2005

Jarvis, H. L., Bennett, A. N., Twiste, M., Phillip, R. D., Etherington, J., & Baker, R. (2017). Temporal Spatial and Metabolic Measures of Walking in Highly Functional Individuals With Lower Limb Amputations. *Archives of Physical Medicine and Rehabilitation, 98*(7), 1389-1399. doi:https://doi.org/10.1016/j.apmr.2016.09.134

Kangude, A., Burgstahler, B., Kakastys, J., & Durfee, W. (2009). Single channel hybrid FES gait system using an energy storing orthosis: preliminary design. *Conf Proc IEEE Eng Med Biol Soc, 2009*, 6798-6801. doi:10.1109/iembs.2009.5333976

Kim, H., Seo, C., Shin, Y. J., Kim, J., & Kang, Y. S. (2015, 7-11 July 2015). *Locomotion control strategy of hydraulic lower extremity exoskeleton robot.* Paper presented at the 2015 IEEE International Conference on Advanced Intelligent Mechatronics (AIM).

Koganezawa, K., Fujimoto, H., & Kato, I. (1987). Multifunctional above-knee prosthesis for stairs' walking. *Prosthet Orthot Int, 11*(3), 139-145. doi:10.3109/03093648709078198

Kogler, H., Scheidl, R., Ehrentraut, M., Guglielmino, E., Semini, C., & Caldwell, D. G. (2010). *A Compact Hydraulic Switching Converter for Robotic Applications*.

Lawson, B. E., Mitchell, J., Truex, D., Shultz, A., Ledoux, E., & Goldfarb, M. (2014). A Robotic Leg Prosthesis: Design, Control, and Implementation. *IEEE Robotics & Automation Magazine, 21*(4), 70-81. doi:10.1109/MRA.2014.2360303

Lay, A. N., Hass, C. J., & Gregor, R. J. (2006). The effects of sloped surfaces on locomotion: A kinematic and kinetic analysis. *Journal of Biomechanics, 39*(9), 1621-1628. doi:https://doi.org/10.1016/j.jbiomech.2005.05.005

Lecture 21: FLOW AND FORCE ANALYSIS OF VALVES. (2017). Retrieved from http://nptel.ac.in/

Lecture 28: ACCUMULATORS. (2017). Retrieved from http://nptel.ac.in/

LESJOFORS. Springs.

MachineDesign. (2002). Accumulators. Retrieved from https://www.machinedesign.com/basics-design/accumulators

MachineDesign. (2007). Optimizing reciprocating motion. Retrieved from https://www.machinedesign.com/archive/article/21828554/optimizing-reciprocating-motion

Mancinelli, C., Patritti, B. L., Tropea, P., Greenwald, R. M., Casler, R., Herr, H., & Bonato, P. (2011). Comparing a passive-elastic and a powered prosthesis in transtibial amputees. *Conf Proc IEEE Eng Med Biol Soc, 2011*, 8255-8258. doi:10.1109/iembs.2011.6092035

Martini, L. J. (1984). *Practical seal design.*: Taylor & Francis Inc.

Matthys, A., Cherelle, P., Van Damme, M., Vanderborght, B., & Lefeber, D. (2012). *Concept and design of the HEKTA (Harvest Energy from the Knee and Transfer it to the Ankle)*

transfemoral prosthesis. Paper presented at the Fourth IEEE RAS/EMBS International Conference on Biomedical Robotics and Biomechatronics, Rome, Italy.

MechDesigner. (2017). Forced and Form Closed Cam Types. Retrieved from http://mechdesigner.support/index.htm?cam-design-arrangements.htm

Medical EXPO. (2018). Dynamic prosthetic foot / Standard / Adult. Retrieved from http://www.medicalexpo.com/prod/roadrunnerfoot/product-105938-707024.html

Mitchell, M., Craig, K., Kyberd, P., Biden, E., & Bush, G. (2013). Design and development of ankle-foot prosthesis with delayed release of plantarflexion. *Journal of rehabilitation research and development, 50*(3), 409-422. doi:10.1682/jrrd.2011.06.0107

Neubauer, B. C. (2017). *Principles of Small-Scale Hydraulic Systems for Human Assistive Machines.* (Ph.D.). UNIVERSITY OF MINNESOTA,

Neubauer, B. C., Nath, J., & Durfee, W. K. (2014). *Design of a Portable Hydraulic Ankle-Foot Orthosis.* Paper presented at the 36th Annual International Conference of the IEEE, Engineering in Medicine and Biology Society (EMBC).

Nickel, E., Sensinger, J., & Hansen, A. (2014). Passive prosthetic ankle-foot mechanism for automatic adaptation to sloped surfaces. *Journal of rehabilitation research and development, 51*(5), 803-814. doi:10.1682/jrrd.2013.08.0177

Otten, A., Voort, C., Stienen, A., Aarts, R., van Asseldonk, E., & van der Kooij, H. (2015). LIMPACT:A Hydraulically Powered Self-Aligning Upper Limb Exoskeleton. *IEEE/ASME Transactions on Mechatronics, 20*(5), 2285-2298. doi:10.1109/TMECH.2014.2375272

Pace, A. (2015). *PROGETTAZIONE DI UN NUOVO PIEDE PROTESICO IBRIDO IN FIBRA DI CARBONIO.* (Master of Science). POLITECNICO DI MILANO,

Pahl, G., Beitz, W., Feldhusen, J., & Grote, K. H. (2007). *Engineering design: A systematic approach.* (Third ed.): Springer.

Parker Hannifin. Bladder Accumulators. In.

Parker Hannifin. Diaphragm Accumulators. In.

Parker Hannifin. (2007a). O-Ring Handbook. In.

Parker Hannifin. (2007b). Parker O-Ring Handbook. In.

Parker Hannifin. (2018). Accumulator, Accessories and Spares Catalogue. In.

Perry, J., Burnfield, J. M., Newsam, C. J., & Conley, P. (2004). Energy expenditure and gait characteristics of a bilateral amputee walking with C-leg prostheses compared with stubby and conventional articulating prostheses. *Archives of Physical Medicine and Rehabilitation, 85*(10), 1711-1717. doi:10.1016/j.apmr.2004.02.028

Pourmovahed, A., & Otis, D. R. (1990). An Experimental Thermal Time-Constant Correlation for Hydraulic Accumulators. *Journal of Dynamic Systems, Measurement, and Control - Transactions of the ASME, 112*, 116-121.

Pratt, G. A., & Williamson, M. M. (1995, 5-9 Aug. 1995). *Series elastic actuators.* Paper presented at the Proceedings 1995 IEEE/RSJ International Conference on Intelligent Robots and Systems. Human Robot Interaction and Cooperative Robots.

Pratt, J., Krupp, B., & Morse, C. (2002). Series elastic actuators for high fidelity force control. *Industrial Robot: An International Journal, 29*(3), 234-241. doi:10.1108/01439910210425522

RAMKO. HYDRAULIC CYLINDERS. In.

Realmuto, J., Klute, G., & Devasia, S. (2015). Nonlinear Passive Cam-Based Springs for Powered Ankle Prostheses. *Journal of Medical Devices, 9*(1). doi:10.1115/1.4028653

REXROTH. (2013). Diaphragm-type accumulator. In.

Rice, J. J., & Schimmels, J. M. (2014). *Design and Evaluation of a Passive Ankle Prosthesis With Rotational Power Generation by a Compliant Coupling Between Leg Deflection and Ankle Rotation.* Paper presented at the ASME 2014 International Design Engineering Technical Conferences and Computers and Information in Engineering Conference.

Rice, J. J., & Schimmels, J. M. (2015). Evaluation of a Two Degree of Freedom Passive Ankle Prosthesis With Powered Push-Off. *Journal of Medical Devices, 9*(3). doi:10.1115/1.4030551

Richter, H., Hui, X., van den Bogert, A., & Simon, D. (2016, 19-22 Sept. 2016). *Semiactive virtual control of a hydraulic prosthetic knee.* Paper presented at the 2016 IEEE Conference on Control Applications (CCA).

Rothbart, H. A. (2004). *Cam Design Handbook* (H. A. Rothbart Ed.). USA: McGraw-Hill Handbooks.

Ruina, A., & Pratap, R. (2019). *Introduction to MECHANICS for engineers*: Springer.

Russell Esposito, E., Aldridge Whitehead, J. M., & Wilken, J. M. (2015). Step-to-step transition work during level and inclined walking using passive and powered ankle-foot prostheses. *Prosthet Orthot Int, 40*(3), 311-319. doi:10.1177/0309364614564021

Saivimal, S., Zhi, Q., Niveditha, M., Wenlong, Z., & Panagiotis, P. (2018). A Soft-Inflatable Exosuit for Knee Rehabilitation: Assisting Swing Phase During Walking. *Frontiers in Robotics and AI, 5*(44). doi:10.3389/frobt.2018.00044

Sawicki, G. S., & Ferris, D. P. (2008). Mechanics and energetics of level walking with powered ankle exoskeletons. *The Journal of Experimental Biology, 211*, 1402-1413. doi:10.1242/jeb.009241

Segal, A. D., Zelik, K. E., Klute, G. K., Morgenroth, D. C., Hahn, M. E., Orendurff, M. S., . . . Czerniecki, J. M. (2012). The effects of a controlled energy storage and return prototype prosthetic foot on transtibial amputee ambulation. *Human Movement Science, 31*(4), 918-931. doi:https://doi.org/10.1016/j.humov.2011.08.005

Shepherd, M. K., & Rouse, E. J. (2017, 29 May-3 June 2017). *Design of a quasi-passive ankle-foot prosthesis with biomimetic, variable stiffness.* Paper presented at the 2017 IEEE International Conference on Robotics and Automation (ICRA).

Shultz, A. H., Mitchell, J. E., Truex, D., Lawson, B. E., & Goldfarb, M. (2013, 6-10 May 2013). *Preliminary evaluation of a walking controller for a powered ankle prosthesis.* Paper presented at the 2013 IEEE International Conference on Robotics and Automation.

SKF. (2011). Linear bearings and units. Technical handbook. In.

SKF. (2013). Rolling bearings. In.

SKF. (2014). Linear bearings and units with SKF factory pre-lubrication. In.

Smith, J. D., & Martin, P. E. (2013). Effects of prosthetic mass distribution on metabolic costs and walking symmetry. *J Appl Biomech, 29*(3), 317-328. doi:10.1123/jab.29.3.317

Smith, W. A., Samorezov, S., Davis, B. L., & Van den Bogert, A. J. (2014). US Patent No.

Sophyn, S., & Koganezawa, K. (2015). *ABOVE KNEE PROSTHESIS FOR ASCENDING/DESCENDING STAIRS WITH NO EXTERNAL ENERGY SOURCE.*

Paper presented at the Assistive Robotics - Proceedings of the 18th International Conference on CLAWAR 2015.

Staros, A., & Murphy, E. F. (1964). *Properties of Fluid Flow Applied to Above-Knee Prostheses*. New York, N.Y.

STEERFORTH. HFR / NFR HYDRAULIC CYLINDERS. In.

Stepien, J. M., Cavenett, S., Taylor, L., & Crotty, M. (2007). Activity levels among lower-limb amputees: self-report versus step activity monitor. *Arch Phys Med Rehabil, 88*(7), 896-900. doi:10.1016/j.apmr.2007.03.016

Sun, J., Fritz, J. M., Del Toro, D. R., & Voglewede, P. A. (2014). Amputee Subject Testing Protocol, Results, and Analysis of a Powered Transtibial Prosthetic Device. *J Med Device, 8*(4), 0410071-0410076. doi:10.1115/1.4027497

Sup, F., Bohara, A., & Goldfarb, M. (2008). Design and Control of a Powered Transfemoral Prosthesis. *THE INTERNATIONAL JOURNAL OF ROBOTICS RESEARCH*.

Sup, F., Varol, H. A., Mitchell, J., Withrow, T. J., & Goldfarb, M. (2009a). Preliminary Evaluations of a Self-Contained Anthropomorphic Transfemoral Prosthesis. *IEEE ASME Trans Mechatron, 14*(6), 667-676. doi:10.1109/tmech.2009.2032688

Sup, F., Varol, H. A., Mitchell, J., Withrow, T. J., & Goldfarb, M. (2009b, June 23-26). *Self-Contained Powered Knee and Ankle Prosthesis: Initial Evaluation on a Transfemoral Amputee*. Paper presented at the 2009 IEEE 11th International Conference on Rehabilitation Robotics, Kyoto International Conference Center, Japan.

Takahashi, K. Z., Horne, J. R., & Stanhope, S. J. (2015). Comparison of mechanical energy profiles of passive and active below-knee prostheses: a case study. *Prosthet Orthot Int, 39*(2), 150-156. doi:10.1177/0309364613513298

The Engineering ToolBox. (2003). Specific Heat and Individual Gas Constant of Gases. Retrieved from https://www.engineeringtoolbox.com/specific-heat-capacity-gases-d_159.html

The Engineering Toolbox. (2008). Rolling Resistance. Retrieved from http://www.engineeringtoolbox.com/rolling-friction-resistance-d_1303.html

The MathWorks Inc. (2018). Hydraulic Fluid. *Simulink*. Retrieved from https://uk.mathworks.com/help/physmod/hydro/ref/hydraulicfluid.html

The Physics Factbook. Density of Steel. Retrieved from https://hypertextbook.com/facts/2004/KarenSutherland.shtml

Unal, R., Behrens, S. M., Carloni, R., Hekman, E. E. G., Stramigioli, S., & Koopman, H. F. J. M. (2010, 26-29 Sept. 2010). *Prototype design and realization of an innovative energy efficient transfemoral prosthesis*. Paper presented at the 2010 3rd IEEE RAS & EMBS International Conference on Biomedical Robotics and Biomechatronics.

Unal, R., Carloni, R., Behrens, S. M., Hekman, E. E. G., Stramigioli, S., & Koopman, H. F. J. M. (2012, 24-27 June 2012). *Towards a fully passive transfemoral prosthesis for normal walking*. Paper presented at the 2012 4th IEEE RAS & EMBS International Conference on Biomedical Robotics and Biomechatronics (BioRob).

Unal, R., Carloni, R., Hekman, E. E. G., Stramigioli, S., & Koopman, H. F. (2010, 18-22 Oct. 2010). *Conceptual design of an energy efficient transfemoral prosthesis*. Paper presented at the 2010 IEEE/RSJ International Conference on Intelligent Robots and Systems.

Unal, R., Klijnstra, F., Behrens, S. M., Hekman, E. E. G., Stramigioli, S., Koopman, H. F. J. M., & Carloni, R. (2014, 25-29 Aug. 2014). *The control of recycling energy strorage capacity for WalkMECHadapt.* Paper presented at the The 23rd IEEE International Symposium on Robot and Human Interactive Communication.

Unal, R., Klijnstra, F., Burkink, B., Behrens, S. M., Hekman, E. E., Stramigioli, S., . . . Carloni, R. (2013). Modeling of WalkMECH: a fully-passive energy-efficient transfemoral prosthesis prototype. *IEEE Int Conf Rehabil Robot, 2013*, 6650406. doi:10.1109/icorr.2013.6650406

van den Bogert, A. J., Samorezov, S., Davis, B. L., & Smith, W. A. (2012). Modeling and Optimal Control of an Energy-Storing Prosthetic Knee. *Journal of Biomechanical Engineering, 134*, 051007-051001/051008. doi:10.1115/1.4006680]

van der Linde, H., Hofstad, C. J., Geurts, A. C., Postema, K., Geertzen, J. H., & van Limbeek, J. (2004). A systematic literature review of the effect of different prosthetic components on human functioning with a lower-limb prosthesis. *Journal of rehabilitation research and development, 41*(4), 555-570. doi:10.1682/jrrd.2003.06.0102

Veale, A. J., & Xie, S. Q. (2016). Towards compliant and wearable robotic orthoses: A review of current and emerging actuator technologies. *Medical Engineering & Physics, 38*(4), 317-325. doi:https://doi.org/10.1016/j.medengphy.2016.01.010

Versluys, R., Beyl, P., Van Damme, M., Desomer, A., Van Ham, R., & Lefeber, D. (2009). Prosthetic feet: State-of-the-art review and the importance of mimicking human ankle-foot biomechanics. *Disability and Rehabilitation: Assistive Technology, 4*(2), 65-75. doi:10.1080/17483100802715092

Ward, J. A., Schroeder, K., Vehon, D., Holgate, R., Boehler, A., & Grimmer, M. (2015). *A RUGGED MICROPROCESSOR CONTROLLED ANKLE-FOOT PROSTHESIS FOR RUNNING.*

Warner, H., Simon, D., & Richter, H. (2016). *Design Optimization and Control of a Crank-Slider Actuator for a Lower-Limb Prosthesis with Energy Regeneration*. Paper presented at the IEEE International Conference on Advanced Intelligent Mechatronics (AIM), Banff, Alberta, Canada.

Waters, R. L., & Mulroy, S. (1999). The energy expenditure of normal and pathologic gait. *Gait and Posture, 9*, 207-231.

Wikipedia. (2020). List of thermal conductivities. Retrieved from https://en.wikipedia.org/wiki/List_of_thermal_conductivities

Williams, R. J., Hansen, A. H., & Gard, S. A. (2009). Prosthetic Ankle-Foot Mechanism Capable of Automatic Adaptation to the Walking Surface. *Journal of Biomechanical Engineering, 131*(3), 035002. doi:10.1115/1.3005335

Wilmot, T., Thomas, G., Montavon, B., Rarick, R., van den Bogert, A., Szatmary, S., . . . Samorezov, S. (2013, April). *Biogeography-Based Optimization for Hydraulic Prosthetic Knee Control.* Paper presented at the Medical Cyber-Physical Systems Workshop, Philadelphia, Pennsylvania.

Wilson, A. B. (1968). *Recent Advances in Above-Knee Prosthetics*. Retrieved from http://www.oandplibrary.com/al/pdf/1968_02_001.pdf

Winter, D. A. (1984). Kinematic and kinetic patterns in human gait: Variability and compensating effects. *Human Movement Science, 3*(1), 51-76. doi:https://doi.org/10.1016/0167-9457(84)90005-8

Winter, D. A. (1991). *Biomechanics and motor control of human gait: Normal, Elderly and Pathological* (2nd ed.): Waterloo Biomechancs.

Winter, D. A. (2009). *Biomechanics and Motor Control of Human Movement* (Fourth ed.): John Wiley & Sons, Inc.

Woo, H., Song, S., Jeon, D., & Kong, K. (2014, 8-11 July 2014). *Design of a compact hydraulic actuation mechanism for active ankle-foot prostheses.* Paper presented at the 2014 IEEE/ASME International Conference on Advanced Intelligent Mechatronics.

Xia, J. (2015). *Modeling and Analysis of Small-Scale Hydraulic Systems.* (PhD). University of Minnesota,

Xia, J., Braun, K. L., & Durfee, W. K. (2011). *Small-Scale Hydraulics for Human Assist Devices*. Paper presented at the Design of Medical Devices Conference (DMD), Minneapolis, MN, USA.

Xia, J., & Durfee, W. K. (2011a). *Analysis of Small-Scale Hydraulic Actuation Systems*. Department of Mechanical Engineering. University of Minnesota. Minneapolis, MN, 55455 USA.

Xia, J., & Durfee, W. K. (2011b). *Modeling of Tiny Hydraulic Cylinders*. Paper presented at the 52nd National Conference on Fluid Power, Las Vegas, Nevada, USA.

Xia, J., & Durfee, W. K. (2014, Sep 10-12). *Experimentally validated models of o-ring seals for tiny hydraulic cylinders.* Paper presented at the Symposium on Fluid Power & Motion Control (FPMC), Bath, United Kingdom.

Yagi, A., Matsumiya, K., Masamune, K., Liao, H., & Dohi, T. (2006). *Rigid-Flexible Outer Sheath Model Using Slider Linkage Locking Mechanism and Air Pressure for Endoscopic Surgery*, Berlin, Heidelberg.

Yali, H., Jia, S., & Wang, X. (2013). Design and Simulation of an Ankle Prosthesis with Lower Power Based on Human Biomechanics. *Robot, 35*. doi:10.3724/SP.J.1218.2013.00276

Young, A. J., & Ferris, D. P. (2017). State of the Art and Future Directions for Lower Limb Robotic Exoskeletons. *IEEE Transactions on Neural Systems and Rehabilitation Engineering, 25*(2), 171-182. doi:10.1109/TNSRE.2016.2521160

Zhang, Y., Finger, S., & Behrens, S. Introduction to Mechanisms. Retrieved from http://www.cs.cmu.edu/~rapidproto/mechanisms/examples.html

Zhu, J., Wang, Q., & Wang, L. (2014). On the Design of a Powered Transtibial Prosthesis With Stiffness Adaptable Ankle and Toe Joints. *IEEE Transactions on Industrial Electronics, 61*(9), 4797-4807. doi:10.1109/TIE.2013.2293691